DISSERTATION

Numerical Study of Quantum Transport in Carbon Nanotube-Based Transistors

ausgeführt zum Zwecke der Erlangung des akademischen Grades
eines Doktors der technischen Wissenschaften

eingereicht an der Technischen Universität Wien
Fakultät für Elektrotechnik und Informationstechnik
von

MAHDI POURFATH

Spengergasse 4-8/2/1
A-1050 Wien, Österreich

Matr. Nr. 0326624
geboren am 18. Juli 1978 in Tehran

Wien, im Juli 2007

Kurzfassung

Um den Anforderungen der Skalierung in der Mikroelektronik gerecht zu werden, wird die Einführung neuer Strukturen und Materialien notwendig. Dazu zählen etwa multiple gate MOSFETs, Carbon Nanotube Feldeffekttransistoren (CNT-FETs) und auf Molekülen basierende Transistoren. Auf Grund der hervorragenden elektronischen Eigenschaften von carbon nanotubes (CNTs) wurden CNT-FETs in den vergangenen Jahren vermehrt als mögliche Alternative zu CMOS Bauelementen untersucht. Einige dieser Eigenschaften sind quasi-ballistischer Ladungsträgertransport, geringe Elektromigration und Unterdrückung von Kurzkanaleffekten auf Grund der ein-dimensionalen Transporteigenshaften. Die nahezu symmetrische Bandstruktur von Valenz- und Leitungsband ermöglicht symmetrische p- und n-Kanal Transistoren für komplementäre Logik. Da CNTs sowohl mit metallischem als auch halbleitendem Verhalten realisiert werden können, ist eine vollständig auf CNTs basierende Elektronik vorstellbar.

Zur Erforschung der in CNT-FETs auftretenden physikalischen Effekte und zur Verbesserung ihrer Leistungskennzahlen und Funktionalität wurden selbstkonsistente quantenmechanische Simulationen durchgeführt. Dazu wurde der Formalismus der Nichtgleichgewichts-GREENschen Funktionen (NEGF) verwendet. Dieser stellt eine sehr mächtige Methode zur Behandlung von Vielteilchensystemen sowohl im thermodynamischen Gleichgewicht als auch im Nichtgleichgewicht dar.

Die numerische Implementierung des NEGF-Formalismus wird mit besonderem Augenmerk auf die Reduktion von Speicher- und Rechenzeitbedarf durchgeführt. Der Fokus auf die rechnerische Effizienz ist notwendig, um kurze Simulationszeiten zu ermöglichen und großangelegte Anwendungen wie Bauelementoptimierung durchführbar zu machen. Zur exakten Analyse sind weiters die Quantentransportgleichungen selbstkonsistent mit der POISSON-Gleichung zu lösen. Dazu wurde ein iteratives Lösungsschema angewandt, wobei das Konvergenzverhalten der Methode einen entscheidenden Faktor darstellt. Das Konvergenzverhalten der selbstkonsistenten Iteration wurde untersucht und daraus Methoden zur Verbesserung der Konvergenzrate entwickelt.

Die numerischen Methoden wurden im Rahmen des vielseitigen, quantenmechanischen Bauelementsimulators VIENNA SCHRÖDINGER-POISSON (VSP) implementiert und zur Untersuchung von CNT-FETs angewandt. Basierend auf den Erkenntnissen aus den Simulationsergebnissen ist ein tieferes Verständnis der Bauelementfunktion und ihrer Abhängigkeit von Material- und Geometrieparametern möglich.

Die ambipolare Leitung in CNT-FETs, welche die Transistoreigenshaften stark beeinträchtigen kann, wurde genauer untersucht. Die Simulationen zeigen, dass dieses Verhalten durch eine Doppel-Gate-Struktur unterdrückt werden kann. Dabei wird die Ladungsträgerinjektion an den Source- und Drain Kontakten unabhängig voneinander gesteuert. Das erste Gate steuert die Ladungsträgerinjektion am Source-Kontakt, während das zweite Gate die parasitäre Ladungsträgerinjektion am Drain-Kontakt unterdrückt.

Da allerdings die Herstellung von Einfach-Gate-Bauelementen praktikabler ist, wurden auch für diese Bauelemente Möglichkeiten zur Reduktion des ambipolaren Leitung untersucht. Es wird gezeigt dass die Eigenshaften von Einfach-Gate CNT-FETs durch Optimierung der Gate-Source und Gate-Drain Abstände enorm verbessert werden können. Die zu Grunde liegenden Effekte unterscheiden sich deutlich von jenen in konventionellen MOSFETs.

Abschließend werden die Auswirkungen der Elektron-Phonon Wechselwirkung auf die Bauelementeigenschaften im Detail untersucht. In Übereinstimmung mit Experimenten zeigen unsere Ergebnisse, dass Streuung mit hochenergetischen Phononen zwar den Strom im eingeschalteten Zustand kaum beeinflusst, jedoch auf Grund von Ladungsansammlung im Kanal die Schaltzeiten merklich verschlechtert. Für Streuung mit niederenergetischen Phononen findet man das umgekehrte Verhalten vor. In den für elektronische Anwendungen geeigneten CNTs dominiert bei Raumtemperatur allerdings Elektron-Phonon Wechselwirkung mit hochenergetischen Phononen. Daher liegt der Strom von CNT-FETs im eingeschalteten Zustand nahe am ballistischen Limit, die Schaltzeiten hingegen deutlich darunter.

Abstract

NOVEL STRUCTURES and materials such as multiple gate MOSFETs, carbon nanotube field-effect transistors (CNT-FETs), and molecular based transistors, are expected to be introduced to meet the requirements for scaling. CNT-FETs have been considered in recent years as potential alternatives to CMOS devices due to excellent electronic properties of carbon nanotubes (CNTs). Some of the interesting electronic properties of CNTs are quasi-ballistic carrier transport, suppression of short-channel effects due to one-dimensional electron transport, nearly symmetric structure of the conduction and valence bands, which is advantageous for complementary applications, and high resistance against electro-migration. Since CNTs can be both metallic or semiconducting, an all-CNT electronics can be envisioned.

To explore the physics of CNT-FETs and to find methods to improve the functionality and performance of these devices we performed self-consistent quantum mechanical simulations. The non-equilibrium Green's function (NEGF) formalism is used in this work. It provides a very powerful technique for evaluating properties of many-particle systems both in thermodynamic equilibrium and also in non-equilibrium situations.

The numerical implementation of the outlined method is presented. Methods to reduce computational cost and memory requirement are discussed. Employing such techniques allows one to perform simulations in a reasonable amount of time, which is essential for large-scale applications such as device optimizations. For accurate analysis we solved the quantum transport equations with the Poisson equation self-consistently. To solve the system of equations we used an iterative method, the convergence of which is a critical issue. We analyzed the convergence behavior of self-consistent simulations and propose methods to improve the convergence behavior.

The numerical methods are implemented in the multi-purpose quantum-mechanical device simulator Vienna Schrödinger-Poisson (VSP) solver, which has extensively been applied to study CNT-FETs. Based on simulation results one can obtain a deeper insight into device operation and its dependence on material and geometrical parameters.

We investigated the ambipolar conduction of CNT-FETs, which deteriorates the device characteristics. Based on the results we propose a double-gate structure to suppress the ambipolar behavior. In this device type carrier injection at the source and drain contacts are controlled separately. The first gate controls carrier injection at the source contact and the second one controls carrier injection at the drain contact, which can be used to suppress parasitic carrier injection.

Reduction of ambipolar conduction of single-gate devices has been studied. We show that the performance of single-gate CNT-FETs can be considerably improved by optimizing the gate-source and gate-drain spacer lengths. The results indicate that the exploited effects are very different from that in conventional MOSFETs.

Finally, the effect of electron-phonon interactions on the device characteristics is discussed in detail. In agreement with experimental data, our results indicate that scattering with high energy phonons reduces the on-current only weakly, but can increase the switching time considerably due to charge pileup in the channel. Scattering with low energy phonons can reduce the on-current more effectively, but has a weaker effect on the switching time. In a CNT at room temperature scattering processes are mostly due to electron-phonon interaction with high energy phonons. Therefore, the on-current of CNT-FETs can be close to the ballistic limit, whereas the switching time is found to be significantly below that limit.

Acknowledgment

I WOULD LIKE to express my deep gratefulness to my thesis adviser, Prof. Hans Kosina. He impressed me with his deep knowledge on semiconductor device modeling and physics and I learned a lot of material from numerous discussions we had. Prof. Siegfried Selberherr, who gave me the opportunity to join his research group, for providing the excellent infrastructure at the Institute for Microelectronics.

I would like to thank Prof. Tibor Grasser for his helps and advises on Minimos-NT. Furthermore, I thank Prof. Erasmus Langer, the head of the Institute for Microelectronics, who was a cooperative and helpful boss.

Discussions with Prof. David Pulfrey, from the University of British Colombia, on adaptive integration and small signal analysis of nanotube transistors are acknowledged.

I thank Prof. Emmerich Bertagnolli that he was willing to serve on my examination committee.

The special thanks goes to Oskar Baumgartner for careful proofreading of my thesis, Andreas Gehring and Enzo Ungersböck who have been always willing to help me with programing topics, Viktor Sverdlov for numerous discussion on quantum transport, Tesfaye Ayalew for giving me important advices for my life, Robert Entner and Martin Wagner for helping me to fix the problems of the operating systems on my PCs, and finally I am grateful to Alireza Sheikholeslami who helped me to have a smooth transition to my new life in Vienna.

I enjoyed the luck to work closely together with Markus Karner and other group members: Siddhartha Dhar, Stefan Holzer, Gerhard Karlowatz, Ling Li, Gregor Meller, Vassil Palankovski, Oliver Triebl, Martin Vasicek, Wilfried Wessner and Robert Wittmann.

Ewald Haslinger, Manfred Katterbauer, and Renate Winkler provided the background work at the Institute, which much too often is completely undervalued. All other members of the Institute for Microelectronics deserve gratitude for assistance and for the stimulating working atmosphere they create.

More important than any other support, my wife Sara provided me with love and understanding. Finally, none of my studies would have been possible without the continuous support of my parents.

Contents

List of Abbreviations and Acronyms

AP	Acoustic phonons
CMOS	Complementary MOS
CNT	Carbon nanotube
CNT-FET	Carbon nanotube FET
CVD	Chemical vapor deposition
DG	Double-gate
DOS	Density of states
FET	Field-effect transistor
ITRS	International Technology Roadmap for Semiconductors
MOS	Metal-oxide-semiconductor
MOSFET	MOS field-effect transistor
NEGF	Non-equilibrium Green's function
OP	Optical phonons
RBM	Radial breathing mode
SEM	Scanning electron microscopy
SB	Schottky barrier
SG	Single-gate
TB	Tight-binding
VSP	Vienna Schrödinger-Poisson solver
SW-CNT	Single wall CNT
MW-CNT	Multi wall CNT

List of Symbols

Notation

x	...	Scalar
x^*	...	Complex conjugate of x
$\mathbf{x}$	...	Vector
$\mathbf{e}_x$	...	Unity vector in direction x
$\mathbf{x} \cdot \mathbf{y}$	...	Scalar inner product
$\partial_t(\cdot)$	...	Partial derivative with respect to t
∇	...	Nabla operator
$\nabla\mathbf{x}$	...	Gradient of $\mathbf{x}$
$\nabla \cdot \mathbf{x}$	...	Divergence of $\mathbf{x}$
$\nabla \cdot \nabla = \nabla^2$	...	Laplace operator
$\underline{A}$	...	Matrix
A_{ij}	...	Elements of the matrix $\underline{A}$
$\underline{A}^\dagger$	...	Conjugate transposed matrix: $A_{ij} = A^*_{ji}$
I	...	Unity matrix
$\det(\cdot)$	...	Determinant of a matrix
G	...	Green's function
H	...	Hamiltonian in the first quantization
$\hat{H}$	...	Hamiltonian in the second quantization
$\hat{\psi}$	...	Field operator
b	...	Annihilation operator for bosons
c	...	Annihilation operator for fermions
$b^\dagger$	...	Creation operator for bosons
$c^\dagger$	...	Creation operator for fermions
$\langle\cdot\rangle$	...	Statistical average
$\otimes$	...	Convolution

Physical Quantities

Symbol	Unit	Description
$q\chi_{\mathrm{CNT}}$	eV	Electron affinity of a CNT
$q\Phi_{\mathrm{CNT}}$	eV	Work function of a CNT
$q\Phi_{\mathrm{M}}$	eV	Work function of the metal
$q\Phi_{\mathrm{Be}}$	eV	Energy barrier height for electrons
$q\Phi_{\mathrm{Bh}}$	eV	Energy barrier height for holes
ϕ	V	Electrostatic potential
$\hbar\omega$	eV	Phonon energy
D_{OP}	eV^2	Electron-optical-phonon coupling coefficient
D_{AP}	eV^2	Electron-acoustic-phonon coupling coefficient
E	eV	Energy
E_{f}	eV	FERMI energy
E_{c}	eV	Conduction band edge energy
E_{v}	eV	Valence band edge energy
E_{g}	eV	Band gap energy
E_{i}	eV	Intrinsic energy
g	$\mathrm{m}^{-1}\mathrm{eV}^{-1}$	Density of states
$\mathbf{J}$	A	Current
k	m^{-1}	Wave number
$\mathbf{k}$	m^{-1}	Wave number vector
ε	$\mathrm{AsV}^{-1}\mathrm{m}^{-1}$	Dielectric permittivity
L_{GS}	m	Gate-source spacer length
L_{DS}	m	Drain-source space length
m	kg	Mass
$\widetilde{M}_{\mathrm{OP}}$	eV/Å	Reduced matrix elements of electron-optical-phonon interaction
$\widetilde{M}_{\mathrm{AP}}$	eV	Reduced matrix elements of electron-acoustic-phonon interaction
n_{B}	1	Bose-EINSTEIN distribution function
n_{F}	1	FERMI-DIRAC distribution function
n	m^{-1}	Electron concentration
p	m^{-1}	Hole concentration
N_{D}	m^{-1}	Concentration of donors
N_{A}	m^{-1}	Concentration of acceptors
$\mathbf{r}$	m	Space vector
ϱ	m^{-1}	Carrier concentration
t	s	Time
T	K	Temperature
U	eV	Potential energy
V_{GS}	V	Gate-source voltage
V_{DS}	V	Drain-source voltage

Constants

h	...	PLANCK's constant	$6.6260755 \times 10^{-34}\,\mathrm{Js}$
$\hbar$	...	Reduced PLANCK's constant	$h/(2\,\pi)$
$\mathrm{k_B}$	...	BOLTZMANN's constant	$1.380662 \times 10^{-23}\,\mathrm{JK^{-1}}$
q	...	Elementary charge	$1.6021892 \times 10^{-19}\,\mathrm{C}$
$\mathrm{m_0}$	...	Electron rest mass	$9.1093897 \times 10^{-31}\,\mathrm{kg}$
ε_0	...	Dielectric constant of vacuum	$8.8541878 \times 10^{-12}\,\mathrm{AsV^{-1}m^{-1}}$
i	...	$\sqrt{-1}$	

Chapter 1

Introduction

THE INCREASING demand for higher computing power, smaller dimensions, and lower power consumption of integrated circuits leads to a pressing need to downscale semiconductor components. However, downscaling of conventional MOSFETs leads to many problems, such as short-channel effects, gate-leakage current, and so forth. Therefore, novel structure and materials such as multiple gate MOSFETs, CNT-FETs, and molecular based transistors, are expected to be introduced to meet the requirements for scaling [1].

Since the discovery of carbon nanotubes (CNTs) by IIJIMA in 1991 [2], significant progress has been achieved in both understanding the fundamental properties and exploring possible engineering applications. The possible application for nano-electronic devices has been extensively explored since the demonstration of the first CNT transistors (CNT-FETs) [3, 4].

CNTs are attractive for nano-electronic applications due to their excellent electrical properties. The phase space for scattering is severely reduced due to the one-dimensional nature of the density of states. The low scattering probability is responsible for high on-current in semiconducting CNT transistors. Due to the chemical stability and perfection of the CNT structure carrier mobility is not affected by processing and roughness scattering as it is in the conventional semi-conductor channel. The fact that there are no dangling bond states at the surface of CNTs allows for a wide choice of gate insulators. This improves gate control while meeting gate leakage constrains. The purely one-dimensional transport properties of the SW-CNTs should lead to a suppression of short-channel effects in transistor devices [5]. Furthermore, the conduction and valence bands are symmetric, which is advantageous for complementary applications, and finally, the combined impact of transport and electrostatic benefits together with the fact that semiconducting CNTs are, unlike silicon, direct-gap materials, suggests applications in opto-electronics as well [6, 7].

Chapter 2 describes the fundamentals of CNTs. It presents a comprehensive overview of electron and phonon properties along with electron-phonon interaction parameters, which are the key points to understand transport phenomena in CNTs. The chapter continues with a brief historical overview of CNT-FETs. The operation of these devices can be explained in terms of SCHOTTKY barriers which are formed at the metal-CNT interfaces. CNT-FETs can operate by modulating the transmission coefficient through these barriers, which results in device characteristics different from that of conventional MOSFETs.

Chapter 3 outlines the theory of the non-equilibrium GREEN's function (NEGF) formalism. Knowledge of the single-particle GREEN's function provides both the complete equilibrium or non-equilibrium properties of the system and the excitation energies of the systems containing one more or one less particle. The many-particle information about the system is cast into self-energies, parts of the equations of motion for the GREEN's functions. GREEN's functions can be expressed as a perturbation expansion, which is the key to approximate the self-energies. GREEN's functions provide a very powerful technique for evaluating properties of many-particle systems both in thermodynamic equilibrium and also in non-equilibrium situations. This formalism has been successfully used to investigate the characteristics of nano-scale transistors [8, 9], CNT-FETs [5, 10], and molecular transistors [11].

Chapter 4 discusses the numerical implementation of the NEGF formalism to study quantum transport in CNT-FETs. To solve the transport equations numerically they have to be discretized. The discretization of the transport equations in both the spatial and energy domain are discussed in detail. We employed a tight-binding HAMILTONian and applied a mode-space transformation to reduce the computational cost. The calculation of self-energies due to electron-phonon interactions are also presented in this chapter. Finally, the iterative method for self-consistent simulation and its convergence rate is studied.

In **Chapter 5** several applications are discussed. By using the described methodology the physics of CNT-FET has been explored. A comprehensive study of the role of electron-phonon interaction on the performance of CNT-FETs is presented. Scaling of some geometrical parameters is investigated and we show that by appropriately selecting these parameters considerable improved performance can be achieved.

Finally, **Chapter 6** briefly summarizes the thesis with some conclusions.

Chapter 2

Fundamentals of Carbon Nanotubes

CARBON MATERIALS are found in a variety of forms such as fullerenes, graphite, carbon fibres, carbon nanotubes, and diamond. The reason why carbon assumes many structural forms is that a carbon atom can form several distinct types of orbital hybridization. The sp^n hybridization is essential for determining the dimensionality of not only carbon based molecules but also carbon based solids. Carbon is the only element in the periodic table that has isomers from zero-dimensions to three-dimensions, see Table 2. In sp^n hybridization, $(n+1)$ σ bonds per carbon atom are formed, which form a skeleton for the local structure of the n-dimensional structure. In sp hybridization, two σ bonds form a one-dimensional chain structure, which is known as a carbyne. Interestingly, sp^2 hybridization, which forms a planer structure in two-dimensional graphite, also forms a planar local structure in the closed polyhedra of the (zero-dimensional) fullerene family and the one-dimensional cylinders called *carbon nanotubes* (CNTs). Carbon fibers which are macroscopic one-dimensional materials are closely related to CNTs, because of their characteristic high length to diameter ratio. A carbon fiber, however, consists of many graphite planes and microscopically exhibits electronic properties that are predominantly two-dimensional. Amorphous graphite, showing mainly sp^2 hybridization, consisting of randomly stacked graphite layer segments. Because of the weak inter-planer interaction between two graphite planes, they can move easily relative to each other, thereby forming a solid lubricant. In this sense, amorphous graphite can behave like a two-dimensional material. Four σ bonds defining a regular tetrahedron are sufficient to form a three-dimensional structure known as the diamond structure. Amorphous carbon is a disordered, three-dimensional material in which both sp^2 and sp^3 hybridization is present.

CNTs are unique nano-structures that can be considered conceptually a prototype one-dimensional quantum wire. The fundamental building block of CNTs is the very long, all-carbon cylindrical single-wall CNT (SW-CNT), one atom in wall thickness and tens of atoms around the circumference (typical diameter $\sim$ 1.4 nm). Initially, CNTs gained great interest in research community because of their exotic electronic properties, and this interest continued as other remarkable properties were discovered and promise of practical applications developed. In this chapter, a brief historical review of CNT research is presented and some basic definitions relevant to the structural properties of CNTs are provided. Finally, application of CNTs in electronics, especially CNT based transistors, are discussed.

Dimension	0-D	1-D	2-D	3-D
Isomer	Fullerene	Nanotubes	Graphite	Diamond
Hybridization	sp^2	sp^2	sp^2	sp^3
Density [g/cm^3]	1.72	1.2 – 2.0	2.26	3.52
Bond Length (Å)	1.40 (C=C)	1.42 (C=C)	1.42 (C=C)	1.54 (C-C)
Electronic Properties	Semiconductor $E_g = 1.9$ eV	Semiconductor or Metal	Semi-metal	Insulator $E_g = 5.47$ eV

Table 2.1: Important carbon isomers [12].

2.1 Historical Overview

Very small diameter (less than 10 nm) carbon filaments were prepared in the 1970's and 1980's through the synthesis of vapor grown carbon fibers by the decomposition of hydrocarbons at high temperatures in the presence of transition metal catalyst particles with diameters of less than 10 nm [13–15]. However, no detailed systematic studies of such very thin filaments were reported in these early years, and it was not until the observation of CNTs in 1991 by Iijima of the NEC laboratory using high resolution transmission electron microscopy [2].

It was Iijima's observation of multi-wall CNTs (MW-CNTs) (see Fig. 2.1) in 1991 [2] that heralded the entry of many scientists into the field of CNTs, stimulated at first by the remarkable one-dimensional quantum effects predicted for their electronic properties, and subsequently by the promise that the remarkable structure and properties of CNTs might give rise to some unique applications. Although the initial experimental observations were for MW-CNTs, SW-CNTs had been the basis for a large body of theoretical studies and predictions that preceded their experimental observation. The most striking of these theoretical developments was the prediction that CNTs could be either semiconductors or metals depending on their characteristics, namely their diameters and the orientation of their hexagons with respect to the CNT axis (chiral angle) [16–18]. Though predicted in 1992, it was not until 1998 that these predicted remarkable electronic properties were corroborated experimentally [19, 20].

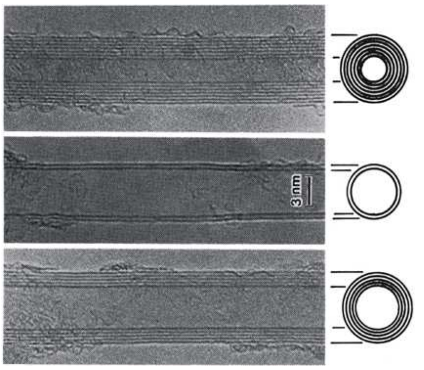

Figure 2.1: The observation of coaxial MW-CNTs by Iijima in 1991 [2].

2.2 Theoretical Background

The structure of CNTs has been explored early by high resolution transmission electron microscopy techniques yielding direct confirmation that the CNTs are seamless cylinders derived from the honeycomb lattice representing a single atomic layer of crystalline graphite, called a *graphene sheet*. The structure of a SW-CNT is conveniently explained in terms of its one-dimensional unit cell, defined by the vectors $\mathbf{C_h}$ and $\mathbf{T}$ as shown in Fig. 2.2.

The circumference of any CNT is expressed in terms of the chiral vector $\mathbf{C_h} = n\mathbf{a_1} + m\mathbf{a_2}$ which connects two crystallographically equivalent sites on a two-dimensional graphene sheet [16]. The construction in Fig. 2.2 depends uniquely on the pair of integers (n, m) which specify the chiral vector. The chiral angle θ is defined as the angle between the chiral vector $\mathbf{C_h}$ and the *zigzag* direction ($\theta = 0$). Three distinct types of CNT structures can be generated by rolling up the graphene sheet into a cylinder as shown in Fig. 2.3. The *zigzag* and *armchair* CNTs correspond to chiral angles of $\theta = 0$ and $\theta = 30°$, respectively, and *chiral* CNTs correspond to $0 < \theta < 30°$. The intersection of the vector $\overrightarrow{OB}$ (which is normal to $\mathbf{C_h}$) with the first lattice point determines the fundamental one-dimensional translation vector $\mathbf{T}$. The unit cell of the one-dimensional lattice is the rectangle defined by the vectors $\mathbf{C_h}$ and $\mathbf{T}$.

The cylinder connecting the two hemispherical caps of the CNT (see Fig. 2.3) is formed by superimposing the two ends of the vector $\mathbf{C_h}$ and the cylinder joint is made along the two lines $\overrightarrow{OB}$ and $\overrightarrow{AB'}$ in Fig. 2.2. The lines $\overrightarrow{OB}$ and $\overrightarrow{AB'}$ are both perpendicular to the vector $\mathbf{C_h}$ at each end of $\mathbf{C_h}$ [16]. In the (n, m) notation for $\mathbf{C_h} = n\mathbf{a_1} + m\mathbf{a_2}$, the vectors $(n, 0)$ or $(0, m)$ denote zigzag CNTs, whereas the vectors (n, m) correspond to chiral CNTs [21]. The CNT diameter d_{CNT} is given by

$$d_{\mathrm{CNT}} \;=\; \frac{|\mathbf{C_h}|}{\pi} \;=\; \frac{\sqrt{3}a_{\mathrm{C-C}}(m^2 \;+\; mn \;+\; n^2)^{1/2}}{\pi}\;, \tag{2.1}$$

where $|\mathbf{C_h}|$ is the length of $\mathbf{C_h}$ and $a_{\mathrm{C-C}}$ is the C-C bond length (1.42 Å). The chiral angle θ is given by $\theta \;=\; \tan^{-1}[\sqrt{3}n/(2m \;+\; n)]$. For the (n, n) armchair CNT $\theta = 30°$ and for the $(n, 0)$ zigzag CNT $\theta = 60°$. From Fig. 2.2 it follows that if one limits θ to the range $0 \leq \theta \leq 30°$, then by symmetry, $\theta = 0$ for a zigzag CNT. Both armchair and zigzag CNTs have a mirror plane and thus are considered achiral. Differences in the CNT diameter d_{CNT} and chiral angle θ give rise to different properties of the various CNTs. The number N of hexagons per unit cell of a CNT, specified by integers (n, m), is given by

$$N \;=\; \frac{2(m^2 \;+\; n^2 \;+\; nm)}{d_{\mathrm{R}}}\;, \tag{2.2}$$

where $d_{\mathrm{R}} = d$ if $n - m$ is not a multiple of $3d$, and $d_{\mathrm{R}} = 3d$ if $n - m$ is a multiple of $3d$, and d is defined as the greatest common divisor (gcd) of (n, m). Each hexagon in the honeycomb lattice contains two carbon atoms. The unit cell area of the CNT is N times larger than that for a graphene layer and consequently the unit cell area for the CNT in reciprocal space is correspondingly $1/N$ times smaller. Table 2.2 provides a summary of relations useful for describing the structure of SW-CNTs [12, 22].

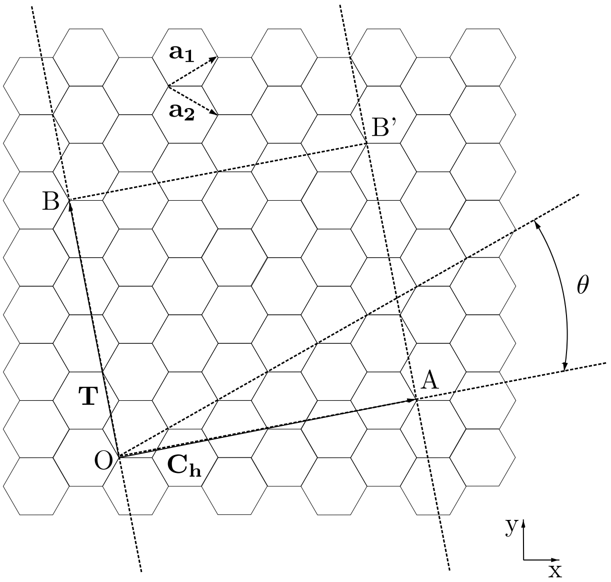

Figure 2.2: The chiral vector $\mathbf{C_h} = n\mathbf{a_1} + m\mathbf{a_2}$ is defined on the honeycomb lattice of carbon atoms by unit vectors $\mathbf{a_1}$ and $\mathbf{a_2}$ and the chiral angle θ with respect to the zigzag axis ($\theta = 0$). The diagram is constructed for $(n, m) = (4, 2)$.

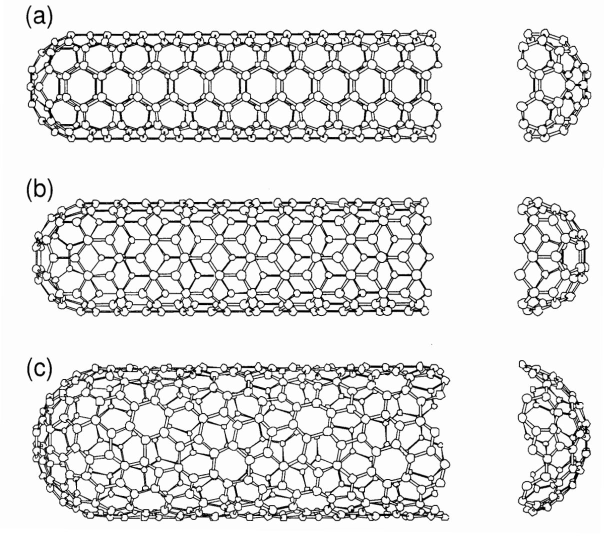

Figure 2.3: Schematic models of SW-CNTs with the CNT axis normal to the chiral vector. The latter is along (a) the $\theta = 30°$ direction for an (n, n) *armchair* CNT, (b) the $\theta = 0$ direction for a $(n, 0)$ *zigzag* CNT, and (c) a general θ direction with $0 < \theta < 30°$ for a (n, m) chiral CNT.

Symbol	Description	Formula
a	length of unit vectors	$a = \sqrt{3}a_{\mathrm{C-C}} = 2.49$ Å, $\quad a_{\mathrm{C-C}} = 1.42$ Å
$\mathbf{a_1}$, $\mathbf{a_2}$	unit vectors	$\left(\frac{\sqrt{3}}{2}, \frac{1}{2}\right) a, \ \left(\frac{\sqrt{3}}{2}, -\frac{1}{2}\right) a$
$\mathbf{b_1}$, $\mathbf{b_2}$	reciprocal lattice vectors	$\left(\frac{1}{\sqrt{3}}, 1\right) \frac{2\pi}{a}, \ \left(\frac{1}{\sqrt{3}}, -1\right) \frac{2\pi}{a}$
$\mathbf{C_h}$	chiral vector	$\mathbf{C_h} = n\mathbf{a_1} + m\mathbf{a_2} \equiv (n, m), \quad (0 \leq \lvert m \rvert \leq n)$
L	length of $\mathbf{C_h}$	$L = \lvert \mathbf{C_h} \rvert = a\sqrt{n^2 + m^2 + nm}$
d_{CNT}	diameter	$d_{\mathrm{CNT}} = \frac{L}{\pi}$
θ	chiral angle	$\tan(\theta) = \frac{\sqrt{3}}{2n + m}$
d	$\gcd(n, m)$	
d_{R}	$\gcd(2n + m, 2m + n)$	
$\mathbf{T}$	translational vector	$\mathbf{T} = t_1\mathbf{a_1} + t_2\mathbf{a_2} \equiv (t_1, t_2)$ $t_1 = \frac{2m + n}{d_{\mathrm{R}}}, \quad t_2 = -\frac{2n + m}{d_{\mathrm{R}}}$
T	length of $\mathbf{T}$	$T = \lvert \mathbf{T} \rvert = \frac{\sqrt{3}L}{d_{\mathrm{R}}}$
N	number of hexagons in the unit-cell	$N = \frac{2(n^2 + m^2 + mn)}{d_{\mathrm{R}}}$

Table 2.2: Structural properties for CNTs [12].

2.3 Nanotube Growth Methods

This section summarizes the progress made in recent years in CNT growth by various methods including arc-discharge, laser ablation, and chemical vapor deposition (CVD).

2.3.1 Arc-Discharge and Laser Ablation

Arc-discharge and laser ablation methods for the growth of CNTs have been actively pursued in the past decades. Both methods involve the condensation of carbon atoms generated from evaporation of solid carbon sources. The temperature involved in these methods are $3000-4000°$ C, close to the melting temperature of graphite.

In arc-discharge, carbon atoms are evaporated by a helium plasma initiated by high currents passed through an opposing carbon anode and cathode. Arc-discharge has been developed into an excellent method for producing both high quality MW-CNTs and SW-CNTs. For the growth of SW-CNTs, a metal catalyst is needed in the arc-discharge system. The first success in producing substantial amount of SW-CNTs by arc-discharge was achieved by BETHUNE and coworkers in 1993 [23], by using a carbon anode containing a small percentage of cobalt in the discharge experiment.

The growth of high quality SW-CNTs was achieved by SMALLEY and coworkers using a laser ablation method [24]. The method utilized intense laser pulses to ablate a carbon target containing 0.5 atomic percent of nickel and cobalt. The target was placed in a tube-furnace heated to 1200°C.

In SW-CNT growth by arc-discharge and laser ablation, typical by-products include fullerene, graphitic polyhedrons with enclosed metal particles, and amorphous carbon in the form of particles or over-coating on the CNT sidewalls.

2.3.2 Chemical Vapor Deposition

The growth process involves a catalyst material at high temperature in a tube furnace and a hydrocarbon gas flowing through the tube reactor for a period of time. Materials grown over the catalyst are collected upon cooling the system to room temperature. The key parameters in CVD growth of CNTs are the hydrocarbons, catalysts and growth temperature. The active catalytic species are typically transition-metal nano-particles formed on a support material such as alumina. The general CNT growth mechanism in a CVD process involves the dissolution and saturation of carbon atoms in the metal nano-particles. The precipitation of carbon from the saturated metal particle leads to the formation of tubular carbon solids in sp^2 structure. Tubular formation is favored over other forms of carbon such as graphitic sheets with open edges. This is because a tube contains no dangling bonds and, therefore, is in a low energy form.

Recent interests in CVD growth of CNTs are also due to the idea that aligned and ordered CNT structures can be grown on surfaces in a controlled manner that is not possible with arc-discharge or laser ablation techniques [25].

Methods developed to obtain MW-CNTs include CVD growth of tubes in the pores of meso-

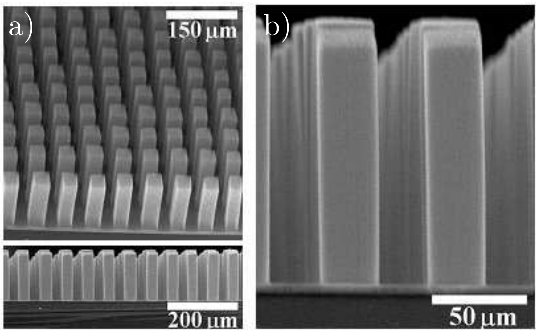

Figure 2.4: Self-aligned MW-CNT arrays grown by CVD on a catalytically patterned porous silicon substrate a) SEM image of tower structures consisting of aligned CNTs and b) SEM image of the side view of the towers [25].

porous silica. Dai and coworkers have devised growth strategies for ordered MW-CNTs and SW-CNTs by CVD on a catalytically patterned substrate [25]. They found that MW-CNTs can self-assemble into aligned structures as they grow, and the driving force for self-alignment is the Van der Waals interaction between CNTs [26]. The growth approach involves catalyst patterning and rational design of the substrate to enhance catalyst-substrate interaction and control the catalyst particle size. Figure 2.4 shows scanning electron microscopy (SEM) images of regularly positioned arrays of CNT towers grown from patterned iron squares on a porous silicon substrate.

Ordered SW-CNT structures can be directly grown by methane CVD on catalytically patterned substrates. A method has been devised to grow suspended SW-CNT networks with directionality on substrates containing lithographically patterned silicon pillars [27, 28]. Contact printing is used to transfer catalyst materials onto the pillar's tops selectively. CVD of methane using these substrates leads to suspended SW-CNTs forming nearly ordered networks with the CNT orientations directed by the pattern of the pillars (Fig. 2.5).

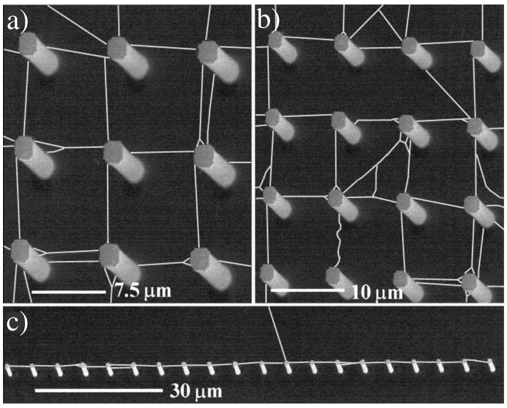

Figure 2.5: Directed growth of suspended SW-CNT a) and b) square of CNTs and c) CNT power-line structure [28].

2.4 Electronic Structure

The energy dispersion relations of SW-CNTs can be calculated using zone folding [18, 29], the tight-binding method [30], and density functional theory [31, 32]. In the simplest method the energy dispersion relations of CNTs are obtained by folding those of graphene.

2.4.1 Electronic Band Structure of Graphene

Within the tight-binding method the two-dimensional energy dispersion relations of graphene can be calculated by solving the eigen-value problem for a HAMILTONian $H_{\mathrm{g-2D}}$ associated with the two carbon atoms in the graphene unit cell [12]. In the SLATER-KOSTER scheme one gets[1]

$$H_{\mathrm{g-2D}} = \begin{bmatrix} 0 & f(k) \\ -f^{\dagger}(k) & 0 \end{bmatrix} . \tag{2.3}$$

where $f(k) = -t(1 + e^{i\mathbf{k}\cdot\mathbf{a_1}} + e^{i\mathbf{k}\cdot\mathbf{a_2}}) = -t(1 + 2e^{\sqrt{3}k_x a/2}\cos(k_y a/2))$ and t is the nearest neighbor C-C tight binding overlap energy[2] [29]. Solution of the secular equation $\det(H_{\mathrm{g-2D}} - EI) = 0$ leads to

$$E^{\pm}_{\mathrm{g-2D}}(\mathbf{k}) = \pm\, t\sqrt{1 + 4\cos\left(\frac{\sqrt{3}k_x a}{2}\right)\cos\left(\frac{k_y a}{2}\right) + \cos^2\left(\frac{k_y a}{2}\right)}\ , \tag{2.4}$$

where the $E^{+}_{\mathrm{g-2D}}$ and $E^{-}_{\mathrm{g-2D}}$ correspond to the π^* and the π energy bands, respectively. Figure 2.6 shows the electronic energy dispersion relations for graphene as a function of the two-dimensional wave-vector **k** in the hexagonal BRILLOUIN zone.

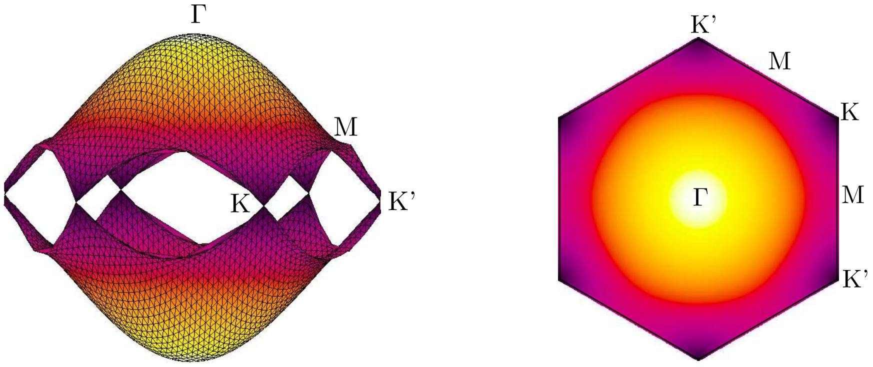

Figure 2.6: The energy dispersion relations for graphene are shown through the whole region of the BRILLOUIN zone. The lower and the upper surfaces denote the valence π and the conduction π^* energy bands, respectively. The coordinates of high symmetry points are $\Gamma = (0, 0)$, $\mathrm{K} = (0, 2\pi/3a)$, and $\mathrm{M} = (2\pi/\sqrt{3}a, 0)$. The energy values at the K, M, and Γ points are 0, t, and $3t$, respectively.

---

[1] We consider only the valence π and the conduction π^* energy band of graphene and CNTs.

[2] Experimentally the value $|t| = 2.7$ eV has been reported [19].

2.4.2 Electronic Band Structure of SW-CNTs

The electronic structure of a SW-CNT can be obtained from that of graphene. Assuming periodic boundary conditions in the circumferential direction characterized by the chiral vector $\mathbf{C_h}$, the wave vector associated with the $\mathbf{C_h}$ direction becomes quantized, while the wave-vector associated with the direction of the translational vector $\mathbf{T}$ (along the CNT axis) remains continuous for a CNT of infinite length. Thus the energy bands consist of a set of one-dimensional energy dispersion relations which are cross sections of those of graphene. Expressions for the reciprocal lattice vectors $\mathbf{K_2}$ along the CNT axis, $(\mathbf{C_h} \cdot \mathbf{K_2} = 0, \mathbf{T} \cdot \mathbf{K_2} = 2\pi)$, and $\mathbf{K_1}$ in the circumferential direction, $(\mathbf{C_h} \cdot \mathbf{K_2} = 0, \mathbf{T} \cdot \mathbf{K_2} = 2\pi)$, are given by (see Table 2.2)

$$\mathbf{K_1} \;=\; \frac{1}{N}(-t_2\mathbf{b_1} \;+\; t_1\mathbf{b_2})\;, \quad \mathbf{K_2} \;=\; \frac{1}{N}(m\mathbf{b_1} \;-\; n\mathbf{b_2})\;. \tag{2.5}$$

The one-dimensional energy dispersion relations of a SW-CNT can be written as

$$E^{\nu}_{\mathrm{CNT}}(k) \;=\; E_{\mathrm{g-2D}}\left(k\frac{\mathbf{K_2}}{|\mathbf{K_2}|} \;+\; \nu\mathbf{K_1}\right)\;, \tag{2.6}$$

where $-\pi/T < k < \pi/T$ is a one-dimensional wave-vector along the CNT axis and $\nu = 1, \ldots, N$. The periodic boundary condition for a CNT gives N discrete k values in the circumferential direction. The N pairs of energy dispersion curves given by (2.6) correspond to the cross sections of the two-dimensional energy dispersion surface of graphene. In Fig. 2.7 several cutting lines near one of the $\mathbf{K}$ points are shown. The separation between two adjacent lines and the length of the cutting lines are given by the $|\mathbf{K_1}| = 2/d_{\mathrm{CNT}}$ and $|\mathbf{K_2}| = 2\pi/T$, respectively. If the cutting line passes through a $\mathbf{K}$ point of the two-dimensional BRILLOUIN zone (Fig. 2.7-a), where the π and π^* energy bands of graphene are degenerate by symmetry, then the one-dimensional energy bands have a zero energy gap. When the $\mathbf{K}$-point is located between to cutting lines, $\mathbf{K}$ is always located in a position one-third of the distance between two adjacent $\mathbf{K_1}$ lines (Fig. 2.8-b) [29] and thus a semiconducting CNT with a finite energy gap is formed. If for a (n, m) CNT, $n - m$ is exactly divisible by 3 the CNT is metallic. CNTs with residuals 1 and 2 of the division $n - m$ by 3 are semiconducting.

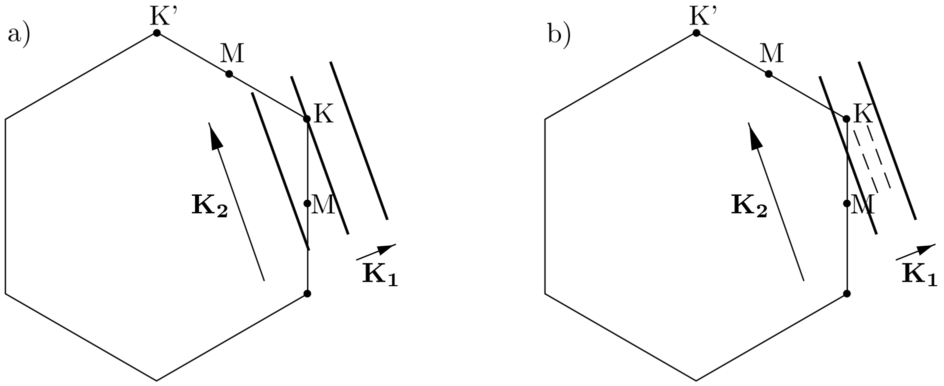

Figure 2.7: The one-dimensional wave-vectors k are shown in the BRILLOUIN zone of graphene as bold lines for (a) metallic and (b) semiconducting CNTs.

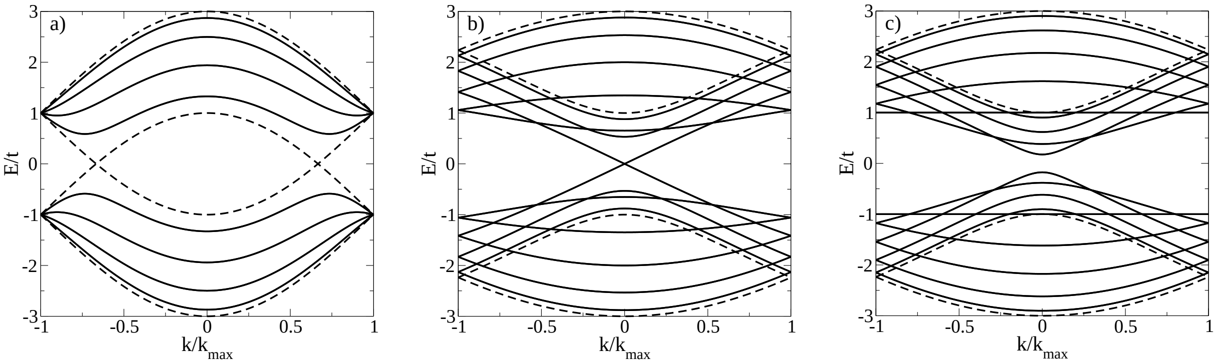

Figure 2.8: One-dimensional energy dispersion relations of a) the $(5,5)$ armchair CNT, b) the $(9,0)$ zigzag CNT, and c) the $(10,0)$ zigzag CNT. $k_{\max}$ for armchair and zigzag CNTs correspond to $k_{\max} = \pi/a$ and $k_{\max} = \pi/\sqrt{3}a$, respectively. Solid lines denote degenerate bands and dashed lines non-degenerate bands.

Figure 2.8 shows the energy dispersion relations for the $(5,5)$ armchair, the $(9,0)$ zigzag, and the $(10,0)$ zigzag CNTs. In general (n,n) armchair CNTs yield $4n$ energy subbands with $2n$ conduction and $2n$ valence bands. Of these $2n$ bands, two are non-degenerate and $n-1$ are doubly degenerate. The degeneracy comes from the two subbands with the same energy dispersion, but different ν-values. All armchair CNTs have a band degeneracy between the highest valence and the lowest conduction band (Fig. 2.8-a). In zigzag CNTs the lowest conduction and the highest valence bands are doubly degenerate (Fig. 2.8-b and Fig. 2.8-c).

In armchair and zigzag CNTs the bands are symmetric with respect to $k = 0$. Since the band of an armchair CNT has a minimum at point $k = 2\pi/3a$, it has a mirror minimum at point $k = -2\pi/3a$ and therefore two equivalent valleys are present around the point $\pm 2\pi/3a$. The bands of zigzag and chiral CNTs can have at most one valley (Fig. 2.8-b and Fig. 2.8-c).

In armchair CNTs the bands cross the FERMI level at $k = \pm 2\pi/3a$. Thus, all they are expected to exhibit metallic conduction [12]. There is no energy gap for the $(9,0)$ CNT at $k = 0$, whereas the $(10,0)$ CNT indeed shows an energy gap.

Electrical conduction is determined by states around the FERMI energy. Therefore, it is useful to develop an approximate relation that describes the dispersion relations in the regions around the FERMI energy $E_{\mathrm{F}} = 0$. This can be done by replacing the expression for $f(k) = -t(1 + 2e^{\sqrt{3}k_x a/2}\cos(k_y a/2))$ in (2.3) with a TAYLOR expansion around the point $(0, \pm 4\pi/3a)$ where the energy gap is zero and $f(k) = 0$. It is straightforward to show that $f(k) \approx (i\sqrt{3}at/2)\,(k_x \mp i\beta_y)$, with $\beta_y \equiv k_y \mp (4\pi/3a)$. The corresponding energy dispersion relation can be written as [33]

$$E_{\mathrm{g-2D}}(\mathbf{k}) \;=\; \pm|f(k)| \;=\; \pm\frac{\sqrt{3}at}{2}\sqrt{k_x^2 + \beta_y^2}\;. \tag{2.7}$$

The energy bands for $(n,0)$ zigzag CNTs can be obtained by imposing the periodic boundary conditions, which define the number of allowed wave-vectors k_y in the circumferential direction as $nk_y a = 2\pi\nu,\ (\nu = 1,\ldots,2n)$. This yields the one-dimensional dispersion relations for the $4n$

states of the $(n, 0)$ zigzag CNT

$$E^{\nu}(k_x) \;=\; \pm\frac{\sqrt{3}at}{2}\sqrt{k_x^2 \;+\; \left[\frac{4\pi}{3a}\left(\frac{3\nu}{2n}-1\right)\right]^2} \;, \quad -\pi/\sqrt{3}a < k_x < \pi/\sqrt{3}a \;. \tag{2.8}$$

Therefore, the energy gap for subband ν can be written as difference between the energies of the $+$ and $-$ branches at $k_x = 0$

$$E_{\mathrm{g}}^{\nu} \;=\; \sqrt{3}at\frac{2\pi}{na}\left(\nu - \frac{2n}{3}\right) \;. \tag{2.9}$$

The energy gap has a minimum value of zero corresponding to $\nu = 2n/3$. If n is not a multiple of three the minimum value of $\nu - 2n/3$ is equal to $1/3$. This means that the minimum energy gap is then given by

$$E_{\mathrm{g}} \;=\; \frac{\sqrt{3}at}{3}\frac{2\pi}{na} \;=\; \frac{2a_{\mathrm{C-C}}t}{d_{\mathrm{CNT}}} \;\approx \frac{0.8\ \mathrm{eV\ nm}}{d_{\mathrm{CNT}}} \;. \tag{2.10}$$

where $d_{\mathrm{CNT}} = na/\pi$ is the diameter of the CNT in nano-meters. Based on (2.8) and (2.9), the DOS for semiconducting zigzag CNTs is given by

$$g(E) \;=\; \sum_{\nu}\frac{8}{3\pi a_{\mathrm{C-C}}t}\frac{E}{\sqrt{E - E_{\mathrm{g}}^{\nu}/2}} \;, \tag{2.11}$$

which is an approximation valid as long as $(E - E_{\mathrm{F}}) \ll t$ [34]. VAN HOVE singularities in the DOS appearing at both the energy minima and maxima of the bands (see Fig. 2.9) are important for determining various solid-state properties of CNTs [35,36]

For all metallic CNTs, independent of their diameter and chirality, due to the nearly linear dispersion relations around the FERMI energy the density of states (DOS) per unit length along the CNT axis is a constant given by $8/3\pi a_{\mathrm{C-C}}t$ [12].

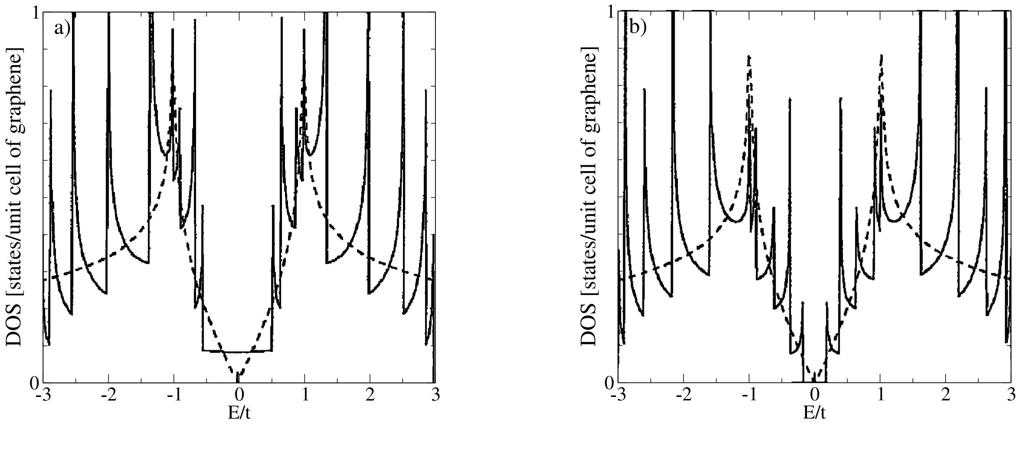

Figure 2.9: The density of states per unit cell of graphene for a) the $(9, 0)$ zigzag CNT which has metallic behavior and b) the $(10, 0)$ zigzag CNT which has semiconducting behavior. Dashed lines show the density of states for the graphene sheet [21].

2.5 Phonon Properties

The phonon dispersion relations of SW-CNTs can be calculated using zone folding [29], tight-binding methods [37–40], density functional theory [41–49], and symmetry-adapted models [50–54]. The phonon dispersion relations of SW-CNTs can be understood by zone folding of the phonon dispersion branches of graphene.

2.5.1 Phonon Dispersion Relations of Graphene

Since there are two carbon atoms, A and B, in the unit cell of graphene, one must consider 6 coordinates. The secular equation to be solved is thus a dynamical matrix of rank 6, such that 6 phonon branches are achieved.

The phonon dispersion relation of the graphene comprises three acoustic (A) branches and three optical (O) branches. The modes are associated with out-of-plane (Z), in-plane longitudinal (L), and in-plane transverse (T) atomic motions (Fig. 2.10-b).

Figure 2.10-b shows the phonon dispersion branches of graphene. The three phonon dispersion branches, which originate from the Γ-point of the Brillouin zone correspond to acoustic modes: an out-of plane mode (ZA), an in-plane transverse mode (TA), and in-plane longitudinal (LA), listed in order of increasing energy. The remaining three branches correspond to optical modes: one out-of plane mode (ZO), and two in-plane modes (TO) and (LO).

While the TA and LA modes display the normal linear dispersion around the Γ-point, the ZA mode shows a q^2 energy dispersion which is explained in [12] as a consequence of the $D_{6\mathrm{h}}$ point-group symmetry of graphene. Another consequence of the symmetry are the linear crossings of the ZA/ZO and the LA/LO modes at the K-point.

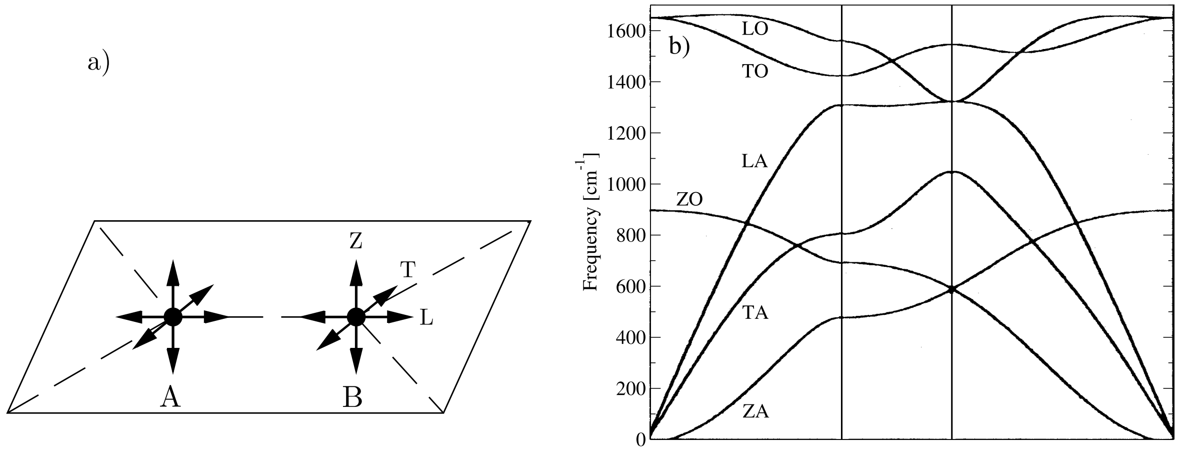

Figure 2.10: a) Atomic motions of carbon atoms in graphence can be along the out-of-plane (Z), in-plane transverse (T), and in-plane longitudinal (L) direction. b) The phonon dispersion branches for a graphene sheet, plotted along high symmetry directions [12].

2.5.2 Phonon Dispersion Relations of SW-CNTs

The phonon dispersion relations for a SW-CNT can be determined by folding that of a graphene layer (see Section 2.4.2). Since there are $2N$ carbon atoms in the unit cell of a CNT, $6N$ phonon dispersion branches for the three-dimensional vibrations of atoms are achieved. The corresponding one-dimensional phonon energy dispersion relation for the CNT is given by

$$\omega_{\mathrm{CNT}}^{\mu\lambda}(q) \;=\; \omega_{\mathrm{g-2D}}^{\lambda}(q\frac{\mathbf{K_2}}{|\mathbf{K_2}|} + \mu\mathbf{K_1}) \;, \tag{2.12}$$

where $\lambda = 1, \;\ldots,\; 6$ denotes the polarization, $\mu = 0, \ldots, N-1$ is the azimuthal quantum number, and $-\pi/T < q \leq \pi/T$ is the wave-vector of phonons. However, the zone-folding method does not always give the correct dispersion relation for a CNT, especially in the low frequency region. For example, the out-of-plane tangential acoustic (ZA) modes of a graphene sheet do not give zero energy at the $q = 0$ when rolled into a CNT. Here, at $q = 0$, all the carbon atoms of the CNT move radially in and out-of-plane radial acoustic vibration, which corresponds to a breathing mode (RBM) with a non-zero frequency [37]. To avoid these difficulties, one can directly diagonalize the dynamical matrix (see Fig. 2.11-a).

Fundamental phonon polarizations in CNTs are radial (R), transverse (T), and longitudinal (L). As shown in Fig. 2.11-b, zone center phonons, also referred to as Γ-point phonons, can belong to the transverse acoustic (TA), the longitudinal acoustic (LA), the radial breathing mode (RBM), the out-of-plane optical branch (RO), the transverse optical (TO), or the longitudinal optical (LO) phonon branch. The LO phonon branch near the Γ-point has an energy of ≈ 190 eV, whereas the energy of the RBM phonon branch is inversely proportional to the CNT diameter

$$\hbar\omega_{\mathrm{RBM}} \approx 28\ \mathrm{meV}/d_{\mathrm{CNT}} \;, \tag{2.13}$$

where d_{CNT} is the diameter of the CNT in nanometer [41, 42]. Zone boundary phonons, also referred to as K-point phonons, are found to be a a mixture of fundamental polarizations [55].

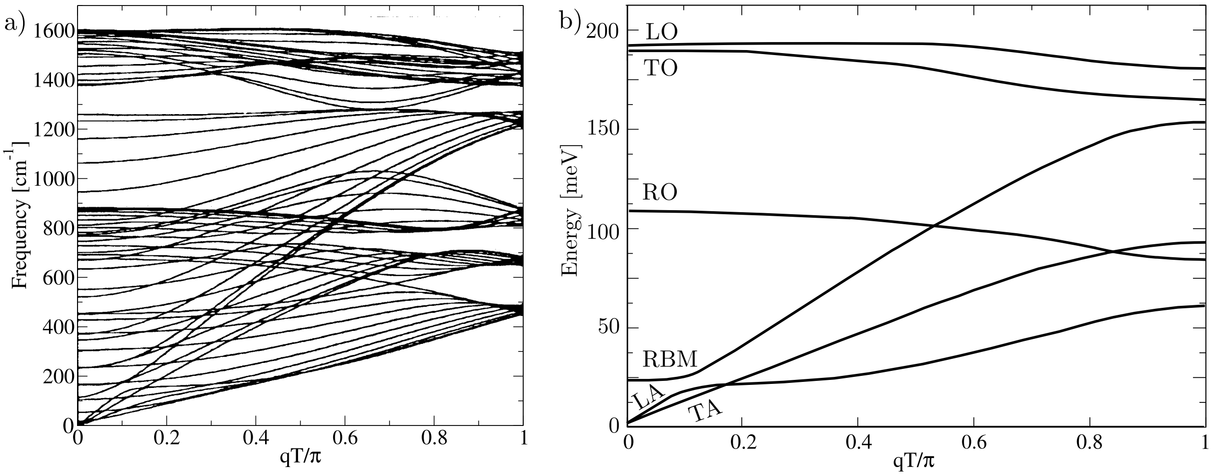

Figure 2.11: The phonon dispersion relations of a) a (10, 10) armchair CNT [12] and b) a (16, 0) zigzag CNT with $\mu = 0$, see (2.5.2) [55].

2.6 Electron-Phonon Interaction

The electron-phonon interaction HAMILTONian for CNTs can be written as [56]

$$\hat{H}_{\mathrm{el-ph}} \;=\; \sum_{k',\nu',k,\nu,\lambda} M_{k',\nu',k,\nu,\lambda} c^{\dagger}_{k',\nu'} c_{k',\nu'} (b_{q,\mu,\lambda} + b^{\dagger}_{-q,-\mu,\lambda}) \;, \tag{2.14}$$

where $c^{\dagger}_{k',\nu'}$ and $c_{k,\nu}$ are the electron creation and annihilation operators, respectively, $b^{\dagger}_{-q,-\mu,\lambda}$ and $b_{q,\mu,\lambda}$ are the phonon creation and annihilation operators, respectively, and $M_{k',\nu',k,\nu,\lambda}$ is the electron-phonon matrix element

$$M_{k',\nu',k,\nu,\lambda} \;=\; \sqrt{\frac{\hbar}{2\rho_{\mathrm{CNT}} L \omega_{q,\mu,\lambda}}}\, \widetilde{M}_{k',\nu',k,\nu,\lambda} \;, \tag{2.15}$$

where ρ_{CNT} is the mass density of the CNT, L is the normalization length, and $\widetilde{M}_{k',\nu',k,\nu,\lambda}$ is the reduced electron-phonon matrix element of the transition from the initial electronic state k,ν to the final state k',ν', where k is the wave-vector and ν is the azimuthal quantum number of electrons. Because of energy conservation for a scattering event it holds $E_{k',\nu'} - E_{k,\nu} = \pm\hbar\omega_{\pm q,\pm\mu,\lambda}$, where q is the wave-vector, μ is the azimuthal quantum number, and λ is the polarization of the phonon. The matrix element obeys selection rules arising from wave-vector and azimuthal quantum number conservation, $q = k' - k$ and $\mu = \nu - \nu'$.

Because in the CNT two degrees of freedom are confined, an electron can only be scattered forward or backward in the axial direction, preserving or changing the sign of the band-velocity, respectively. The scattering processes invoke either *intra-subband* or *inter-subband* transitions. The intra-subband processes are important for the electrical and the heat transport in CNTs and for the relaxation of an excited electron or hole in the same subband. The inter-subband processes contribute to the radiation-less relaxation of electrons (holes) from a given subband to a subband with a lower (higher) energy [56]. The scattering of electrons can take place within a given valley or between two valleys. The two possibilities being termed *intra-valley* and *inter-valley* scattering processes.

2.6.1 Electron-Phonon Matrix Elements

An important case is the intra-subband scattering of electrons, $\nu' = \nu$, therefore, $\mu = 0$ (Fig. 2.11-b) and λ can be any of six different phonon polarizations. One can omit the index μ and write the phonon frequency as $\omega_{\lambda}(q)$ and the reduced electron-phonon matrix element for a given band as $\widetilde{M}_{k',\nu',k,\nu,\lambda} = \widetilde{M}_{\lambda}(q)$, where the weak dependence on k is neglected.

For intra-valley processes, most of the phonons have $q \approx 0$ and are referred to as Γ-point phonons. Near the Γ point a linear dispersion relation for acoustic phonons is assumed,

$$\omega_{\mathrm{AP}}(q) \;\approx\; \upsilon_{\mathrm{AP}}|q| \;, \tag{2.16}$$

where υ_{AP} is the acoustic phonon velocity. For optical phonons the energy is assumed to be independent of the phonon wave-vector

$$\omega_{\mathrm{OP}}(q) \;\approx\; \omega_{\mathrm{OP}} \;. \tag{2.17}$$

Near the Γ-point the reduced electron-phonon matrix elements can be approximated by

$$\widetilde{M}_{\mathrm{AP}}(q) \approx \widetilde{M}_{\mathrm{AP}}|q| \tag{2.18}$$

for acoustic phonons and by

$$\widetilde{M}_{\mathrm{OP}}(q) \approx \widetilde{M}_{\mathrm{OP}} \tag{2.19}$$

for optical phonons [56]. Phonons inducing inter-valley processes have a wave-vector of $|q| \approx q_{\mathrm{K}}$, where q_{K} is a wave-number corresponding to the K-point of the Brillouin zone of graphite. For such phonons one can neglect the q-dependence, $\omega_{\mathrm{K}}(q) \approx \omega_{\mathrm{K}}$ and $\widetilde{M}_{\mathrm{K}}(q) \approx \widetilde{M}_{\mathrm{K}}$ [56].

To calculate the electron-phonon matrix elements one can employ the orthogonal tight-binding [57], the non-orthogonal tight-binding [56], and density functional theory [58] for the band-structure and a force constant model for the lattice dynamics [12, 59]. Electron-phonon matrix elements depend on the chirality and the diameter of the CNT [56–58]. Figure 2.12 shows the reduced matrix elements for intra-subband intra-valley transitions in semiconducting zigzag and chiral CNTs as a function of the CNT radius [56].

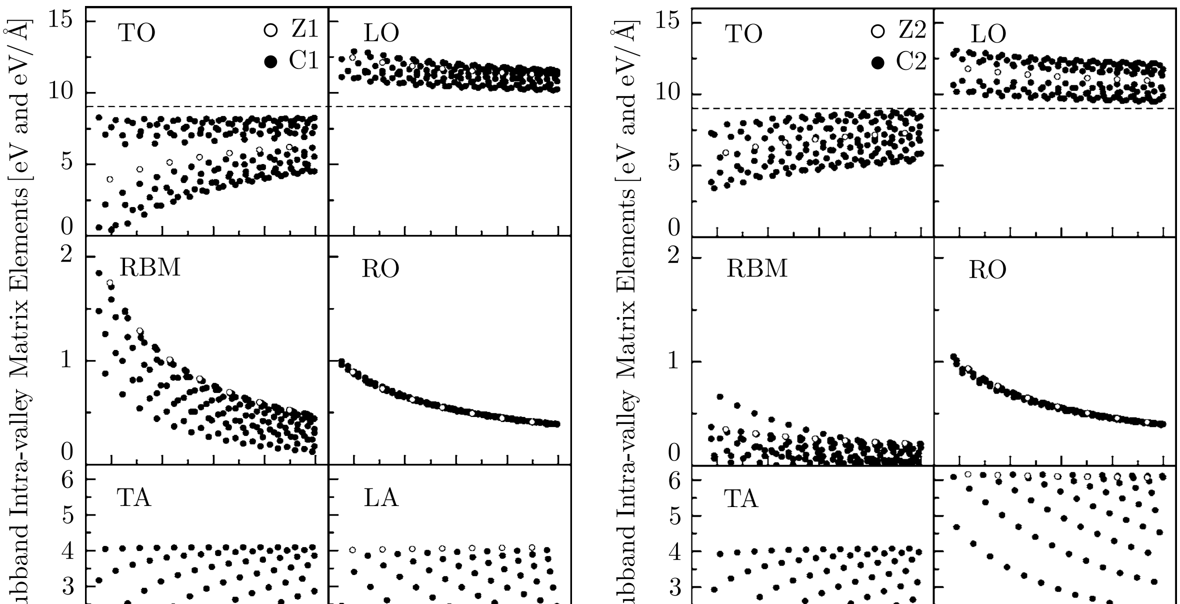

Figure 2.12: The calculated intra-valley intra-subband reduced electron-phonon matrix elements $\widetilde{M}_{\mathrm{AP}}$ (in eV) and $\widetilde{M}_{\mathrm{OP}}$ (in eV/Å) for zigzag (open circles) and chiral (closed) CNTs with the radius range from 3.5 Å to 12 Å. The results for CNTs with residuals 1 and 2 of the division $n - m$ by 3 are shown in the left and right figures, respectively. Open and closed circles denote the results for zigzag (Z) and chiral (C) CNTs, respectively. All results are for the lowest conduction band [56].

2.7 Transport Properties

Considering an electric current in a square wire with a width W and a length L, the resistance is given by OHM's law

$$R = \rho \frac{L}{W^2} \tag{2.20}$$

where ρ is the resistivity. In a macroscopic conductor, the resistivity ρ is a physical property which does not generally depend on either the length of the wire L or the voltage applied to the sample but only on the material. However, when the size of the wire becomes small compared with the characteristic lengths for the motion of electrons, then ρ depends on the length L through quantum effects. In the quantum regime, electrons act like waves that show interference effects. Such devices are usually referred to as mesoscopic systems[3]. In the following subsections the characteristics of ballistic and diffusive transport regimes are reviewed. These regimes pertain to transport in CNTs under appropriate conditions.

2.7.1 Ballistic Transport

For ballistic transport one can consider an ideal case where electrons are not scattered on the wire of length L connected to two electrodes, 1 and 2 (see Fig. 2.13). Since two electrodes have a large electron capacity, the FERMI energy for electrodes 1 and 2 are constants denoted by E_{F_1} and E_{F_2}, ($E_{\mathrm{F}_1} > E_{\mathrm{F}_2}$), respectively. If there are no reflections of electrons at the electrodes, $k > 0$ states are occupied primarily by electrons coming from the left contact while the $k < 0$ states are occupied primarily by electrons coming from the right contact. Consequently the occupation factors for the $k > 0$ and $k < 0$ states are given by the FERMI functions for the left and right contacts, respectively.

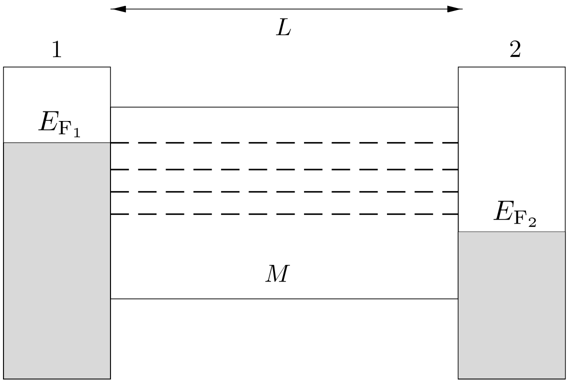

Figure 2.13: A ballistic conductor with length L is connected to two electrodes 1 and 2 with FERMI energies E_{F_1} and E_{F_2}, respectively. M is the number of channels for electrons to propagate from the electrode 1 to 2.

---

[3] A mesoscopic system is a solid small enough in size, so that the interference of electron wave-functions can be observed. A typical size of a mesoscopic system is around $1-100$ nm which is larger than the microscopic size of around $1-10$ Å and smaller than the macroscopic size which is more than 1 μm [60].

Because of the confinement of electronic states in the direction perpendicular to the current flow, there are several energy subbands $E^\nu(k)$. Thus the total current is given by the sum of the microscopic currents of all the subbands $E^\nu(k)$. The subbands are also called channels. The number of channels is a function of energy, which is denoted by $M(E)$. An electron which has a velocity of $\upsilon = \hbar^{-1}(\partial E/\partial k)$ in an unoccupied state contributes to the microscopic current $I = \mathrm{q}/t_\mathrm{t}$, in which t_t is the carrier transit time $t_\mathrm{t} = L/\upsilon$. Then the total current is given by [60]

$$\begin{aligned}
I &= \frac{\mathrm{q}}{L}\sum_{l,k}\frac{1}{\hbar}\frac{\partial E^\nu(k)}{\partial k}\left[f(E^\nu - E_{\mathrm{F}_1}) \;-\; f(E^\nu - E_{\mathrm{F}_2})\right] \;, \\
&= \frac{\mathrm{q}}{L}\frac{2L}{2\pi}\sum_{l}\int dk\,\frac{1}{\hbar}\frac{\partial E^\nu(k)}{\partial k}\left[f(E^\nu - E_{\mathrm{F}_1}) \;-\; f(E^\nu - E_{\mathrm{F}_2})\right] \;, \\
&= \frac{2\mathrm{q}}{\mathrm{h}}\int dE\;\left[f(E^\nu - E_{\mathrm{F}_1}) \;-\; f(E^\nu - E_{\mathrm{F}_2})\right]\; M(E) \;, \\
&\approx \frac{2\mathrm{q}^2}{\mathrm{h}}\;M\;\frac{\left[E_{\mathrm{F}_1} \;-\; E_{\mathrm{F}_2}\right]}{\mathrm{q}} \;,
\end{aligned} \tag{2.21}$$

where the sum over k is converted to the integral. In (2.21) a spin degeneracy of 2 and the inverse of the level spacing $L/2\pi$ is introduced and $M(E)$ is assumed to be constant over the integration range. One can easily show that for $T = 0$ K only states with $E_{\mathrm{F}_2} < E < E_{\mathrm{F}_1}$ contribute to the total current. If the width of a wire is very small (less than 1 nm), $M = 1$ even for $E_{\mathrm{F}_1} - E_{\mathrm{F}_2} = 1$ eV. On the other hand, if the width of a wire is on the order of 1 μm and $E_{\mathrm{F}_1} - E_{\mathrm{F}_2} = 1$ eV, the number of channels M becomes very large (10^6).

Since $V = (E_{\mathrm{F}_1} - E_{\mathrm{F}_2})/\mathrm{q}$ is the voltage between the electrodes, the resistance of the ballistic conductor is given by

$$R_\mathrm{c} \;=\; \frac{\left(E_{\mathrm{F}_1} - E_{\mathrm{F}_2}\right)/\mathrm{q}}{I} \;=\; \frac{\mathrm{h}}{2\mathrm{q}^2}\frac{1}{M} \;, \tag{2.22}$$

where R_c is called the contact resistance and $\mathrm{h}/2q^2$ is the quantized resistance

$$R_0 \;=\; \frac{\mathrm{h}}{2\mathrm{q}^2} \;\approx 12.9k\Omega \;. \tag{2.23}$$

This contact resistance arises from the mismatch of the numbers of conduction channels in the mesoscopic conductor and the macroscopic metal lead [60]. In addition to this quantum-mechanical contact resistance, there are other sources of contact resistance, such as that produced by poor coupling between the mesoscopic conductor and the leads. The inverse of (2.22) gives the contact conductance $G_\mathrm{c} = G_0 M$ where $G_0 = 2\mathrm{q}^2/\mathrm{h}$ denotes the quantized conductance. Thus in a wire without scattering the conductance is proportional to M. The quantized resistance and conductance can be observed in clean semiconductors at very low temperature on samples which have a small number of channels M [61]. If one considers the range of $M(E)$ for a SW-CNT with a diameter of $1 - 2$ nm, one finds that $M = 1$ under low bias conditions, $E_{\mathrm{F}_1} - E_{\mathrm{F}_2} < 1$ eV. In a zigzag SW-CNT close to the FERMI energy the bands are doubly degenerate, and thus the total conductance is $G = 2G_0$.

In case of coherent transport, the wave-function is determined by the SCHRÖDINGER equation. The phase and amplitude of the wave-function at electrode 2 can be obtained from those at electrode 1. The resistance and the conductance are thus given by

$$R \;=\; \frac{\mathrm{h}}{2\mathrm{q}^2}\frac{1}{M\mathcal{T}} \;, \qquad G \;=\; \frac{2\mathrm{q}^2}{\mathrm{h}}\; M\,\mathcal{T} \;, \tag{2.24}$$

where $\mathcal{T}$ is the transmission probability for a channel extending from electrode 1 to electrode 2. Here it is assumed again that $\mathcal{T}$ is constant near the FERMI energy. Equation (2.24) is known as the LANDAUER formula. It can be applied only if the wave-function spreads over the whole sample.

The resistance R_w for a single channel of a mesoscopic wire is given in terms of the transmission probability $\mathcal{T}$ as

$$R_\mathrm{w} \;=\; R \;-\; R_\mathrm{c} \;=\; R_0\,\frac{1-\mathcal{T}}{\mathcal{T}} \;\equiv\; R_0\,\frac{\mathcal{R}}{\mathcal{T}} \;. \tag{2.25}$$

The reflected wave-function, which is proportional to $\mathcal{R} = 1-\mathcal{T}$, causes a voltage drop in the wire.

2.7.2 Diffusive Transport

In case of incoherent transport, the electron wave-functions can not be described by a single phase over the entire sample. If one considers multiple reflections, for example between scattering centers $i = 1$ and $i = 2$, the overall transmission probability $\mathcal{T}_{12}$ between these two scattering centers is given by

$$\mathcal{T}_{12} \;=\; \mathcal{T}_1\mathcal{T}_2\,\left(1 \;+\; \mathcal{R}_1\mathcal{R}_2 \;+\; \mathcal{R}_1^2\mathcal{R}_2^2 \;+\; \ldots\,\right) \;=\; \frac{\mathcal{T}_1\mathcal{T}_2}{1-\mathcal{R}_1\mathcal{R}_2} \;, \tag{2.26}$$

where the effect of interference during a scattering event is neglected. One can rewrite (2.26) as

$$\frac{1-\mathcal{T}_{12}}{\mathcal{T}_{12}} \;=\; \frac{1-\mathcal{T}_1}{\mathcal{T}_1} \;+\; \frac{1-\mathcal{T}_2}{\mathcal{T}_2} \;. \tag{2.27}$$

Using the formula for the resistance given by (2.25) and (2.27), one can see that the resistance of the wire is additive, $R_{12} = R_1 + R_2$. Applying this result to the case of N scatterers yields

$$R \;-\; R_\mathrm{c} \;=\; R_0 \sum_i \frac{1-\mathcal{T}_i}{\mathcal{T}_i} \;\sim N\; R_0\;\frac{1-\mathcal{T}}{\mathcal{T}} \;. \tag{2.28}$$

where $\mathcal{T}$ is an average transmission probability for an individual scattering event over a mean free path. Thus the total resistance is given by a series connection of microscopic resistances. This is nothing but OHM's law, according to which the microscopic resistance is proportional to L.

2.8 CNTs in Electronics

The one-dimensional nature of CNTs severely reduces the phase space for scattering, allowing CNTs to realize maximum possible bulk mobility of this material. The low scattering probability and high mobility are responsible for high on-current of CNT transistors. Furthermore, the chemical stability and perfection of the CNT structure suggests that the carrier mobility at high gate fields may not be affected by processing and roughness scattering as in the conventional semiconductor channel. Similarly, low scattering together with the strong chemical bonding and high thermal conductivity allows metallic CNTs to withstand extremely high current densities (up to $\sim 10^9$ A/cm^2).

Electrostatics is improved in these devices as well. The fact that there are no dangling bond states at the surface of CNTs allows for a much wider choice of gate insulators other than conventional SiO_2. This improved gate control without any additional gate leakage becomes very important in scaled devices with effective SiO_2 thickness below 1 nm. Also, the strong one-dimensional electron confinement and full depletion in the nanometer-scale diameter of the SW-CNTs (typically $1-2$ nm) should lead to a suppression of short-channel effects in transistors [5].

The combined impact of transport and electrostatic benefits together with the fact that semiconducting CNTs are, unlike silicon, direct-gap materials, suggest applications in opto-electronics as well [6, 7]. As far as integration is concerned, semiconducting CNTs benefit from their band structure which exhibits essentially the same effective mass for electrons and holes. This should enable similar mobilities and performance of n-type and p-type transistors which is necessary for a complementary metal-oxide semiconductor (CMOS)-like technology. Finally, since CNTs can be both metallic and semiconducting, an all-CNT electronics can be envisioned. In this case, metallic CNTs could act as high current carrying local interconnects [62], while semiconducting CNTs would form the active devices. The most important appeal of this approach is an ability to fabricate one of the critical device dimensions (the CNT diameter) reproducibly using synthetic chemistry.

2.8.1 Fabrication and Performance of CNT-FETs

The first CNT field effect transistors (CNT-FETs) were reported only a few years after the initial discovery of CNTs [3,4]. These early devices, shown schematically in Fig. 2.14-a, were relatively simple in structure: Noble metal (gold or platinum) electrodes were lithographically patterned atop an oxide-coated, heavily doped silicon wafer, and a single-walled CNT was deposited atop the electrodes. The metal electrodes served as the source and drain, and the CNT was the active channel. The doped substrate served as the gate electrode, separated from the CNT channel by a thick ($\sim 100-200$ nm) oxide layer. These devices displayed clear p-type transistor action, with gate voltage modulation of the drain current over several orders of magnitude. The devices displayed high parasitic resistance (≥ 1 MΩ), low drive current, low transconductance ($g_m \sim 1$ nS), high sub-threshold slope ($S = [d(\log_{10} I_\mathrm{d})/dV_\mathrm{g}]^{-1} \sim 1$ V/decade), and no current saturation. Due to the thick gate dielectric, these devices required large values of the gate voltage (several volts) to turn on, making them unattractive for practical applications.

Following these initial results, advances in CNT-FET device structures and processing yielded

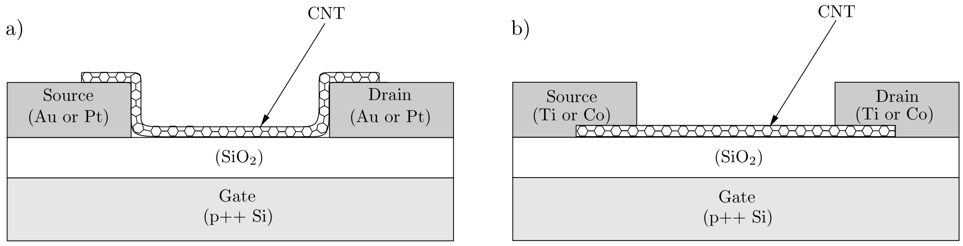

Figure 2.14: a) Schematic structure of first CNT-FETs, with CNT draped over metal electrodes. b) Improved CNT-FET structure, with metal electrodes deposited upon the CNT, followed by thermal processing to improve contact. The substrate serves as the gate for both device structures, and it is separated from the CNT by a thick oxide layer.

improvements in their electrical characteristics. Rather than laying the CNT down upon the source and drain electrodes, relying on weak van der Waals forces for contact, the CNTs were first deposited on the substrate, and the electrodes were patterned on top of the CNTs, as shown in Fig. 2.14-b. In addition to Au, Ti and Co were used [63–65] with a thermal annealing step to improve the metal-CNT contact. In the case of Ti, the thermal processing leads to the formation of TiC at the metal-CNT interface [64], resulting in a significant reduction in the contact resistance from several MΩ to $\sim$ 30 kΩ. On-state currents $\sim$ 1 μA were measured, with a transconductance of $\sim$ 0.3 μS — an improvement of more than two orders of magnitude relative to the van der Waals contacted devices. This CNT-FET device configuration has been extensively studied in the literature. More recently, it has been found that Pd forms a low resistance contact to CNTs for p-type devices [66]. It is speculated [66] that Pd offers improved sticking or wetting interaction to the CNT surface relative to other metals, as well as good Fermi level alignment relative to the CNT conduction band. This point will be explored further in Section 2.8.2.

As mentioned above, early CNT-FETs were p-type in air (hole conduction). The role of the ambient on CNT-FET conduction will be discussed in Section 2.8.3, however, it was found that n-type conduction could be achieved by doping from an alkali (electron donor) gas [67] or by thermal annealing in vacuum [64]. In addition, it is possible to achieve an intermediate state, in which both electron and hole injection occur, resulting in ambipolar conduction [64]. The ability to controllably fabricate both p-type and n-type CNT-FETs is a key to the formation of complementary metal oxide semiconductor (CMOS) logic circuits.

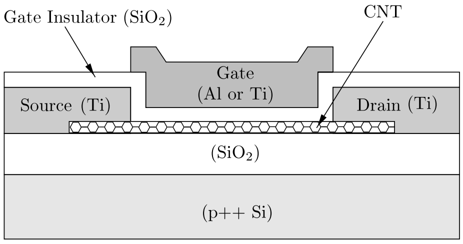

Figure 2.15: Schematic cross-section of top-gate CNT-FET.

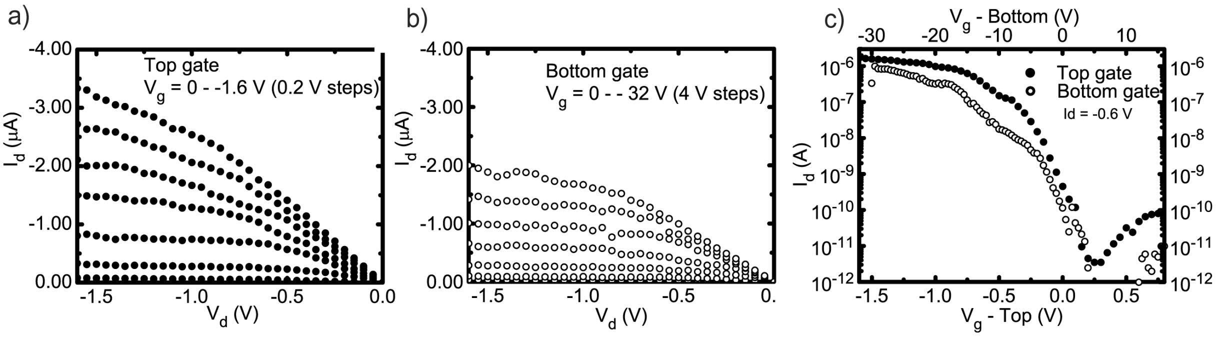

Figure 2.16: Electrical characteristics of the CNT-FET shown in Fig. 2.15 for both top-gate and bottom-gate operation. The oxide thicknesses for the top-gate and the bottom-gate are 15 nm and 120 nm, respectively. Output characteristics for a) top-gate and b) bottom-gate operation. c) Transfer characteristics [68].

Early experiments on CNT-FETs were built upon oxidized silicon wafers, with the substrate itself serving as the gate and a thermally grown oxide film, typically $\sim$ 100 nm or thicker, serving as the gate dielectric. The thick gate oxide required relatively high gate voltages ($\sim$ 10 V) to turn on the devices, and the use of the substrate as the gate implied that all CNT-FETs must be turned on and off together, precluding the implementation of complex circuits. A more advanced CNT-FET structure [68] is shown in Fig. 2.15. The device comprises a top-gate separated from the CNT channel by a thin gate dielectric. The top-gate allows independent addressing of individual devices, making it more amenable to integration in complex circuits, while the thin gate dielectric improves the gate to channel coupling, enabling low voltage operation. In addition, the reduction of the capacitance due to gate-source and gate-drain overlap suggests that such a device structure would be appropriate for high frequency operation. Such a CNT-FET can also be switched using the conductive substrate as a bottom gate, allowing for direct comparison between top and bottom gate operation. Comparison of the output characteristics for top and bottom-gate operation of the device in Fig. 2.15 are shown in Fig. 2.16-a and Fig. 2.16-b, respectively. Operating the device with the top-gate yields distinctly superior performance relative to bottom gate operation, with a lower threshold voltage (-0.5V vs. -12V) and higher transconductance (3.25 μS vs. 0.1 μS). Figure 2.16-c shows superior sub-threshold behavior for top-gate operation with an order of magnitude improvement in sub-threshold slope (130 mV/decade vs. 2V/decade).

In order to gauge whether or not CNT-FETs have potential for future nano-electronic applications, it is important to compare their electrical performance to those of advanced silicon devices. Wind et al. [68] demonstrated that although the device structure is far from optimized, the electrical characteristics, such as the on-current and the transconductance of the device shown in Fig. 2.15 exceeds those of state-of-the-art silicon MOSFETs. Further enhancements to CNT-FET structures, such as the use of high dielectric constant gate insulators [69,70], and additional improvements in the metal-CNT contact resistance at the source and drain [66] have lead directly to improved CNT-FET performance. Such improvements can be also applied to n-type CNT-FETs [71].

2.8.2 Schottky Barrier Model of CNT-FET Operation

In general a charge transfer will take place at the metal-CNT interface leading to band-bending and the creation of a Schottky barrier. For example, a CNT-FET with titanium-carbide contacts shows equal hole and electron currents depending on the sign of the applied gate bias, so called ambipolar conduction [64]. This suggests the existence of two barriers, one for electrons and one for holes, of approximately equal height, implying that each must be about half the band-gap ($E_g/2 \approx 300$ meV). Applying conventional semiconductor analysis, which assumes that thermionic emission contributes mostly to the total current through a Schottky barrier, indeed yields similar thermal activation barriers for electrons and holes, however, on the order of 10 meV [64]. This finding suggested that the thermionic contribution alone cannot account for the observed current levels, which is supported by modeling results showing that Schottky barriers in one-dimension are much thinner than their planar analogues [72, 73]. Consequently, carrier tunneling through these thin barriers becomes the dominant conduction mechanism and cannot be neglected when quantifying the barrier height [74].

Similar conclusions can be drawn from the sub-threshold behavior of CNT-FETs, in particular when plotted as a function of gate oxide thickness. The switching behavior of a MOSFET is described by the inverse sub-threshold slope, $S \simeq (k_B T/\mathrm{q})\ln(10)(1 + C_D/C_g)$ where C_D and C_g are the depletion and gate capacitance, respectively. In the case of a fully depleted device, C_D is zero and, therefore, S depends only on the temperature, having a value of 65 mV/decade at room temperature. The original CNT-FETs with thick gate oxides in back-gated geometry had unexpectedly high S values of approximately 1 V/decade. On the other hand, when devices are fabricated using thinner oxides, such as the top-gated CNT-FET in [68], the value of S dropped significantly into the range of $100 - 150$ mV/decade [68], 80 mV/decade [75], and $67 - 70$ mV/decade [76]. Such a dependence of S is not consistent with the bulk switching mechanism which should give 65 mV/decade in the long channel limit. Instead, this kind of scaling of the sub-threshold slope with oxide thickness is compatible with the existence of sizeable Schottky barriers at the metal-CNT interfaces, and theoretical modeling showed that the gate field impact on this interface is responsible for the observed improvement in S [77, 78], see Fig. 2.17.

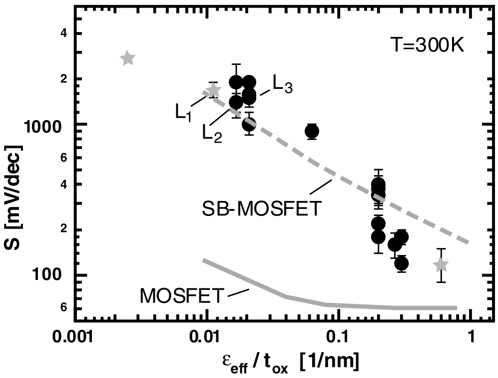

Figure 2.17: Inverse sub-threshold slope S as a function of gate capacitance. Symbols are experimental data. Lines represent calculations for MOS-FETs with (dashed line) and without (solid line) Schottky barriers of 0.3 eV [77].

Further evidence of the presence of Schottky barriers in CNT-FET devices is found in local gating experiments, where the on-current is shown to increase significantly by application of a local potential from a metal coated scanning probe tip only at the positions above the metal-CNT interface [79]. Similarly, the impact of Schottky barriers in the sub-threshold characteristics of the CNT-FET is clearly observed in transistors with multiple top-gates [80]. In this case, local gates over the metal-CNT interface are used to electrostatically thin the Schottky barriers and reduce the value of S closer to that of the bulk switching device [80].

Hole (electron) injection into the CNT depends on the line-up of the metal Fermi level and the valence (conduction) band of the CNT, which is defined here as the Schottky barrier height. In this picture, other details of the contacts such as any changes in the metal-CNT coupling as a function of the curvature of the CNT are incorporated in an *effective* Schottky tunneling barrier height. This barrier height depends on a number of material parameters such as the band-gap of the CNT, work-function difference, as well as the interface quality. The CNT band-gap is inversely proportional to the diameter of the CNT, according to (2.10). Figure 2.18-a shows qualitative band diagrams for CNT-FETs with different diameters. Assuming a constant work function for all CNTs[4], the Schottky barrier increases linearly with increasing band-gap. On a log scale, current injection through the Schottky barrier is inversely proportional to the barrier height. Therefore, the CNT-FET with a small diameter delivers low on-current. The choice of the metal contacts also affects the device performance. Figure 2.18-b depicts the band diagrams for CNT-FETs using different source and drain contact materials. Identical energy band-gaps are drawn here to represent CNTs of the same diameter. CNT-FETs with Pd contacts deliver the highest on-current (Fig. 2.18-c), since Pd has the highest work function (5.1 eV), which forms a low Schottky barrier height to the valence band of the CNT. The trend shown follows that of the clean metal work functions: 4.3 eV for Ti and 4.1 eV for Al.

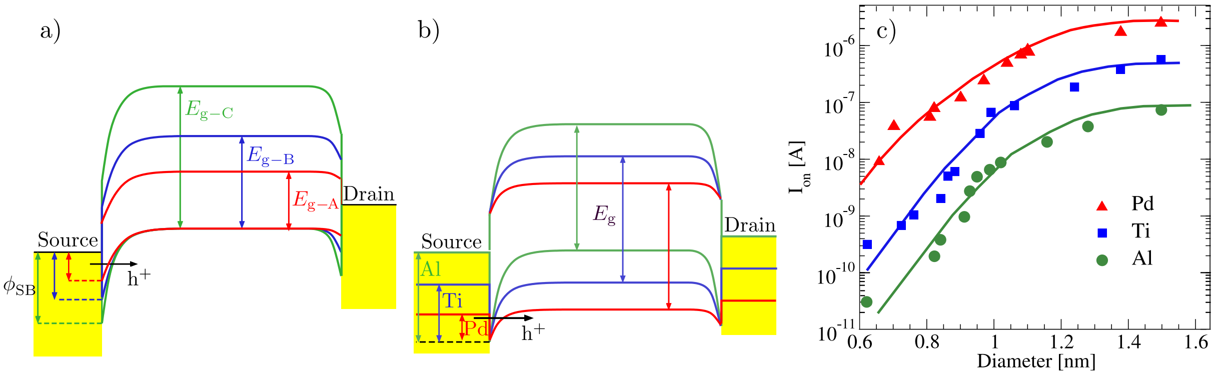

Figure 2.18: a) Schematic band diagram showing the different Schottky barrier heights for b) CNT-FETs with the same contact, but with different CNT diameters and b) CNT-FETs with the same diameter, but using Pd, Ti, and Al contacts, respectively. c) Plot of the on-current as a function of the CNT diameter [81].

---

[4] The work function is defined as the sum of the CNT electron affinity and half of the band-gap in the bulk.

2.8.3 Environmental Influences on the Performance of CNT-FETs

The effect of ambient air on the performance and functionality of CNT-FETs can be also understood within the framework of the SCHOTTKY barrier model of conduction. In particular, this model helps to clarify and separate the effects due to the bulk of the CNT channel from those arising from the effects at the contact between the metal electrode and the CNT.

It has been proposed that e.g. oxygen adsorption leads to doping of CNTs [82]. However, as shown in Fig. 2.19-a, the effect of oxygen on the transport properties of a CNT-FET is a reversible transition from p-type (devices prepared in air) to n-type after annealing the transistor in vacuum [83]. In contrast, the deposition of an n-type dopant such as potassium (Fig. 2.19-b) shifts the transfer characteristics with respect to the gate voltage. It is known that the work function of a metal surface is altered significantly upon the adsorption of gases due to the formation of interface dipoles. Thus, the local work function of the metal electrode can be modified considerably by the adsorption of oxygen at the contacts. If the work function of the metal electrode changes the line-up of the metal FERMI energy with the CNT, bands will shift[5] [73].

Figures 2.19-c and 2.19-d compare the effect of doping with that of a shift in the line-up, i.e. a reduction of the SCHOTTKY barrier height to the conduction band and an increase of that to the valence band or vice versa. While n-type doping shifts the transport curves to more negative gate voltages, a change in the work function promotes either the p-type or the n-type branch of conduction and reduces the other.

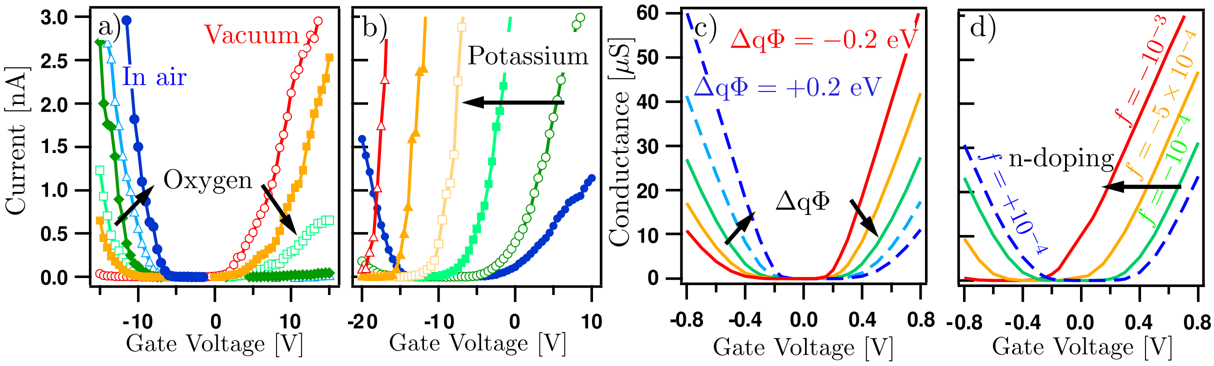

Figure 2.19: Effect of gas adsorption and doping on the operation of CNT-FETs. a) and b) are experimental data and c) and d) numerical calculations. In a) a vacuum annealed n-type FET has been exposed to increasing amounts of oxygen until the ambient is reached. In b) the curves from right to left correspond to increasing deposited amounts of potassium. In c) the work function difference between metal and CNT is changed from −0.2 eV to +0.2 eV in steps of +0.1 eV [78, 84].

---

[5] Note that this is unique for the contact between a metal and a CNT. In a conventional, planar semiconductor device the position of the FERMI energy is pinned by metal-induced gap states [72].

2.8.4 Prototype CNT-FET Circuits

The promising characteristics of individual CNT-FETs have lead to initial attempts at integration of several CNT-FETs into useful circuits that can perform a logic operation, or function as memories [85] or sensors [86]. In the following, we limit our discussion to advances in logic circuitry. The CNT logic gates have been, in most cases, based on a complementary technology analogous to silicon CMOS, which is important as it may ease integration of CNTs onto this well established technology.

The first complementary (CMOS-like) logic gates were reported by Derycke and co-workers [67]. In that work, two different techniques were used to produce n-type devices. An inverter gate was created by combining two CNT-FETs: a p-type device in the ambient and a vacuum annealed n-type device. A more compact and integrated approach uses potassium doping to convert one of two CNT-FETs built on the same CNT to n-type. The masking of the other transistor which remained p-type was accomplished by photo-resist. The circuit had a voltage gain of about two, suggesting that integration, without signal degradation, of many devices along a single CNT can be accomplished. Shortly thereafter, Bachtold and co-workers [87] used p-type CNT-FETs along with resistors to build prototype logic gates based on an older transistor-resistor scheme. They went a step further in complexity and wired three such inverter gates to form a ring oscillator. The large parasitic capacitances severely degraded the performance of the circuit which oscillated at only about 5 Hz. Later Javey and co-workers [70] used another scheme for converting p-type into n-type CNT-FETs and to wire up CMOS inverters with gains in excess of ten and CMOS ring oscillators with frequencies in the 100 Hz range. Very recently Chen and co-workers [88] reported CMOS ring oscillators operating at frequencies up to 52 MHz (see Fig. 2.20). However, these reported frequencies are well below the expected AC response of CNT-FETs, which is difficult to assess because of the relatively small current signals in these devices. Most recently, the non-linear current-voltage characteristics of CNT-FETs were used to demonstrate that DC characteristics of CNT-FETs are not affected by AC fields at least up to 500 MHz [89]. However, operation up to 10 GHz [90] and later 50 GHz [91] have been reported, albeit with considerable signal attenuation.

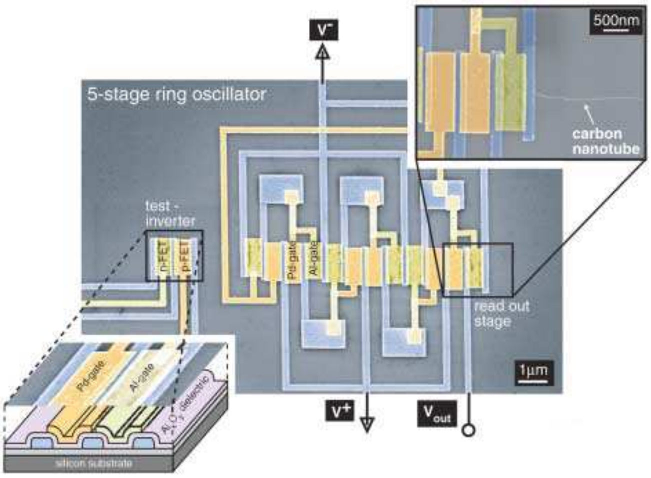

Figure 2.20: Image of CNT-FET circuit reported by Chen et al. [88].

Chapter 3

Quantum Transport Models

THIS CHAPTER outlines the theory of the non-equilibrium Green's function (NEGF) techniques for modeling transport phenomena in semiconductor devices. The NEGF techniques, initiated by Schwinger [92], Kadanoff, and Baym [93] allow ones to study the time evolution of a many-particle quantum system. Knowledge of the single-particle Green's function provides both the complete equilibrium or non-equilibrium properties of the system and the excitation energies of the systems containing one more or one less particle. The many-particle information about the system is cast into self-energies, parts of the equations of motion for the Green's functions. Green's functions can be expressed as a perturbation expansion, which is the key to approximate the self-energies. The NEGF techniques provide a very powerful technique for evaluating properties of many-particle systems both in thermodynamic equilibrium and also in non-equilibrium situations.

The basic approach developed in the early 1970s has became increasingly popular during the last 10 years. The motivation for the development of the NEGF tunneling formalism was the metal-insulator-metal tunneling experiments that received much attention during the 1960s [94]. The accelerated use of the approach was motivated by experimental investigations of mesoscopic physics made possible by high quality semiconductor hetero-structures grown by molecular beam epitaxy. In 1988, Kim and Arnold were the first to apply the NEGF formalism to such a system, specifically, a resonant tunneling diode [95]. As experimental methods progressed allowing finer manipulation of matter and probing into the nano-scale regime, the importance of quantum effects and tunneling continuously increased. The theory was adapted to address the current systems of interest ranging from mesoscopics to single-electronics, nano-scaled FETs, and molecular electronics.

The general formalism for NEGF calculations of current in devices was first described in a series of papers in the early 1970s [96–99]. The partitioning of an infinite system into left contact, device, and right contact, and the derivation of the open boundary self-energies for a tight-binding model was presented in [96]. This theory was re-derived for a continuum representation in [97], tunneling through localized impurity states was considered in [98], and a treatment of phonon assisted tunneling was derived in [99]. In 1976, the formalism was first applied to a multi-band model (two-bands) to investigate tunneling [100] and diagonal disorder [101], and in 1980 it was extended to model time-dependent potentials [102].

The applications of the NEGF techniques have been extensive including quantum optics [103], quantum corrections to the Boltzmann transport equation [104, 105], high field transport in bulk systems [106], and electron transport through nano-scaled systems. Over the last decade, NEGF techniques have become widely used for modeling high-bias, quantum electron and hole transport in a wide variety of materials and devices: III-V resonant tunnel diodes [95,107–122], electron waveguides [123], superlattices used as quantum cascade lasers [124], Si tunnel diodes [125, 126], ultra-scaled Si MOSFETs [8, 127–130], Si nano-pillars [131–133], carbon nanotubes [134–145], metal wires [146, 147], organic molecules [148–164], superconducting weak links [165], and magnetic leads [136, 166, 167]. Physics that have been included are open-system boundaries [96], full-band-structure [116–118, 125, 126, 168], band-tails [126], the self-consistent Hartree potential [109, 115, 169], exchange-correlation potentials within a density functional approach [11,115,135,146,149,150,152], acoustic, optical, intra-valley, inter-valley, and inter-band phonon scattering, alloy disorder and interface roughness scattering in Born type approximations [110–116, 124–126], photon absorption and emission [124], energy and heat transport [120], single-electron charging and non-equilibrium Kondo systems [170–176], shot noise [113, 119, 177], A.C. [108,178–183], and transient response [180,184]. Time-dependent calculations are described further in [185]. General tutorials on the NEGF techniques [60, 186] and the applications can be found in [116, 187, 188].

This chapter continues with a tutorial derivation of the standard expressions, where one shall rely on the *second quantization* formulation. A brief description to this formalism is presented in Appendix A. Various formulations of many-particle Green's function theory exist. For instance, in equilibrium theory there is both a zero-temperature as well as a finite-temperature (Matsubara) formalism [185, 189, 190], which are described briefly next. Then, the formulation of the more general non-equilibrium finite-temperature theory which also applies to equilibrium situations as a special case is introduced and the kinetic equations for this formalism are discussed. Applying Wick theorem, a perturbation expansion of Green's functions can be achieved. Such expansions provide methods to approximate self-energies due to various scattering mechanisms. Finally, a comparison of the Green's function formalism with other transport models is presented.

3.1 Equilibrium Zero Temperature GREEN's Function

In many-particle problems it is common to use the interaction representation (see Appendix B)

$$\hat{H} \;=\; \hat{H}_0 \;+\; \hat{H}^{\mathrm{int}} \;, \tag{3.1}$$

where H_0 is the non-interacting HAMILTONian and H^{int} is the perturbation, which contains all the interactions, i.e. $\hat{H}^{\mathrm{int}} = \hat{H}_{\mathrm{el-el}} + \hat{H}_{\mathrm{el-ph}}$.

3.1.1 Definition of the GREEN's Function

The time-ordered single-particle GREEN's function at zero temperature is defined as [189]

$$G(\mathbf{r}, t; \mathbf{r}', t') \;=\; -\frac{i}{\hbar}\frac{\langle\Psi_0|T_{\mathrm{t}}\{\hat{\psi}_{\mathrm{H}}(\mathbf{r}, t)\hat{\psi}^{\dagger}_{\mathrm{H}}(\mathbf{r}', t')\}|\Psi_0\rangle}{\langle\Psi_0|\Psi_0\rangle} \;, \tag{3.2}$$

where $|\Psi_0\rangle$ is the ground-state of the interacting system in the HEISENBERG picture (Appendix B) and T_{t} is the time-ordering operator defined in (B.21). The field operator $\hat{\psi}_{\mathrm{H}}(\mathbf{r}, t)$ in the HEISENBERG picture is given by

$$\hat{\psi}_{\mathrm{H}}(\mathbf{r}, t) \;=\; e^{i\hat{H}t/\hbar}\hat{\psi}(\mathbf{r})e^{-i\hat{H}t/\hbar} \;. \tag{3.3}$$

Inserting (3.3) into (3.2), the physical interpretation of the GREEN's function becomes obvious

$$G(\mathbf{r}, t; \mathbf{r}', t') \;=\; -\frac{i}{\hbar}\frac{\langle\Psi_0|T_{\mathrm{t}}\{e^{i\hat{H}t/\hbar}\hat{\psi}(\mathbf{r})e^{-i\hat{H}(t-t')/\hbar}\hat{\psi}^{\dagger}(\mathbf{r}')e^{-i\hat{H}t'/\hbar}\}|\Psi_0\rangle}{\langle\Psi_0|\Psi_0\rangle} \;, \tag{3.4}$$

If $t > t'$, the GREEN's function $G(\mathbf{r}, t; \mathbf{r}', t')$ is the probability amplitude that a particle created at time t' at place $\mathbf{r}'$ moves to time t and place $\mathbf{r}$. This follows from the definition of $G(\mathbf{r}, t; \mathbf{r}', t')$. At zero time the system is at the ground-state Ψ_0. The system then evolves to time t' with the operator $e^{-i\hat{H}t'/\hbar}$. At this time $\hat{\psi}^{\dagger}(\mathbf{r}', t')$ creates a particle at place $\mathbf{r}'$. Then, the system continues its evolution from t' to t with the operator $e^{-i\hat{H}(t-t')/\hbar}$, after which $\hat{\psi}(\mathbf{r}, t)$ annihilates the particle at place $\mathbf{r}$. The system returns to the initial ground-state with the operator $e^{i\hat{H}t/\hbar}$. In a similar way, if $t' > t$, the field operator creates a hole at time t, and the system then propagates according to the HAMILTONian $\hat{H}$. These holes can be interpreted as particles traveling backward in time [191]. The probability amplitude that a hole created at time t at place $\mathbf{r}$ moves to time t' and place $\mathbf{r}'$ is again just the GREEN's function for $t < t'$.

To calculate $G(\mathbf{r}, t; \mathbf{r}', t')$, a perturbation expansion is very useful. However, the definition of the GREEN's function in (3.2) does not allow a direct solution, since it involves the exact ground-states of the interacting HAMILTONian $\hat{H}$, which is one of the things to be calculated. In the interaction representation the HAMILTONian is expressed in terms of the non-interacting and interacting parts, see the equation (3.1). The ground state of the non-interacting part, $\hat{H}_0$, can be calculated easily. Therefore, one tries to express the ground state of the interacting system $|\Psi_0\rangle$ in terms of the ground state of the non-interacting one $|\phi_0\rangle$. For that purpose, in equation (B.18) one adds to the operator $\hat{H}^{\mathrm{int}}_{\mathrm{I}}(t)$ a factor $e^{-|\epsilon|t}$, which switches the interaction off at $t \to \pm\infty$ [189]. The non-interacting ground state $|\phi_0\rangle$ is assigned to the system at $t \to -\infty$ and the connection to $|\Psi_0\rangle$ is formed by the GELL-MANN and Low theorem [192]

$$|\Psi(0)\rangle \;=\; \hat{S}(0, -\infty)|\phi_0\rangle \;, \tag{3.5}$$

where the $\hat{S}$ operator in defined in Appendix B.4. The traditional argument is that one starts from $t \to -\infty$ with a wave function ϕ_0 which does not contain the effects of the interaction $\hat{H}^{\mathrm{int}}$. The operator $\hat{S}(0, -\infty)$ brings this wave function up to the present, $t = 0$ [189]. Thus one has the wave function which contains the effects of the interaction $\hat{H}^{\mathrm{int}}$, so that it is an eigenstate of $\hat{H}$. As $t \to \infty$, one gets

$$|\Psi(\infty)\rangle \;=\; \hat{S}(\infty, -\infty)|\phi_0\rangle \;. \tag{3.6}$$

One possible assumption is that $|\Psi(\infty)\rangle$ must be related to ϕ_0. The system returns to its ground state for $t \to \infty$ except for a phase factor [190] $|\Psi(\infty)\rangle = e^{iL}|\phi_0\rangle$ which implies that,

$$\langle\phi_0|\hat{S}(\infty, -\infty)|\phi_0\rangle \;=\; e^{iL}. \tag{3.7}$$

An alternative to this assumption is discussed in Section 3.3.2.

Using the relation (3.5) for the ground-state, equation (3.2) becomes

$$\begin{aligned}
G(\mathbf{r}, t; \mathbf{r}', t') \;&= -\frac{i}{\hbar}\frac{\langle\phi_0|\hat{S}(-\infty, 0)T_{\mathrm{t}}\{\hat{\psi}_{\mathrm{H}}(\mathbf{r}, t)\hat{\psi}^{\dagger}_{\mathrm{H}}(\mathbf{r}', t')\}\hat{S}(0, -\infty)|\phi_0\rangle}{\langle\phi_0|\hat{S}(-\infty, 0)\hat{S}(0, -\infty)|\phi_0\rangle} \\
&= -\frac{i}{\hbar}\frac{\langle\hat{S}(-\infty, 0)T_{\mathrm{t}}\{\hat{S}(0, t)\hat{\psi}_{\mathrm{I}}(\mathbf{r}, t)\hat{S}(t, 0)\hat{S}(0, t')\hat{\psi}^{\dagger}_{\mathrm{I}}(\mathbf{r}', t')\hat{S}(t', 0)\}\hat{S}(0, -\infty)\rangle_0}{\langle\hat{S}(-\infty, 0)\hat{S}(0, -\infty)\rangle_0} \\
&= -\frac{i}{\hbar}\frac{\langle\hat{S}(\infty, 0)T_{\mathrm{t}}\{\hat{S}(0, t)\hat{\psi}_{\mathrm{I}}(\mathbf{r}, t)\hat{S}(t, t')\hat{\psi}^{\dagger}_{\mathrm{I}}(\mathbf{r}', t')\hat{S}(t', 0)\}\hat{S}(0, -\infty)\rangle_0}{\langle\hat{S}(\infty, -\infty)\rangle_0} \\
&= -\frac{i}{\hbar}\frac{\langle T_{\mathrm{t}}\{\hat{S}(\infty, -\infty)\hat{\psi}_{\mathrm{I}}(\mathbf{r}, t)\hat{\psi}^{\dagger}_{\mathrm{I}}(\mathbf{r}', t')\}\rangle_0}{\langle\hat{S}(\infty, -\infty)\rangle_0}\;,
\end{aligned} \tag{3.8}$$

where the short-hand notation $\langle\ldots\rangle_0 = \langle\phi_0|\ldots|\phi_0\rangle$ is introduced to represent the expectation value over the ground-state of the non-interacting system at zero temperature. The transition from the first to the second line is achieved by using (B.13) for converting the HEISENBERG representation of operators into the interaction representation. The second step is obtained by taking account of the properties of the $\hat{S}$ operators described in Appendix B.4 and the return of the system to its ground-state as $t \to \infty$. In the forth line the operator $\hat{S}(\infty, -\infty)$ contains several time intervals (∞, t), (t, t'), and $(t', -\infty)$. The T_{t} operator automatically sorts these intervals so that they act in their proper sequences. Replacing operator $\hat{S}$ with its formal definition (see (B.24)) one gets

$$G(\mathbf{r}, t; \mathbf{r}', t') \;= -\frac{i}{\hbar}\frac{\langle T_{\mathrm{t}}\{\exp\left(-\frac{i}{\hbar}\int\limits_{-\infty}^{\infty} dt_1 \hat{H}^{\mathrm{int}}_{\mathrm{I}}(t_1)\right)\hat{\psi}_{\mathrm{I}}(\mathbf{r}, t)\hat{\psi}^{\dagger}_{\mathrm{I}}(\mathbf{r}', t')\}\rangle_0}{\langle T_{\mathrm{t}}\{\exp\left(-\frac{i}{\hbar}\int\limits_{-\infty}^{\infty} dt_1 \hat{H}^{\mathrm{int}}_{\mathrm{I}}(t_1)\right)\}\rangle_0}\;. \tag{3.9}$$

3.2 Equilibrium Finite Temperature GREEN's Function

In Section 3.1 the GREEN's function for a system under equilibrium at zero temperature has been introduced. Furthermore, the GREEN's function was readily expressed as perturbation expansion in the interaction picture. In this section, the GREEN's function for a system under equilibrium at finite temperature is presented. The GREEN's function at finite temperature has a simple perturbation expansion similar to that for the GREEN's function at zero temperature and also enables us to evaluate the properties of the system.

3.2.1 Equilibrium Ensemble Average

At finite temperatures, one assumes that the particle, either electron or phonon, is interacting with a bath of other particles. The exact state of all these other particles is not known, since they are fluctuating between different configurations. At finite temperature under thermodynamic equilibrium the state of a system is described by the equilibrium density operator $\hat{\rho}$ (see Appendix C). In treating such systems, it will be most convenient to use the grand canonical ensemble, which allows for a variable number of particles. Therefore, the system is considered to be in contact with a heat bath of temperature T and a particle reservoir characterized by the FERMI energy E_F. With the definition $\hat{K} = \hat{H} - E_\mathrm{F}\hat{N}$, where $\hat{N}$ is the particle number operator, the statistical operator can be written as

$$\hat{\rho} = \frac{e^{-\beta\hat{K}}}{\mathrm{Tr}[e^{-\beta\hat{K}}]} , \tag{3.10}$$

where the short-hand notation $\beta = 1/k_\mathrm{B}T$ is used. The operator $\hat{K}$ may be interpreted as a *grand canonical* HAMILTONian. Given the density operator, the ensemble average of any operator $\hat{O}$ can be calculated as

$$\begin{aligned} \langle\hat{O}\rangle &= \mathrm{Tr}[\hat{\rho}\hat{O}] , \\ &= \frac{\mathrm{Tr}[e^{-\beta\hat{K}}\hat{O}]}{\mathrm{Tr}[e^{-\beta\hat{K}}]} . \end{aligned} \tag{3.11}$$

Therefore, the single-particle GREEN's function at finite temperature can be defined as

$$\begin{aligned} G(\mathbf{r},t;\mathbf{r}',t') &= -\frac{i}{\hbar}\langle T_\mathrm{t}\{\hat{\psi}_\mathrm{H}(\mathbf{r},t)\hat{\psi}^\dagger_\mathrm{H}(\mathbf{r}',t')\}\rangle , \\ &= -\frac{i}{\hbar}\frac{\mathrm{Tr}[e^{-\beta\hat{K}}T_\mathrm{t}\{\hat{\psi}_\mathrm{H}(\mathbf{r},t)\hat{\psi}^\dagger_\mathrm{H}(\mathbf{r}',t')\}]}{\mathrm{Tr}[e^{-\beta\hat{K}}]} . \end{aligned} \tag{3.12}$$

At this stage, this form of the GREEN's function does not admit the WICK decomposition, because the WICK theorem described in Section 3.4.1 requires a dependence on the non-interacting HAMILTONian $\hat{H}_0$ for both the field operators and the thermal average. A way around this problem is the MATSUBARA technique [193], where one introduces a complex time $\tau = it$ and a new physical quantity, the MATSUBARA (imaginary time) GREEN's function $\mathcal{G}(\mathbf{r},\tau;\mathbf{r}',\tau')$. The representation of operators with imaginary time arguments is given in Appendix B.5.

3.2.2 MATSUBARA GREEN's **Function**

The single particle MATSUBARA GREEN's function is defined as

$$\begin{aligned}\mathcal{G}(\mathbf{r},\tau;\mathbf{r}',\tau') &= -\frac{1}{\hbar}\langle T_\tau\{\hat{\psi}_\mathrm{K}(\mathbf{r},\tau)\hat{\psi}^\dagger_\mathrm{K}(\mathbf{r}',\tau')\}\rangle\ , \\ &= -\frac{1}{\hbar}\frac{\mathrm{Tr}[e^{-\beta\hat{K}}T_\tau\{\hat{\psi}_\mathrm{K}(\mathbf{r},\tau)\hat{\psi}^\dagger_\mathrm{K}(\mathbf{r}',\tau')\}]}{\mathrm{Tr}[e^{-\beta\hat{K}}]}\ .\end{aligned} \tag{3.13}$$

The GREEN's function now may be rewritten in the interaction picture

$$\begin{aligned}\mathcal{G}(\mathbf{r},\tau;\mathbf{r}',\tau') &= -\frac{1}{\hbar}\frac{\mathrm{Tr}[e^{-\beta\hat{K}}T_\tau\{\hat{\psi}_\mathrm{K}(\mathbf{r},\tau)\hat{\psi}^\dagger_\mathrm{K}(\mathbf{r}',\tau')\}]}{\mathrm{Tr}[e^{-\beta\hat{K}}]}\ , \\ &= -\frac{1}{\hbar}\frac{\mathrm{Tr}[e^{-\beta\hat{K}_0}\hat{\mathcal{S}}(\beta\hbar,0)T_\tau\{\hat{\psi}_\mathrm{K}(\mathbf{r},\tau)\hat{\psi}^\dagger_\mathrm{K}(\mathbf{r}',\tau')\}]}{\mathrm{Tr}[e^{-\beta\hat{K}_0}\hat{\mathcal{S}}(\beta\hbar,0)]}\ , \\ &= -\frac{1}{\hbar}\frac{\mathrm{Tr}[e^{-\beta\hat{K}_0}\hat{\mathcal{S}}(\beta\hbar,0)T_\tau\{\hat{\mathcal{S}}(0,\tau)\hat{\psi}_\mathrm{I}(\mathbf{r},\tau)\hat{\mathcal{S}}(\tau,0)\hat{\mathcal{S}}(0,\tau')\hat{\psi}^\dagger_\mathrm{I}(\mathbf{r}',\tau')\hat{\mathcal{S}}(\tau',0)\}]}{\mathrm{Tr}[e^{-\beta\hat{K}_0}\hat{\mathcal{S}}(\beta\hbar,0)]}\ , \\ &= -\frac{1}{\hbar}\frac{\mathrm{Tr}[e^{-\beta\hat{K}_0}T_\tau\{\hat{\mathcal{S}}(\beta\hbar,\tau)\hat{\psi}_\mathrm{I}(\mathbf{r},\tau)\hat{\mathcal{S}}(\tau,\tau')\hat{\psi}^\dagger_\mathrm{I}(\mathbf{r}',\tau')\hat{\mathcal{S}}(\tau',0)\}]}{\mathrm{Tr}[e^{-\beta\hat{K}_0}\hat{\mathcal{S}}(\beta\hbar,0)]}\ , \\ &= -\frac{1}{\hbar}\frac{\mathrm{Tr}[e^{-\beta\hat{K}_0}T_\tau\{\hat{\mathcal{S}}(\beta\hbar,0)\hat{\psi}_\mathrm{I}(\mathbf{r},\tau)\hat{\psi}^\dagger_\mathrm{I}(\mathbf{r}',\tau')\}]}{\mathrm{Tr}[e^{-\beta\hat{K}_0}\hat{\mathcal{S}}(\beta\hbar,0)]}\ ,\end{aligned} \tag{3.14}$$

where (B.34) is employed for the transition from the first to the second line and (B.27) for the transition from the second to third line. Equation (3.14) has precisely the structure analyzed in (3.8). The operator $\hat{\mathcal{S}}$ can be expanded as (see (B.33))

$$\mathcal{G}(\mathbf{r},\tau;\mathbf{r}',\tau') = \\ -\frac{1}{\hbar}\frac{\mathrm{Tr}\left[e^{-\beta\hat{K}_0}\sum_{n=0}^{\infty}\frac{1}{n!}\left(\frac{-1}{\hbar}\right)^n\int_0^{\beta\hbar}d\tau_1\dots\int_0^{\beta\hbar}d\tau_n T_\tau\{\hat{K}^\mathrm{int}(\tau_1)\dots\hat{K}^\mathrm{int}(\tau_n)\hat{\psi}_\mathrm{I}(\mathbf{r},\tau)\hat{\psi}^\dagger_\mathrm{I}(\mathbf{r}',\tau')\}\right]}{\mathrm{Tr}\left[e^{-\beta\hat{K}_0}\sum_{n=0}^{\infty}\frac{1}{n!}\left(\frac{-1}{\hbar}\right)^n\int_0^{\beta\hbar}d\tau_1\dots\int_0^{\beta\hbar}d\tau_n T_\tau\{\hat{K}^\mathrm{int}(\tau_1)\dots\hat{K}^\mathrm{int}(\tau_n)\}\right]}\ , \tag{3.15}$$

where the denominator is just the perturbation expansion of the grand partition function. However, it serves to eliminate all disconnected diagrams, exactly as in the zero-temperature formalism. It is apparent that the perturbation expansion of the MATSUBARA GREEN's function (3.15) is very similar to that of the zero temperature GREEN's function (3.31). MATSUBARA [193] has proved that there exists a generalized WICK theorem (see Section 3.4.1) that deals only with the ensemble average of operators and relies on the detailed form of the statistical operator $e^{\beta\hat{K}_0}$.

3.3 Non-Equilibrium GREEN's Functions

In Section 3.2 the GREEN's function for a system under equilibrium at finite temperature has been introduced. In this section, a more general formalism for systems under non-equilibrium conditions at finite temperature is presented. First, the ensemble average of an operator under non-equilibrium is defined. Then the contour-ordered non-equilibrium GREEN's function (NEGF) formalism is introduced and the equation of motion for the GREEN's function is presented. Finally, it will be shown that a perturbation expansion similar to the equilibrium theory can be achieved.

3.3.1 Non-Equilibrium Ensemble Average

We employ the standard device for obtaining a non-equilibrium state. At time t_0, prior to which the system is assumed to be in thermodynamic equilibrium with a reservoir, the system is exposed to a disturbance represented by the contribution $\hat{H}^{\mathrm{ext}}$ to the HAMILTONian. The external perturbation can for instance be a time varying electric field, a light excitation pulse, and so forth. The total HAMILTONian is thus given by

$$\hat{\mathscr{H}}(t) \;=\; \hat{H}_0 \;+\; \hat{H}^{\mathrm{int}} \;+\; \hat{H}^{\mathrm{ext}} \;=\; \hat{H} \;+\; \hat{H}^{\mathrm{ext}} \;, \tag{3.16}$$

where $\hat{H}^{\mathrm{ext}} = 0$ for $t < t_0$. One is not restricted to using the statistical equilibrium state at times prior to t_0 as the initial condition. As shown by [194], a non-equilibrium situation can be maintained through contact with a reservoir. A discussion of the coupling of a system to a reservoir has been studied in [195].

Non-equilibrium statistical mechanics is concerned with calculating average values $\langle \hat{O}_{\mathscr{H}}(t) \rangle$ of physical observables for times $t > t_0$. Given the density operator $\hat{\rho}$, the average of any operator $\hat{O}$ is then defined as (C.8)

$$\langle \hat{O}_{\mathscr{H}}(t) \rangle \;\equiv \mathrm{Tr}[\hat{\rho}\; \hat{O}_{\mathscr{H}}(t)] \;, \tag{3.17}$$

where $\hat{O}_{\mathscr{H}}(t)$ is an operator in the HEISENBERG picture.

The non-equilibrium GREEN's function can be defined as

$$G(\mathbf{r},t,\mathbf{r}',t') \;=\; -\frac{i}{\hbar}\langle T_{\mathrm{t}}\{\hat{\psi}_{\mathscr{H}}(\mathbf{r},t)\hat{\psi}^{\dagger}_{\mathscr{H}}(\mathbf{r}',t')\}\rangle \;, \tag{3.18}$$

where $\hat{\psi}_{\mathscr{H}}$ is the field operator in the HEISENBERG picture evolving with the HAMILTONian $\hat{\mathscr{H}}$ defined in (3.16) and the bracket $\langle \ldots \rangle$ is the statistical average with the density operator defined in (3.17).

One can evaluate GREEN's functions by using WICK's theorem, which enables us to decompose many-particle GREEN's functions into sums and products of single-particle GREEN's functions (see Section 3.4.1). The restriction of the WICK theorem necessitates that the field operators and the density operator have to be represented in the interaction picture, or equivalently, their time evolution is governed by the non-interacting HAMILTONian $\hat{H}_0$. The contour-ordered GREEN's function, which is introduced next, provides a suitable framework for this purpose.

3.3.2 Contour-Ordered GREEN's Function

To express the field operators in the interaction representation an operator $\hat{S}$ is defined (see Appendix B.4) and applied for calculating the GREEN's functions as in Section 3.1.1. The time in (3.8) is taken over the interval $(-\infty, \infty)$. The state at $t \to -\infty$ is well defined as the ground-state of the non-interacting system $|\phi_0\rangle$. The interactions are turned on slowly. At $t = 0$ the fully interacting ground state is $|\Psi(0)\rangle = \hat{S}(0, -\infty)|\phi_0\rangle$. The state at $t \to \infty$ must be defined carefully. If the interactions remain on, then this state is not well described by the non-interacting ground state. Alternatively, one could require that the interactions are turned off at large times, which returns the system to the ground-state $|\phi_0\rangle$.

SCHWINGER [92] suggested another method of handling the asymptotic limit $t \to -\infty$. He proposed that the time integral in the $\hat{S}$ operator has two parts; one goes from $(-\infty, t)$ while the second goes from $(t, -\infty)$. The integration path is a contour, which starts and ends at $-\infty$. The advantage of this method is that one starts and ends the S operator expansion with a known state $|\Psi(-\infty)\rangle = |\phi_0\rangle$. Instead of the time-ordering operator (B.21), a contour-ordering operator can be employed. The contour-ordering operator T_C orders the time labels according to their order on the contour C. Under equilibrium condition the contour-ordered method gives results that are identical to the time-ordered method described in Section 3.1.1. The main advantage of the contour-ordered method is in describing non-equilibrium phenomena using GREEN's functions. Non-equilibrium theory is entirely based upon this formalism, or equivalent methods.

Any operator $\hat{O}_\mathcal{H}$ in the HEISENBERG picture can be transformed into the interaction picture (see (B.13))

$$\hat{O}_\mathcal{H} \;=\; \hat{S}(t_0, t)\; \hat{O}_\mathrm{I}\; \hat{S}(t, t_0)\;. \tag{3.19}$$

Analogous to the derivation of (B.24), it can be shown that the $\hat{S}$ operator is given by

$$\hat{S}(t, t_0) \;=\; T_\mathrm{t}\{\exp\left(-\frac{i}{\hbar}\int\limits_{t_0}^{t} dt'\hat{H}_\mathrm{I}^\mathrm{ext}(t')\right)\;\exp\left(-\frac{i}{\hbar}\int\limits_{t_0}^{t} dt'\hat{H}_\mathrm{I}^\mathrm{int}(t')\right)\}\;, \tag{3.20}$$

where the operators are in the interaction representation. The ordinary time-ordering can also be written as ordering along contour branches C_1 and C_2 as depicted in Fig. 3.1

$$\begin{aligned}
\hat{S}(t, t_0) \;&=\; T_{C_1}\{\exp\left(-\frac{i}{\hbar}\int\limits_{C_1} dt\hat{H}_\mathrm{I}^\mathrm{ext}(t)\right)\;\exp\left(-\frac{i}{\hbar}\int\limits_{C_1} dt\hat{H}_\mathrm{I}^\mathrm{int}(t)\right)\}\\
\hat{S}(t_0, t) \;&=\; T_{C_2}\{\exp\left(-\frac{i}{\hbar}\int\limits_{C_2} dt\hat{H}_\mathrm{I}^\mathrm{ext}(t)\right)\;\exp\left(-\frac{i}{\hbar}\int\limits_{C_2} d\tau\hat{H}_\mathrm{I}^\mathrm{int}(t)\right)\}\;.
\end{aligned} \tag{3.21}$$

By combining two contour branches, $C = C_1 \cup C_2$, (3.19) can be rewritten as

$$\begin{aligned}
\hat{O}_\mathcal{H}(t) \;&=\; T_\mathrm{C}\{\hat{S}_\mathrm{C}^\mathrm{ext}\;\hat{O}_\mathrm{H}\}\;,\\
&=\; T_\mathrm{C}\{\hat{S}_\mathrm{C}^\mathrm{ext}\;\hat{S}_\mathrm{C}^\mathrm{int}\;\hat{O}_\mathrm{I}\}\;,\\
&=\; T_\mathrm{C}\{\hat{S}_\mathrm{C}\;\hat{O}_\mathrm{I}\}\;,
\end{aligned} \tag{3.22}$$

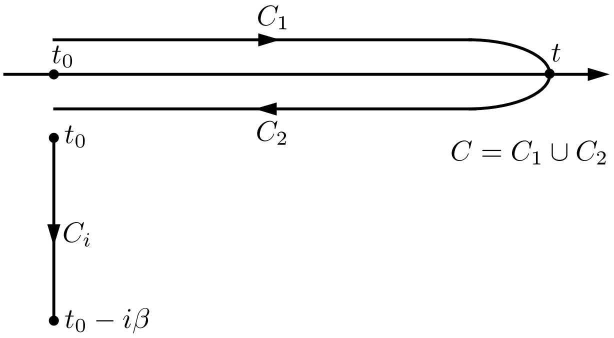

Figure 3.1: The contour $C = C_1 \cup C_2$ runs on the real axis, but for clarity its two branches C_1 and C_2 are shown slightly away from the real axis. The contour C_i runs from t_0 to $t_0 - i\beta$.

where,

$$\begin{aligned}\hat{S}_{\mathrm{C}} &= \exp\left(-\frac{i}{\hbar}\int_C dt \hat{H}_{\mathrm{I}}^{\mathrm{ext}}(t)\right) \exp\left(-\frac{i}{\hbar}\int_C dt \hat{H}_{\mathrm{I}}^{\mathrm{int}}(t)\right) , \\ &= \hat{S}_{\mathrm{C}}^{\mathrm{ext}} \; \hat{S}_{\mathrm{C}}^{\mathrm{int}} .\end{aligned} \tag{3.23}$$

In equation (3.17) $\hat{\rho}$ describes the equilibrium state of the system before the external perturbation $\hat{H}^{\mathrm{ext}}$ is turned on. Interactions $\hat{H}^{\mathrm{int}}$, which are switched on adiabatically at $-\infty$, are present in $\hat{\rho}$. However, to apply WICK's theorem (Section 3.4.1), one has to work with non-interacting operators. A methodology similar to the MATSUBARA theory can be applied to express the many-particle density operator $\hat{\rho}$ in terms of the single-particle density operator $\hat{\rho}_0$, see Appendix B.5. If the contour $C_i = [t_0, t_0 - i\beta]$ is chosen (Fig. 3.1), then (B.34) takes the form

$$e^{-\beta \hat{K}} = e^{-\beta \hat{K}_0} \; \hat{S}_{C_i} . \tag{3.24}$$

Therefore, (3.17) can be rewritten as

$$\langle \hat{O}_{\mathscr{H}}(t) \rangle = \frac{\mathrm{Tr}[e^{-\beta \hat{K}_0} T_{C_i} \hat{S}_{C_i} \hat{O}_{\mathscr{H}}(t)]}{\mathrm{Tr}[e^{-\beta \hat{K}_0} T_{C_i} \hat{S}_{C_i}]} , \tag{3.25}$$

Using the relations (3.22) and (3.25), the GREEN's function in (3.18) becomes [196]

$$G(\mathbf{r}, t, \mathbf{r}', t') = -\frac{i}{\hbar} \frac{\mathrm{Tr}[e^{-\beta \hat{K}_0} T_{C_i} \hat{S}_{C_i} \; T_C \hat{S}_C \; \hat{\psi}_{\mathrm{I}}(\mathbf{r}, t) \hat{\psi}_{\mathrm{I}}^{\dagger}(\mathbf{r}', t')]}{\mathrm{Tr}[e^{-\beta \hat{K}_0} T_{C_i} \hat{S}_{C_i} \; T_C \hat{S}_C]} . \tag{3.26}$$

The twofold expansion of the density operator and the field operators may conveniently be combined to a single expansion. The two contours C_i and C can be combined together, $C^* = C \cup C_i$ (Fig. 3.2), and a contour-ordering operator $T_{C^*} = T_{C_i} T_C$, which orders along C^*, can be introduced. Hence, a point on C is always earlier than a point on C_i. Furthermore, we define an interaction representation with respect to $\hat{H}_0$ on C and with respect to $\hat{K}_0$ on C_i. Therefore,

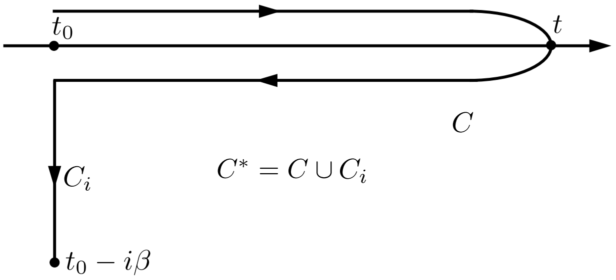

Figure 3.2: The contour $C^* = C_i \cup C$, runs from t_0 to t_0 and from t_0 to $t_0 - i\beta$.

the GREEN's function in (3.18) is given by

$$\begin{aligned} G(\mathbf{r}, t, \mathbf{r}', t') &= -\frac{i}{\hbar} \frac{\mathrm{Tr}[e^{-\beta \hat{K}_0} T_{C^*}\{\hat{S}_{C^*} \hat{\psi}_{\mathrm{I}}(\mathbf{r}, t) \hat{\psi}_{\mathrm{I}}^{\dagger}(\mathbf{r}', t')\}]}{\mathrm{Tr}[e^{-\beta \hat{K}_0} T_{C^*} \hat{S}_{C^*}]} \\ &= -\frac{i}{\hbar} \langle T_{C^*}\{\hat{S}_{C^*} \hat{\psi}_{\mathrm{I}}(\mathbf{r}, t) \hat{\psi}_{\mathrm{I}}^{\dagger}(\mathbf{r}', t')\}\rangle_0 \ , \end{aligned} \tag{3.27}$$

where $\langle \ldots \rangle_0$ represents the statistical average with respect to $\hat{\rho}_0$. From here we assume that all statistical averages are with respect to $\hat{\rho}_0$ and drop the 0 from the brackets $\langle \ldots \rangle_0$.

3.3.3 KELDYSH **Contour**

If one does not consider initial correlations, one can let $t_0 \to -\infty$. Since we assume that the GREEN's function falls off sufficiently rapidly as a function of the separation of its time arguments, one can neglect the part of the contour C_i extending from t_0 to $t_0 - i\beta$ [197]. It has been shown that by explicitly taking the initial correlations into account [198–201] the neglect of this part of the contour corresponds to the neglect of initial correlations. The initial condition, that the system is assumed to be in equilibrium before the external perturbation is turned on, can then be imposed directly on the DYSON equation in integral form. This provides an independent demonstration that, for cases where initial correlations can be neglected, one can discard the contribution of the contour from t_0 to $t_0 - i\beta$. The contours C^* and C become identical, as they both start and end at $-\infty$. They can be extended beyond the largest time by considering that the time-evolution operator is a unitary, and one then obtains the contour C_K introduced by KELDYSH [202].

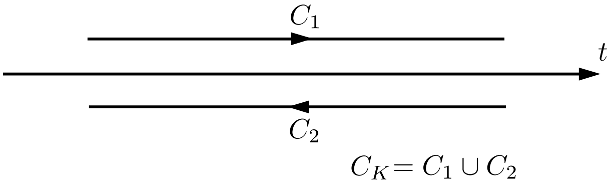

Figure 3.3: KELDYSH contour branches $C_1 = (-\infty, \infty)$ and $C_2 = (\infty, -\infty)$.

3.4 Perturbation Expansion of the GREEN's Function

In previous sections GREEN's functions at zero and finite temperatures have been defined. It was shown that the GREEN's functions can be written in terms of the $\hat{S}$ operator

$$G(\mathbf{r},t,\mathbf{r}',t') \;=\; -\frac{i}{\hbar}\langle T\{\hat{S}\ \hat{\psi}_{\mathrm{I}}(\mathbf{r},t)\hat{\psi}^{\dagger}_{\mathrm{I}}(\mathbf{r}',t')\}\rangle\ , \tag{3.28}$$

where $\hat{S}$ includes the effects of interactions and external perturbations

$$\hat{S} \;=\; \exp\left(-\frac{i}{\hbar}\int dt\ \hat{H}^{\mathrm{int}}_{\mathrm{I}}(t)\right)\ . \tag{3.29}$$

Unfortunately, it is not possible to give an analytical solution for $G(\mathbf{r},t;\mathbf{r}',t')$, unless the interaction perturbation $\hat{H}^{\mathrm{int}}$ is set equal to zero. This gives the non-interacting GREEN's function (see Appendix D)

$$G_0(\mathbf{r},t;\mathbf{r}',t') \;=\; -\frac{i}{\hbar}\langle T\{\hat{\psi}_{\mathrm{I}}(\mathbf{r},t)\hat{\psi}^{\dagger}_{\mathrm{I}}(\mathbf{r}',t')\}\rangle\ , \tag{3.30}$$

which is central for any perturbation expansion.

This section proceeds the calculation of the GREEN's function by expanding the $\hat{S}$ operator as series of products of $\hat{H}^{\mathrm{int}}_{\mathrm{I}}$ in the numerator and the denominator. By expanding the $\hat{S}$ operator one obtains (see (B.20))

$$G(\mathbf{r},t;\mathbf{r}',t') = -\frac{i}{\hbar}\frac{\langle\sum\limits_{n=0}^{\infty}\frac{1}{n!}\left(\frac{-i}{\hbar}\right)^{n}\int dt_1\ldots\int dt_n\ T\{\hat{H}^{\mathrm{int}}_{\mathrm{I}}(t_1)\ldots\hat{H}^{\mathrm{int}}_{\mathrm{I}}(t_n)\hat{\psi}_{\mathrm{I}}(\mathbf{r},t)\hat{\psi}^{\dagger}_{\mathrm{I}}(\mathbf{r}',t')\}\rangle}{\langle\sum\limits_{n=0}^{\infty}\frac{1}{n!}\left(\frac{-i}{\hbar}\right)^{n}\int dt_1\ldots\int dt_n\ T_{\mathrm{t}}\{\hat{H}^{\mathrm{int}}_{\mathrm{I}}(t_1)\ldots\hat{H}^{\mathrm{int}}_{\mathrm{I}}(t_n)\}\rangle}\ . \tag{3.31}$$

The expansion of the numerator of the GREEN's function in (3.31) can be written as

$$G_{\mathrm{N}} \;=\; \underbrace{\langle T_{\mathrm{t}}\ \{\hat{\psi}_{\mathrm{I}}(\mathbf{r},t)\hat{\psi}^{\dagger}_{\mathrm{I}}(\mathbf{r}',t')\}\rangle}_{G^0_{\mathrm{N}}} \;+\; \underbrace{\langle T_{\mathrm{t}}\{-\frac{i}{\hbar}\int dt_1\hat{H}^{\mathrm{int}}_{\mathrm{I}}(t_1)\hat{\psi}_{\mathrm{I}}(\mathbf{r},t)\hat{\psi}^{\dagger}_{\mathrm{I}}(\mathbf{r}',t')\}\rangle}_{G^1_{\mathrm{N}}} \;+\;\ldots\ , \tag{3.32}$$

where the superscript denotes the order of perturbation. The zero-order perturbation leads to non-interacting GREEN's function $G^0_{\mathrm{N}} = i\hbar G_0$. WICK's theorem allows us to write each of these brackets in terms of non-interacting GREEN's function and the interaction potential. The same procedure can be applied to the denominator. The terms in the expansion of the denominator, $\langle S(\infty,-\infty)\rangle$, are called *vacuum polarization terms* [191].

Different expansion terms achieved from the WICK theorem can be translated into FEYNMAN diagrams (Appendix E). FEYNMAN introduced the idea of representing different contributions obtained from the WICK decomposition by drawings. These drawings, called diagrams, are very useful for providing an insight into the physical processes which these terms represent. The FEYNMAN diagrams provide an illustrative way to solve many-body problems and the perturbation expansion of GREEN's functions.

3.4.1 WICK Theorem

The WICK decomposition allows a perturbation expansion of GREEN's functions. It always holds for zero-temperature GREEN's functions and only under the condition that field operators must be given in the interaction picture (Appendix B.2). Their time evolution is governed by the non-interacting HAMILTONian $\hat{H}_0$, and $\hat{H}^{\text{int}}$ is treated as a perturbation. If these conditions are fulfilled, WICK's theorem states that the expectation values of products of field operators is equal to the sum of expectation values of all possible pairs of operators and that each of these pairs will be a non-interacting single-particle GREEN's function

$$\langle T_{\mathrm{t}}\{\hat{O}_1\hat{O}_2\ldots\hat{O}_n\}\rangle \;=\; \sum_{P_d} \langle T_{\mathrm{t}}\{\hat{O}_1\hat{O}_2\}\rangle_0 \langle T_{\mathrm{t}}\{\hat{O}_3\hat{O}_4\}\rangle_0 \ldots \langle T_{\mathrm{t}}\{\hat{O}_{n-1}\hat{O}_n\}\rangle \; . \tag{3.33}$$

The sum runs over all P_d distinct permutations of the n indices. It should be noticed that brackets such as (3.33) vanish if the number of creation and annihilation operators is not the same. If the number of annihilated particles is not the same as the number of created particles, then the system will not come back to its ground-state. As a result the expectation value over the ground-state vanishes. With the same reasoning one concludes that if both operators appearing in a bracket are annihilation or creation operators, the expectation value disappears, otherwise one obtains an expression proportional to the non-interacting GREEN's function G_0.

The most general proof of this theorem is due to [203], where it is shown rigorously that the theorem holds exactly if the operators to be averaged are non-interacting and the density operator, which appears in the finite temperature formalism (see (3.15) and (3.26)), is a single-particle operator. Therefore, one can use the WICK theorem to get a perturbation expansion for the GREEN's function. The only formal difference from the equilibrium theory is the appearance of integration over a contour instead of integration over the inverse temperature interval for the case of finite temperature or the real axis for the case of zero temperature.

A few simple rules should be noted when making these pairings. The first is that a sign change occurs each time the positions of two neighboring FERMIon operators are interchanged.

The second rule concerns the time-ordering of combinations of operators representing different excitations. For example, a bracket with a mixture of electron and phonon operators can be separated into electron and phonon parts, since electron operators commute with phonon operators. WICK's theorem can be also applied to brackets of phonon operators. Since phonons are Bosons, sign does not change when exchanging positions of operators.

The third rule is a method of treating the time-ordering of two operators which are applied at the same time. The time-ordered product is undefined at equal times. To remove this ambiguity, the following interpretation can be applied

$$\langle T_{\mathrm{t}}\{\hat{\psi}_{\mathrm{I}}(\mathbf{r},t)\hat{\psi}^{\dagger}_{\mathrm{I}}(\mathbf{r}',t)\} = \lim_{t'\to t^{+}} \langle T_{\mathrm{t}}\{\hat{\psi}_{\mathrm{I}}(\mathbf{r},t)\hat{\psi}^{\dagger}_{\mathrm{I}}(\mathbf{r}',t')\}\rangle_0 \; . \tag{3.34}$$

WICK's theorem has been applied to calculate first-order perturbation expansions in Section 3.4.2. It can be also applied for higher-order perturbations.

3.4.2 First-Order Perturbation Expansion

The electron-electron interaction up to the first-order perturbation is studied here. In the interaction representation the operator corresponding to this kind of interaction is given by

$$\hat{H}_{\mathrm{I}}^{\mathrm{el-el}}(t_1) = \hat{V}_{\mathrm{I}}(t_1) = \frac{1}{2}\int d\mathbf{r_1}\int d\mathbf{r_2}\hat{\psi}_{\mathrm{I}}^{\dagger}(\mathbf{r_1},t_1)\hat{\psi}_{\mathrm{I}}^{\dagger}(\mathbf{r_2},t_1)V(\mathbf{r_1}-\mathbf{r_2})\hat{\psi}_{\mathrm{I}}(\mathbf{r_2},t_1)\hat{\psi}_{\mathrm{I}}(\mathbf{r_1},t_1)\ , \tag{3.35}$$

where the COULOMB interaction potential is assumed to be an instantaneous potential proportional to a delta function δ_{t_1,t_2}. The first-order term of the perturbation expansion is given by

$$\begin{aligned} G_{\mathrm{N}}^{1} &= \langle T_{\mathrm{t}}\{-\frac{i}{\hbar}\int dt_1\hat{V}_{\mathrm{I}}(t_1)\hat{\psi}_{\mathrm{I}}(\mathbf{r},t)\hat{\psi}_{\mathrm{I}}^{\dagger}(\mathbf{r}',t')\}\rangle \\ &= \frac{1}{2}\left(\frac{-i}{\hbar}\right)\int dt_1\int d\mathbf{r_1}\int d\mathbf{r_2}V(\mathbf{r_1}-\mathbf{r_2}) \\ &\quad\times\ \underbrace{\langle T_{\mathrm{t}}\{\hat{\psi}_{\mathrm{I}}^{\dagger}(\mathbf{r_1},t_1)\hat{\psi}_{\mathrm{I}}^{\dagger}(\mathbf{r_2},t_1)\hat{\psi}_{\mathrm{I}}(\mathbf{r_2},t_1)\hat{\psi}_{\mathrm{I}}(\mathbf{r_1},t_1)\hat{\psi}_{\mathrm{I}}(\mathbf{r},t)\hat{\psi}_{\mathrm{I}}^{\dagger}(\mathbf{r}',t')\}\rangle}_{F_{\mathrm{N}}^{1}}\ , \end{aligned} \tag{3.36}$$

$$\begin{aligned} F_{\mathrm{N}}^{1} = [\ &+\langle T_{\mathrm{t}}\{\hat{\psi}_{\mathrm{I}}(\mathbf{r_1},t_1)\hat{\psi}_{\mathrm{I}}^{\dagger}(\mathbf{r_1},t_1)\}\rangle\ \langle T_{\mathrm{t}}\{\hat{\psi}_{\mathrm{I}}(\mathbf{r_2},t_1)\hat{\psi}_{\mathrm{I}}^{\dagger}(\mathbf{r_2},t_1)\}\rangle\ \langle T_{\mathrm{t}}\{\hat{\psi}_{\mathrm{I}}(\mathbf{r},t)\hat{\psi}_{\mathrm{I}}^{\dagger}(\mathbf{r}',t')\}\rangle \\ &-\langle T_{\mathrm{t}}\{\hat{\psi}_{\mathrm{I}}(\mathbf{r_1},t_1)\hat{\psi}_{\mathrm{I}}^{\dagger}(\mathbf{r_1},t_1)\}\rangle\ \langle T_{\mathrm{t}}\{\hat{\psi}_{\mathrm{I}}(\mathbf{r},t)\hat{\psi}_{\mathrm{I}}^{\dagger}(\mathbf{r_2},t_1)\}\rangle\ \langle T_{\mathrm{t}}\{\hat{\psi}_{\mathrm{I}}(\mathbf{r_2},t_1)\hat{\psi}_{\mathrm{I}}^{\dagger}(\mathbf{r}',t')\}\rangle \\ &+\langle T_{\mathrm{t}}\{\hat{\psi}_{\mathrm{I}}(\mathbf{r_2},t_1)\hat{\psi}_{\mathrm{I}}^{\dagger}(\mathbf{r_1},t_1)\}\rangle\ \langle T_{\mathrm{t}}\{\hat{\psi}_{\mathrm{I}}(\mathbf{r},t)\hat{\psi}_{\mathrm{I}}^{\dagger}(\mathbf{r_2},t_1)\}\rangle\ \langle T_{\mathrm{t}}\{\hat{\psi}_{\mathrm{I}}(\mathbf{r_1},t_1)\hat{\psi}_{\mathrm{I}}^{\dagger}(\mathbf{r}',t')\}\rangle \\ &-\langle T_{\mathrm{t}}\{\hat{\psi}_{\mathrm{I}}(\mathbf{r_2},t_1)\hat{\psi}_{\mathrm{I}}^{\dagger}(\mathbf{r_1},t_1)\}\rangle\ \langle T_{\mathrm{t}}\{\hat{\psi}_{\mathrm{I}}(\mathbf{r_1},t_1)\hat{\psi}_{\mathrm{I}}^{\dagger}(\mathbf{r_2},t_1)\}\rangle\ \langle T_{\mathrm{t}}\{\hat{\psi}_{\mathrm{I}}(\mathbf{r},t)\hat{\psi}_{\mathrm{I}}^{\dagger}(\mathbf{r}',t')\}\rangle \\ &+\langle T_{\mathrm{t}}\{\hat{\psi}_{\mathrm{I}}(\mathbf{r},t)\hat{\psi}_{\mathrm{I}}^{\dagger}(\mathbf{r_1},t_1)\}\rangle\ \langle T_{\mathrm{t}}\{\hat{\psi}_{\mathrm{I}}(\mathbf{r_1},t_1)\hat{\psi}_{\mathrm{I}}^{\dagger}(\mathbf{r_2},t_1)\}\rangle\ \langle T_{\mathrm{t}}\{\hat{\psi}_{\mathrm{I}}(\mathbf{r_2},t_1)\hat{\psi}_{\mathrm{I}}^{\dagger}(\mathbf{r}',t')\}\rangle \\ &-\langle T_{\mathrm{t}}\{\hat{\psi}_{\mathrm{I}}(\mathbf{r},t)\hat{\psi}_{\mathrm{I}}^{\dagger}(\mathbf{r_1},t_1)\}\rangle\ \langle T_{\mathrm{t}}\{\hat{\psi}_{\mathrm{I}}(\mathbf{r_2},t_1)\hat{\psi}_{\mathrm{I}}^{\dagger}(\mathbf{r_2},t_1)\}\rangle\ \langle T_{\mathrm{t}}\{\hat{\psi}_{\mathrm{I}}(\mathbf{r_1},t_1)\hat{\psi}_{\mathrm{I}}^{\dagger}(\mathbf{r}',t')\}\rangle\ ]\ . \end{aligned} \tag{3.37}$$

By replacing the brackets by GREEN's functions one gets

$$\begin{aligned} G_{\mathrm{N}}^{1} = &\ \frac{1}{2}\left(\frac{-i}{\hbar}\right)\int dt_1\int d\mathbf{r_1}\int d\mathbf{r_2}V(\mathbf{r_1}-\mathbf{r_2}) \\ \times\ [\ &\underbrace{+i\hbar\ G_0(\mathbf{r_1},t_1;\mathbf{r_1},t_1)\ i\hbar\ G_0(\mathbf{r_2},t_1;\mathbf{r_2},t_1)\ i\hbar\ G_0(\mathbf{r},t;\mathbf{r}',t')}_{(a)} \\ &\underbrace{-i\hbar\ G_0(\mathbf{r_1},t_1;\mathbf{r_1},t_1)\ i\hbar\ G_0(\mathbf{r},t;\mathbf{r_2},t_1)\ i\hbar\ G_0(\mathbf{r_2},t_1;\mathbf{r}',t')}_{(b)} \\ &\underbrace{+i\hbar\ G_0(\mathbf{r_2},t_1;\mathbf{r_1},t_1)\ i\hbar\ G_0(\mathbf{r},t;\mathbf{r_2},t_1)\ i\hbar\ G_0(\mathbf{r_1},t_1;\mathbf{r}',t')}_{(c)} \\ &\underbrace{-i\hbar\ G_0(\mathbf{r_2},t_1;\mathbf{r_1},t_1)\ i\hbar\ G_0(\mathbf{r_1},t_1;\mathbf{r_2},t_1)\ i\hbar\ G_0(\mathbf{r},t;\mathbf{r}',t')}_{(d)} \\ &\underbrace{+i\hbar\ G_0(\mathbf{r},t;\mathbf{r_1},t_1)\ i\hbar\ G_0(\mathbf{r_1},t_1;\mathbf{r_2},t_1)\ i\hbar\ G_0(\mathbf{r_2},t_1;\mathbf{r}',t')}_{(e)} \\ &\underbrace{-i\hbar\ G_0(\mathbf{r},t;\mathbf{r_1},t_1)\ i\hbar\ G_0(\mathbf{r_2},t_1;\mathbf{r_2},t_1)\ i\hbar\ G_0(\mathbf{r_1},t_1;\mathbf{r}',t')}_{(f)}]\ . \end{aligned} \tag{3.38}$$

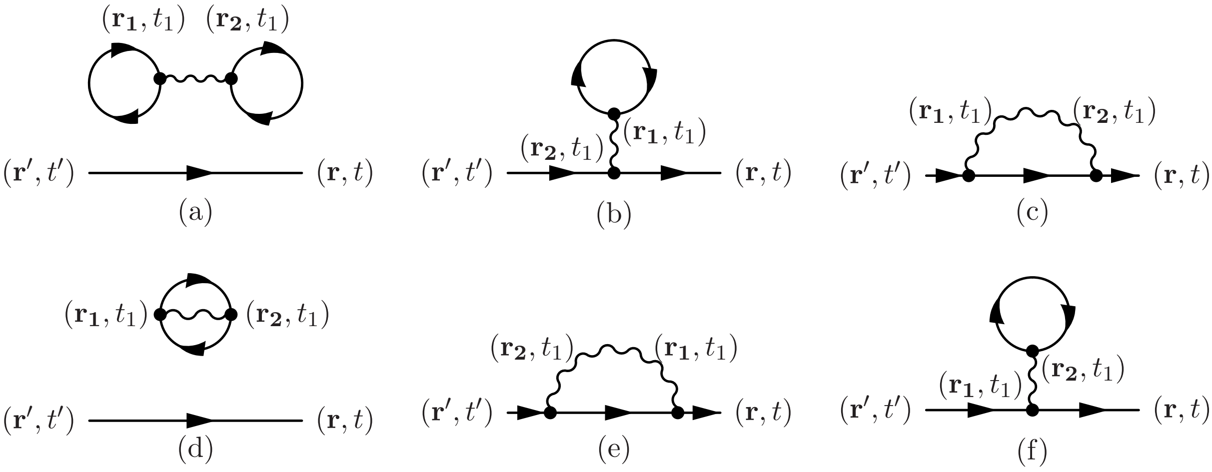

Figure 3.4: FEYNMAN diagrams of the first-order perturbation terms G^1_{N}.

FEYNMAN diagrams for the corresponding terms are shown in Fig. 3.4. In the first-order example the connected diagrams (*b*) and (*f*) are equal, as are the diagrams (*c*) and (*e*); they differ only in that the integration variables $\mathbf{r_1}$ and $\mathbf{r_2}$ are interchanged, whereas the COULOMB potential is symmetric under this substitution. It is therefore sufficient to retain just one diagram of each type, simultaneously omitting the factor 1/2 in front of (3.38). For the nth-order perturbation there are $n!$ possible interchanges of integration variables. Therefore, the repetition of the same diagrams cancels the factor $1/n!$ in (3.31).

Diagram (*a*) and (*d*) contain sub-units that are not connected by any lines to the rest of the diagram. Feynman diagrams in which all parts are not connected are called *disconnected diagrams*. Equation (3.38) shows that such diagrams are typically have GREEN's function and interactions whose arguments close on themselves. As a result the contribution of this sub-unit can be factored out of the expression for G_{N}. The same procedure can be applied for the denominator. In this cases, the second term of the expansion includes only two non-vanishing terms which are only disconnected diagrams of (3.38), namely (a) and (d).

$$\begin{aligned} G^1_{\mathrm{D}} &= \frac{1}{2}\left(\frac{-i}{\hbar}\right)\int dt_1 \int d\mathbf{r} \int d\mathbf{r}' V(\mathbf{r}-\mathbf{r}') \\ &\times [\quad +i\hbar\, G_0(\mathbf{r_1}, t_1; \mathbf{r_1}, t_1)\; i\hbar\, G_0(\mathbf{r_2}, t_1; \mathbf{r_2}, t_1) \\ &\qquad -i\hbar\, G_0(\mathbf{r_2}, t_1; \mathbf{r_1}, t_1)\; i\hbar\, G_0(\mathbf{r_1}, t_1; \mathbf{r_2}, t_1)]\ , \end{aligned} \tag{3.39}$$

As a result, these terms cancel the disconnected diagrams of the numerator and the resulting GREEN's function consists of only connected diagrams. It can be shown that in general the vacuum polarization terms cancel the disconnected diagrams in the expansion of the GREEN's function [204]. As a result the GREEN's function is just the summation of all topologically different connected diagrams [185]

$$\begin{aligned} &G(\mathbf{r}, t; \mathbf{r}', t') = \\ &-\frac{i}{\hbar}\langle \sum_{n=0}^{\infty} \frac{1}{n!}\left(\frac{-i}{\hbar}\right)^n \int dt_1 \ldots \int dt_n\; T\{\hat{H}^{\mathrm{int}}_{\mathrm{I}}(t_1)\ldots \hat{H}^{\mathrm{int}}_{\mathrm{I}}(t_n)\hat{\psi}_{\mathrm{I}}(\mathbf{r}, t)\hat{\psi}^{\dagger}_{\mathrm{I}}(\mathbf{r}', t')\}\rangle_{\mathrm{conn}}\ . \end{aligned} \tag{3.40}$$

3.5 Dyson Equation

The Dyson equation can be achieved by classifying the various contributions in arbitrary Feynman diagrams. Dyson's equation summarizes the Feynman-Dyson perturbation theory in a particularly compact form. The exact Green's function can be written as the non-interacting Green's function plus all connected terms with a non-interacting Green's function at each end, see (3.40). This structure is shown in Fig. 3.5, where the double line denotes G and the single line G_0.

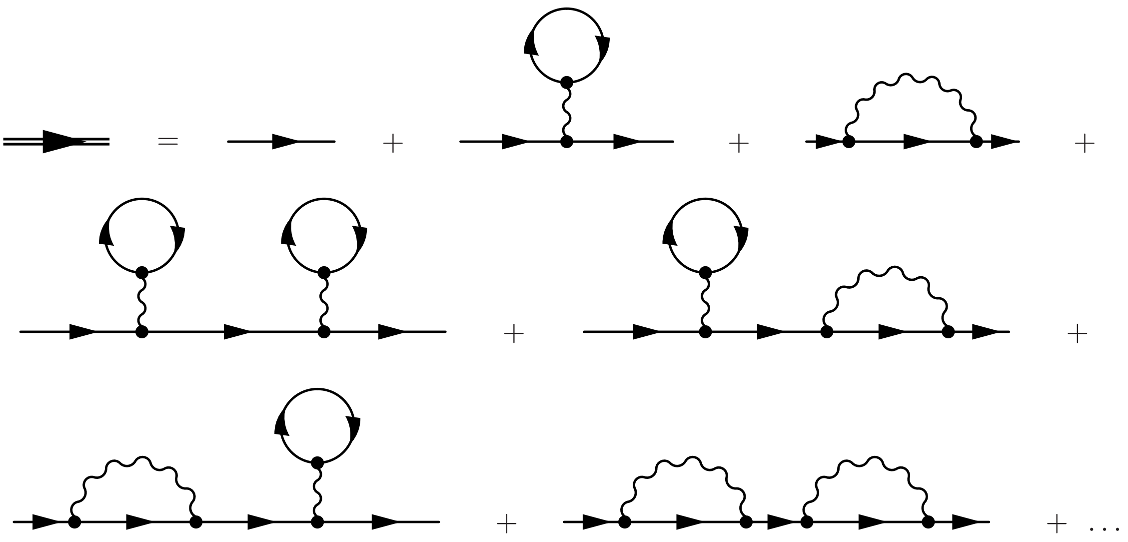

Figure 3.5: The Green's function expanded in terms of connected diagrams.

By introducing the concept of self-energy Σ the structure in Fig. 3.5 takes the form shown Fig. 3.6.

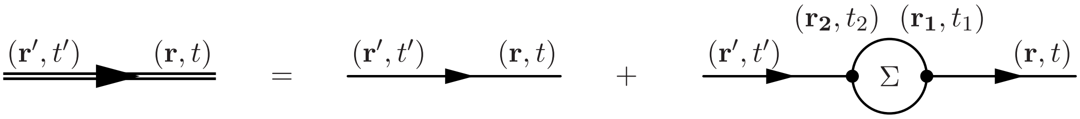

Figure 3.6: Feynman diagrams showing the general structure of G.

The corresponding analytic expression is given by

$$G(\mathbf{r}, t; \mathbf{r}', t') \;=\; G_0(\mathbf{r}, t; \mathbf{r}', t') \;+\; \int d1 \int d2 \; G_0(\mathbf{r}, t; 1) \; \Sigma(12) \; G_0(2; \mathbf{r}', t') \;, \tag{3.41}$$

where the abbreviation $1 \equiv (\mathbf{r_1}, t_1)$ and $\int d1 \equiv \int d\mathbf{r_1} \int dt_1$ is used. The self-energy Σ describes the renormalization of single-particle states due to the interaction with the surrounding many-particle system and the Dyson equation determines the renormalized Green's function.

Another important concept is the *proper self-energy insertion* which is a self-energy insertion that can not be separated into two pieces by cutting a single-particle line. By definition, the

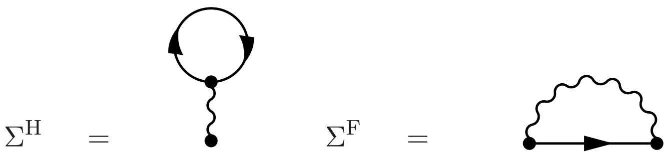

Figure 3.7: FEYNMAN diagrams of the first-order proper self-energies.

proper self-energy is the sum of all proper self-energy insertions, and will be denoted by Σ^*. Using the perturbation expansion, one can define the proper self-energy Σ^* as an irreducible part of the GREEN's function. Based on this definition first-order proper self-energies, which are resulted from the first-order expansion of the GREEN's function (see Section 3.4.2), are shown in Fig. 3.7. These diagrams are irreducible parts of Fig. 3.4-b and Fig. 3.4-c and are referred to as the HARTREE (Σ^{H}) and the FOCK (Σ^{F}) self-energies.

The self-energy can also in principle be introduced variationally [203]. A variational derivation of the self-energies for the electron-electron and electron-phonon interactions is presented in Appendices F.1 and F.2, respectively. It follows from these definitions that the self-energy consists of a sum of all possible repetitions of the proper self-energy

$$\Sigma(\mathbf{r},t;\mathbf{r}',t') \;=\; \Sigma^*(\mathbf{r},t;\mathbf{r}',t') \;+\; \int d1 \int d2\; \Sigma^*(\mathbf{r},t;1)\; G_0(12)\; \Sigma^*(2;\mathbf{r}',t') \;+\; \ldots \;. \tag{3.42}$$

Correspondingly, the GREEN's function in (3.41) can be rewritten as

$$G(\mathbf{r},t;\mathbf{r}',t') \;=\; G_0(\mathbf{r},t;\mathbf{r}',t') \;+\; \int d1 \int d2\; G_0(\mathbf{r},t;1)\; \Sigma^*(12)\; G_0(2;\mathbf{r}',t') \;+\; \ldots \;, \tag{3.43}$$

which can be summed formally to yield an *integral equation* (DYSON equation) for the exact GREEN's function which is shown in Fig. 3.8.

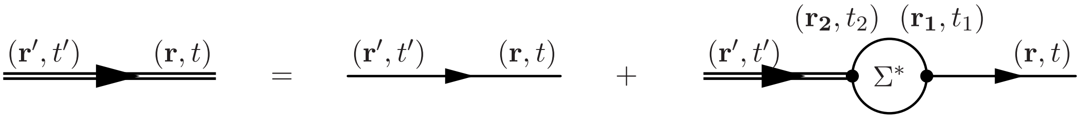

Figure 3.8: FEYNMAN diagrams representing DYSON's equation.

The corresponding analytic expression is given by

$$G(\mathbf{r},t;\mathbf{r}',t') \;=\; G_0(\mathbf{r},t;\mathbf{r}',t') \;+\; \int d1 \int d2\; G_0(\mathbf{r},t;1)\; \Sigma^*(12)\; G(2;\mathbf{r}',t') \;. \tag{3.44}$$

The validity of (3.44) can be verified by iterating the right hand-side, which reproduces (3.43) term by term. In a similar manner, one can show that the DYSON equation can be also written as

$$G(\mathbf{r},t;\mathbf{r}',t') \;=\; G_0(\mathbf{r},t;\mathbf{r}',t') \;+\; \int d1 \int d2\; G(\mathbf{r},t;1)\; \Sigma^*(12)\; G_0(2;\mathbf{r}',t') \;. \tag{3.45}$$

3.6 Approximation of the Self-Energy

An exact evaluation of the self-energy is possible only for some rather pathological cases. For real systems one has to rely on approximation schemes. Hence, a natural approach is to retain the single-particle picture and assume that each particle moves in a single-particle potential that comes from its average interaction with all of the other particles. Thus, as a first-order approximation one can keep just the first-order contribution to the proper self-energy $\Sigma^* \approx \Sigma_1$ (see Fig. 3.7). This approximation corresponds to summing an infinite class of diagrams containing arbitrary iterations of Σ_1. Therefore, any approximation for Σ^* generates an *infinite-order* series for the GREEN's function (see Fig. 3.5).

However, using non-interacting GREEN's function in self-energies, which is referred to as BORN *approximation*, is not fully consistent, since the background particles contributing to the self-energy are treated as non-interacting. In reality, of course, these particles also move in an average potential coming from the presence of all the other particles. Thus instead of non-interacting GREEN's functions (single lines), one has to use the exact GREEN's function (double line) in the proper self-energy, as shown in Fig. 3.9. Since the exact GREEN's function G both determines and is determined by the proper self-energy Σ^*, this approximation is known as the *self-consistent* BORN *approximation* (see Appendix F.3). The self-consistent approach preserves conservation laws (Appendix F.3), for example, the continuity equation holds valid (Section 3.9.4). Throughout this work the self-consistent BORN approximation is applied.

Figure 3.9: FEYNMAN diagrams of the self-consistent first-order proper self-energies.

3.6.1 Elecron-Electron Interaction

The self-consistent HARTREE self-energy due to electron-electron interaction is given by [205]

$$\begin{aligned}
\Sigma_{\text{el}-\text{el}}(\mathbf{r_1},t_1) &= -i\hbar \int dt_3 \int d\mathbf{r_3}\ \delta_{t_1,t_3}\ V(\mathbf{r_1}-\mathbf{r_3})G(\mathbf{r_3},t_3;\mathbf{r_3},t_3)\ , \\
&= -i\hbar \int d\mathbf{r_3}\ V(\mathbf{r_1}-\mathbf{r_3})G(\mathbf{r_3},t_1;\mathbf{r_3},t_1)\ , \\
&= \int d\mathbf{r_3}\ V(\mathbf{r_1}-\mathbf{r_3})n(\mathbf{r_3},t_1)\ , \\
&= \int d\mathbf{r_3}\ \frac{\mathrm{q}^2}{4\pi\epsilon|\mathbf{r_1}-\mathbf{r_3}|}\frac{\varrho(\mathbf{r_3},t_1)}{-\mathrm{q}}\ , \\
&= -\mathrm{q}\phi(\mathbf{r_1})\ .
\end{aligned} \tag{3.46}$$

where $\varrho(\mathbf{r},t)/(-\mathrm{q}) = n(\mathbf{r},t) = -i\hbar G(\mathbf{r},t,\mathbf{r},t)$ (see Section 3.9.1). The potential ϕ resulting from the HARTREE self-energy is in fact the solution of the POISSON equation with the charge density ϱ. The HARTREE self-energy is instantaneous.

3.6.2 Electron-Phonon Interaction

The electron-phonon interaction HAMILTONian can be written as [190]

$$\hat{H}_{\mathrm{I}}^{\mathrm{el-ph}}(t_1) \;=\; \int d\mathbf{r_1}\;\hat{\psi}_{\mathrm{I}}^{\dagger}(\mathbf{r_1},t_1)\left(\sum_{\mathbf{q_1},\lambda} e^{i\mathbf{q_1}\cdot\mathbf{r_1}} M_{\mathbf{q_1}}\hat{A}_{\mathbf{q_1}}(t_1)\right)\hat{\psi}_{\mathrm{I}}(\mathbf{r_1},t_1)\;, \tag{3.47}$$

where $\hat{A}_{\mathbf{q},\lambda}(t) = (b_{\mathbf{q},\lambda}e^{-i\omega_{\mathbf{q},\lambda}t} + b^{\dagger}_{-\mathbf{q},\lambda}e^{+i\omega_{\mathbf{q},\lambda}t})$, $b_{\mathbf{q},\lambda}$ and $b^{\dagger}_{\mathbf{q},\lambda}$ are the annihilation and creation operators for phonons with wave-vector $\mathbf{q}$, polarization λ, and energy $\hbar\omega_{\mathbf{q},\lambda}$, and $M_{\mathbf{q},\lambda}$ is the electron-phonon interaction matrix element. The zero-order perturbation gives the non-interacting GREEN's function. The first-order term of the perturbation expansion must vanish because it contains the factor $\langle\hat{A}_{\mathbf{q},\lambda}\rangle$ which is zero since the factors $\langle b_{\mathbf{q},\lambda}\rangle$ and $\langle b^{\dagger}_{\mathbf{q},\lambda}\rangle$ are zero [190]. Similarly, all the odd terms vanish because their time-ordered bracket for phonons contains an odd number of $\hat{A}_{\mathbf{q},\lambda}$ factors. Applying the WICK theorem (Section 3.4.1), only the even terms contribute to the perturbation expansion for the electron-phonon interaction

$$\begin{aligned}
G_{\mathrm{N}}^{1} \;&=\; \langle T_{\mathrm{t}}\{\frac{1}{2}\left(\frac{-i}{\hbar}\right)^2\int dt_1\;\hat{H}_{\mathrm{I}}^{\mathrm{el-ph}}(t_1)\hat{\psi}_{\mathrm{I}}(\mathbf{r},t)\hat{\psi}_{\mathrm{I}}^{\dagger}(\mathbf{r}',t')\}\rangle\\
&=\; \frac{1}{2}\left(\frac{-i}{\hbar}\right)^2\int dt_1\int dt_2\int d\mathbf{r_1}\int d\mathbf{r_2}\\
&\quad\times\;\underbrace{\langle T_{\mathrm{t}}\{\hat{\psi}_{\mathrm{I}}^{\dagger}(\mathbf{r_1},t_1)\hat{\psi}_{\mathrm{I}}^{\dagger}(\mathbf{r_2},t_2)\hat{\psi}_{\mathrm{I}}(\mathbf{r_2},t_2)\hat{\psi}_{\mathrm{I}}(\mathbf{r_1},t_1)\hat{\psi}_{\mathrm{I}}(\mathbf{r},t)\hat{\psi}_{\mathrm{I}}^{\dagger}(\mathbf{r}',t')\}\rangle}_{F_{\mathrm{N}}^{1}}\\
&\quad\underbrace{\times\;\sum_{\mathbf{q_1},\mathbf{q_2},\lambda} e^{i\mathbf{q_1}\cdot\mathbf{r_1}}e^{i\mathbf{q_2}\cdot\mathbf{r_2}}M_{\mathbf{q_1},\lambda}M_{\mathbf{q_2},\lambda}\langle A_{\mathbf{q_1},\lambda}(t_1)A_{\mathbf{q_2},\lambda}(t_2)\rangle}_{K_{\mathrm{N}}^{1}}\;,
\end{aligned} \tag{3.48}$$

where the expansion of time-ordered products of electron operators (F_{N}^{1}) has been calculated before, see (3.37). Notice that, due to the properties of the annihilation and creation operators for Bosons [190], $\langle A_{\mathbf{q_1},\lambda}(t_1)A_{\mathbf{q_2},\lambda}(t_2)\rangle = 0$ unless $\mathbf{q_2} = -\mathbf{q_1}$, therefore, one obtains

$$K_{\mathrm{N}}^{1} = \sum_{\mathbf{q_1},\lambda} e^{i\mathbf{q_1}\cdot(\mathbf{r_1}-\mathbf{r_2})}M^2_{\mathbf{q_1},\lambda}\;i\hbar D_{\lambda_0}(\mathbf{q_1},t_1,t_2)\;, \tag{3.49}$$

where $D_{\lambda_0}(\mathbf{q_1},t_1,t_2)$ is the non-interacting phonon GREEN's function (see Appendix D). FEYNMAN diagrams for this expansion are similar to Fig. 3.4, but one should only replace the COULOMB interactions with non-interacting phonon GREEN's functions [190]. However, the contributions of the diagrams (a), (b), and (f) are zero. They are non-zero only if the phonon wave-vector $\mathbf{q}$ is zero, but such phonon is either a translation of the crystal or a permanent strain, and neither of these meant to be in the HAMILTONian. The lowest order self-energies due to electron-phonon interaction are also referred to as HARTREE and FOCK self-energy by analogy to the treatment of the electron-electron interaction. However, the HARTREE self-energy due to electron-phonon interaction is zero since it corresponds to phonons with $\mathbf{q} = \mathbf{0}$. The analytical expression regarding the contribution of the self-consistent FOCK self-energy (Fig. 3.9) is given by [112]

$$\Sigma_{\mathrm{el-ph}}(\mathbf{r_1},t_1;\mathbf{r_2},t_2) \;=\; i\hbar\sum_{\mathbf{q_1},\lambda} e^{i\mathbf{q_1}\cdot(\mathbf{r_1}-\mathbf{r_2})}M^2_{\mathbf{q_1},\lambda}G(\mathbf{r_1},t_1;\mathbf{r_2},t_2)D_{\lambda}(\mathbf{q_1};t_1,t_2)\;. \tag{3.50}$$

3.7 Analytical Continuation

The contour representation is rather impractical in calculations, and one prefers to work with real time integrals. The procedure of converting the contour into real-time integrals is called analytic continuation [185]. We followed here the formulation by LANGRETH [206]. In this section we are only concerned with temporal variables, therefore, spatial variables have been suppressed.

3.7.1 Real Time Formalism

The contour C_K depicted in Fig. 3.3 consists of two two branches, C_1 and C_2. Each of the time arguments of the GREEN's function can reside either on the first or second part of the contour. Therefore, contour-ordered GREEN's function thus contains four different GREEN's functions

$$G(t,t') \;=\; \begin{cases} G^{>}(t,t') & t\,\in\,\mathrm{C}_2,\; t'\,\in\,\mathrm{C}_1 \\ G^{<}(t,t') & t\,\in\,\mathrm{C}_1,\; t'\,\in\,\mathrm{C}_2 \\ G_{\mathrm{t}}(t,t') & t,t'\,\in\,\mathrm{C}_1 \\ G_{\tilde{\mathrm{t}}}(t,t') & t,t'\,\in\,\mathrm{C}_2 \end{cases} .$$

The *greater* ($G^{>}$), *lesser* ($G^{<}$), *time-ordered* (G_{t}), and *anti-time-ordered* ($G_{\tilde{\mathrm{t}}}$) GREEN's functions can be defined as

$$\begin{aligned} G^{>}(t,t') &= -i\hbar^{-1}\langle\hat{\psi}_{\mathrm{H}}(t)\hat{\psi}^{\dagger}_{\mathrm{H}}(t')\rangle \;, \\ G^{<}(t,t') &= +i\hbar^{-1}\langle\hat{\psi}^{\dagger}_{\mathrm{H}}(t')\hat{\psi}_{\mathrm{H}}(t)\rangle \;, \\ G_{\mathrm{t}}(t,t') &= -i\hbar^{-1}\langle T_{\mathrm{t}}\{\hat{\psi}_{\mathrm{H}}(t)\hat{\psi}^{\dagger}_{\mathrm{H}}(t')\}\rangle \;, \\ &= -\theta(t-t')i\hbar^{-1}\langle\hat{\psi}_{\mathrm{H}}(t)\hat{\psi}^{\dagger}_{\mathrm{H}}(t')\rangle \;+\; \theta(t'-t)i\hbar^{-1}\langle\hat{\psi}^{\dagger}_{\mathrm{H}}(t')\hat{\psi}_{\mathrm{H}}(t)\rangle \;, \\ &= +\theta(t-t')G^{>}(t,t') \;+\; \theta(t'-t)G^{<}(t,t') \;, \\ G_{\tilde{\mathrm{t}}}(t,t') &= -i\hbar^{-1}\langle T_{\tilde{\mathrm{t}}}\{\hat{\psi}_{\mathrm{H}}(t)\hat{\psi}^{\dagger}_{\mathrm{H}}(t')\}\rangle \;, \\ &= -\theta(t'-t)i\hbar^{-1}\langle\hat{\psi}_{\mathrm{H}}(t)\hat{\psi}^{\dagger}_{\mathrm{H}}(t')\rangle \;+\; \theta(t-t')i\hbar^{-1}\langle\hat{\psi}^{\dagger}_{\mathrm{H}}(t')\hat{\psi}_{\mathrm{H}}(t)\rangle \;, \\ &= +\theta(t'-t)G^{>}(t,t') \;+\; \theta(t-t')G^{<}(t,t') \;, \end{aligned} \tag{3.51}$$

where the time-ordering operator T_{t} is defined in (B.21). The anti-time-ordering operator $T_{\tilde{\mathrm{t}}}$ can be defined in a similar manner. Since $G_{\mathrm{t}} + G_{\tilde{\mathrm{t}}} = G^{>} + G^{<}$, there are only three linearly independent functions. The freedom of choice reflects itself in the literature, where a number of different conventions can be found. For our purpose the most suitable functions are the $G^{\gtrless}$, and the retarded (G^{r}) and advanced (G^{a}) GREEN's functions defined as

$$\begin{aligned} G^{\mathrm{r}}(t,t') &= +\theta(t-t')[G^{>}(t,t') - G^{<}(t,t')] \;, \\ G^{\mathrm{a}}(t,t') &= +\theta(t'-t)\;[G^{<}(t,t') - G^{>}(t,t')] \;. \end{aligned} \tag{3.52}$$

It is straightforward to show that $G^{\mathrm{r}} - G^{\mathrm{a}} = G^{>} - G^{<}$.

3.7.2 Langreth Theorem

The next step is replacing contour by real time integrals in the Dyson equation. In that equation one encounters the following contour integrals

$$D(t,t') \;=\; \int\limits_{\mathrm{C}} d\tau\; A(t,\tau)B(\tau,t')\;, \tag{3.53}$$

and their generalizations involving products of three or more terms. To evaluate (3.53) one can assume that t is on the first half of the contour and t' is on the latter half. In view of the discussion of (3.51), we are thus analyzing a lesser function. The next step is to deform the contour as indicated in Fig. 3.10. Thus (3.53) becomes

$$D^{<}(t,t') \;=\; \int\limits_{\mathrm{C}_1} d\tau\; A(t,\tau)B^{<}(\tau,t') \;+\; \int\limits_{\mathrm{C}_2} d\tau\; A^{<}(t,\tau)B^{<}(\tau,t')\;. \tag{3.54}$$

Here, in appending the label $<$ to the function B in the first term we made use of the fact that as long as the integration variable τ is confined on the contour C_1 it is less than t' (in the contour sense) . A similar argument applies to the second term. Considering the first term in (3.54) the integration can be split into two parts

$$\begin{aligned}\int\limits_{\mathrm{C}_1} d\tau\; A(t,\tau)B^{<}(\tau,t') \;&=\; \int\limits_{-\infty}^{t} dt_1\; A^{>}(t,t_1)B^{<}(t_1,t') + \int\limits_{t}^{-\infty} dt_1\; A^{<}(t,t_1)B^{<}(t_1,t')\;,\\ &\equiv\; \int\limits_{-\infty}^{\infty} dt_1\;\; A^{\mathrm{r}}(t,t_1)B^{<}(t_1,t')\;,\end{aligned} \tag{3.55}$$

where the definition of the retarded function (3.52) has been used. A similar analysis can be applied to the second term involving contour C_2, where the advanced function is generated. Putting the two terms together, one gets the first of Langreth's results [185]

$$D^{<}(t,t') \;=\; \int\limits_{-\infty}^{\infty} dt_1\; [A^{\mathrm{r}}(t,t_1)B^{<}(t_1,t') \;+\; A^{<}(t,t_1)B^{\mathrm{a}}(t_1,t')]\;. \tag{3.56}$$

The same result applies for the greater function just by replacing the $<$ labels by the $>$ labels. It is easy to generalize the result (3.56) to a product of three functions. The retarded and analogously the advanced component of a product of functions defined on the contour can be derived by repeated use of the definitions (3.51) and (3.52) and the result (3.56).

$$\begin{aligned}D^{\mathrm{r}}(t,t') \;&=\; \theta(t-t')[D^{>}(t,t')-D^{<}(t,t')]\\ &=\; \theta(t-t')\int\limits_{-\infty}^{\infty} dt_1\; [A^{\mathrm{r}}(B^{>}-B^{<})+(A^{>}-A^{<})B^{\mathrm{a}}]\\ &=\; \theta(t-t')\left[\int\limits_{-\infty}^{t} dt_1(A^{>}-A^{<})(B^{>}-B^{<})+\int\limits_{-\infty}^{t'} dt_1(A^{>}-A^{<})(B^{<}-B^{>})\right]\\ &=\int\limits_{t'}^{t} dt_1\; A^{\mathrm{r}}(t,t_1)B^{\mathrm{r}}(t_1,t')\end{aligned} \tag{3.57}$$

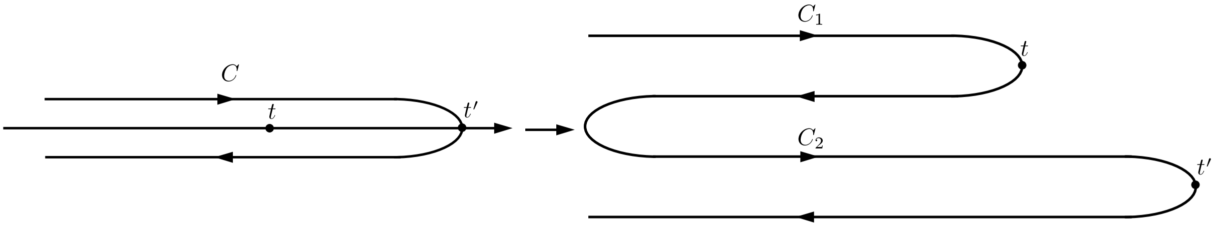

Figure 3.10: Deformation of contour C into contours C_1 and C_2.

In the self-energies another structure occurs

$$D(\tau,\tau') \;=\; A(\tau,\tau')B(\tau,\tau')\ , \tag{3.58}$$

where τ and τ' are contour variables. The derivation of the required formula is similar to the analysis presented above [185]

$$\begin{aligned} D^{\gtrless}(t,t') \;&=\; A^{\gtrless}(t,t')B^{\gtrless}(t,t')\ , \\ D^{\mathrm{r}}(t,t') \;&=\; A^{<}(t,t')B^{\mathrm{r}}(t,t') \;+\; A^{\mathrm{r}}(t,t')B^{<}(t,t') \;+\; A^{\mathrm{r}}(t,t')B^{\mathrm{r}}(t,t')\ . \end{aligned} \tag{3.59}$$

The rules provided by the Langreth theorem are summarized in Table 3.1.

Contour	Real axis
$D = \int\limits_{\mathrm{C}} AB$	$D^{\gtrless} = \int\limits_{\mathrm{t}} [A^{\mathrm{r}}B^{\gtrless} + A^{\gtrless}B^{\mathrm{a}}]$ $D^{\mathrm{r}} = \int\limits_{\mathrm{t}} A^{\mathrm{r}}B^{\mathrm{r}}$
$D = \int\limits_{\mathrm{C}} ABC$	$D^{\gtrless} = \int\limits_{\mathrm{t}} [A^{\mathrm{r}}B^{\mathrm{r}}C^{\gtrless} + A^{\mathrm{r}}B^{\gtrless}C^{\mathrm{a}} + A^{\gtrless}B^{\mathrm{a}}C^{\mathrm{a}}]$ $D^{\mathrm{r}} = \int\limits_{\mathrm{t}} A^{\mathrm{r}}B^{\mathrm{r}}C^{\mathrm{r}}$
$D(\tau,\tau') = A(\tau,\tau')B(\tau,\tau')$	$D^{\gtrless}(t,t') = A^{\gtrless}(t,t')B^{\gtrless}(t,t')$ $D^{\mathrm{r}}(t,t') = A^{<}(t,t')B^{\mathrm{r}}(t,t') + A^{\mathrm{r}}(t,t')B^{<}(t,t') + A^{\mathrm{r}}(t,t')B^{\mathrm{r}}(t,t')$

Table 3.1: Rules for analytic continuation derived from the Langreth theorem.

3.8 Quantum Kinetic Equations

In this section the equations of motion (in real time) for the non-equilibrium GREEN's functions are introduced. There are two different, but equivalent, formulations: the KADANOFF-BAYM and the KELDYSH formulation. These are treated in the following subsections. Finally, kinetic equations under steady-state condition are presented.

3.8.1 The KADANOFF-BAYM Formulation

The starting point of the derivation is the differential form of the DYSON equation. By assuming that $[i\hbar\partial_{t_1} - \hat{H}_0(1)]G_0(12) = \delta_{1,2}$, equation (3.44) and (3.45) can be rewritten as [203]

$$\Big[+i\hbar\partial_{t_1} \;-\; \hat{H}_0(1)\Big]\, G(12) \;=\; \delta_{1,2} \;- i\hbar \int\limits_{C} d3\; \Sigma(13)\; G(32)\ , \tag{3.60}$$

$$\Big[-i\hbar\partial_{t_2} \;-\; \hat{H}_0(2)\Big]\, G(12) \;=\; \delta_{1,2} \;- i\hbar \int\limits_{C} d3\; G(13)\; \Sigma(32)\ . \tag{3.61}$$

Note that the singular part of the self-energy on the contour, which corresponds to the HARTREE self-energy (Section 3.6), does not appear explicitly in the kinetic equations, but is included in the potential energy of the single-particle HAMILTONian $\hat{H}_0$, see (F.7).

Using the LANGRETH rules (Table 3.1) and fixing the time arguments of the GREEN's functions in (3.60) and (3.61) at opposite sides of the contour, one obtains the KADANOFF-BAYM equations [93, 203]

$$\Big[+i\hbar\partial_{t_1} \;-\; \hat{H}_0(1)\Big]\, G^{\gtrless}(12) \;=\; \int d3\; \Sigma^{\mathrm{r}}(13)\; G^{\gtrless}(32) \;+\; \int d3\; \Sigma^{\gtrless}(13)\; G^{\mathrm{a}}(32)\ , \tag{3.62}$$

$$\Big[-i\hbar\partial_{t_2} \;-\; \hat{H}_0(2)\Big]\, G^{\gtrless}(12) \;=\; \int d3\; G^{\mathrm{r}}(13)\; \Sigma^{\gtrless}(32) \;+\; \int d3\; G^{\gtrless}(13)\; \Sigma^{\mathrm{a}}(32)\ . \tag{3.63}$$

One should note that the delta-function term in (3.60) and (3.61) vanishes identically, because the time-labels required in the construction of $G^<$ and $G^>$ are, by the definition on different branches of the contour.

The KADANOFF-BAYM equations determine the time evolution of the GREEN's functions, but they do not determine the consistent initial values. This information is contained in the original DYSON equations (3.44) and (3.45), and lost in the derivation. To have a closed set of equations, the KADANOFF-BAYM equations must be supplemented with DYSON equations for G^{r} and G^{a}. By subtracting (3.63) from (3.62), one finds the equation satisfied by G^{r} [203]

$$\Big[+i\hbar\partial_{t_1} \;-\; \hat{H}_0(1)\Big]\, G^{\mathrm{r}}(12) - \int d3\; \Sigma^{\mathrm{r}}(13)\; G^{\mathrm{r}}(32) \;=\; \delta_{1,2}\ , \tag{3.64}$$

$$\Big[-i\hbar\partial_{t_2} \;-\; \hat{H}_0(2)\Big]\, G^{\mathrm{r}}(12) - \int d3\; \Sigma^{\mathrm{r}}(13)\; G^{\mathrm{r}}(32) \;=\; \delta_{1,2}\ . \tag{3.65}$$

Similar relations hold for the advanced GREEN's functions.

3.8.2 Keldysh **Formulation**

For certain applications in classical transport theory it is advantageous to write the Boltzmann equation as an integral equation, rather than an integro-differential equation. An analogous situation holds in quantum kinetics. Instead of working with the Kadanoff-Baym equations (3.62) and (3.63), it may be useful to consider their integral forms. Historically, Keldysh [202] derived his alternative form almost simultaneously and independently of Kadanoff and Baym. However, the Keldysh and Kadanoff-Baym formalisms are equivalent.

By applying Langreth's rules to the Dyson equation (3.44) one obtains

$$G^{<} \;=\; G_0^{<} \;+\; G_0^{\mathrm{r}}\,\Sigma^{\mathrm{r}}\,G^{<} \;+\; G_0^{\mathrm{r}}\,\Sigma^{<}\,G^{\mathrm{a}} \;+\; G_0^{<}\,\Sigma^{\mathrm{a}}\,G^{\mathrm{a}}\;. \tag{3.66}$$

For convenience a notation where a product of two terms is interpreted as a matrix product in the internal variables (space, time, etc.) has been used. One can proceed by iteration with respect to $G^{<}$. Iterating once, and regrouping the terms one obtains

$$\begin{aligned} G^{<} \;=\;& (1 \;+\; G_0^{\mathrm{r}}\,\Sigma^{\mathrm{r}})\,G_0^{<}\,(1 \;+\; \Sigma^{\mathrm{a}}\,G^{\mathrm{a}}) \\ &+\; (G_0^{\mathrm{r}} \;+\; G_0^{\mathrm{r}}\,\Sigma^{\mathrm{r}}\,G_0^{\mathrm{r}})\,\Sigma^{<}\,G^{\mathrm{a}} \\ &+\; G_0^{\mathrm{r}}\,\Sigma^{\mathrm{r}}\,G_0^{\mathrm{r}}\,\Sigma^{\mathrm{r}}\,G^{<}\;. \end{aligned} \tag{3.67}$$

The form of (3.67) suggests that infinite order iterations results in [185]

$$G^{<} \;=\; (1 \;+\; G^{\mathrm{r}}\,\Sigma^{\mathrm{r}})\,G_0^{<}\,(1 \;+\; \Sigma^{\mathrm{a}}\,G^{\mathrm{a}}) \;+\; G^{\mathrm{r}}\,\Sigma^{<}\,G^{\mathrm{a}}\;. \tag{3.68}$$

Equation (3.68) is equivalent to Keldysh's results. In the original work, however, it was written for another function, $G_K \equiv G^{<} + G^{>}$. This difference is only of minor significance [185].

The first term on the right hand-side of (3.68) accounts for the initial conditions. One can show that this term vanishes for steady-state systems, if the system was in a non-interacting state in the infinite past [185]. Thus, in many applications it is sufficient to only keep the second term.

Similar steps can be followed to obtain the kinetic equation for $G >$. In integral form these equations can be written as

$$G^{\gtrless}(12) \;=\; \int d3 \int d4\; G^{\mathrm{r}}(13)\;\Sigma^{\gtrless}(34)\;G^{\mathrm{a}}(42)\;. \tag{3.69}$$

The relation between the Keldysh equation and the Kadanoff-Baym equation is analogous to the relation between an ordinary differential equation plus a boundary condition and the corresponding integral equation.

3.8.3 Steady-State Kinetic Equations

Under steady-state condition the GREEN's functions depend on time differences. One usually FOURIER transforms the time difference coordinate, $\tau = t - t'$, to energy

$$G(\mathbf{r_1}, \mathbf{r_2}; E) = \int \frac{d\tau}{\hbar}\, e^{iE\tau/\hbar} G(\mathbf{r_1}, \mathbf{r_2}; \tau)\ . \tag{3.70}$$

Under steady-state condition the quantum kinetic equations, (3.64), (3.65), and (3.69), can be written as [60]:

$$\left[E - \hat{H}_0(\mathbf{r_1})\right] G^{\mathrm{r}}(\mathbf{r_1}, \mathbf{r_2}; E) \ - \ \int d\mathbf{r_3}\ \Sigma^{\mathrm{r}}(\mathbf{r_1}, \mathbf{r_3}; E)\ G^{\mathrm{r}}(\mathbf{r_3}, \mathbf{r_2}; E) \ = \ \delta_{\mathbf{r_1},\mathbf{r_2}}\ , \tag{3.71}$$

$$G^{\lessgtr}(\mathbf{r_1}, \mathbf{r_2}; E) \ = \ \int d\mathbf{r_3} \int d\mathbf{r_4}\ G^{\mathrm{r}}(\mathbf{r_1}, \mathbf{r_3}; E)\ \Sigma^{\lessgtr}(\mathbf{r_3}, \mathbf{r_4}; E)\ G^{\mathrm{a}}(\mathbf{r_4}, \mathbf{r_2}; E)\ , \tag{3.72}$$

where Σ is the total self-energy. A similar transformation can be applied to self-energies. However, to obtain self-energies one has to first apply LANGRETH's rules and then FOURIER transform the time difference coordinate to energy. We consider the self-energies discussed in Section 3.6. The evaluation of the HARTREE self-energy due to electron-electron interaction is straightforward, since it only includes the electron GREEN's function. However, the lowest-order self-energy due to electron-phonon interaction contains the products of the electron and phonon GREEN's functions. Using LANGRETH's rules (Table 3.1) and then FOURIER transforming the self-energies due to electron-phonon interaction, (3.50) takes the form

$$\Sigma^{\gtrless}_{\mathrm{el-ph}}(\mathbf{r_1}, \mathbf{r_2}; E) \ = \ i \sum_{\mathbf{q},\lambda} \int \frac{d(\hbar\omega_{\mathbf{q},\lambda})}{2\pi}\ e^{i\mathbf{q}\cdot(\mathbf{r_1}-\mathbf{r_2})}\ M^2_{\mathbf{q},\lambda} G^{\gtrless}(\mathbf{r_1}, \mathbf{r_2}; E - \hbar\omega_{\mathbf{q},\lambda}) D^{\lessgtr}_{\lambda}(\mathbf{q}, \hbar\omega_{\mathbf{q},\lambda})\ , \tag{3.73}$$

To calculate the retarded self-energy, however, it is more straightforward to FOURIER transform the relation $\Sigma^{\mathrm{r}}(\tau) = \theta(\tau)[\Sigma^{>}(\tau) - \Sigma^{<}(\tau)]$, see (3.52). By defining the broadening function Γ

$$\Gamma(\mathbf{r_1}, \mathbf{r_2}; E) = i[\Sigma^{>}(\mathbf{r_1}, \mathbf{r_2}; E) \ - \ \Sigma^{<}(\mathbf{r_1}, \mathbf{r_2}; E)] \ = \ 2\Im\mathrm{m}\Sigma^{<}(\mathbf{r_1}, \mathbf{r_2}; E)\ , \tag{3.74}$$

the retarded self-energy is given by the convolution of $-i\Gamma(E)$ and the FOURIER transform of the step function [33]

$$\Sigma^{\mathrm{r}}(E) \ = \ -i\Gamma(E) \otimes \left(\frac{\delta(E)}{2} \ + \ \frac{i}{2\pi E}\right)\ , \tag{3.75}$$

where $\otimes$ denotes the convolution. Therefore, the retarded self-energy is given by [116]

$$\Sigma^{\mathrm{r}}(\mathbf{r_1}, \mathbf{r_2}; E) \ = \ -\frac{i}{2}\Gamma(\mathbf{r_1}, \mathbf{r_2}; E) \ + \ \mathrm{P}\int \frac{dE'}{2\pi} \frac{\Gamma(\mathbf{r_1}, \mathbf{r_2}; E')}{E - E'}\ , \tag{3.76}$$

where P stands for principal part.

3.9 Relation to Observables

Observables such as particle and current densities are directly linked to the greater and lesser Green's functions. In this section some of the most important observables and their relations to the Green's functions are discussed.

3.9.1 Electron and Hole Density

The electron and hole concentration are respectively given by

$$\begin{aligned} n(\mathbf{r},t) &= \langle \hat{\psi}^{\dagger}(\mathbf{r},t)\hat{\psi}(\mathbf{r},t)\rangle \ , \\ &= -i\hbar G^{<}(\mathbf{r},t;\mathbf{r},t) \ , \end{aligned} \tag{3.77}$$

$$\begin{aligned} p(\mathbf{r},t) &= \langle \hat{\psi}(\mathbf{r},t)\hat{\psi}^{\dagger}(\mathbf{r},t)\rangle \ , \\ &= +i\hbar G^{>}(\mathbf{r},t;\mathbf{r},t) \ . \end{aligned} \tag{3.78}$$

Under steady-state condition (see Section 3.8.3) these relations can be written as [60]

$$n(\mathbf{r}) = -i\int \frac{dE}{2\pi} G^{<}(\mathbf{r},E) \ . \tag{3.79}$$

$$p(\mathbf{r}) = +i\int \frac{dE}{2\pi} G^{>}(\mathbf{r},E) \ . \tag{3.80}$$

The total space charge density is given by

$$\varrho(\mathbf{r}) = q\left(p(\mathbf{r}) - n(\mathbf{r})\right) \ . \tag{3.81}$$

3.9.2 Spectral Function and Local Density of States

The spectral function is defined as

$$A(\mathbf{r},\mathbf{r}';E) = i\left[G^{\mathrm{r}}(\mathbf{r},\mathbf{r}';E) - G^{\mathrm{a}}(\mathbf{r},\mathbf{r}';E)\right] \ . \tag{3.82}$$

The spectral function provides information about the nature of the allowed electronic states, regardless whether they are occupied or not, and can be considered as a generalized density of states. The diagonal elements of the spectral function give the local density of states

$$\rho(\mathbf{r};E) = \frac{1}{2\pi}A(\mathbf{r},\mathbf{r};E) = -\frac{1}{\pi}\Im\mathrm{m}\left[G^{\mathrm{r}}(\mathbf{r},\mathbf{r};E)\right] \ . \tag{3.83}$$

The trace of the spectral function represents the density of states

$$N(E) = \mathrm{Tr}\left[A(E)\right] = \int d\mathbf{r}\ A(\mathbf{r},\mathbf{r};E) \ . \tag{3.84}$$

3.9.3 Current Density

To derive an equation for the current density one uses the conservation law of quantum mechanical variables [93]. The starting point is the subtraction of equation (3.62) from (3.63)

$$i\hbar\,(\partial_{t_1}+\partial_{t_2})\,G^<(12) \;+\; \frac{\hbar^2}{2m}\,[(\nabla_{\mathbf{r_1}} \;+\; \nabla_{\mathbf{r_2}})(\nabla_{\mathbf{r_1}} \;-\; \nabla_{\mathbf{r_2}})]\,G^<(12) \;-\; [U(1)-U(2)]G^<(12) \;=$$

$$+\int d3\;\left[\Sigma^{\mathrm{r}}(13)\;G^<(32) \;+\; \Sigma^<(13)\;G^{\mathrm{a}}(32) \;+\; G^{\mathrm{r}}(13)\;\Sigma^<(32) \;+\; G^<(13)\;\Sigma^{\mathrm{a}}(32)\;\right]\;, \tag{3.85}$$

where $H_0(1) = -\hbar^2/2m\nabla_1^2 + U(1)$ has been assumed. By taking the limit $1 \rightarrow 2$ ($\mathbf{r_2} \rightarrow \mathbf{r_1}$ and $t_2 \rightarrow t_1$) and assuming that the right-hand-side of (3.85) approaches zero in this limit, one obtains

$$i\hbar \lim_{t_2\rightarrow t_1}[\partial_{t_1}G^<(12) \;+\; \partial_{t_2}G^<(12)] \;+\; \nabla\cdot\left(\frac{\hbar^2}{2m}\lim_{\mathbf{r_2}\rightarrow\mathbf{r_1}}(\nabla_{\mathbf{r_1}} \;-\; \nabla_{\mathbf{r_2}})G^<(12)\right) \;=\; 0\;. \tag{3.86}$$

By multiplying both sides by $-\mathrm{q}$ and recalling the definition of the charge density, one recovers the continuity equation

$$\partial_{t_1}\varrho(\mathbf{r_1},t_1) \;+\; \nabla\cdot\mathbf{J}(\mathbf{r_1},t_1) \;=0\;, \tag{3.87}$$

where the current density is defined as

$$\mathbf{J}(\mathbf{r_1},t_1) \;=-\frac{i\hbar^2\mathrm{q}}{2m}\lim_{\mathbf{r_2}\rightarrow\mathbf{r_1}}(\nabla_{\mathbf{r_1}} \;-\; \nabla_{\mathbf{r_2}})\,G^<(\mathbf{r_1},t_1;\mathbf{r_2},t_1)\;. \tag{3.88}$$

Under steady-state condition the current density takes the form [60]

$$\mathbf{J}(\mathbf{r_1}) \;=\; -\frac{i\hbar\mathrm{q}}{2m}\int\frac{dE}{2\pi}\lim_{\mathbf{r_2}\rightarrow\mathbf{r_1}}(\nabla_{\mathbf{r_1}} \;-\; \nabla_{\mathbf{r_2}})\,G^<(\mathbf{r_1},\mathbf{r_2},E)\;. \tag{3.89}$$

3.9.4 Current Conservation

The current is conserved as long as the right-hand-side of (3.85) approaches zero as $2 \rightarrow 1$

$$\lim_{2\rightarrow 1}\int d3\;\left[\Sigma^{\mathrm{r}}(13)\;G^<(32) \;+\; \Sigma^<(13)\;G^{\mathrm{a}}(32) \;+\; G^{\mathrm{r}}(13)\;\Sigma^<(32) \;+\; G^<(13)\;\Sigma^{\mathrm{a}}(32)\;\right] \;=0\;, \tag{3.90}$$

The current is obviously conserved if there is no interaction, whereas the situation is different in the interacting case. As described in Section 3.6, the interactions are described in terms of appropriate self-energies. However, self-energies can often be obtained approximately only. Therefore, one could choose an approximation which violates the continuity equation, which, of course, is not physical. It is straightforward to show that the approximated self-energy due to electron-phonon interaction within the self-consistent BORN approximation (3.50) preserves the current continuity.

3.10 Comparison of Transport Models

Established techniques used to address dissipative quantum transport can be classified according to the state functions they are based upon: the non-equilibrium GREEN's function (NEGF), the density matrix, and the WIGNER function. All three approaches are based on fundamental equations of motion and are equivalent at the most general level of formal description of a dissipative quantum system.

The resulting system of integral-differential equations for the GREEN's function $G(\mathbf{r_1}, t_1; \mathbf{r_2}, t_2)$, or the density matrix $\rho(\mathbf{r_1}, \mathbf{r_2}; t_1, t_2)$, or the WIGNER function $f(\mathbf{r}, \mathbf{p}, \omega, t)$ would in many cases too complex to allow for a direct numerical solution. For example, the lesser GREEN's function $G^{<}(\mathbf{r_1}, t_1; \mathbf{r_2}, t_2)$ in the coordinate representation depends on two positions arguments $\mathbf{r_1}, \mathbf{r_2}$ and two time arguments t_1, t_2. For a numerical solution, each argument of the GREEN's function needs to be discretized. In the case of a three dimensional system the total number of unknowns to be evaluated would be $N_{\text{tot}} = (N_x \cdot N_y \cdot N_z \cdot N_t)^2$. Assuming 100 grid points for each argument this results in the astronomical number $N_{\text{t}} = 10^{16}$. Even in the two-dimensional case the number of unknowns is still very large, $N_{\text{t}} = 10^{10}$, resulting in prohibitively large memory requirement.

Approximations and simplifications must necessarily be incorporated in order to make the problem numerically tractable. It is mainly these simplifying assumptions that make the difference between the approaches. The assumptions are usually physically motivated and may be different in the different formalisms. For instance, the approximations to simplify the equations for the GREEN's functions in real-space may not be suitable to the WIGNER equation, and vice versa.

The hierarchy of the transport models is shown in Fig. 3.11. In what follows we briefly outline strong points and shortcomings of techniques based on the GREEN's function, the density matrix, and the WIGNER function.

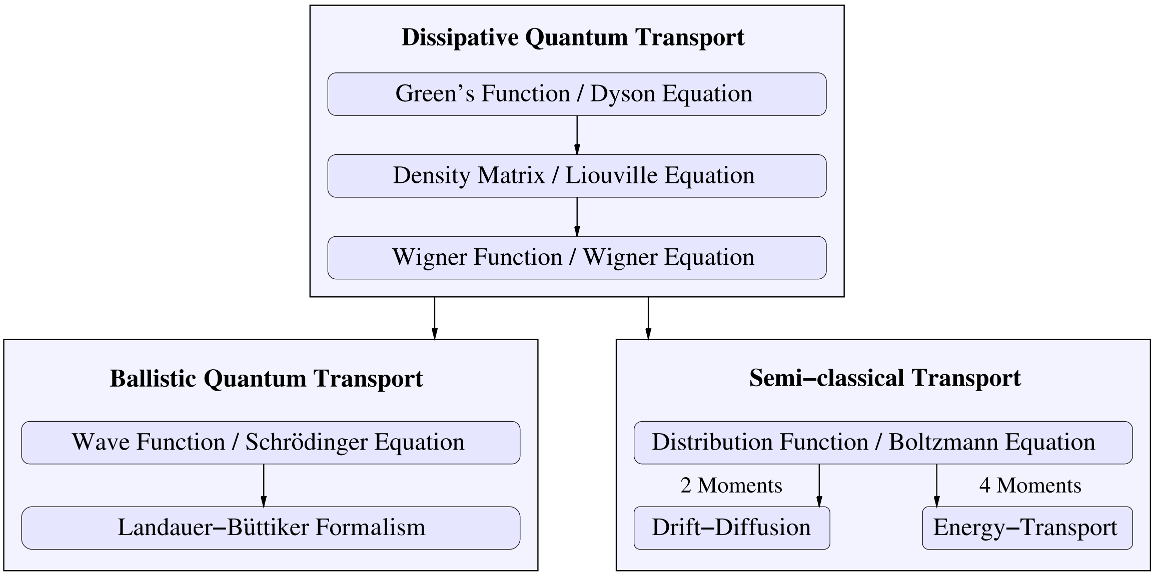

Figure 3.11: The hierarchy of quantum and semi-classical transport models [207].

3.10.1 Non-Equilibrium GREEN's Function

Throughout this chapter the NEGF formalism has been described. GREEN's functions in general have two position and two time arguments $G(\mathbf{r_1}, t_1; \mathbf{r_2}, t_2)$. Under steady-state condition one can FOURIER transform the time difference $\tau = t_1 - t_2$ to energy E to obtain $G(\mathbf{r_1}, \mathbf{r_2}; E)$ (Section 3.8.3), which can further be transformed via the WIGNER-WEYL procedure into $G(\mathbf{r}, \mathbf{k}; E)$.

The NEGF method addresses the problem of dissipative quantum transport in a consistent and complete way. Therefore, the method is computationally expensive and applied to systems in a steady-state [60]. The quantum device region is coupled to the reservoirs by contact self-energies (Appendix G), while dissipation is introduced via the scattering self-energies.

When scattering via a self-energy is introduced, the determination of the GREEN's function requires inversion of a matrix of huge rank. To reduce the computational cost, the *local scattering approximation* is frequently used [112, 208]. In this approximation the scattering self-energy terms are diagonal in coordinate representation. It allows one to employ the recursive algorithm for computing the GREEN's functions, see Appendix H [8, 116]. The local approximation is well justified for electron-phonon scattering caused by deformation potential interaction (Section 4.6). However, it is not justified for scattering by polar optical phonons, surface roughness, and ionized impurities.

In order to reduce the computational cost even further, systems with simplified grid requirements are considered. The mode-space approach (Section 4.4) [9] takes only a relatively small number of transverse modes, N_{mode}, into consideration. For the remaining, one-dimensional transport problem the number of unknowns reduces to $N_{\mathrm{tot}} = N_{\mathrm{mode}} \cdot N_x^2 \cdot N_E$, where N_E is the number of energy grid points.

It can be shown that the quantum ballistic formalism can be fully recovered from the NEGF formalism as a special case, where no dissipative scattering occurs in the system [33]. Another important point is that the NEGF formalism looks very different from the LANDAUER-BÜTTIKER formalism [209, 210]. The NEGF formalism focuses on the internal state of the conductor. By contrast, in the LANDAUER approach the central quantity is the transmission function from one contact to another. The internal state of the conductor usually never appears in this formalism. However, the transmission function can be expressed in terms of internal quantities. One can precisely obtain this result from the NEGF formalism as well when non-dissipative transport is assumed.

3.10.2 Master Equation for the Density Matrix

The evolution for the density matrix is described by a quantum LIOUVILLE equation.

$$\frac{\partial \rho}{\partial t} \;=\; \frac{i}{\hbar}[\rho, H] \; . \tag{3.91}$$

To simplify the equation, the limit of weak interaction between the device and the heat bath is applied. Coarse-graining in time results in a MARKOVian system. The resulting quantum LIOUVILLE equation for the reduced density matrix is $\frac{\partial \rho}{\partial t} = \frac{i}{\hbar}[\rho, H] + \mathcal{L}\{\rho\}$ and describes the quantum evolution of a system with loss [211].

Irreversible or energy-dissipating processes always involve transitions between quantum states. Such processes are described, at the simplest level, by a master or rate equation. The time evolution of such systems is determined by the rates of transition between states $|\mathbf{k}\rangle$. These rates are usually estimated using the FERMI *golden rule*

$$W_{\mathbf{k}',\mathbf{k}} \;=\; \frac{2\pi}{\hbar}|\langle\mathbf{k}'|H|\mathbf{k}\rangle|^2 \; \delta_{E_\mathbf{k},E_{\mathbf{k}'}} \; , \tag{3.92}$$

where $W_{\mathbf{k}',\mathbf{k}}$ is the transition rate from the state $\mathbf{k}$ to the state $\mathbf{k}'$. The δ function ensures energy conservation. If one assumes that these transitions occur independently within any small time interval (the MARKOV assumption), the transition rate from state $\mathbf{k}'$ to state $\mathbf{k}$ will produce changes in the corresponding occupation factors $d\rho_\mathbf{k} = -d\rho_{\mathbf{k}'} = W_{\mathbf{k}',\mathbf{k}}\rho_{\mathbf{k}'}dt$. The occupation of the state $\mathbf{k}$ increases and that of the state $\mathbf{k}'$ decreases as a result of this particular process, and the amount of change depends only on the occupation of the initial state[1]. If one sums over all possible transition processes, one obtains the master equation

$$\frac{\partial \rho_\mathbf{k}}{\partial t} \;=\; \sum_{\mathbf{k}'\neq\mathbf{k}} \left[W_{\mathbf{k},\mathbf{k}'}\rho_{\mathbf{k}'}(t) \;-\; W_{\mathbf{k}',\mathbf{k}}\rho_\mathbf{k}(t)\right] \; . \tag{3.93}$$

The PAULI master equation [212] is a frequently used model of irreversible processes in simple quantum systems. It can be derived from elementary quantum mechanics along with a MARKOV assumption.

In order to evaluate transport, the device under consideration must be coupled to external reservoirs. Coupling introduces carrier exchange between device and reservoirs, which are assumed to be in thermal equilibrium. The difference between the electrochemical potentials of the reservoirs causes current through the device. Therefore, it is essential to properly include the coupling to the reservoirs in the master equation.

In the the PAULI master equation approach developed by FISCHETTI, this coupling is introduced in a phenomenological manner [213, 214]. Application of the PAULI master equation is restricted to stationary systems, since in the non-stationary case the current continuity would be violated [215]. Another issue is that the PAULI master equation can only be justified for devices where the quantum region is shorter than the phase coherence length [213].

A solution free from the above mentioned shortcoming of phenomenological coupling of the device to the reservoirs was suggested by GEBRAUER and CAR [216, 217]. They impose periodic boundary conditions upon the unperturbed system. This approach can be also used to describe transients.

---

[1] Here the PAULI exclusion principle which leads to a nonlinear master equation is neglected

3.10.3 The Wigner Distribution Function

Another approach capable of handling both quantum coherent propagation and dissipative scattering effects is based on the Wigner distribution function. The Wigner quasi-probability distribution was introduced by Wigner in 1932 [218] to study quantum corrections to classical statistical mechanics. The goal was to replace the wave-function that appears in the Schrödinger equation with a probability distribution in phase space. A classical particle has a definite position and momentum and hence, is represented by a point in phase space. For a collection (ensemble) of particles, the probability of finding a particle at a certain position in phase space is given by a probability distribution. This does not hold in quantum mechanics due to the uncertainty principle. Instead, the Wigner quasi-probability distribution plays an analogous role, it is defined as the density matrix in a mixed coordinate/momentum representation [218, 219]. But the Wigner quasi-probability distribution does not satisfy all the properties of a probability distribution. On the other hand it satisfies boundedness properties unavailable to the classical distributions. For instance, the Wigner distribution can and normally does go negative for states which have no classical model and a convenient indicator of quantum-mechanical interference.

Applying the Wigner-Weyl transformation to the Liouville equation gives the kinetic equation for the Wigner function

$$\frac{\partial f_{\mathrm{w}}(\mathbf{r},\mathbf{k},t)}{\partial t} + \mathbf{v} \cdot \nabla_{\mathbf{r}} f_{\mathrm{w}} + \frac{\mathbf{F}}{\hbar} \cdot \nabla_{\mathbf{k}} f_{\mathrm{w}} - \int d\mathbf{k}' \, V_{\mathrm{w}}(\mathbf{r},\mathbf{k}-\mathbf{k}') \, f_{\mathrm{w}}(\mathbf{r},\mathbf{k}',t) + \left(\frac{\partial f_{\mathrm{w}}}{\partial t}\right)_{\mathrm{coll}} = 0 \, , \tag{3.94}$$

where the kernel of the potential operator is given by

$$V_{\mathrm{w}}(\mathbf{r},\mathbf{k}) = \frac{1}{i\hbar(2\pi)^3} \int d\mathbf{s} \, \left(V(\mathbf{r}+\frac{\mathbf{s}}{2}) - V(\mathbf{r}-\frac{\mathbf{s}}{2}) + \mathbf{s}\cdot\mathbf{F} \right) \exp(-i\mathbf{k}\cdot\mathbf{s}) \, . \tag{3.95}$$

A practically used approximation to incorporate realistic scattering processes into the Wigner equation is to utilize the Boltzmann scattering operator [219, 220], or by an even simpler scheme such as the relaxation time approximation [221]. The inclusion of dissipation through the Boltzmann scattering operator, although intuitively appealing, raises some concerns about the validity of such procedure. The Boltzmann scattering operator is semi-classical by its nature, and represents a good approximation for sufficiently smooth device potentials. To account for scattering more rigorously, spectral information has to be included into the Wigner function, resulting in an energy-dependence in addition to the momentum dependence [190].

The kinetic equation for the Wigner function is similar to the semi-classical Boltzmann equation, except for a non-local potential term. In the case of a slowly varying potential this non-local term reduces to the local classical force term, and the semi-classical description given by the Boltzmann equation is obtained from the Wigner equation. The Boltzmann equation is the basis for the standard models of electron transport in semiconductors in a semi-classical approximation. By far the most widely used technique for solving the Boltzmann equation has been the Monte Carlo method [222]. Transport models based on the Boltzmann transport equation can be derived using the method of moments [223–225] which yields the drift-diffusion model [226], the energy-transport and hydrodynamic models [227], or higher-order transport models [228]. Furthermore, an approximate solution can be obtained by expressing the distribution function as a series expansion which leads to the spherical harmonics approach [229, 230].

Chapter 4

Implementation

NOVEL STRUCTURES and materials such as deca-nanometer Si bulk MOSFETs, multiple gate MOSFETs, CNT-FETs and molecular based transistors, are expected to be introduced to meet the requirements for scaling [1]. A deep understanding of quantum effects in nanoelectronic devices helps to improve their functionality and to develop new device types. For that purpose extensive computer simulation are required.

A multi-purpose quantum-mechanical solver, the VIENNA SCHRÖDINGER-POISSON solver (VSP), with the aim to aid theoretical as well as experimental research on nano-scale electronic devices, has been developed [231]. VSP is a quantum mechanical solver for closed as well as open boundary problems. The software is written in C++ using state-of-the-art software design techniques. The chosen software architecture allows one to add new models easily. Critical numerical calculations are performed with stable and powerful numerical libraries such as BLAS, LAPACK, and ARPACK. VSP holds a graphical user interface written in JAVA, as well as an XML based interface. Furthermore, VSP has an open software application interface and can be used within third party simulation environments.

This chapter describes the implementation of the outlined NEGF formalism into VSP. For an accurate analysis it is essential to solve the coupled system of transport and POISSON equations self-consistently [163]. The discretization of the POISSON equation and quantum transport equation is studied in this chapter.

A tight-binding HAMILTONian is used to describe transport phenomena in CNT-FETs. The mode-space transformation used in this work reduces the computational cost considerably. The mode-space approach takes only a relatively small number of transverse modes into consideration. To reduce the computational cost even further, we used the local scattering approximation [112]. In this approximation the scattering self-energy terms are diagonal in coordinate representation. We show that the local approximation is well justified for electron-phonon scattering caused by deformation potential interaction.

We investigate methods of generating adaptive energy grids for the transport equations and their effect on the convergence behavior of the self-consistent iteration. Our results indicate that for accurate and fast convergent simulations the energy grid must be carefully adapted.

4.1 Electrostatic Potential and the POISSON Equation

Planar CNT-FETs constitute the majority of devices fabricated to date, mostly due to their relative simplicity and moderate compatibility with existing manufacturing technologies. However, coaxial devices (see Fig. 4.1) are of special interest because their geometry allows for better electrostatic control than their planar counterparts. These devices would exhibit wrap-around gates that maximize capacitive coupling between the gate electrode and the CNT channel. Presently, the closest approximation to this geometry are electrolyte-gated devices [232, 233]. Alternative structures that place CNTs vertically with respect to the substrate have already been used for field-emission applications [234, 235]. Coaxial CNT-FETs could be fashioned by placing CNTs inside the cavities of a porous material such as alumina, surrounding them by gate electrodes.

Appropriate treatment of the electrostatic potential in the device is essential for accurately predicting the device characteristics [236]. The electron-electron interaction self-energy of lowest order yields the HARTREE potential, which is the solution of the POISSON equation

$$\nabla \cdot \varepsilon \nabla \phi \; = \; -\varrho \tag{4.1}$$

where ϱ is the total charge density, given (in cylindrical coordinates) by [237]

$$\varrho \; = \; \frac{\mathrm{q}[p(z) - n(z)]\delta(r - r_{\mathrm{CNT}})}{2\pi r} \; . \tag{4.2}$$

Here, n and p denote the electron and hole concentration per unit length, respectively, and r_{CNT} is the radius of the CNT. In (4.2) $\delta(r)/r$ is the DIRAC delta function in cylindrical coordinates, implying that the carrier density is approximated by a sheet charge distributed along the insulator-CNT interface [237]. Due to azimuthal symmetry in wrap-around gate devices, the carriers are uniformly distributed as a function of the azimuthal angle.

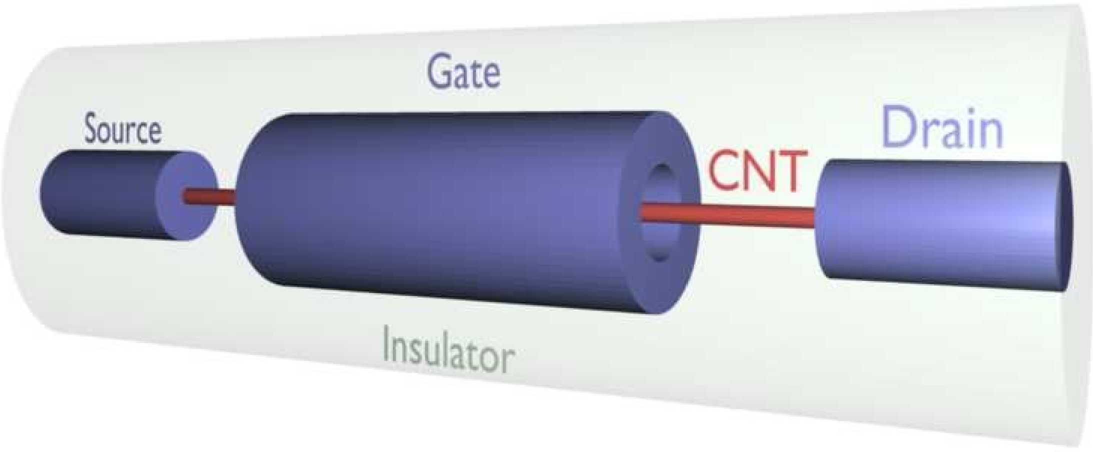

Figure 4.1: Schematic of the coaxial CNT-FET.

4.1.1 Discretization of the POISSON Equation

To solve partial differential equations numerically, they are usually discretized. For that reason, the domain $\mathcal{V}$ where the equations are posed has to be partitioned into a finite number of sub-domains $\mathcal{V}_i$, which are usually obtained by a VORONOI tessellation [238, 239]. In order to obtain the solution with a desired accuracy, the equation system is approximated in each of these sub-domains by algebraic equations. The unknowns of this system are approximations of the continuous solutions at the discrete grid points in the domain [226]. Several approaches for the discretization of the partial differential equations have been proposed. It has been found to be advantageous to apply the finite boxes discretization scheme for semiconductor device simulation [226]. This method considers the integral form of the equation for each sub-domain, which is the so-called control volume $\mathcal{V}_i$ associated with the grid point P_i. By applying the GAUSS integral theorem, the POISSON equation (4.1) is integrated as

$$\oint_{\partial\mathcal{V}} \varepsilon\nabla\phi \cdot d\mathbf{A} + \int_{\mathcal{V}} \varrho \, dV = 0 . \tag{4.3}$$

Finally, the discretized equation for point i with neighbor points j can be written implicitly as

$$F_i = \sum_j \overline{\varepsilon}_{ij} \frac{\phi_j - \phi_i}{d_{ij}} A_{ij} + \varrho_i V_i = 0 , \tag{4.4}$$

with d_{ij} is the distance between grid point P_i and P_j, A_{ij} as the interface area between the domains $\mathcal{V}_i$ and $\mathcal{V}_j$, and V_i as the volume of the domain $\mathcal{V}_i$. For position-dependent ε, one can use here some average, e.g. $\overline{\varepsilon}_{ij} = (\varepsilon_i + \varepsilon_j)/2$. Equation (4.4) can be generally written as

$$F_i = \sum_j F_{ji} + G_i = 0 , \tag{4.5}$$

where j runs over all neighboring grid points in the same segment, F_{ji} is the flux between points j and i, and G_i is the source term (see Fig. 4.2). Grid points on the boundary $\partial\mathcal{V}$ are defined as having neighbor grid points in other segments. Thus, for boundary elements (4.5) does not represent the complete control function F_i, since all fluxes into the contact or the other segment are missing. For that reason, the information for these boxes has to be completed by taking the boundary conditions into account.

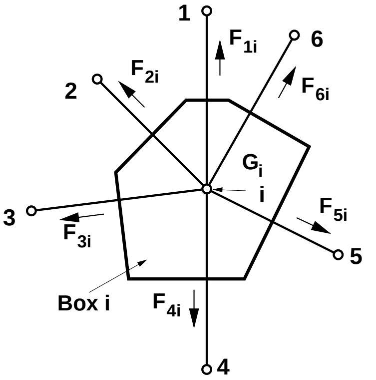

Figure 4.2: Box i with six neighbors [240].

4.1.2 Boundary Conditions

DIRICHLET boundary conditions are introduced at the source, drain, and gate contacts. Potentials are conveniently measured relative to the source potential. The amount of bending of the vacuum enegy level along the length of the CNT is given by $E_{\mathrm{vac}}(z) = -\mathrm{q}\phi(z)$, since we assume that the local electrostatic potential rigidly shifts the CNT band-structure. The conduction and valence band-edges of the CNT are given by

$$\begin{aligned} E_{\mathrm{c}}(z) &= -\,\mathrm{q}\phi(z) \;+\; \mathrm{q}\Phi_{\mathrm{Be}} \;, \\ E_{\mathrm{v}}(z) &= -\,\mathrm{q}\phi(z) \;-\; \mathrm{q}\Phi_{\mathrm{Bh}} \;. \end{aligned} \tag{4.6}$$

The SCHOTTKY barrier heights for electrons ($\mathrm{q}\Phi_{\mathrm{Be}}$) and holes ($\mathrm{q}\Phi_{\mathrm{Bh}}$) at the metal-CNT interface are given by (see Fig. 4.3)

$$\begin{aligned} \mathrm{q}\Phi_{\mathrm{Be}} &= +\,\mathrm{q}\Phi_{\mathrm{M}} \;-\; \mathrm{q}\chi_{\mathrm{CNT}} \;, \\ \mathrm{q}\Phi_{\mathrm{Bh}} &= -\,\mathrm{q}\Phi_{\mathrm{Be}} \;+\; E_{\mathrm{g}} \;, \end{aligned} \tag{4.7}$$

where $\mathrm{q}\Phi_{\mathrm{M}}$ is the work function of the metal contact, $\mathrm{q}\chi_{\mathrm{CNT}}$ is the electron affinity of the CNT, and E_{g} is the band-gap of the CNT. The work function of CNT $\mathrm{q}\Phi_{\mathrm{CNT}}$ is defined as the sum of the CNT electron affinity and half of the band-gap in the bulk. Figure 4.3 shows the band diagram at the metal-CNT interface with $\Phi_{\mathrm{M}} = \Phi_{\mathrm{CNT}}$. The work function of the CNT is assumed to be $\Phi_{\mathrm{CNT}} = 4.5$ eV [4]. In an intrinsic CNT (un-doped) the FERMI level of the CNT is located in the middle of the band-gap. Under these conditions, equal SCHOTTKY barrier heights for both electrons and holes are achieved. If the work functions of metal and CNT do not align, band-bending near the contact occurs and SCHOTTKY barrier heights for electrons and holes will be different. For example, if the work function of the metal contact is larger than that of the CNT ($\Phi_{\mathrm{M}} > \Phi_{\mathrm{CNT}}$) the SCHOTTKY barrier height for holes is smaller than that for electrons. As a result, a p-type CNT-FET is achieved, where holes are the majority carriers.

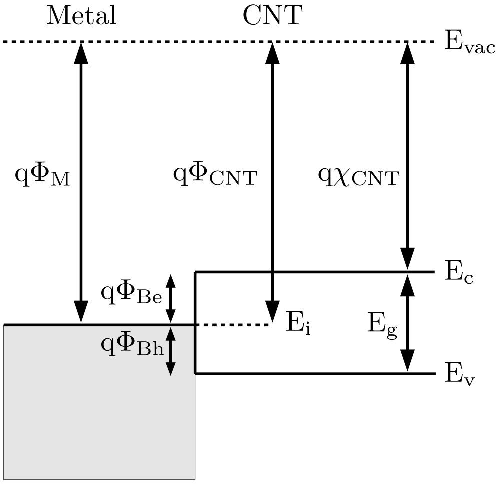

Figure 4.3: Band diagram at the metal-CNT interface with $\Phi_{\mathrm{M}} = \Phi_{\mathrm{CNT}}$.

4.1.3 Interface Conditions

To account for interface conditions, grid points located at the boundary of the segments (see Fig. 4.4-a) are assigned three values, one for each segment (see Fig. 4.4-b) and a third value assigned directly to the interface, which can be used to formulate more complicated interface conditions such as, for example, interface charges.

As discussed in Section 4.1, charges on the CNT are approximated as sheet charges at the CNT-insulator interface. The boundary flux due to interface charges is simply added to the segment fluxes given by (4.5)

$$\begin{aligned} F_i \ + \ F_{i'',i} \quad &= \ 0 \ , \\ F_{i'} \ + \ F_{i'',i'} \ &= \ 0 \ , \end{aligned} \tag{4.8}$$

with

$$\begin{aligned} F_{i'',i} \quad &= \ \frac{\varrho_{i''} A_i}{2} \ , \\ F_{i'',i'} \quad &= \ \frac{\varrho_{i''} A_{i'}}{2} \ , \end{aligned} \tag{4.9}$$

where $A_i = A_{i'}$ and $\varrho_{i''}$ is the interface charge density at some point i'' along the insulator-CNT interface given by (4.2). This method satisfies the condition of the discontinuity of the electric displacement in the presence of interface charges. For the CNT the free-space relative permittivity, $\varepsilon_{\mathrm{CNT}} = 1$, is assumed [241].

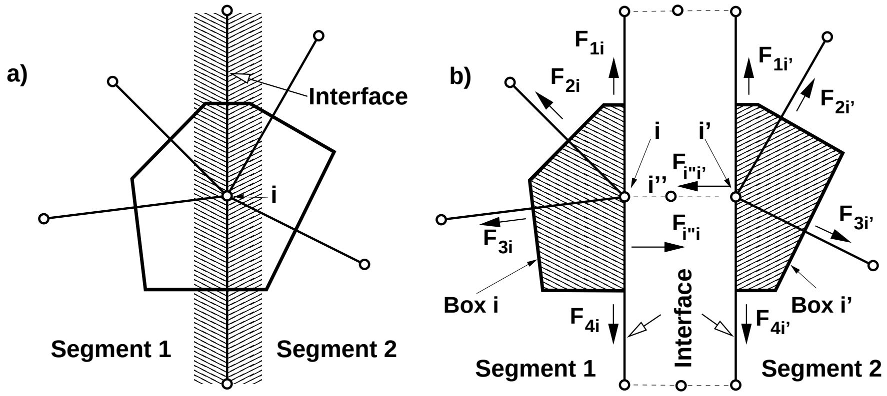

Figure 4.4: Interface points as given in a) are split into three different points having the same geometrical coordinates b) [240].

4.2 Basis Functions and Matrix Representation

For the purpose of discretization one can expand the HAMILTONian, self-energies, and GREEN's functions in terms of some basis functions to obtain the corresponding matrices. In the *tight-binding method* one can take the basis functions to be any set of localized functions, such as atomic s- and p-orbitals [116, 122], WANNIER functions [242], and so forth. A common approximation used to describe the HAMILTONian of layered structures consists of non-vanishing interactions only between *nearest neighbor* layers. That is, each layer i interacts only with itself and its nearest neighbor layers $i-1$ and $i+1$. Then the single particle HAMILTONian of the layered structure is a *block tri-diagonal matrix*, where diagonal blocks $\underline{H}_i$ represent the Hamiltonian of layer i and off-diagonal blocks $\underline{t}_{i,i+1}$ represent interaction between layers i and $i+1$

$$\underline{H} \;=\; \begin{bmatrix} \bullet & \bullet & \bullet & & & & & & & \\ \bullet & \underline{H}_1 & \underline{t}_{12} & & & & & & & \\ & \underline{t}_{12}^{\dagger} & \underline{H}_2 & \underline{t}_{2,3} & & & & & & \\ & & \bullet & \bullet & \bullet & & & & & \\ & & & & \bullet & \bullet & \bullet & & & \\ & & & & & \underline{t}_{N-2,N-1}^{\dagger} & \underline{H}_{N-1} & \underline{t}_{N-1,N} & & \\ & & & & & & \underline{t}_{N-1,N}^{\dagger} & \underline{H}_N & \bullet & \\ & & & & & & & \bullet & \bullet & \bullet \end{bmatrix} , \tag{4.10}$$

where $\underline{t}_{i+1,i} = \underline{t}_{i,i+1}^{\dagger}$. The matrix representation of the kinetic equations (3.71) and (3.72) are

$$[E\underline{I} - \underline{H} - \underline{\Sigma}_{\mathrm{Scat}}^{\mathrm{r}}]\, \underline{G}^{\mathrm{r}} \;=\; \underline{I} \;, \tag{4.11}$$

$$\underline{G}^{\gtrless} \;=\; \underline{G}^{\mathrm{r}}\, \underline{\Sigma}_{\mathrm{Scat}}^{\gtrless}\, \underline{G}^{\mathrm{a}} \;, \tag{4.12}$$

where $\underline{\Sigma}_{\mathrm{Scat}}$ is the self-energy due to scattering processes and $\underline{G}^{\mathrm{a}} = [\underline{G}^{\mathrm{r}}]^{\dagger}$ [60]. One can partition the layered structure into left contact with index L, device region with index D, and right contact with index R (Fig. 4.5). The device corresponds to the region where one solves the transport equations and the contacts are the highly conducting regions connected to the device. While the device region consists of only N layers, the matrix equation corresponding to (4.11) is infinitely dimensional due to the semi-infinite contacts. As shown in Appendix G the influence of the semi-infinite contacts can be folded into the device region by adding a self-energy to the device region. This can be viewed as an additional self-energy due to the transitions between the device and the contacts. In the next sections the matrix representation of the HAMILTONian and self-energies are discussed in detail.

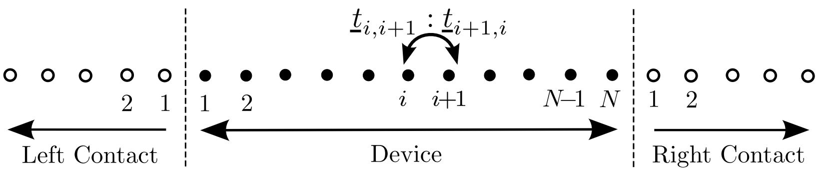

Figure 4.5: Partitioning of the simulation domain into device region and left and right contacts. Each point corresponds to a layer.

4.3 Tight-Binding HAMILTONian

The general form of the tight-binding HAMILTONian for electrons in a CNT can be written as

$$\hat{H} \;=\; \sum_{i,p} U_i^p c_{i,p}^{\dagger} c_{i,p} \;+\; \sum_{i,j,p,q} t_{i,j}^{p,q} c_{i,p}^{\dagger} c_{j,q} \;. \tag{4.13}$$

The sum is taken over all rings i, j along the transport direction, which is assumed to be the z-direction of the cylindrical coordinate system, and over all atomic locations p,q in a ring. We use a nearest-neighbor tight-binding π-bond model [10, 243]. Each atom in an sp^2-coordinated CNT has three nearest neighbors, located $a_{\mathrm{C-C}}$ away. The band-structure consists of π-orbitals only, with the hopping parameter $t = V_{\mathrm{pp}\pi} = -2.77$ eV and zero on-site potential. Furthermore, it is assumed that the electrostatic potential U rigidly shifts the on-site potentials. Such a tight-binding model is adequate to model transport properties in un-deformed CNTs.

In this work we consider zigzag CNTs. However, this method can be readily extended to armchair or chiral CNTs. Within the nearest-neighbor approximation, only the following parameters are non zero [10]

$$\begin{aligned} t_{i,i-1}^{p,q} \;&=\; t_{i-1,i}^{p,q} \;=\; t\ \delta_{p\pm a/2,q} \ , \quad \forall i = 2k \ , \\ t_{i,i+1}^{p,q} \;&=\; t_{i+1,i}^{p,q} \;=\; t\ \delta_{p,q} \ . \qquad\;\; \forall i = 2k \ . \end{aligned} \tag{4.14}$$

Figure 4.6 shows that a zigzag CNT is composed of rings (layers) of A- and B-type carbon atoms, where A and B represent the two carbon atoms in a unit cell of graphene. Each A-type ring is adjacent to a B-type ring. Within nearest-neighbor tight-binding approximation the total HAMILTONian matrix is block tri-diagonal [243]

$$\underline{H} = \begin{bmatrix} \underline{H}_1 & \underline{t}_2 & & & & \\ \underline{t}_2^{\dagger} & \underline{H}_2 & \underline{t}_1 & & & \\ & \underline{t}_1 & \underline{H}_3 & \underline{t}_2^{\dagger} & & \\ & & \underline{t}_2 & \underline{H}_4 & \underline{t}_1 & \\ & & & \underline{t}_1 & \underline{H}_5 & \bullet \\ & & & & \bullet & \bullet \end{bmatrix} , \tag{4.15}$$

where the diagonal blocks, $\underline{H}_i$, describe the coupling within an A-type or B-type carbon ring and off-diagonal blocks, $\underline{t}_1$ and $\underline{t}_2$, describe the coupling between adjacent rings. It should be noted that the odd numbered HAMILTONian $\underline{H}_i$ refer to A-type rings and the even numbered one to B-type rings. Each A-type ring couples to the next B-type ring according to $\underline{t}_2$ and to the previous B-type ring according to $\underline{t}_1$. Each B-type ring couples to the next A-type ring according to $\underline{t}_1$ and to the previous A-type ring according to $\underline{t}_2$. In a $(n, 0)$ zigzag CNT, there are n carbon atoms in each ring, thus, all the sub-matrices in (4.15) have a size of $n \times n$.

In the nearest-neighbor tight binding approximation, carbon atoms within a ring are not coupled to each other so that $\underline{H}_i$ is a diagonal matrix. The value of a diagonal entry is the potential at that carbon atom site. In the case of a coaxially gated CNT, the potential is constant along the CNT circumference. As a result, the sub-matrices $\underline{H}_i$ are given by the potential at the respective carbon ring times the identity matrix

$$\underline{H}_i \;=\; \underline{U}_i \;= U_i\ \underline{I} \ , \tag{4.16}$$

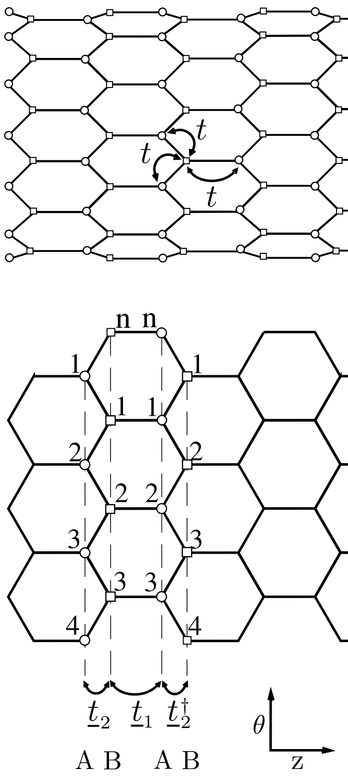

Figure 4.6: Layer layout of a $(n, 0)$ zigzag CNT. Circles are rings of A-type carbon atoms and squares rings of B-type carbon atoms. The coupling coefficient between nearest neighbor carbon atoms is t. The coupling matrices between rings are denoted by $\underline{t}_1$ and $\underline{t}_2$, where $\underline{t}_1$ is a diagonal matrix and $\underline{t}_2$ is non-diagonal.

There are two types of coupling matrices between nearest carbon rings, $\underline{t}_1$ and $\underline{t}_2$. As shown in Fig. 4.6, the first type, $\underline{t}_1$, only couples an A(B) carbon atom to its B(A) counterpart in the neighboring ring. The coupling matrix is just the tight-binding coupling parameter times an identity matrix,

$$\underline{t}_1 = t\underline{I} \; . \tag{4.17}$$

The second type of coupling matrix, $\underline{t}_2$, couples an A(B) atom to two B(A) neighbors in the adjacent ring. The coupling matrix is

$$\underline{t}_2 = \begin{bmatrix} t & & & t \\ t & t & & \\ & t & t & \\ & & \bullet & \bullet \end{bmatrix} . \tag{4.18}$$

The period of the zigzag CNT in the longitudinal direction contains four rings, ABAB, and has a length of $3a_{\mathrm{C-C}}$. Therefore, the average distance between the rings is

$$\Delta z = \frac{3a_{\mathrm{C-C}}}{4} \; . \tag{4.19}$$

4.4 Mode-Space Transformation

A mode space approach significantly reduces the size of the HAMILTONian matrix [9]. Due to quantum confinement along the CNT circumference, circumferential modes appear and transport can be described in terms of these modes. If M modes contribute to transports, and if $M < n$, then the size of the problem is reduced from $n \times N$ to $M \times N$, where N is number of carbon rings along the CNT. If the potential profile does not vary sharply along the CNT, subbands are decoupled [9] and one can solve M one-dimensional problems of size N.

Mathematically, one performs a basis transformation on the HAMILTONian of the $(n, 0)$ zigzag CNT to decouple the problem into n one-dimensional mode space lattices [243]

$$\begin{aligned}\underline{H}' &= \begin{bmatrix} \underline{S}^\dagger &&&&& \\ & \underline{S}^\dagger &&&& \\ && \underline{S}^\dagger &&& \\ &&& \underline{S}^\dagger && \\ &&&& \underline{S}^\dagger & \\ &&&&& \bullet \end{bmatrix} \begin{bmatrix} \underline{U}_1 & \underline{t}_2 &&&& \\ \underline{t}_2^\dagger & \underline{U}_2 & \underline{t}_1 &&& \\ & \underline{t}_1 & \underline{U}_3 & \underline{t}_2^\dagger && \\ && \underline{t}_2 & \underline{U}_4 & \underline{t}_1 & \\ &&& \underline{t}_1 & \underline{U}_5 & \bullet \\ &&&& \bullet & \bullet \end{bmatrix} \begin{bmatrix} \underline{S} &&&&& \\ & \underline{S} &&&& \\ && \underline{S} &&& \\ &&& \underline{S} && \\ &&&& \underline{S} & \\ &&&&& \bullet \end{bmatrix} \\ &= \begin{bmatrix} \underline{U}_1' & \underline{t}_2' &&&& \\ \underline{t}_2'^\dagger & \underline{U}_2' & \underline{t}_1' &&& \\ & \underline{t}_1' & \underline{U}_3' & \underline{t}_2'^\dagger && \\ && \underline{t}_2' & \underline{U}_4' & \underline{t}_1' & \\ &&& \underline{t}_1' & \underline{U}_5' & \bullet \\ &&&& \bullet & \bullet \end{bmatrix} ,\end{aligned} \tag{4.20}$$

with

$$\begin{aligned} \underline{U}_i' &= \underline{S}^\dagger \, \underline{U}_i \, \underline{S} \, , \\ \underline{t}_1' &= \underline{S}^\dagger \, \underline{t}_1 \, \underline{S} \, , \\ \underline{t}_2' &= \underline{S}^\dagger \, \underline{t}_2 \, \underline{S} \, , \end{aligned} \tag{4.21}$$

where $\underline{S}$ is the transformation matrix from the real space basis to the mode space basis. The purpose is to decouple the modes after the basis transformation, i.e., to make the HAMILTONian matrix blocks between different modes equal to zero. This requires that after the transformation, the matrices $\underline{U}_i$, $\underline{t}_1$, and $\underline{t}_2$, become diagonal. Since $\underline{U}_i$ and $\underline{t}_1$ are identity matrices multiplied by a constant, they remain unchanged and diagonal after any basis transformation, $\underline{U}_i' = \underline{U}_i$ and $\underline{t}_1' = \underline{t}_1$. To diagonalize $\underline{t}_2$, elements of the transformation matrix $\underline{S}$ have to be the eigen-vectors of $\underline{t}_2$. These eigen-vectors are plane waves with wave-vectors satisfying the periodic boundary condition around the CNT. The eigen-values are

$$t_2^\nu = 2te^{-i\pi\nu/n} \cos(\pi\nu/n) \, , \tag{4.22}$$

where $\nu = 1, 2, \ldots, n$ [243]. The phase factor in (4.22) has no effect on the results such as charge and current density, thus it can be omitted and $t_2^\nu = 2t\cos(\pi\nu/n)$ can be used instead.

After the basis transformation all sub-matrices, $\underline{U}_i$, $\underline{t}_1$, and $\underline{t}_2$ are diagonal. By reordering the basis according to the modes, the Hamiltonian matrix takes the form

$$\underline{H}^{'} = \begin{bmatrix} \underline{H}^1 & & & & \\ & \underline{H}^2 & & & \\ & & \bullet & & \\ & & & \underline{H}^{\nu} & \\ & & & & \bullet \end{bmatrix} , \tag{4.23}$$

where $\underline{H}^{\nu}$ is the Hamiltonian matrix for the νth mode [243]

$$\underline{H}^{\nu} = \begin{bmatrix} U_1 & t_2^{\nu} & & & & \\ t_2^{\nu} & U_2 & t & & & \\ & t & U_3 & t_2^{\nu} & & \\ & & t_2^{\nu} & U_4 & t & \\ & & & t & U_5 & \bullet \\ & & & & \bullet & \bullet \end{bmatrix} . \tag{4.24}$$

The one-dimensional tight-binding Hamiltonian H^{ν} describes a chain of atoms with two sites per unit cell and on-site potential U and hopping parameters t and t_2^{ν} (Fig. 4.7). The spatial grid used for device simulation corresponds to the circumferential rings of carbon atoms. Therefore, the rank of the matrices for each subband are equal to the total number of these rings N. Self-energies can be also transformed into mode space Σ^{ν}, see Section 4.5 and Section 4.6. The Green's functions can therefore be defined for each subband (mode) and one can solve the system of transport equations for each subband independently

$$[E\underline{I} - \underline{H}^{\nu} - \underline{\Sigma}^{\mathrm{r}^{\nu}}]\, \underline{G}^{\mathrm{r}^{\nu}} = \underline{I} \,, \tag{4.25}$$

$$\underline{G}^{\gtrless^{\nu}} = \underline{G}^{\mathrm{r}^{\nu}}\, \underline{\Sigma}^{\gtrless^{\nu}}\, \underline{G}^{\mathrm{a}^{\nu}} \,. \tag{4.26}$$

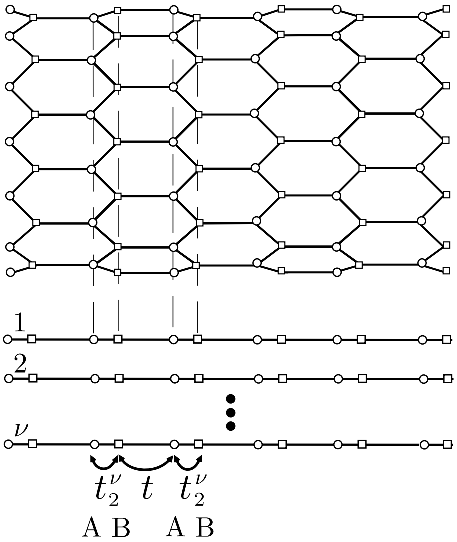

Figure 4.7: Zigzag CNT and the corresponding one-dimensional chain with two sites per unit cell with hopping parameters t and $t_2^{\nu} = 2t\cos(\pi\nu/n)$.

4.5 Contact Self-Energies

Boundary conditions have to be specified to model the contacts, which act as a source or drain for electrons. While the matrix representing the Hamiltonian of the device has a finite dimension, the total Hamiltonian matrix is infinite dimensional due to the semi-infinite contacts.

The influence of the contacts can be folded into the device region. Due to the transitions between the device and the contacts, the influence of the contacts can be demonstrated by adding contact self-energies to the total self-energy [60]. The self-energy matrices for the contacts and the Hamiltonian matrix for the device have the same rank, but the self-energy matrices are highly sparse. For example, only one carbon ring at the source end of the channel couples to the source, thus only one sub-matrix is non-zero for the source self-energy. Similarly, only one sub-matrix is non-zero for the drain self-energy. As shown in Appendix G, non-zero blocks of the contact self-energies are given by

$$\begin{aligned} \underline{\Sigma}^{\mathrm{r}}_{L} &= \underline{t}^{\dagger}_{LD}\, \underline{g}^{\mathrm{r}}_{L_{1,1}}\, \underline{t}_{LD} \ , \\ \underline{\Sigma}^{\mathrm{r}}_{R} &= \underline{t}^{\dagger}_{RD}\, \underline{g}^{\mathrm{r}}_{R_{1,1}}\, \underline{t}_{RD} \ , \end{aligned} \tag{4.27}$$

$$\begin{aligned} \underline{\Sigma}^{<}_{L} &= +i\, \underline{\Gamma}_{L}\, f_{L} \ , \\ \underline{\Sigma}^{<}_{R} &= +i\, \underline{\Gamma}_{R}\, f_{R} \ , \end{aligned} \tag{4.28}$$

$$\begin{aligned} \underline{\Sigma}^{>}_{L} &= -i\, \underline{\Gamma}_{L}\, (1 - f_{L}) \ , \\ \underline{\Sigma}^{>}_{R} &= -i\, \underline{\Gamma}_{R}\, (1 - f_{R}) \ , \end{aligned} \tag{4.29}$$

where sub-scripts L and R denote the left (source) and right (drain) contacts, respectively, $f_{L,R}$ are the Fermi factor of the contacts, $\underline{g}^{\mathrm{r}}_{L,R}$ are the surface Green's function of the contacts, and finally the broadening functions are defined as

$$\begin{aligned} \underline{\Gamma}_{L} &= i\, (\underline{\Sigma}^{\mathrm{r}}_{L} - \underline{\Sigma}^{\mathrm{a}}_{L}) &&= -2\Im\mathrm{m}[\underline{\Sigma}^{\mathrm{r}}_{L}] \ , \\ \underline{\Gamma}_{R} &= i\, (\underline{\Sigma}^{\mathrm{r}}_{R} - \underline{\Sigma}^{\mathrm{a}}_{R}) &&= -2\Im\mathrm{m}[\underline{\Sigma}^{\mathrm{r}}_{R}] \ . \end{aligned} \tag{4.30}$$

Surface Green's functions can be calculated using a recursive relation described in Appendix G.3. In this section two types of contacts are discussed: semi-infinite CNTs acting as the source and drain contacts and Schottky type metal-CNT contacts. The respective surface Green's functions and self-energies for the both contact types are derived next.

In mode-space representation (see Section 4.4) the matrices in (4.27) to (4.30) become one-dimensional. Thus, the respective quantities for each mode can be treated as numbers and the computational cost decreases considerably.

4.5.1 Semi-Infinite CNT Contacts

Figure 4.8 shows carbon rings of A or B-type coupled to a semi-infinite CNT acting as a contact. Each circle (rectangle) represents a carbon ring consisting of A or B-type carbon atoms. The carbon ring couples to the nearest ring, with a coupling matrix of $\underline{t}_1$ or $\underline{t}_2$, and $\underline{g}^{\mathrm{r}}_{L_{i,i}}$ is the surface GREEN's function for the ith ring in the left extension, ordered from the channel-contact interface. The recursive relation (G.22) can be applied to the CNT in Fig. 4.8 and gives

$$\begin{aligned} [\underline{A}_{L_1} \;-\; \underline{t}_2\, \underline{g}^{\mathrm{r}}_{L_{2,2}} \underline{t}_2^{\dagger}]\; \underline{g}^{\mathrm{r}}_{L_{1,1}} &= \underline{I}\;, \\ [\underline{A}_{L_2} \;-\; \underline{t}_1\, \underline{g}^{\mathrm{r}}_{L_{3,3}} \underline{t}_1^{\dagger}]\; \underline{g}^{\mathrm{r}}_{L_{2,2}} &= \underline{I}\;, \end{aligned} \tag{4.31}$$

where $\underline{A}_{L_i} = E\underline{I}_i - \underline{U}_{L_i} - \underline{\Sigma}^{\mathrm{r}}_{\mathrm{Scat}_{i,i}}$ (see Appendix G.1), and $\underline{t}_1$ and $\underline{t}_2$ are given by (4.17) and (4.18), respectively. Since the potential is invariant inside the contact, $\underline{A}_{L_1} = \underline{A}_{L_2}$. Furthermore, $\underline{g}^{\mathrm{r}}_{L_{3,3}} = \underline{g}^{\mathrm{r}}_{L_{1,1}}$ due to the periodicity of the CNT lattice. Using these relations, (4.31) represent two coupled matrix equations with two unknowns, $\underline{g}^{\mathrm{r}}_{L_{1,1}}$ and $\underline{g}^{\mathrm{r}}_{L_{2,2}}$, which can be solved by iteration. However, in mode-space representation matrices $\underline{t}_1$ and $\underline{t}_2$ are replaced by the numbers $t_1 = t$ and t_2^{ν}, respectively. As a result, the surface GREEN's function for each mode can be calculated analytically by solving a quadratic equation

$$g^{\mathrm{r}^{\nu}}_{L_{1,1}} \;=\; \frac{A^2_{L_1} \;+\; t_1^2 \;-\; {t_2^{\nu}}^2 - \sqrt{\left[A^2_{L_1} \;+\; t_1^2 \;-\; {t_2^{\nu}}^2\right]^2 \;-\; 4A^2_{L_1}\, t_1^2}}{2A_{L_1}\, t_1^2}\;. \tag{4.32}$$

The self-energy of the left contact for the νth mode is therefore given by

$$\Sigma^{\mathrm{r}^{\nu}}_{L} \;=\; t_1^2\, g^{\mathrm{r}^{\nu}}_{L_{1,1}} \tag{4.33}$$

A similar relation holds for the right contact self-energy.

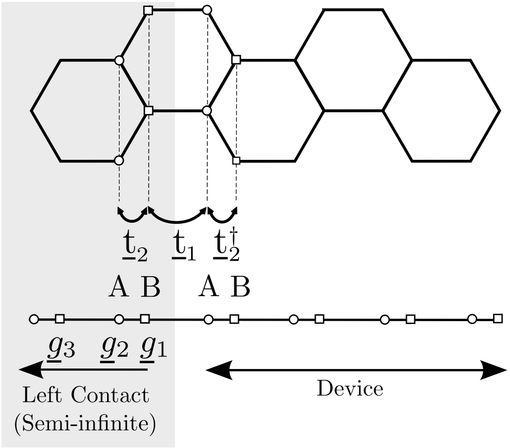

Figure 4.8: Computing the surface GREEN's function for the left contact. The surface GREEN's function for the ith ring inside the contact is g_i.

4.5.2 Schottky Type Metal-CNT Contacts

At the metal-CNT interface a Schottky barrier (SB) forms, which governs the operation of CNT-FETs (Section 2.8.2). The metal region acts as a source and a sink of electrons in the device region. In this work Pd contacts are assumed. For transport calculation based on a simplified tight-binding Hamiltonian, describing only the interaction between d_z orbitals of Pd and p_z orbitals of the carbon atoms, the self-energy for this SB contact can be written as

$$\Sigma_{\mathrm{SB}}^{\mathrm{r}^{\nu}} = t_{\mathrm{M-C}}^{2} \, g_{\mathrm{M}_{1,1}}^{\mathrm{r}} \tag{4.34}$$

where $t_{\mathrm{M-C}}$ is the hopping parameter between metal and carbon atoms and $g_{\mathrm{M}_{1,1}}^{\mathrm{r}}$ is the surface Green's function of the metal contact. The contact model in (4.34) assumes injection from the contact into all CNT subbands.

Based on *ab-initio* calculations, it has been shown that the electronic band structure of the Pd-graphene system near the Fermi level can be reproduced by considering the hybridization between graphene and Pd bands, using $t_{\mathrm{Pd-C}} = 0.15$ eV [244].

The surface Green's function contains information about the band-structure of the metal contact. To calculate the surface Green's function, one has to specify an appropriate Hamiltonian for the contacts, for example one can employ the tight-binding method [156], density functional theory [244], or extended Hückel theory [245]. Contacts can be approximated as semi-infinite leads along the transport axis, and infinite in the transverse direction. Therefore, the surface Green's function can be calculated iteratively along the transport direction (Section G.3).

Figure 4.9 shows the bulk and surface density of states of an Au-contact modeled using extended Hückel theory [245]. The density of states and as a result the contact self-energy depend on energy. However, the density of states near the Fermi level does not vary sharply. Since transport phenomena occur mostly due to electrons close to the Fermi level, one can assume that the contact self-energy at all energies is equal to $\Sigma(E_{\mathrm{F}})$. For Pd contacts we used the results of ab-initio calculations reported in [244].

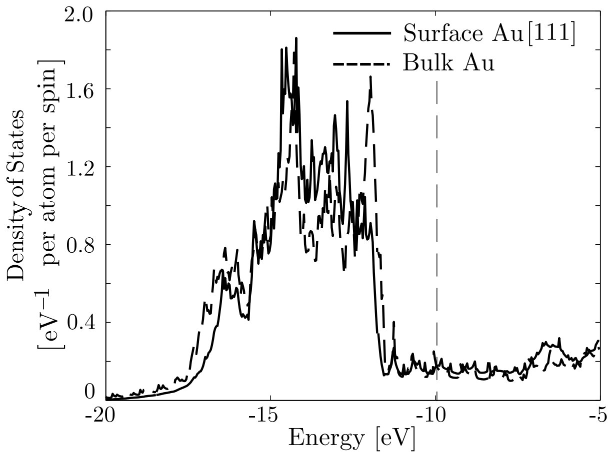

Figure 4.9: Calculated bulk and surface density of states for Au ($E_{\mathrm{F}} = -10$ eV) [245].

4.6 Scattering Self-Energies

The lowest-order electron-phonon self-energies are introduced in Section 3.6 and the steady-state form of these self-energies has been derived in Section 3.8.3. By transforming the self-energies (3.73) into mode-space one obtains [10]

$$\Sigma^{\gtrless\nu}_{\mathrm{el-ph}_{i,j}}(E) \;=\; i\sum_{q,\lambda}\int\frac{d(\hbar\omega_{q,\lambda})}{2\pi}\; e^{iq(z_i-z_j)}M^2_{q,\lambda,\nu}G^{\gtrless\nu}_{i,j}(E-\hbar\omega_{q,\lambda})D^{\gtrless}_{\lambda}(q,\hbar\omega_{q,\lambda})\;, \tag{4.35}$$

where z_i is the position of some lattice point i along the CNT axis. Note that due to the one-dimensional nature of CNTs, the coordinate and wave-vector variables are all one-dimensional. In (4.35) only intra-subband scattering process are considered (see Section 2.6). To include inter-subband scattering processes the summation in (4.35) would have to run over the all subbands ν' with the electron-phonon matrix elements $M_{q,\lambda,\nu,\nu'}$.

The electron-phonon self-energies in the self-consistent Born approximation are expressed in terms of the full electron and phonon Green's functions. One should therefore study the influence of the bare electron states on the phonons first, and then calculate the effect on the electrons of the renormalized phonon states [190]. In this work we assume that the phonon renormalization can be neglected. By doing so we miss to capture a possible reduction of the phonon lifetime. The above considerations also appeal to the Migdal theorem [246] which states that the phonon-induced renormalization of the electron-phonon vertex (see Appendix F.2) scales with the ratio of the electron mass to the ion mass [189]. Therefore, one can assume that the phonon bath is in thermal equilibrium so that the full phonon Green's function D_λ can be replaced by the non-interacting Green's functions D_{λ_0} from (D.16). As a result (4.35) can be written as

$$\begin{aligned}\Sigma^{<\nu}_{\mathrm{el-ph}_{i,j}}(E) \;=\; &\sum_{q,\lambda} e^{iq(z_i-z_j)}M^2_{q,\lambda}\\ &\times[(n_\mathrm{B}(\hbar\omega_{q,\lambda})+1)\,G^{<\nu}_{i,j}(E+\hbar\omega_{q,\lambda}) \;+\; n_\mathrm{B}(\hbar\omega_{q,\lambda})G^{<\nu}_{i,j}(E-\hbar\omega_{q,\lambda})]\;,\end{aligned} \tag{4.36}$$

$$\begin{aligned}\Sigma^{>\nu}_{\mathrm{el-ph}_{i,j}}(E) \;=\; &\sum_{q,\lambda} e^{iq(z_i-z_j)}M^2_{q,\lambda}\\ &\times[(n_\mathrm{B}(\hbar\omega_{q,\lambda})+1)\,G^{>\nu}_{i,j}(E-\hbar\omega_{q,\lambda}) \;+\; n_\mathrm{B}(\hbar\omega_{q,\lambda})G^{>\nu}_{i,j}(E+\hbar\omega_{q,\lambda})]\;,\end{aligned} \tag{4.37}$$

where the first term on the right hand side is due to phonon emission and the second term due to phonon absorption. The summation over wave-vector q in (4.36) and (4.37) can be generally transformed into an integral over the first Brillouin zone

$$\sum_q \;=\; \frac{L}{2\pi}\int dq\;, \tag{4.38}$$

where L is the normalization length and the limits of the integral are $\pm 3a_{\mathrm{C-C}}$ which is the period of the carbon rings, see (4.3). To calculate electron-phonon self-energies the integral in (4.38) must be evaluated.

4.6.1 Scattering with Optical Phonons

In this section the self-energies due to the interaction of electrons with optical phonons (OP) are evaluated. As discussed in Section 2.6, the phonon energy and the reduced electron-phonon matrix elements for OP phonons are approximately constant and independent of the phonon wave-vector. Under this assumption all terms except the exponential term in (4.36) and (4.37) can be taken out of the integral (4.38) and one obtains [55]

$$\int_{-\pi/(3a_{\mathrm{C-C}})}^{\pi/(3a_{\mathrm{C-C}})} \frac{dq}{2\pi} \exp(iq(z_i - z_j)) = \begin{cases} \dfrac{1}{3a_{\mathrm{C-C}}} , & z_i - z_j = 0 \\ 0 , & z_i - z_j = k \times 3a_{\mathrm{C-C}} \end{cases} , \tag{4.39}$$

where k is an integer number. One has to multiply the above result by a factor of 4, for the number of rings in the lattice period [55]. Equation (4.39) justifies the approximation which only considers diagonal elements of the electron-phonon self-energy. As discussed in Section 4.3, by employing the nearest neighbor tight-binding method (block) tri-diagonal matrices are achieved. Keeping only diagonal elements of the electron-phonon self-energy, the matrices remain (block) tri-diagonal. Therefore, an efficient recursive method (Appendix H) can be used to calculate the inverse matrices. This implies considerable reduction of computational cost and memory requirement.

Using the result of (4.39) and the relations (2.15) and (2.19) the self-energy due to scattering with optical phonons can be written as

$$\Sigma^{<^{\nu}}_{\mathrm{OP}_{i,j}}(E) = \delta_{i,j} D_{\mathrm{OP}}[(n_{\mathrm{B}}(\hbar\omega_{\mathrm{OP}}) + 1)\, G^{<^{\nu}}_{i,j}(E + \hbar\omega_{\mathrm{OP}}) \; + \; n_{\mathrm{B}}(\hbar\omega_{\mathrm{OP}}) G^{<^{\nu}}_{i,j}(E - \hbar\omega_{\mathrm{OP}})] , \tag{4.40}$$

$$\Sigma^{>^{\nu}}_{\mathrm{OP}_{i,j}}(E) = \delta_{i,j} D_{\mathrm{OP}}[(n_{\mathrm{B}}(\hbar\omega_{\mathrm{OP}}) + 1)\, G^{>^{\nu}}_{i,j}(E - \hbar\omega_{\mathrm{OP}}) \; + \; n_{\mathrm{B}}(\hbar\omega_{\mathrm{OP}}) G^{>^{\nu}}_{i,j}(E + \hbar\omega_{\mathrm{OP}})] , \tag{4.41}$$

where D_{OP} is given by

$$\begin{aligned} D_{\mathrm{OP}} &= \frac{\hbar}{2\rho_{\mathrm{CNT}}\, L\, \omega_{\mathrm{OP}}} \widetilde{M}^2_{\mathrm{OP}} \frac{L}{\Delta z} , \\ &= \frac{\hbar}{2n\; m_{\mathrm{C}}\; \omega_{\mathrm{OP}}} \widetilde{M}^2_{\mathrm{OP}} , \end{aligned} \tag{4.42}$$

where $\Delta z = 3a_{\mathrm{C-C}}/4$ (see (4.3)). In the second line in (4.42) the mass density of a $(n, 0)$ zigzag CNT has been replaced $\rho_{\mathrm{CNT}} = nm_{\mathrm{C}}/\Delta z$, where m_{C} is the mass of a carbon atom.

The retarded self-energy can be calculated as (3.76)

$$\Sigma^{\mathrm{r}}_{\mathrm{OP}_{i,j}}(E) = -\frac{i}{2}\Gamma_{\mathrm{OP}_{i,j}}(E) \; + \; \mathrm{P}\int \frac{dE'}{2\pi} \frac{\Gamma_{\mathrm{OP}_{i,j}}(E')}{E - E'} , \tag{4.43}$$

where

$$\Gamma_{\mathrm{OP}_{i,j}}(E) = i[\Sigma^{>}_{\mathrm{OP}_{i,j}}(E) \; - \; \Sigma^{<}_{\mathrm{OP}_{i,j}}(E)] \; = \; 2\Im\mathrm{m}[\Sigma^{<}_{\mathrm{OP}_{i,j}}(E)] . \tag{4.44}$$

Since the lesser and greater self-energies are assumed to be diagonal the retarded self-energy is also diagonal.

4.6.2 Scattering with Acoustic Phonons

Interaction with acoustic phonons (AP) can be approximated as elastic scattering, $E \pm \hbar\omega_{\mathrm{AP}} \approx E$. As discussed in Section 2.6, near the Γ-point a linear dispersion relation for acoustic phonons is assumed, $\omega_{\mathrm{AP}}(q) \approx \upsilon_{\mathrm{AP}}|q|$, where υ_{AP} is the acoustic phonon velocity. Furthermore, at room temperature low energy phonons have an appreciable occupation, such that

$$n_{\mathrm{B}} \approx n_{\mathrm{B}} + 1 \approx \frac{k_{\mathrm{B}}T}{\hbar\upsilon_{\mathrm{AP}}|q|} \gg 1 \ . \tag{4.45}$$

With equation (4.45) and the elastic approximation the contributions due to phonon emission and absorption become equal and can be lumped into one term. As a result, by using the relations (2.15) and (2.19) the self-energies due to acoustic phonon interaction are written as

$$\begin{aligned} \Sigma^{\gtrless\nu}_{\mathrm{AP}_{i,j}}(E) &= \sum_q e^{iq(z_i-z_j)} \frac{\hbar}{2\rho_{\mathrm{CNT}}\ L\ \upsilon_{\mathrm{AP}}|q|}\ \widetilde{M}^2_{\mathrm{AP}}|q|^2\ \times 2\frac{k_{\mathrm{B}}T}{\hbar\upsilon_{\mathrm{AP}}|q|} G^{\gtrless\nu}_{i,j}(E)\ , \\ &= \sum_q e^{iq(z_i-z_j)} \frac{k_{\mathrm{B}}T}{\rho_{\mathrm{CNT}}\ L\ \upsilon^2_{\mathrm{AP}}}\ \widetilde{M}^2_{\mathrm{AP}}\ G^{\gtrless\nu}_{i,j}(E)\ . \end{aligned} \tag{4.46}$$

With the exception of the exponential term all terms in (4.46) can be taken out of the sum and one can convert the sum into an integral over q, see (4.38) and (4.39). The self-energies simplify to

$$\Sigma^{\gtrless\nu}_{\mathrm{AP}_{i,j}}(E) = \delta_{i,j}\ D_{\mathrm{AP}}\ G^{\gtrless\nu}_{i,j}(E)\ , \tag{4.47}$$

where similar to (4.42) D_{AP} is given by

$$\begin{aligned} D_{\mathrm{AP}} &= \frac{k_{\mathrm{B}}T}{\rho_{\mathrm{CNT}}\ L\ \upsilon^2_{\mathrm{AP}}}\ \widetilde{M}^2_{\mathrm{AP}}\ \frac{L}{\Delta z}\ , \\ &= \frac{k_{\mathrm{B}}T}{n\ m_{\mathrm{C}}\ \upsilon^2_{\mathrm{AP}}}\ \widetilde{M}^2_{\mathrm{AP}}\ . \end{aligned} \tag{4.48}$$

A discussion similar to that in Section 4.6.1 gives a justification to keep only diagonal elements of the self-energy due to the interaction of electrons with acoustic phonons.

By substituting (4.47) in (3.76) the retarded self-energy is obtained as

$$\Sigma^{\mathrm{r}\nu}_{\mathrm{AP}_{i,j}}(E) = \delta_{i,j}\ D_{\mathrm{AP}}\ G^{\mathrm{r}\nu}_{i,j}(E)\ , \tag{4.49}$$

Due to the approximations made the retarded self-energy for scattering with acoustic phonons is simplified and directly related to the retarded GREEN's function.Therefore, one does not need to evaluate the integrals like (4.43), which implies a considerable saving of computational cost.

4.7 Evaluation of Observables

To solve the POISSON equation in a self-consistent scheme one has to know the carrier density profile in the device. To study device characteristics the current through the device needs to be calculated. In this section the numerical evaluation of these two observables is discussed.

4.7.1 Carrier Density

The GREEN's function matrices $G^{\gtrless\nu}_{i,j}$ are defined in the basis set of ring numbers i, j and subbands ν. Thus the diagonal elements correspond to the spectrum of carrier occupation (3.79) of those basis sites with a given energy E. So the total electron and hole density (per unit length) at a site i is given by [55]

$$n_i = -4i\sum_{\nu}\int\frac{dE}{2\pi}\,\frac{G^{<\nu}_{i,i}}{\Delta z}\,, \tag{4.50}$$

$$p_i = +4i\sum_{\nu}\int\frac{dE}{2\pi}\,\frac{G^{>\nu}_{i,i}}{\Delta z}\,, \tag{4.51}$$

where the summation runs over all the subbands contributing to transport and Δz is the average distance between rings (4.3). The factor 4 in (4.50) and (4.51) is due to double spin and double subband degeneracy (Section 2.4.2). To evaluate these integrals numerically the energy grid should be selected such that the numerical error of the calculation can be controlled. This issue is discussed in Section 4.8.

4.7.2 Current

By expanding the GREEN's function in terms of the basis functions the continuity equation (3.87) can be derived as

$$\underbrace{-\frac{i\hbar\mathrm{q}}{\Delta z}\lim_{t_2\to t_1}\Big(\partial_{t_1}G^{<}_{i,i}(t_1,t_2) + \partial_{t_2}G^{<}_{i,i}(t_1,t_2)\Big)}_{\partial_t\varrho} + \underbrace{\frac{J_{i+1/2}(t_1) - J_{i-1/2}(t_1)}{\Delta z}}_{\nabla\cdot\mathbf{J}} = 0\,, \tag{4.52}$$

where $J_{i+1/2}$ represents the current passing through a point between $i+1$ and i. Note that J has a unit of A rather than A/m^2 due to the one-dimensional nature of CNTs. The time derivative of the GREEN's functions can be replaced by the relation (3.62)

$$\begin{aligned}\partial_t\varrho_i &= -\frac{\mathrm{q}}{\Delta z}\sum_j\Big\{[H_{i,j}G^{<}_{j,i}(t,t) - G^{<}_{i,j}(t,t)H_{j,i}]\\ &\quad + \int dt'\,[\Sigma^{\mathrm{r}}_{i,j}(t,t')\,G^{<}_{j,i}(t',t) + \Sigma^{<}_{i,j}(t,t')\,G^{\mathrm{a}}_{j,i}(t',t)\\ &\quad + G^{\mathrm{r}}_{i,j}(t,t')\,\Sigma^{<}_{j,i}(t',t) + G^{<}_{i,j}(t,t')\,\Sigma^{\mathrm{a}}_{j,i}(t',t)\,]\Big\}\,,\\ &= -\frac{J_{i+1/2}(t) - J_{i-1/2}(t)}{\Delta z}\,,\end{aligned} \tag{4.53}$$

where the term inside the integral is zero due to the condition stated in (3.90).

The next step is separating $J_{i+1/2}$ from $J_{i-1/2}$ by decomposing equation (4.52). Caroli proposed the following ansatz in [96]. The current J is the difference between the flow of particles from left to right and from right to left. This leads to the following expression for J_i [96]

$$J_{i+1/2}(t) \;=\; -\mathrm{q} \sum_{j\geq i+1} \sum_{k\leq i} \Big(H_{j,k} G^{<}_{k,j}(t,t) \;-\; G^{<}_{j,k}(t,t) H_{k,j} \Big) \;. \tag{4.54}$$

It is straightforward to show that (4.54) along with an expression for J_{i-1} satisfies (4.53).

Under steady-state condition one can transform the time difference coordinate to energy to obtain

$$\begin{aligned} J_{i+1/2} \;&=\; -\frac{\mathrm{q}}{\hbar} \sum_{j\geq n+1} \sum_{k\leq n} \int \frac{dE}{2\pi} \Big(H_{j,k} G^{<}_{k,j}(E) \;-\; G^{<}_{j,k}(E) H_{k,j} \Big) \;, \\ &=\; -\frac{\mathrm{q}}{\hbar} \sum_{j\geq n+1} \sum_{k\leq n} \int \frac{dE}{2\pi} \; 2\, \Re\mathrm{e}[H_{j,k} G^{<}_{k,j}(E)] \;, \end{aligned} \tag{4.55}$$

Based on the nearest neighbor tight-binding method in mode-space (see Section 4.4) equation (4.55) can be simplified to

$$J^{\nu}_{i+1/2} \;=\; \frac{4\mathrm{q}}{\hbar} \sum_{\nu} \int \frac{dE}{2\pi} \; 2\, \Re\mathrm{e}[t^{\nu}_{i+1,i} G^{<\nu}_{i,i+1}] \;\;, \tag{4.56}$$

where the summation runs over all the subbands contributing to transport. The factor 4 in (4.56) is due to double spin and double subband degeneracy.

4.7.3 Discussion

The carrier concentration is related to the diagonal elements of the Green's function. The calculation of the current requires only the nearest off-diagonal elements of the Green's function. Furthermore, the HAMILTONian matrix is tridiagonal. Considering these factors one can employ an efficient method, such as the recursive Green's method, to calculate only the required elements of the Green's functions.

The recursive method has been proposed in [8, 116]. A brief description of the method is presented in Appendix H. The operations required to solve for all elements of $\underline{G}^{\mathrm{r}}$ with a size of $N \times N$ scales as N^3. However, the required operations for the recursive method scales linearly with N [8].

4.8 Selection of the Energy Grid

For a numerical solution of the transport equations one has to discretize the GREEN's functions in the energy domain. However, due to the presence of narrow resonances at some energies one has to be careful about the selection of the energy grid. An approximation for the electron concentration due to a confined state is derived. This analytical function is used as a reference for comparing the results of the non-adaptive and adaptive methods of selecting the energy grid.

4.8.1 Confined States

The non-interacting GREEN's functions for electrons are given by (D.6). For a bound state with the well-defined energy E_0 the GREEN's function is given by $G_0^\mathrm{r}(E) = [E - E_0 + i\eta]^{-1}$, where $\eta = 0^+$ is a small positive number. The renormalized retarded GREEN's function in the presence of interaction is given by the DYSON equation

$$\begin{aligned} G^\mathrm{r}(E) &= \frac{1}{[G_0^\mathrm{r}(E)]^{-1} \; - \; \Sigma^\mathrm{r}(E)} \\ &= \frac{1}{E \; - \; E_0 \; - \; \Sigma^\mathrm{r}(E)} \; , \end{aligned} \tag{4.57}$$

The self-energy has imaginary and real parts

$$\Sigma^\mathrm{r} \; = \; \Delta \; + \; i\Gamma/2 \; . \tag{4.58}$$

The imaginary part is interpreted as damping of the particle motion. It is related to the finite life-time of the state. The real part causes an energy shift, which may also change the effective mass or group velocity. Under equilibrium condition the lesser GREEN's function is given by (see (D.10))

$$\begin{aligned} G^<(E) &= i n_\mathrm{F} A(E) \\ &= i n_\mathrm{F} \times -2\Im\mathrm{m}[G_0^\mathrm{r}(E)] \\ &= i n_\mathrm{F} \; \frac{\Gamma}{(E - E_0 + \Delta)^2 + (\Gamma/2)^2} \; . \end{aligned} \tag{4.59}$$

The lesser GREEN's function is of LORENTZian shape [60]. The peak of the resonance is shifted by Δ and is broadened by Γ, as shown in the inset of Fig. 4.10. In open systems, localized states broaden due to the coupling to contacts ($\Gamma > 0$), even in the absence of scattering processes.

The electron concentration for each of the confined states can be calculated as

$$n \; = \int\limits_{E_\mathrm{min}}^{E\mathrm{max}} \frac{dE}{2\pi} \; n_\mathrm{F} \frac{\Gamma}{(E - E_0 + \Delta)^2 + (\Gamma/2)^2} \; . \tag{4.60}$$

We assume that the FERMI level is far above the resonance, $E_F \gg E_0 - \Delta$, so that the FERMI factor can be replaced by 1. Equation (4.60) is used as a reference function for comparing the results of different numerical integration methods.

4.8.2 Non-adaptive Energy Grid

One can straightforwardly divide the integration domain into N_{E} equidistant intervals $\Delta E = (E_{\max} - E_{\min})/N_{\mathrm{E}}$. A disadvantage of this method is that the numerical error can not be predefined. This problem is more pronounced when the integrand is not smooth. To evaluate (4.60) numerically a trapezoidal rule and an equidistant grid spacing are used. The dependence of the accuracy on the following two parameters is studied, namely the grid spacing, ΔE, and the relative distance between the peak and the nearest grid point, δE. These parameters are normalized as $\alpha = \Delta E/\Gamma$ and $\beta = \delta E/\Gamma$. The relative error in calculating the carrier concentration, $(n - \tilde{n}(\alpha))/n$, as a function of grid spacing is shown in Fig. 4.10. Here, n is the analytically exact value of the carrier concentration (4.60) and $\tilde{n}$ refers to the numerically calculated carrier concentration as a function of α and β.

The variation of the calculated carrier concentration $(\tilde{n}(0) - \tilde{n}(\beta))/\tilde{n}(0)$ with respect to the shift of energy points is shown in Fig. 4.11. The reference $\beta = 0$ implies that one of the grid points aligns with the peak of the resonance. The oscillatory behavior depends on the grid spacing. A shift equal to the grid spacing gives the same result. As a measure of the sensitivity of the calculated carrier concentration with respect to grid positions $\partial\tilde{n}/\tilde{n}\partial\beta$ is shown in Fig. 4.12. To reduce this sensitivity, a very fine grid spacing has to be adopted. This quantity is characteristic of the numerical error, and needs to be controlled to avoid convergence problem in the self-consistent iteration loop (see Section 4.9.2).

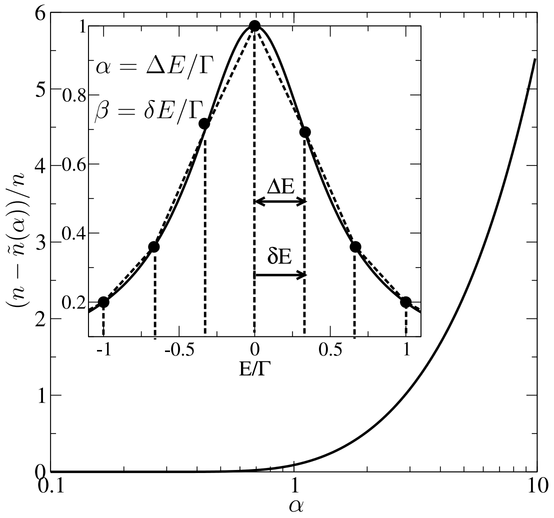

Figure 4.10: The relative error in evaluating the carrier concentration, $(n - \tilde{n}(\alpha))/n$, with respect to the grid spacing is shown. The inset shows the normalized LORENTZian shape of the density of states of a bound state. The peak of the resonance is shifted to the zero point. At E $= \pm\Gamma/2$ the function is half of its maximum. The solid line shows the exact function and the dashed curve shows the approximation of the function based on the Trapezoidal rule. The grid spacing is ΔE and the shift of energy grids from the reference point is δE. These parameters are normalized as $\alpha = \Delta E/\Gamma$ and $\beta = \delta E/\Gamma$. The reference $\beta = 0$ implies that the one of the grid points aligns with the peak of the resonance. The parameters in this figure are $\alpha = 1/3$ and $\beta = 0$.

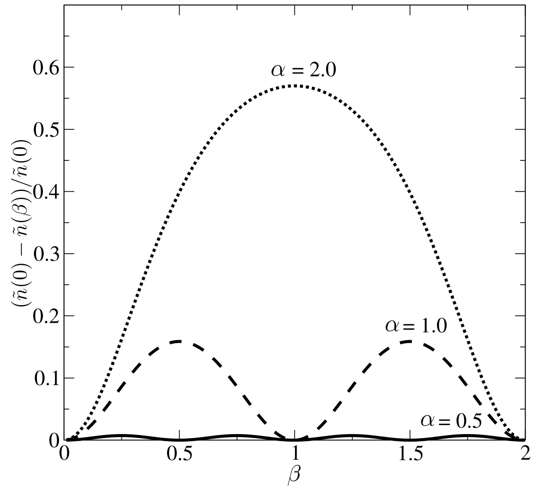

Figure 4.11: The relative variation of the calculated carrier concentration $(\tilde{n}(0) - \tilde{n}(\beta))/\tilde{n}(0)$ with respect to the normalized position β of energy grid points.

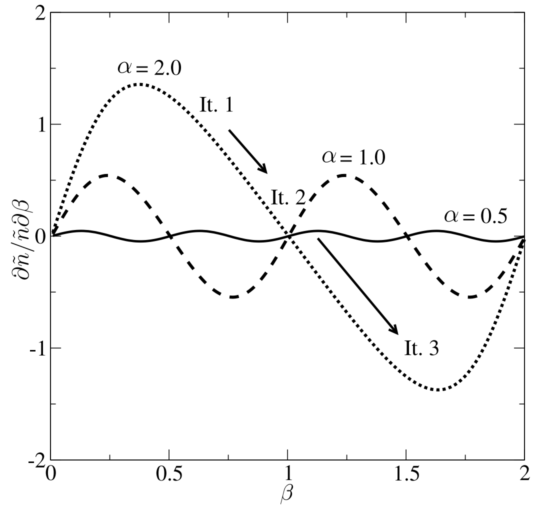

Figure 4.12: The relative sensitivity of the calculated carrier concentration $\partial\tilde{n}/\tilde{n}\partial\beta$ with respect to the position of energy grid points. This term originates from the numerical error in the evaluation of the carrier concentration. For coarse grid spacing $\alpha > 1$, this quantity increases considerably.

In summary, the accuracy of the non-adaptive method strongly depends on the grid spacing and the position of grid points. If the grid spacing is sufficiently fine, $\alpha < 1$, the numerical error is small, but it increases considerably for coarser grid spacing, $\alpha > 1$. For accurate results a grid spacing smaller than Γ has to be employed. For example, to resolve a resonance of $\Gamma \approx 1$ μeV width in an energy range of 1 eV more than 10^6 energy grid points are required, which would severely increase the computational cost. For even narrower resonances, (eg. $\Gamma \approx 1$ neV), an equidistant grid is no longer feasible. To avoid these problems an adaptive method needs to be employed.

4.8.3 Adaptive Energy Grid

There is a variety of methods available for numerical adaptive integration [247]. Adaptive strategies divide the integration interval into sub-intervals and, typically, employ a progressive formula in each sub-interval with some fixed upper limit on the number of points. If the required accuracy is not achieved by the progressive formula, the sub-interval is bisected and a similar procedure carried out on each half. This sub-division process is carried out recursively until the desired accuracy is achieved. An obvious way to obtain an error estimate is based on the comparison between two quadrature approximations [248]. However, due to the dependence of such procedures on the underlying integration formulae, this method may not be reliable [249]. Error estimation with sequences of *null rules* has been proposed as a simple solution [250]. In adaptive quadrature algorithms the error estimate governs the decision on whether to accept the current approximation and terminate or to continue. Therefore, both the efficiency and the reliability depend on the error estimation algorithm. The decision to further subdivide a region may be based on either *local* or *global* information. Local information refers only to the region being currently processed, while global information refers obviously to data concerning all regions. Integration programs based on global subdivision strategies are more efficient and reliable [251].

In this work a global error estimator based on the null rules method has been employed [249]. The efficiency of this method is studied for the LORENTZian function (4.60). Figure 4.13-a shows the number of required energy grid points for an interval $[-1, 1]$ eV versus the relative error ϵ of the integration. The required number of energy grid points versus the width of the resonance, Γ, is shown Fig. 4.13-b. To resolve a very narrow resonance ($\Gamma \approx 10^{-9}$ eV) with a very high accuracy ($\epsilon = 10^{-6}$) only a few hundred grid points ($N_\mathrm{E} \approx 500$) are required.

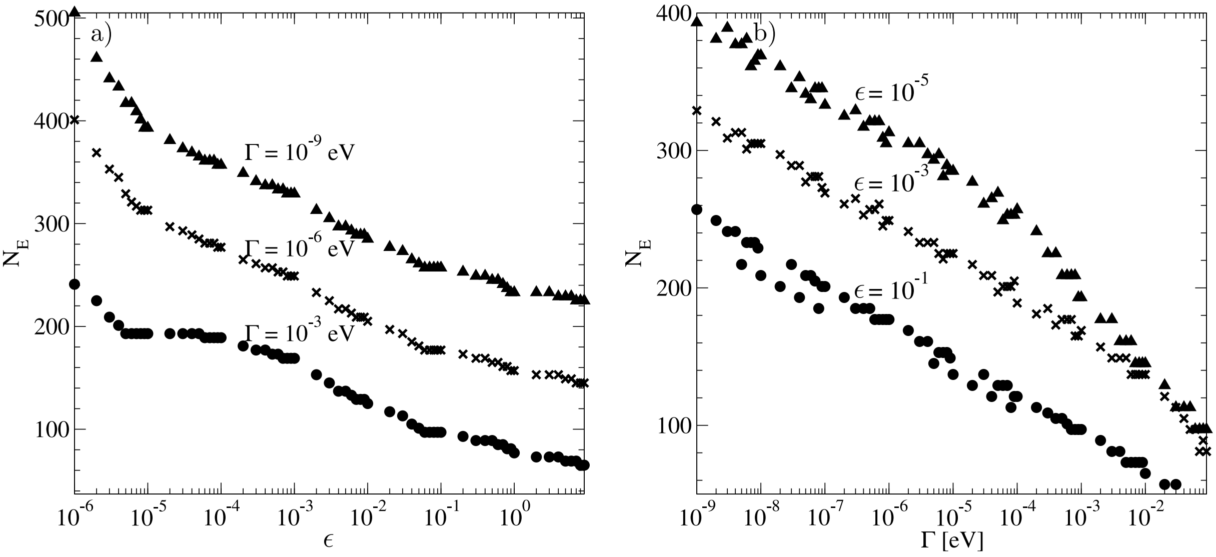

Figure 4.13: a) shows the number of required energy grid points versus the maximum desired relative error, ϵ, in the adaptive integration method. b) shows the number of required energy grid points versus the width of the resonance, Γ. The LORENTZian function (4.60) is used as a reference.

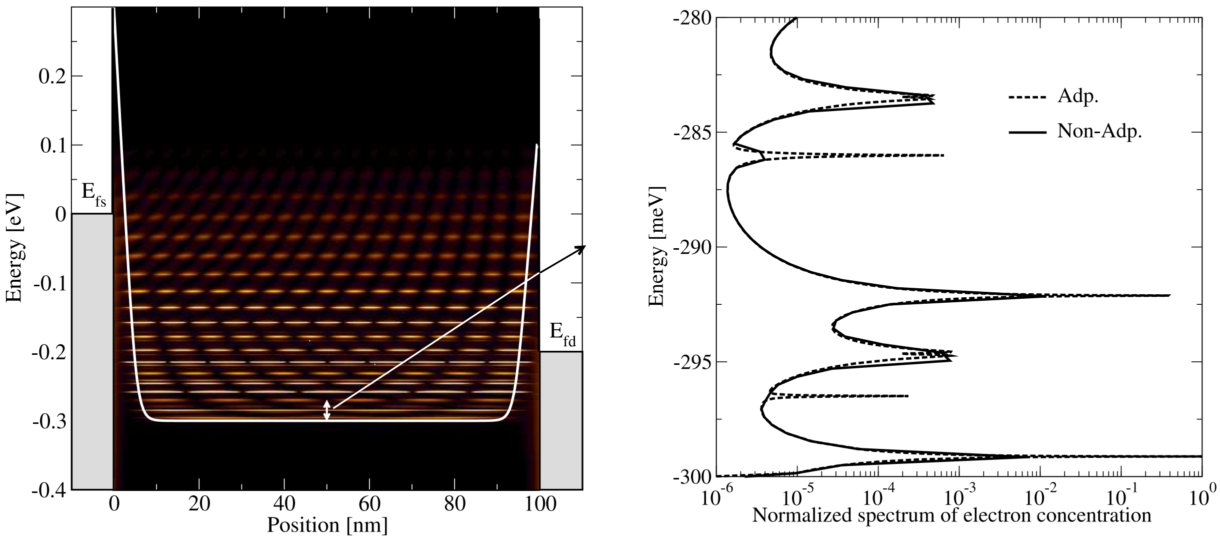

Figure 4.14: The left figure shows the normalized spectrum of the carrier concentration in a Schottky type CNT-FET. The right figure shows the spectrum of the carrier concentration in the middle of the device for the energy range shown by the arrow. The results achieved from the adaptive and non-adaptive method are compared. With the aid of the adaptive method narrow and close resonances are resolved with a total number of $N_{\mathrm{E}} \approx 1000$ energy grid points, whereas the non-adaptive method misses some resonances with the same number of energy grid points.

Figure 4.14 shows the normalized spectrum of the carrier concentration in a Schottky type CNT-FET (see Section 2.8.2). The length of the device is 50 nm. Energy barriers at the metal-CNT interfaces cause longitudinal confinement in the tube. Since the device is quite long, the spacing between confined states is very small. In CNTs the electron-phonon interaction is rather weak and the confining SCHOTTKY barriers are thick, such that resonances are only weakly broadened, (see Chapter 5). Due to phonon absorption and emission processes there will be more resonances compared to the ballistic case. In this case, if a non-adaptive method is employed the numerical error in the calculation of the carrier concentration can be large. The right part of Fig. 4.14 compares the results achieved from the adaptive and non-adaptive methods. The relative error in the electron density of the non-adaptive method reaches up to 53% in the middle of the device.

In [252] the resonant states have been determined by an eigenvalue solver for finding the roots of the characteristic equation. However, this method has several drawbacks. Due to the non-linearity introduced by the self-energies, a non-linear eigenvalue solver has to be employed. Usually non-linear solvers are based on NEWTON's method. Using a non-linear solver for each iteration can increase the simulation time severely and introduce additional convergence problems. For example, most solvers fail to find narrow resonances located closely to each other. The output of the solver is the energy position and the width of the resonance, but not any information about the shape of the resonance. In general the shape of resonances deviates from the ideal LORENTZian shape. The grid has to be allocated based on an initial guess. This implies that the accuracy of the calculated carrier concentration can not be predefined and strongly depends on the how close the initial guess is to the actual solution. With the adaptive method the discussed problems do not occur.

4.9 Self-Consistent Simulations

For an accurate analysis it is essential to solve the coupled system of transport and Poisson equations self-consistently [163]. The iterative method for solving this coupled system is presented. Thereafter, the convergence behavior of the self-consistent iteration is studied.

4.9.1 Self-Consistent Iteration Scheme

Figure 4.15 depicts the block diagram of the iterative procedure employed to solve the coupled system of transport and Poisson equations. All the procedures are discussed in the following.

We solve the kinetic equations in mode-space, (4.25) and (4.26), to obtain the Green's functions. The required elements for calculating the Green's functions are the Hamiltonian, and the electron-phonon and contact self-energies. As discussed in Section 4.4, diagonal elements of the Hamiltonian are potential energies, which can be obtained from the solution of the Poisson equation, and off-diagonal elements represent the coupling between adjacent rings of carbon atoms in the CNT. Given the contact properties and the contact-device coupling parameters, the contact self-energy $\underline{\Sigma}_C^{\mathrm{r}^\nu}$ can be calculated once at the start of the simulation (see Section 4.5).

The calculation of the electron-phonon self-energy is presented in Section 4.6. Within the self-consistent Born approximation of the electron-phonon self-energy (Section 3.6), the non-interacting Green's function G_0 is replaced by the full Green's function G. However, the full Green's is the not known and has to be calculated. As a result, a coupled system of equations is achieved which can be solved by iteration

$$\underline{G}^{\mathrm{r}^{\nu\langle m\rangle}} \;=\; [E\underline{I} - \underline{H}^{\nu} - \underline{\Sigma}_{\mathrm{e-ph}}^{\mathrm{r}^{\nu\langle m-1\rangle}} - \underline{\Sigma}_{C}^{\mathrm{r}^{\nu}}] \;, \tag{4.61}$$

where m denotes the iteration number. For the first step the electron-phonon self-energy is assumed to be zero and the Green's function is calculated from the kinetic equation. The next iteration starts with the calculation of the electron-phonon self-energy based on the Green's function from the previous iteration. The updated electron-phonon self-energy is then used for the calculation of the Green's function. This iteration continues till a convergence criterion is satisfied. The mentioned procedure should be followed for each subband (mode) and finally the total charge density is calculated.

In semi-classical simulations, the coupled system of the transport and Poisson equations is solved by Gummel's or Newton's method [226]. Both Gummel's method [253] and a variation of Newton's method [254] can be employed in self-consistent quantum mechanical simulations. While Gummel's method has a fast initial error reduction, for Newton's method it is very important that the initial guess is close to the solution. The computational cost per iteration of Newton's method can be much higher than that for Gummel's method.

We employed Gummel's method, where after convergence of the electron-phonon self-energy the Poisson equation is solved once. Based on the updated electrostatic potential, the Green's functions and the electron-phonon self-energy are iterated again. These two iterations continue until a convergence criterion is satisfied. Finally, the total current through the device is calculated.

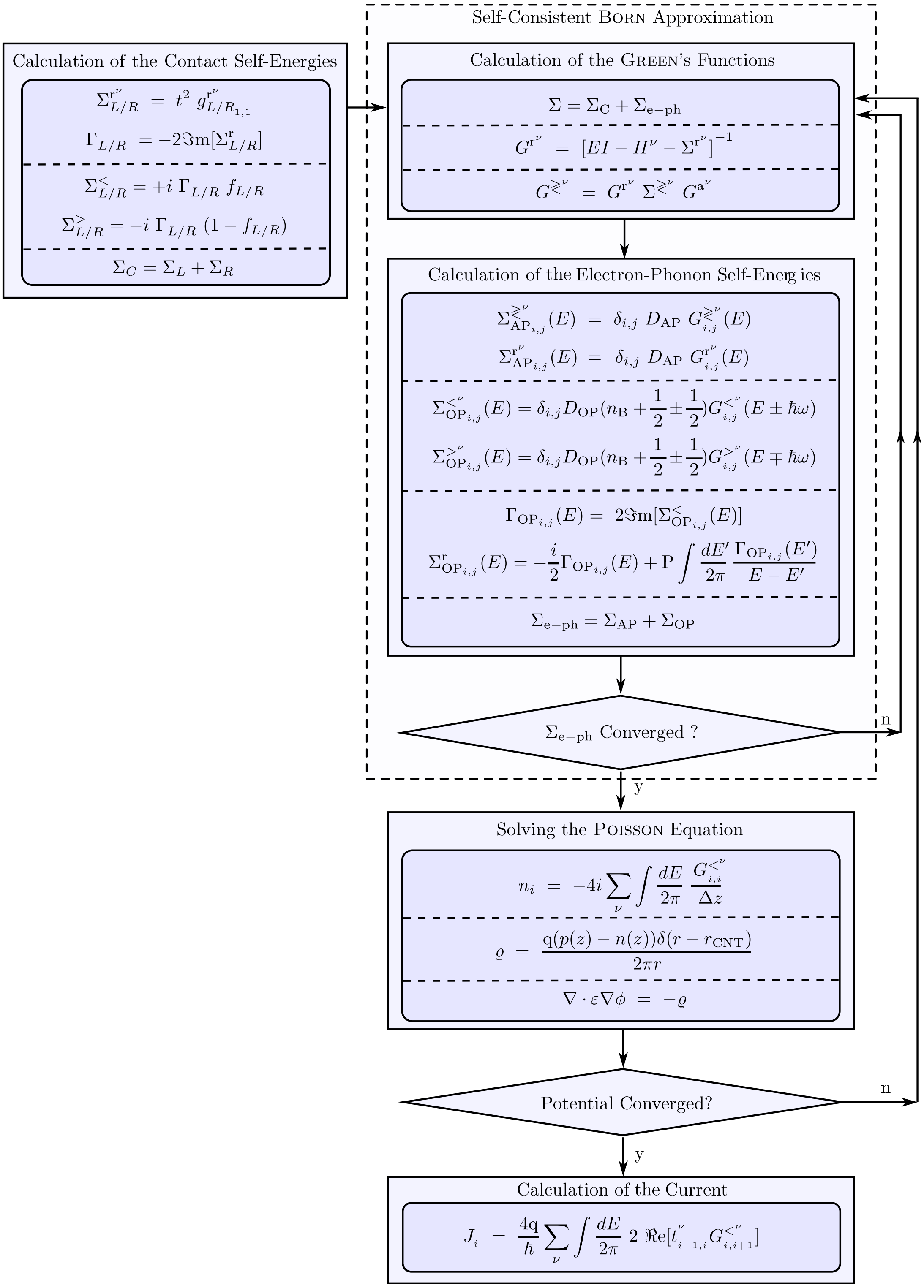

Figure 4.15: Block diagram of the iterative procedure employed to solve the coupled system of transport and POISSON equations. For the first step an initial guess for the electron-phonon self-energy is required, here we assumed $\Sigma_{\mathrm{e-ph}} = 0$.

4.9.2 Convergence of the Self-Consistant Simulations

The coupled system of transport and POISSON equation can be solved by iteration with appropriate numerical damping, which terminates if a convergence criterion is satisfied [255]. In this work, the maximum element of the potential update, corresponding to $L_\infty = |\phi^k - \phi^{k-1}|_\infty$, is considered as a measure of convergence.

One of the reasons causing convergence problems [256, 257] is the exponential dependence of the carrier concentration on the electrostatic potential, $n \propto \exp(q\phi/k_\mathrm{B}T)$. A small potential variation causes large variation in the carrier concentration

$$\frac{\partial n}{n\partial\phi} \approx \frac{\mathrm{q}}{k_\mathrm{B}T} \ . \tag{4.62}$$

As a result, a strong damping is required in many cases, which increases the simulation time. To avoid this problem a non-linear POISSON equation is generally employed [258]. Solving a non-linear POISSON equation takes that exponential dependence into account. Compared to the linear POISSON equation, it leads to faster convergence in both semi-classical [258] and quantum mechanical [257, 259] transport simulations. In this work the GUMMEL method along with a non-linear POISSON equation is employed.

However, we show that an inappropriate energy grid for the discretization of the transport equations can be another reason of convergence problems in quantum transport simulations. It is demonstrated that with adaptive energy grids the iterative solution can converge very fast and the simulation time can decrease considerably.

In Section 4.8.2 it was shown that with a shift of an equidistant grid the calculated carrier concentration can change sharply. This sensitivity resulting from the numerical error causes convergence problems in the self-consistent loop. In all non-adaptive methods some fixed energy grid is adopted. In successive iterations of the POISSON and transport equations, the electrostatic potential changes and this in turn affects the relative distance between resonance energies and the energy grid points. As a result, the evaluated carrier concentration can vary sharply in one iteration step, which affects the calculated electrostatic potential for the next iteration. For a quantitative analysis one can assume that the shift of energy grid is due to the variation of the electrostatic potential, $\mathrm{q}\partial\phi = \delta E = \Gamma\partial\beta$.

$$\frac{\partial\tilde{n}}{\tilde{n}\partial\phi} = \frac{\mathrm{q}}{\Gamma}\frac{\partial\tilde{n}}{\tilde{n}\partial\beta} \tag{4.63}$$

The sensitivity of the calculated carrier concentration with respect to energy grid shifts defined by (4.63) is shown in Fig. 4.12. For a relatively coarse grid, $\alpha \approx 2-3$, the sensitivity (4.63) can be approximated as

$$\frac{\partial\tilde{n}}{\tilde{n}\partial\phi} \approx \frac{\mathrm{q}}{\Gamma} \tag{4.64}$$

In this case the contribution of a resonance of width $\Gamma \leq \mathrm{k_B T}$ will be larger than (4.62). To reduce the effect of this term, a fine grid spacing must be used ($\alpha \leq 1$). The non-adaptive method requires many grid points to resolve fine resonances, while the adaptive method puts many energy grid points only close to resonances and few ones off the resonance. Therefore, the adaptive method keeps the total number of grid points quite low and maintains a high accuracy.

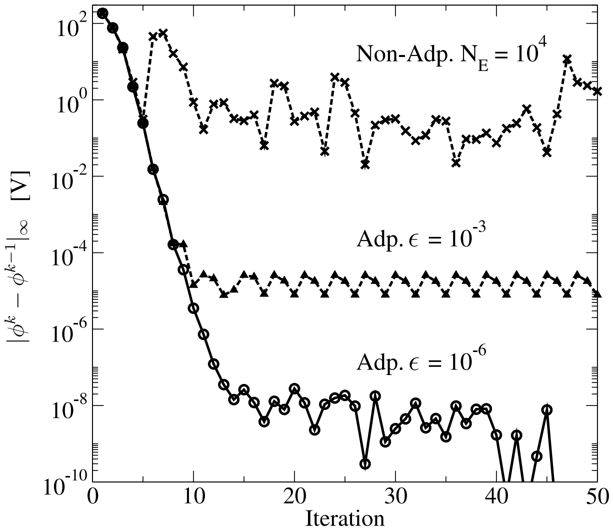

Figure 4.16: The infinity norm of the potential update after each iteration.

The convergence of the self-consistent loop using the adaptive and non-adaptive methods is studied. With the non-adaptive method 10^4 energy grid points are used. For the adaptive method, relative errors of $\epsilon = 10^{-3}$ and $\epsilon = 10^{-6}$ are assumed. Fig. 4.16 shows the infinity norm of the potential update after each iteration. With the adaptive method the norm of the potential update decreases exponentially and finally reaches a limit which depends on the error tolerance of the integration. With the non-adaptive method the norm of the potential update oscillates and no convergence is achieved. Fig. 4.17 shows the calculated carrier concentration due to several confined states, based on four successive iterations of the non-adaptive method. From the first to the second iteration the carrier concentration changes very sharply. Therefore, at the first iteration one is close to the highly sensitive region (see Fig. 4.12). From the second to the third iteration the carrier concentration changes only little, which can be mapped to the low sensitive region. From the third to the forth iteration the variation is large, which implies that we are again close to the highly sensitive region. This sequence continues and prevents convergence. To avoid this problem a fine grid spacing can be used, which decreases the sensitivity in all regions. As it was shown in Fig. 4.10 the non-adaptive method requires a grid spacing smaller than Γ for accurate result.

By reducing $\epsilon = 10^{-3}$ to $\epsilon = 10^{-6}$ in the adaptive method the self-consistent iteration yields more accurate results, but the number of required energy grid points increases, which increases the simulation time of each iteration. Fig. 4.18 shows the infinity norm of the potential update versus CPU-time. A suitable criterion for the termination of the self-consistent loop was found as $\mathrm{q}|\phi^k - \phi^{k-1}|_\infty < \mathrm{k_B T}/10$. If the maximum potential update in the device is much smaller than $\mathrm{k_B T}$, the carrier concentration will change only weakly during the next iteration. For most of the simulations performed such a criterion was satisfied for $\epsilon \approx 10^{-3}$.

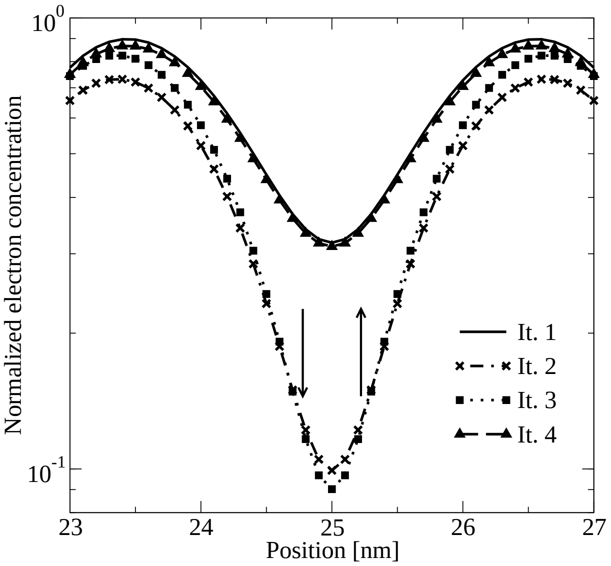

Figure 4.17: Explanation of the oscillation in the calculated carrier concentration in successive self-consistent iterations. The results are for a non-adaptive method with 10^4 grid points. The sensitivity of the calculations for each of these iterations is shown in Fig. 4.12. The first and the third iterations are in a high sensitive region, while the second and the forth iterations are in a low sensitive region.

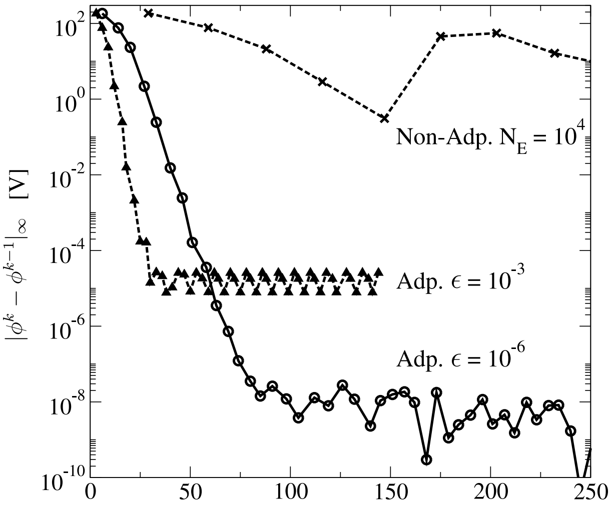

Figure 4.18: The infinity norm of the potential update versus CPU-time. Simulations based on the adaptive method converge fast and the minimum achievable norm of the potential update depends on the accuracy of the integration. The non-adaptive method does not convergence.

Chapter 5

Applications

FAST SWITCHING and high $I_{\mathrm{on}}/I_{\mathrm{off}}$ current ratio are the most important characteristics required for future nano-electronic applications. Based on the quantum transport model outlined in Chapter 4 both the static and dynamic response of CNT-FETs are investigated. Based on the result we propose methods to improve the functionality and performance of such devices.

In the first section the ambipolar conduction of CNT-FETs, which results in performance limitation, is studied in detail. We propose a double-gate structure to suppress this behavior. Simulation results indicate that a considerable improvement of device characteristics can be achieved by employing this structure. In this device type carrier injection at the source and drain contacts are controlled separately.

However, since the fabrication of single-gate devices is more feasible than their double-gate counterpart, we focus on such devices in the next section. Scaling of the gate-insulator thickness and the effect of relative permittivity of the gate-insulator on the performance of single-gate CNT-FETs have been studied in the literature [5, 260, 261].

We analyze scaling of the gate-source and gate-drain spacer length of single-gate CNT-FETs, which has not yet been studied in the literature. By increasing the gate-drain spacer length the ambipolar conduction decreases and the $I_{\mathrm{on}}/I_{\mathrm{off}}$ ratio increases. Furthermore, the parasitic capacitances are reduced which results in reduced switching time. By increasing the gate-source spacer length both the on-current and parasitic capacitances decrease. We show that by optimizing this spacer length the performance of the device can be significantly enhanced. The results indicate that these effects can be very different from that in conventional MOSFETs.

Next we study a new device type, the gate controlled tunneling CNT-FET. The effect of the source and drain doping on the performance of these devices is investigated. We show that by using an asymmetric doping the $I_{\mathrm{on}}/I_{\mathrm{off}}$ ratio increases.

Finally, the effect of electron-phonon interactions on the device characteristics is discussed in detail. In agreement with experimental data, our results indicate that electron phonon interactions can affect the DC current of CNT-FETs only weakly whereas the switching response of such devices can be affected significantly.

5.1 Double-Gate Design

The operation of CNT-FETs can be described in terms of carrier injection through the SCHOTTKY barrier at the metal-CNT interface (see Section 2.8.2). However, the ambipolar conduction results in performance limitation [64,261,262]. In this section the ambipolar conduction is studied in detail. Then, a double-gate design is proposed to suppress this behavior effectively. The first gate controls carrier injection at the source contact and the second one controls carrier injection at the drain contact, which can be used to suppress parasitic carrier injection. The effect of the second gate voltage on the performance of the device has been investigated. Our results indicate that by applying a proper voltage range to the second gate improved device characteristics can be achieved.

5.1.1 Ambipolar Conduction

A single-gate CNT-FET with symmetric gate-source and gate-drain spacer lengths is shown in Fig. 5.1. It is assumed that the SCHOTTKY barrier heights for electrons and holes are equal. The output and transfer characteristics of this device for different biases are shown in Fig. 5.2 and Fig. 5.3, respectively. To obtain a better insight into the device operation the band-edge profiles along the device are also shown.

Fig. 5.2 and Fig. 5.3 show that electron current through the source-sided barrier is both tunneling and thermionic emission. However, there is a parasitic current due to the thermionic emission of holes across the drain sided barrier. If the drain voltage becomes higher than the gate voltage, the thickness of the drain-sided SCHOTTKY barrier for holes is reduced. As a result, the parasitic band-to-band tunneling current of holes increases and ambipolar conduction occurs.

The current contributions of electrons and holes are represented by blue and red curves, respectively. Note that at transition points electrons and holes have the same contribution to the total current, whereas in other regions either the electron or hole contribution will dominate. The results indicate that the ambipolar conduction has a detrimental effect on the device operation in both the on- and off-state.

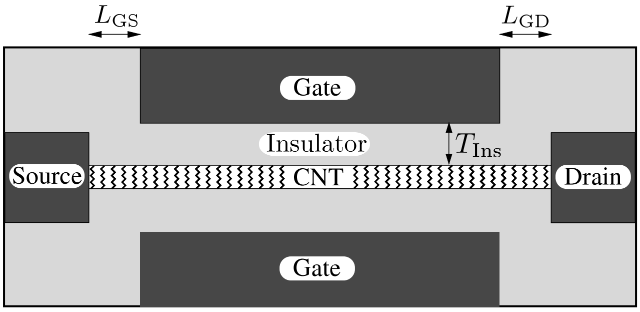

Figure 5.1: Sketch of the single-gate (SG) structure. $T_{\mathrm{Ins}} = 10$ nm and $L_{\mathrm{GS}} = L_{\mathrm{GD}} = 4$ nm.

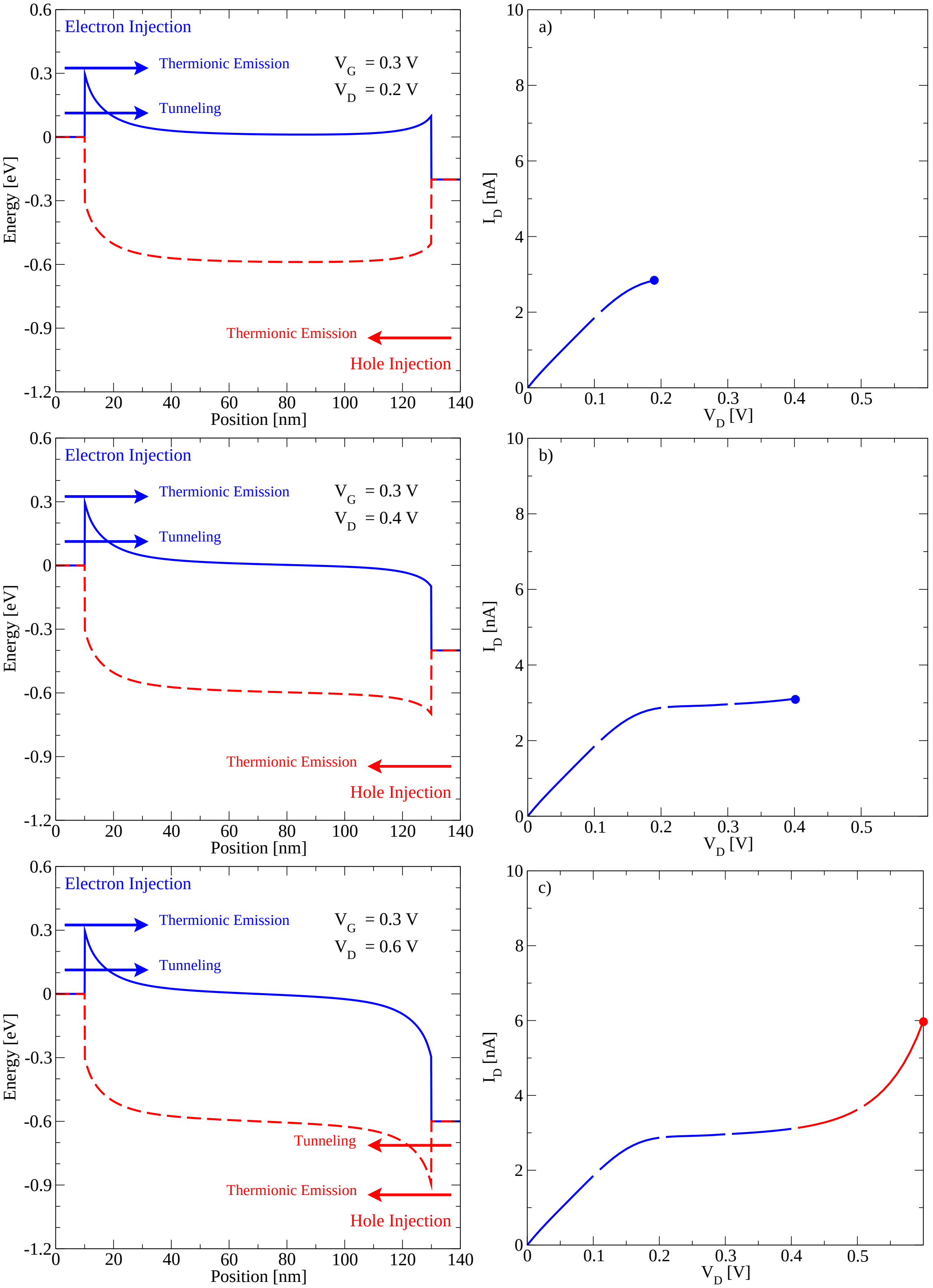

Figure 5.2: Right figures show the output characteristics and left ones the corresponding band-edge profile. a) $V_\mathrm{D} = 0.2$ V, b) $V_\mathrm{D} = 0.4$ V, and c) $V_\mathrm{D} = 0.6$ V.

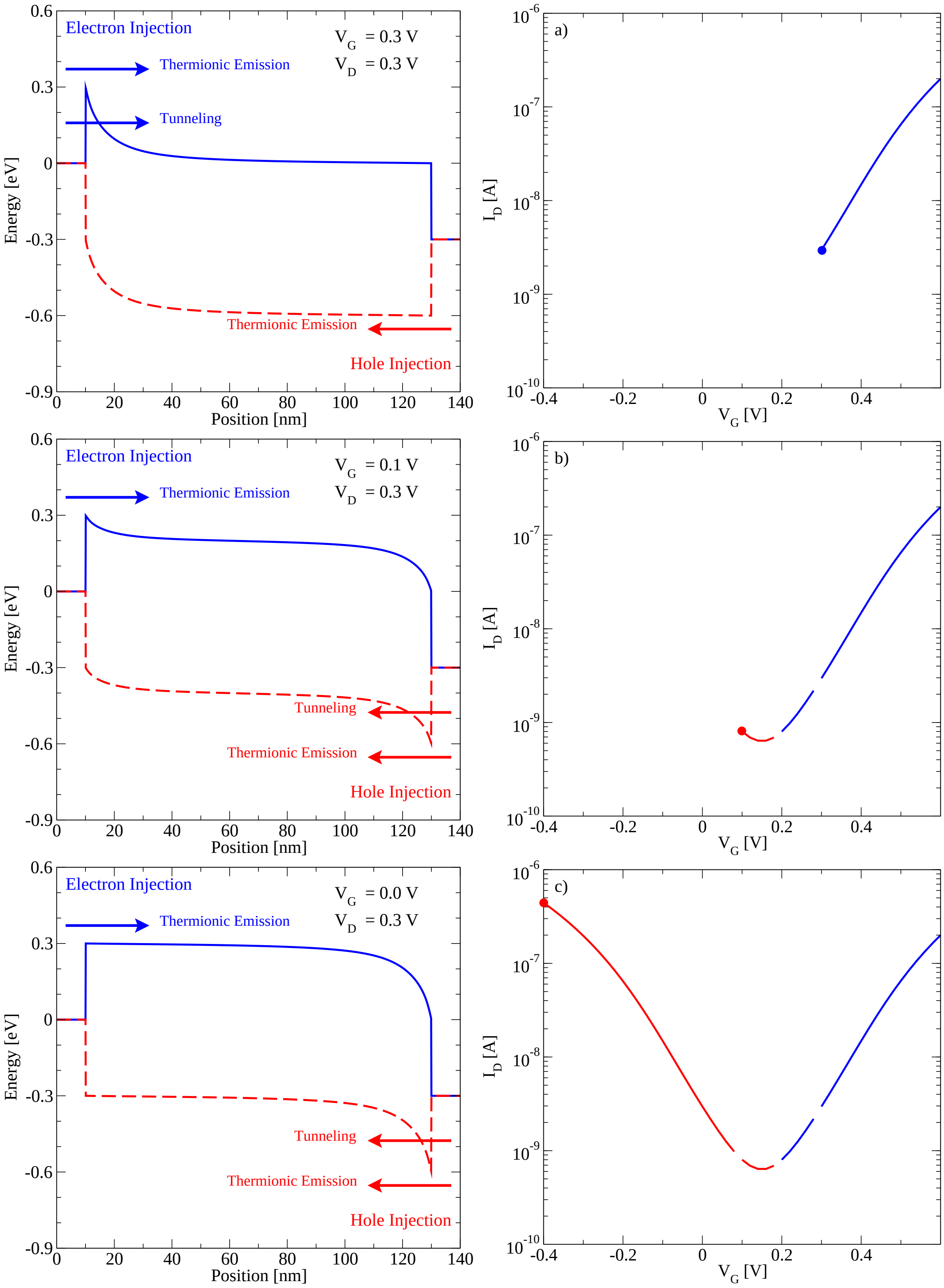

Figure 5.3: Right figures show the transfer characteristics and left ones the corresponding band-edge profile. a) $V_{\mathrm{G}} = 0.3$ V, b) $V_{\mathrm{G}} = 0.1$ V, and c) $V_{\mathrm{G}} = 0.0$ V.

5.1.2 Double-Gate CNT-FET

To suppress the ambipolar behavior of CNT-FETs and improve the performance of these devices, we propose a double-gate structure as shown in Fig. 5.4. The first gate controls the carrier injection at the source contact, which determines the on-current, and the second one controls the carrier injection at the drain contact, which determines the off-current.

If the drain voltage is applied to the second gate, at any drain voltage the band edge profile near the drain will be nearly flat, as shown in Fig. 5.5-b. In consequence the parasitic tunneling current of holes is suppressed and the parasitic current is limited to thermionic emission of holes over the drain-sided SCHOTTKY barrier.

By applying a voltage higher than the maximum drain voltage to the second gate, thermionic emission of holes over the drain-sided barrier decreases exponentially and consequently a lower off-current is achieved (Fig. 5.5). It should be noted that if the drain voltage reaches a value higher than the second gate voltage, parasitic hole current will increase again.

The output characteristics of the double-gate structure is shown in Fig. 5.6-a. If the second gate is biased at the drain voltage, the drain current will not increase until the drain voltage reaches the first gate voltage. The reason for this behavior is that carriers in the channel see a thick barrier near the drain contact until the drain voltage reaches a value higher than the first gate voltage (see Fig. 5.6-b). If the second gate is biased at a voltage higher than the maximum drain voltage, carries in the channel face a thin barrier even at low drain voltages while the holes barrier at the drain contact is thick.

It is of advantage to apply the drain voltage to the second gate, because parasitic capacitances between the second gate and the drain are avoided, no separate voltage source for the second gate is needed, and the fabrication is more feasible. The off-current is determined by the thermionic emission current over the SCHOTTKY barrier. The drain current, however, is small until the drain voltage reaches a value higher than the first gate voltage. By applying a voltage higher than the maximum drain voltage to the second gate, a high $I_{\text{on}}/I_{\text{off}}$ ratio can be obtained.

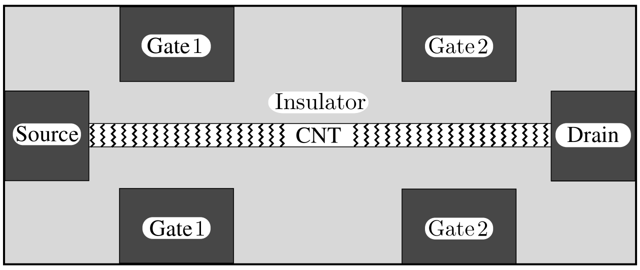

Figure 5.4: Sketch of the double-gate (DG) structure.

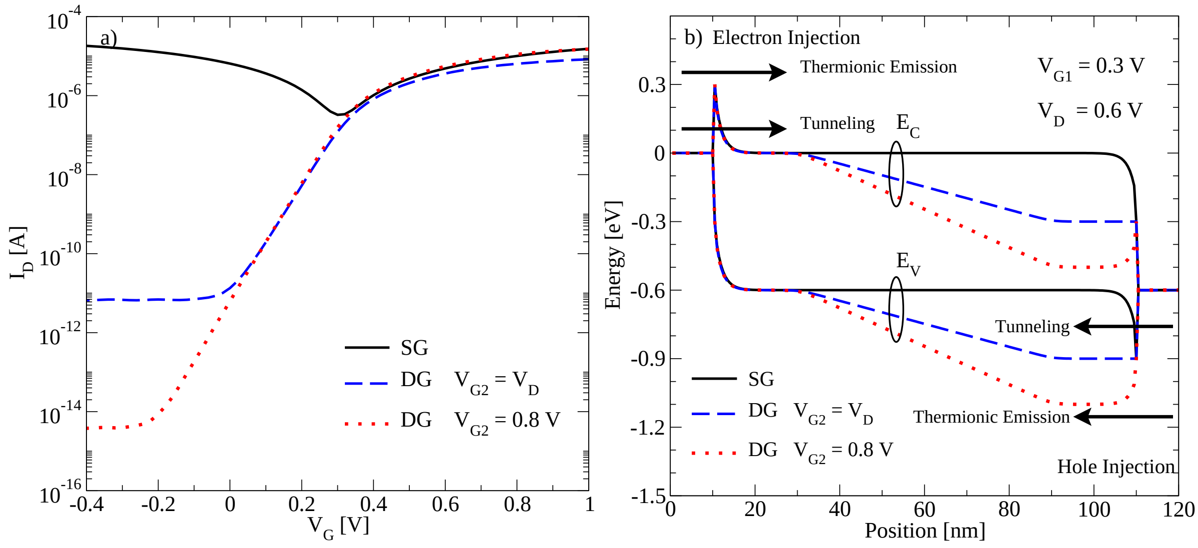

Figure 5.5: a) Comparison of the transfer characteristics of the single-gate (SG) and double-gate (DG) structure at $V_D = 0.6$ V. Two different biases are assumed for the second gate. b) Comparison of the band edges profile, along the SG and DG structure. $T_{\text{Ins}} = 4$ nm and $L_{\text{GS}} = L_{\text{GD}} = 2$ nm.

Regarding the separation between the two gates several parameters should be considered: By decreasing this separation, the parasitic capacitance between the gates increases which deteriorates the frequency response of the device. Also because of the narrow band gap of CNTs, at certain operating voltages the band to band tunneling current will increase by decreasing this distance, which affects the off-current.

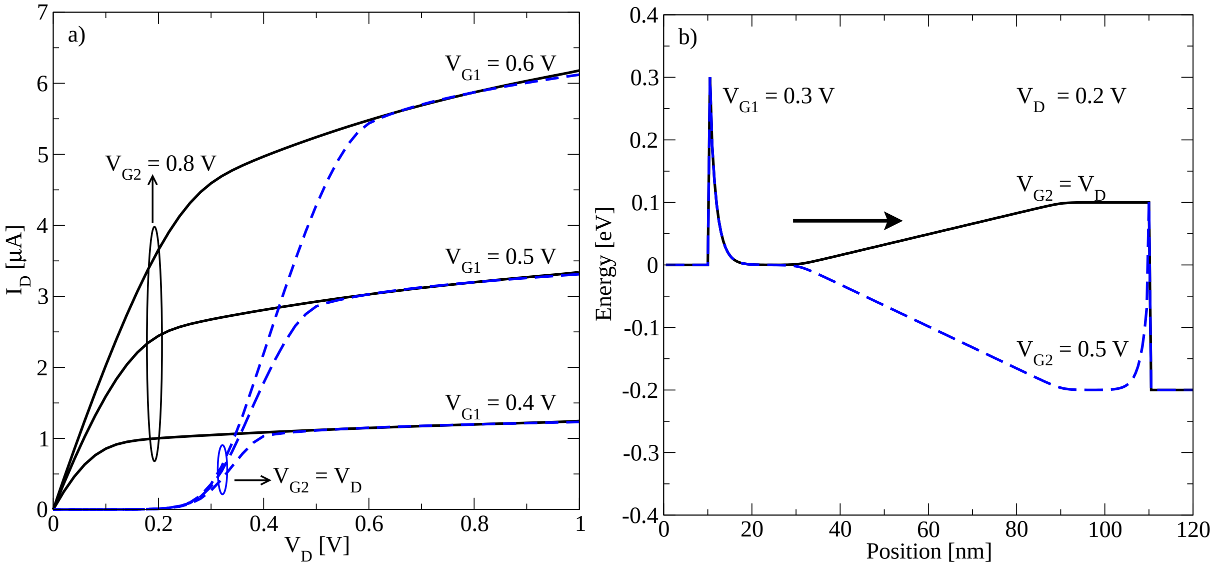

Figure 5.6: a) Output characteristics of the double-gate (DG) structure. b) Conduction band edge profile of the DG structure at low drain biases.

5.2 Asymmetric Single-Gate Design

In Section 5.1 we showed that an extra gate close to the drain-sided SCHOTTKY barrier can effectively suppress the parasitic current, which results from ambipolar conduction. However, due to some technological limitations using an extra gate may not be suitable for some applications. In this section we show that by asymmetric scaling of the gate-source and gate-drain spacer length of a single-gate device the ambipolar conduction can be reduced. Furthermore, appropriate selection of the gate-source and gate-drain spacer length results in considerable reduction of parasitic capacitances. As a result, improved device characteristics can be achieved. Results for devices with different barrier heights at the metal-CNT interface are discussed.

5.2.1 Gate-Source Spacer Length

The output and transfer characteristics for a device with zero barrier height for electrons is shown in Fig. 5.7. The increase of the gate-source spacer length results in a decrease of the on-current while the off-current is not affected. The on-current is mostly due to carrier injection through the source sided SCHOTTKY barrier whereas the off-current in CNT-FETs is mostly due to parasitic carrier injection at the drain sided SCHOTTKY barrier, (see Section 5.2.2). Therefore, the off-current is not affected by the scaling of the gate-source spacer length.

Both tunneling and thermionic emission contribute to the current. The thermionic emission current is controlled by the barrier height and is independent of the barrier width. On the other hand, the tunneling current decreases exponentially with the barrier width. Fig. 5.8 shows that by increasing the gate-source spacer length the width of the SCHOTTKY barrier at the source-sided metal-CNT interface is increased. As a result, the current is reduced.

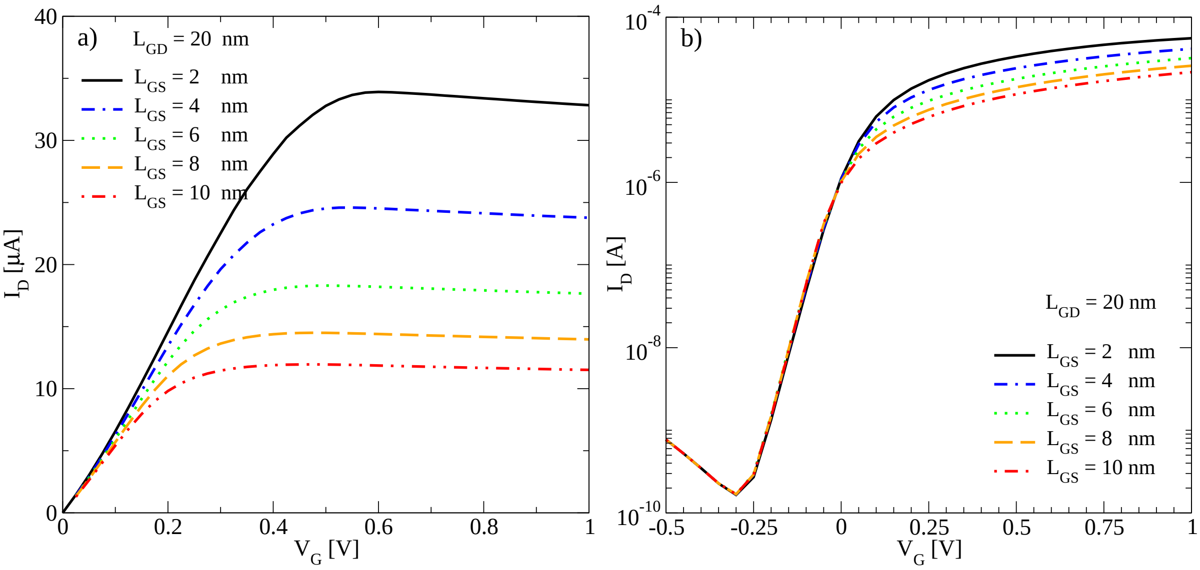

Figure 5.7: The effect of the gate-source spacer length (L_{GS}) on a) the output characteristics with $V_{\mathrm{G}} = 0.5$ V and b) the transfer characteristics with $V_{\mathrm{D}} = 0.8$ V. The results are for a device with zero barrier height for electrons ($q\Phi_{\mathrm{Be}} = 0$).

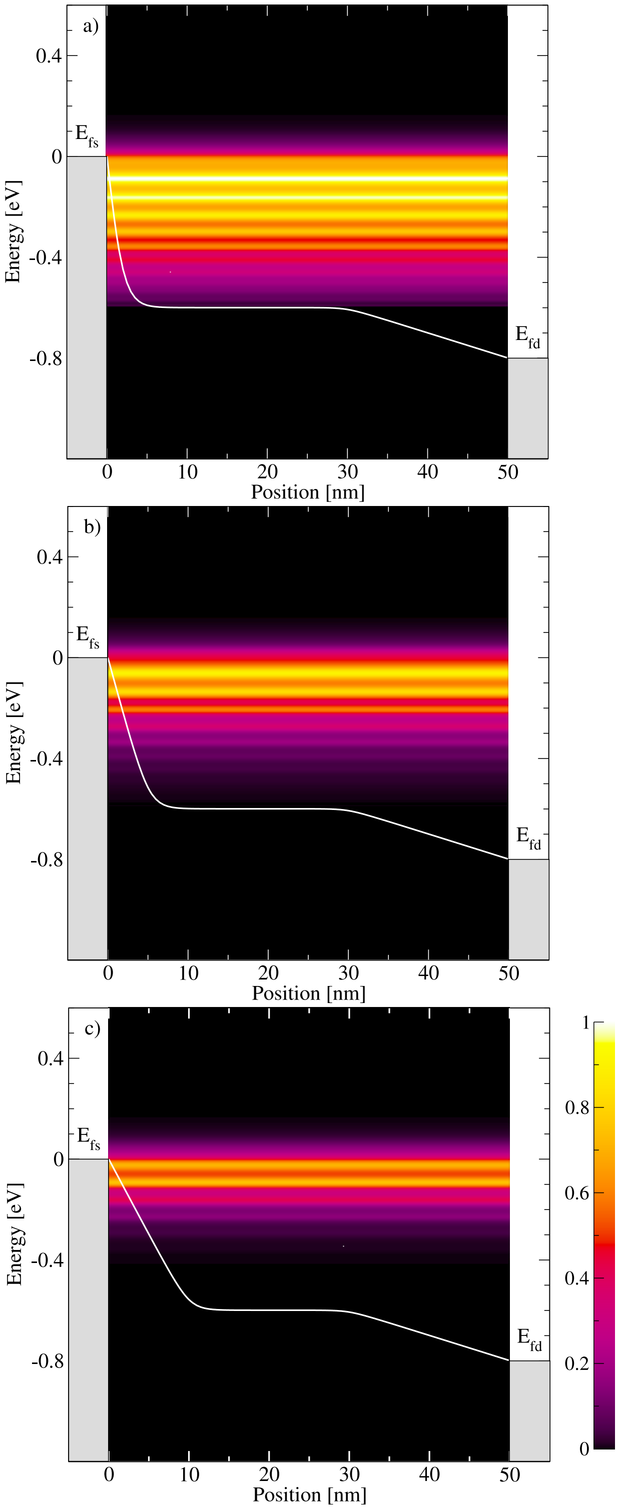

Figure 5.8: The effect of the gate-source spacer length (L_{GS}) on the current. The normalized current spectrum based on a ballistic transport model for a devices with zero barrier height for electrons is shown for a) $L_{\mathrm{GS}} = 1$ nm, b) $L_{\mathrm{GS}} = 5$ nm, and c) $L_{\mathrm{GS}} = 10$ nm. The bias point is $V_{\mathrm{G}} = 0.6$ V and $V_{\mathrm{D}} = 0.8$ V.

Figure 5.9 shows the relative variation of the on-current versus the gate-source spacer length for devices with negative, zero, and positive barrier height for electrons, assuming ballistic transport. The results indicate that scaling of the gate-source space length affects the on-current of devices with positive barrier height more effectively.

Figure 5.10 shows the current density spectrum for devices with negative, zero, and positive barrier height for electrons, assuming ballistic transport. Electrons with energies lower than the barrier height have to tunnel through the source-sided metal-CNT interface barrier to reach the channel, whereas electrons with higher energies are injected by thermionic emission. The relative contributions of thermionic and tunneling strongly depend on the barrier height and the bias point. As shown in Fig. 5.10, at high gate bias even for devices with zero or negative barrier height the tunneling current contributes considerably to the total current. However, in a device with negative barrier height the tunneling current has a smaller contribution to the total current as compared to devices with non-negative barrier height. Therefore, the current is less sensitive to the variation of the gate-source spacer length (Fig. 5.9).

In conclusion, the on-current of all device types decreases as the gate-source spacer length increases. The reduction of the on-current strongly depends on the relative contribution of the tunneling current. To improve the static response it is more appropriate to reduce the gate-source spacer length. However, the reduction of this spacer results in an increase of the gate-source parasitic capacitances which can severely affect the dynamic response of the device. For optimal performance the length of this spacer has to be carefully selected, see Section 5.3.

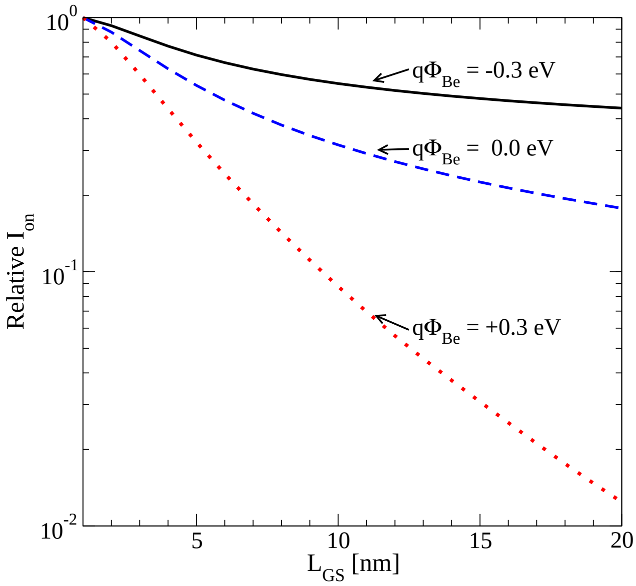

Figure 5.9: The relative variation of the on-current versus the gate-source spacer length (L_{GS}) for devices with different barrier heights for electrons. In a device with negative barrier height the tunneling current has a smaller contribution to the total current as compared to other device types. Therefore, the current is less sensitive to the variation of the gate-source spacer length.

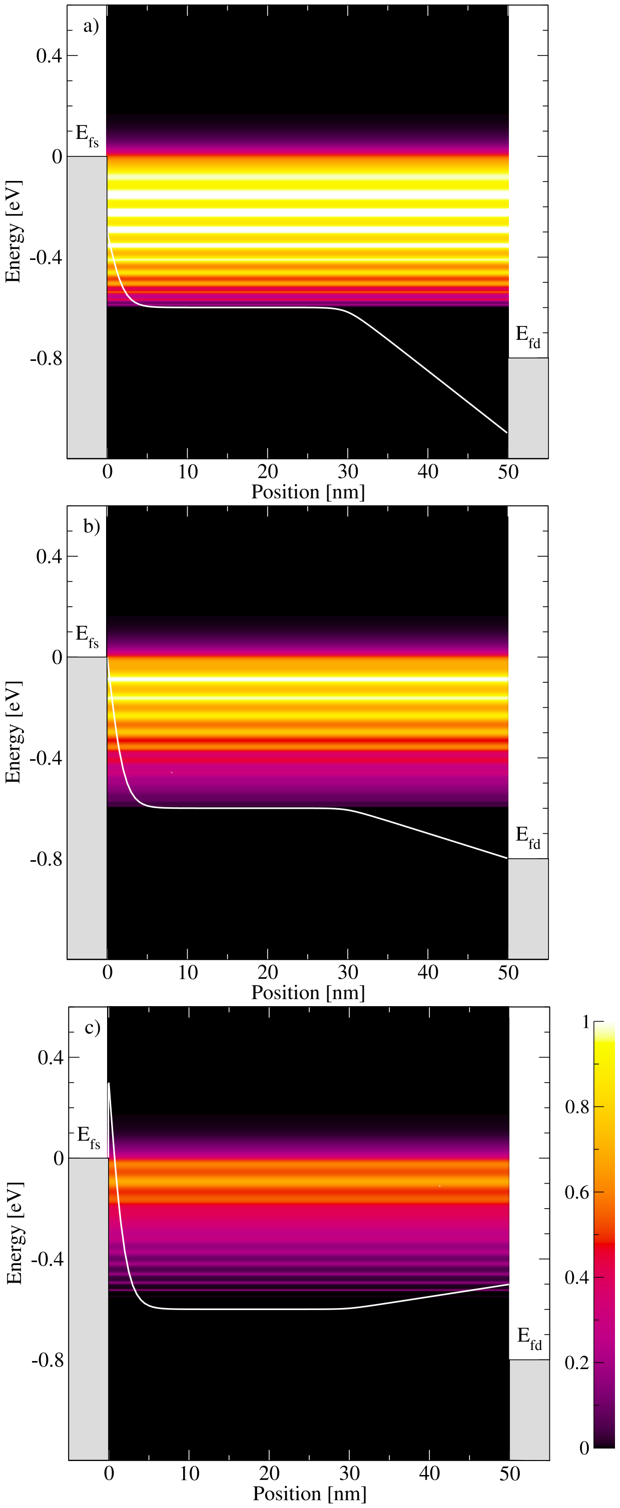

Figure 5.10: The effect of the barrier height at the metal-CNT interface on the current. The normalized current spectrum based on a ballistic model transport is shown for a device with a) negative ($q\Phi_{\mathrm{Be}} = -0.3$ eV), b) zero ($q\Phi_{\mathrm{Be}} = 0$), and c) positive barrier height for electrons ($q\Phi_{\mathrm{Be}} = +0.3$ eV). The operating point is $V_{\mathrm{G}} = 0.6$ V and $V_{\mathrm{D}} = 0.8$ V.

5.2.2 Gate-Drain Spacer Length

The transfer characteristics for a device with zero barrier height for electrons is shown in Fig. 5.11-a. In the off-regime the drain current starts to increase due to ambipolar conduction. By further increasing the drain bias this phenomenon becomes more apparent (see Section 5.1.1). Fig. 5.11-b shows that if the drain voltage becomes higher than the gate voltage, the thickness of the drain-sided metal-CNT barrier for holes is reduced. As a result, the parasitic band-to-band tunneling current of holes increases. By increasing the gate-drain spacer length, the band edge profile near the drain contact is less affected by the gate voltage. Therefore, the barrier for holes at the drain-side is thicker and the parasitic tunneling current of holes is suppressed. Fig. 5.11-a shows that, the off-current decreases considerably, as the gate-drain spacer length increases, while the on-current is only weakly affected.

Fig. 5.12 compares the increase of the $I_{\mathrm{on}}/I_{\mathrm{off}}$ ratio as a function of the gate-drain spacer length. In a device with negative barrier height more improvement is achieved. A smaller barrier height for electrons results in a larger barrier height for holes. A negative barrier height for electrons gives a positive barrier height for holes, implying that the tunneling process contributes predominantly the hole current. As a result, for a device with negative barrier height for electrons the parasitic hole tunneling current can be more effectively suppressed than for other device types.

Fig. 5.13 compares the effect of the gate-drain spacer length on the output characteristics for devices with different barrier heights. In the device with positive barrier height for electrons, the current at low drain biases decreases as the gate-drain spacer length increases. This behavior

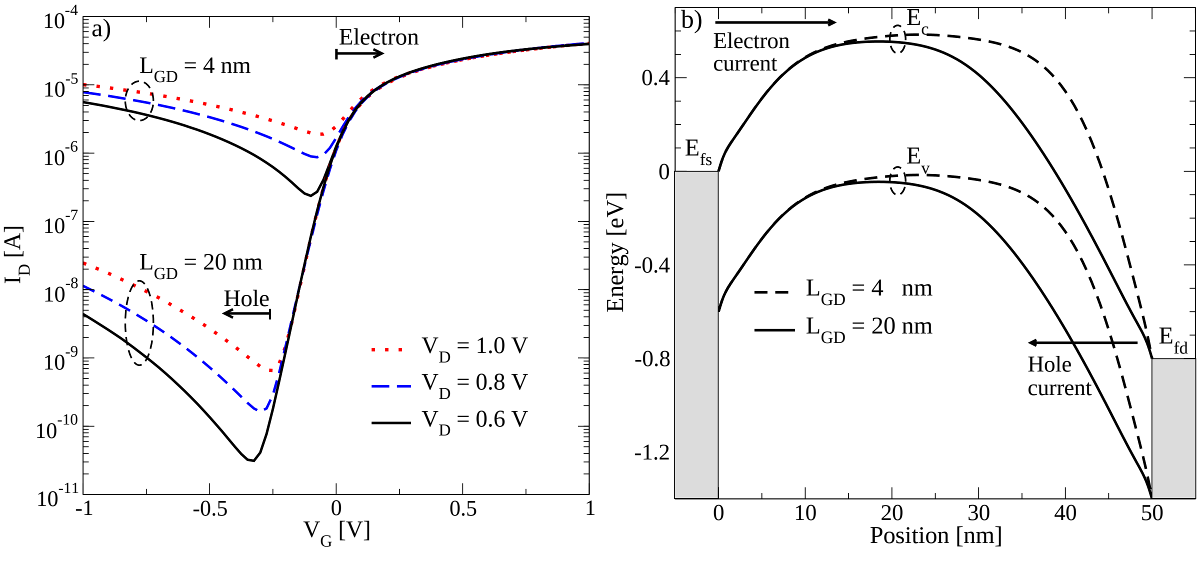

Figure 5.11: a) Transfer characteristics at different drain biases. The increase of the off-current is due to parasitic hole injection at the drain contact. By increasing the gate-drain spacer length (L_{GD}) the parasitic current of holes at the drain contact decreases. b) Comparison of the band-edge profile for devices with $L_{\mathrm{GD}} = 4$ nm and $L_{\mathrm{GD}} = 20$ nm. $V_{\mathrm{G}} = 0.6$ V and $V_{\mathrm{D}} = 0.8$ V. As L_{GD} increases, the band-bending near the drain contact decreases, and the drain-sided metal-CNT barrier is thicker.

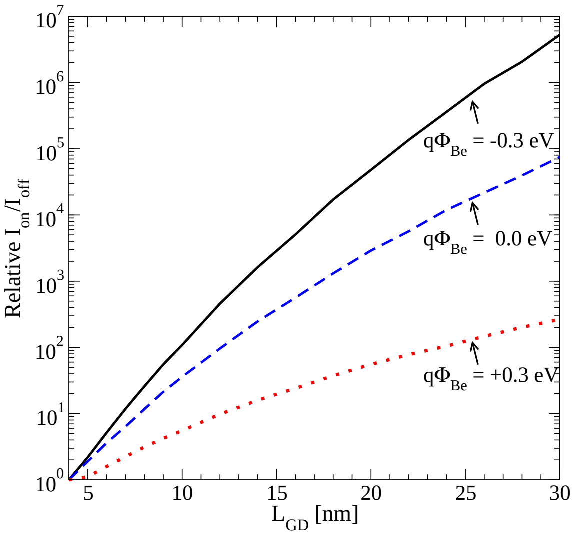

Figure 5.12: The ratio of the $I_{\mathrm{on}}/I_{\mathrm{off}}$ ratio versus the gate-drain spacer length (L_{GD}) for devices with different barrier heights for electrons. Increasing the gate-drain spacer length improves the $I_{\mathrm{on}}/I_{\mathrm{off}}$ ratio for all devices. The device with negative barrier height shows the largest improvement. As the barrier height for electrons decreases, the barrier height for holes increases. Therefore, in a device with negative barrier height for electrons the barrier height for holes is positive. In this case the hole current is more sensitive to the variation of the gate-drain spacer length than it is for other device types. For all results $V_{\mathrm{D}} = 0.6$ V was assumed.

can well be understood by considering Fig. 5.10-c. In a device with positive barrier height, electrons in the channel face a barrier at the drain-sided metal-CNT interface. Similar to what we discussed for the gate-source spacer length, with increasing gate-drain spacer length the thickness of the drain-sided metal-CNT barrier increases, such that the drain current will be reduced. If the drain voltage becomes higher than the gate voltage, most of the electrons can reach the drain contact by thermionic emission. In devices with negative and zero barrier height this problem is less apparent, since even at low drain voltages a drain sided-barrier does not form, see Fig. 5.10-a and Fig. 5.10-b.

It should be noticed that, as opposed to conventional MOSFETs, increasing the length of the un-gated area determined by the gate-drain spacer does not increase the channel resistance. In conventional MOSFETs the resistivity of the channel is modulated, when the gate voltage attracts or repels carriers from the channel. For an enhancement-type device the resistance of the un-gated region is high. In contrast, the intrinsic conductance of CNTs is independent from the gate voltage. In conventional MOSFETs carrier transport is diffusive, while in CNT based transistors carrier transport is nearly ballistic. To make a fair comparison with conventional MOSFETs, the effect of the gate-drain spacer length on the output characteristics is investigated for both the ballistic and diffusive transport limit. To study diffusive transport in CNT based transistors an artificially large value for the electron-phonon coupling strength and a small value for the phonon energy is chosen (see Section 5.5.3). Fig. 5.13 shows that even in the case of diffusive transport the length of the un-gated region has a negligible effect on the on-current.

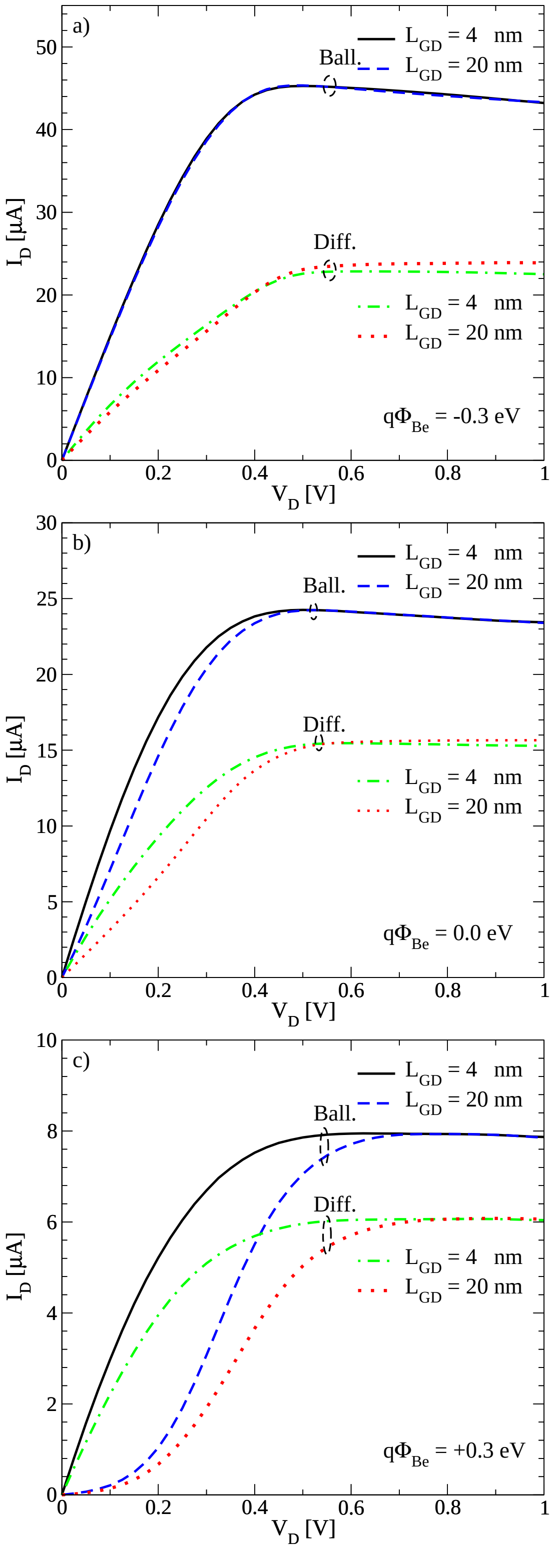

Figure 5.13: The effect of the gate-drain spacer length (L_{GD}) on the output characteristics for a device with a) negative, b) zero, and c) positive barrier height for electrons. In all cases the results are shown for both ballistic and diffusive transport. For diffusive transport the parameters $D = 10^{-1}$ eV^2 and $\hbar\omega = 25$ meV were used.

5.3 Device Optimization

The gate-delay time with respect to the $I_{\mathrm{on}}/I_{\mathrm{off}}$ ratio can be used to compare devices with different geometries and material properties [263]. The gate-delay time is defined next and it is approximated for CNT-FETs. Then we show that by appropriate selection of the spacer lengths the gate-delay time with respect to the $I_{\mathrm{on}}/I_{\mathrm{off}}$ ratio can be well optimized.

5.3.1 Gate-Delay Time of CNT-FETs

The gate-delay time, which characterizes the switching response of the transistor, is an important metric for digital electronic applications. The gate-delay time of a transistor is defined as time taken to charge a constant gate capacitance C_{G} to a voltage V_{DD} at a constant current I_{on}

$$\tau = \frac{C_{\mathrm{G}}\, V_{\mathrm{DD}}}{I_{\mathrm{on}}} \; . \tag{5.1}$$

The total gate capacitance is given by $C_{\mathrm{G}} = C_{\mathrm{GG}}+C_{\mathrm{GS}}+C_{\mathrm{GD}}$, where C_{GS} and C_{GD} are the gate-source and gate-drain parasitic capacitances, and C_{GG} can be written as $C_{\mathrm{G}}^{-1} = {C_{\mathrm{Ins}}}^{-1}+{C_{\mathrm{CNT}}}^{-1}$, where C_{Ins} is the gate insulator capacitance and C_{Q} is the so called *quantum capacitance* given by [264]

$$C_{\mathrm{Q}} = \frac{\partial Q_{\mathrm{CNT}}}{\partial \phi_{\mathrm{CNT}}} \; , \tag{5.2}$$

where ϕ_{CNT} is the electrostatic potential on the surface of the CNT and Q_{CNT} is the total charge along the CNT. Given the one-dimensional density of states and assuming equilibrium conditions, (5.2) can be approximated as [264–266]

$$C_{\mathrm{Q}} \approx \frac{8\mathrm{q}^2}{\mathrm{h}\upsilon_{\mathrm{F}}} \approx 400\ \mathrm{aF}/\mu\mathrm{m} \; , \tag{5.3}$$

where the twofold band and spin degeneracy is included. If thin and high-κ insulators are used, then $C_{\mathrm{Ins}} \gg C_{\mathrm{Q}}$ and $C_{\mathrm{GG}} \approx C_{\mathrm{Q}}$, implying that the potential on the CNT becomes equal to the gate potential (perfect coupling). This regime is called *quantum capacitance limit* in which the device is potential-controlled rather than charge-controlled [267]. The insulator capacitance, occurring between the CNT and a cylindrical gate, is given by

$$C_{\mathrm{Ins}} = \frac{2\pi\kappa\varepsilon_0}{\ln(T_{\mathrm{Ins}}/R_{\mathrm{CNT}}+1)} \; , \tag{5.4}$$

where T_{Ins} is the gate insulator thickness and R_{CNT} is the radius of the CNT. Assuming a $\mathrm{HfO_2}$ gate insulator with a thickness of 2 nm, $C_{\mathrm{Ins}} \approx 1500\mathrm{aF}/\mu\mathrm{m}$, satisfying the condition of the quantum capacitance limit ($C_{\mathrm{Q}} \ll C_{\mathrm{Ins}}$). Parasitic capacitances are usually much larger than the quantum capacitance ($C_{\mathrm{GS}}+C_{\mathrm{GD}} \gg C_{\mathrm{Q}}$) [268, 269]. Therefore, the gate capacitance can be approximated as

$$C_{\mathrm{G}} \approx C_{\mathrm{GS}} + C_{\mathrm{GD}} \; . \tag{5.5}$$

5.3.2 Optimized Spacer Length

In Section 5.2.1 it was shown that by increasing the gate-source spacer length the parasitic capacitance between these two contacts is reduced, and so does the on-current. In Section 5.2.2 it was shown that by increasing the gate-drain spacer length the $I_{\mathrm{on}}/I_{\mathrm{off}}$ ratio increases. At the same time, by increasing the gate-drain spacer length the parasitic capacitance between these two contacts decreases, which results in a reduced gate-delay time. Fig. 5.14 shows the effect of the gate-drain spacer length on the gate-delay time versus the $I_{\mathrm{on}}/I_{\mathrm{off}}$ ratio, which indicates a significant performance improvement by increasing the gate-drain spacer length.

Since the gate-delay time is proportional to the parasitic capacitance and inversely proportional to the on-current (5.1), there is an optimal value for the gate-source spacer length, $\mathrm{L}_{\mathrm{GS0}}$, which minimizes the gate-delay time. The optimal value for the gate-source spacer length is achieved if

$$\frac{\partial \tau}{\partial L_{\mathrm{GS}}}\bigg|_{\mathrm{L_{GS0}}} = \frac{1}{C_{\mathrm{G}}}\frac{\partial C_{\mathrm{G}}}{\partial L_{\mathrm{GS}}}\bigg|_{\mathrm{L_{GS0}}} - \frac{1}{I_{\mathrm{on}}}\frac{\partial I_{\mathrm{on}}}{\partial L_{\mathrm{GS}}}\bigg|_{\mathrm{L_{GS0}}} = 0 \ . \tag{5.6}$$

Fig. 5.15 shows the sensitivity of the on-current with respect to the gate-source spacer length for devices with zero and positive barrier heights for electrons. For thinner insulators the width of the source-sided barrier decreases, resulting in a higher tunneling current contribution to the total current and a higher sensitivity of the on-current to L_{GS} (see Section 5.2.1).

The optimal gate-source spacer length for a device with zero barrier height for electrons is $L_{\mathrm{GS}}\approx$ 6 nm for T_{Ins} = 2 nm and L_{GD} = 20 nm. For devices with positive barrier heights the optimal value of the gate-source spacer length is smaller than that of a device with zero barrier height due to the higher sensitivity of the on-current with respect to the gate-source spacer length.

Note that the optimal value for L_{GS} depends on L_{GD}. For small values of L_{GD} the gate-drain

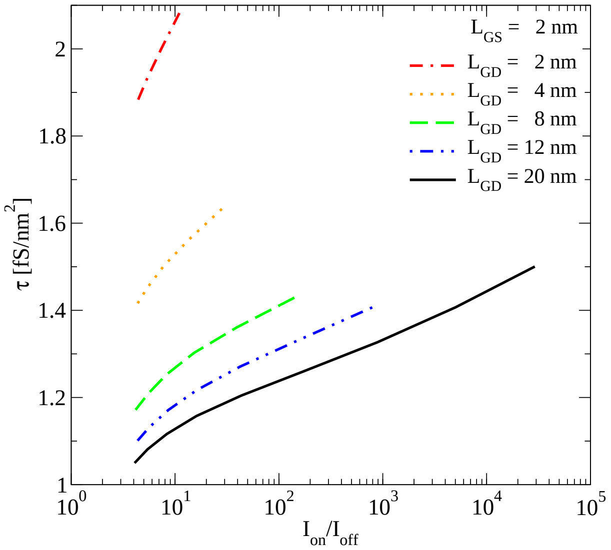

Figure 5.14: The effect of L_{GD} on the gate-delay time versus the $I_{\mathrm{on}}/I_{\mathrm{off}}$ ratio for a device with zero barrier height for electrons ($\mathrm{q}\Phi_{\mathrm{Be}} = 0$). L_{GS} = 2 nm and V_{D} = 0.8 V.

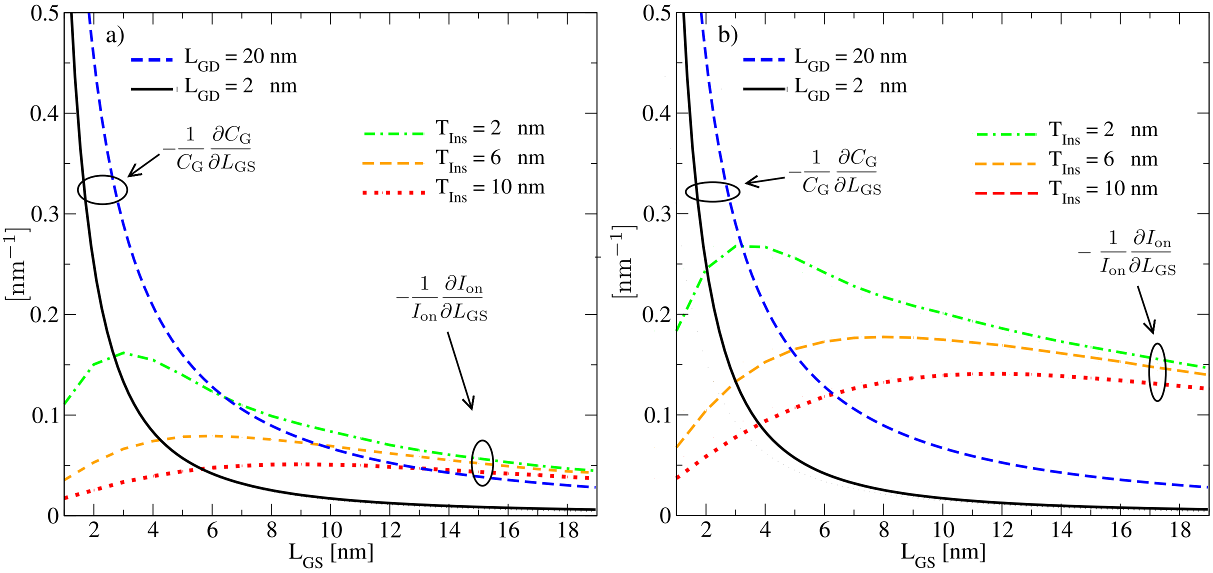

Figure 5.15: The sensitivity of the parasitic capacitance and the on-current with respect to L_{GS} for a device with a) zero barrier height ($\mathrm{q}\Phi_{\mathrm{Be}} = 0$) and b) positive barrier height ($\mathrm{q}\Phi_{\mathrm{Be}} = 0.3$ eV) for electrons. The intersection of the curves gives the optimum L_{GS0} which minimizes τ.

parasitic capacitance dominates the gate-source parasitic capacitance. Therefore, any further decrease of the gate-source spacer length does not improve the gate-delay time. As shown in Fig. 5.16, the optimal value of the gate-source spacer length for the given material and geometrical parameters results in optimized device characteristics.

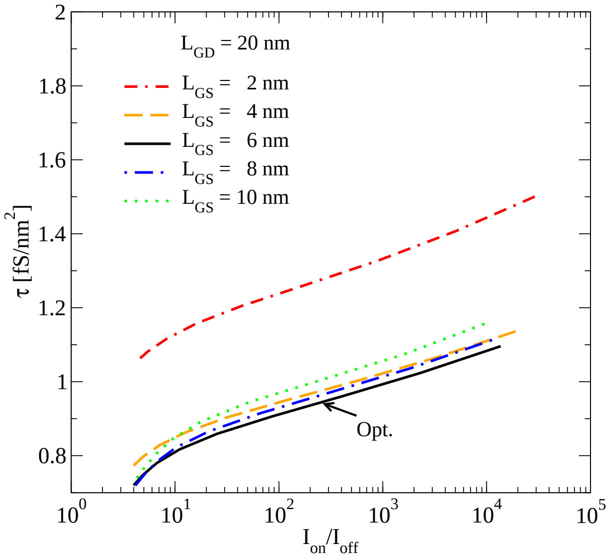

Figure 5.16: The effect of L_{GS} on the gate-delay time versus the $I_{\mathrm{on}}/I_{\mathrm{off}}$ ratio for a device with zero barrier height for electrons ($\mathrm{q}\Phi_{\mathrm{Be}} = 0$). $V_{\mathrm{D}} = 0.8$ V. The optimal L_{GS} for both device types are shown.

5.4 Tunneling CNT-FETs

To reduce the parasitic capacitance the spacing between the gate-source and the gate-drain contacts can be increased. The extension region can be of n or p-type leading to n/i/n or p/i/p devices. Unlike conventional semiconductors in which doping is introduced by ion implantation, doping of CNTs requires controlling the electrostatics of the CNT environment (see Section 2.8.3) by additional gates [270], molecules [271], or metal ions [272].

In n/i/n or p/i/p devices the gate controls the thermionic emission current [270]. Aggressively scaled devices of this type suffer from charge pile-up in the channel [273,274], which deteriorates the off-current substantially and ultimately limits the achievable $I_{\text{on}}/I_{\text{off}}$ ratio [273]. To overcome this obstacle a gate-controlled tunneling FET (T-CNT-FET) has been proposed [275].

In T-CNT-FET devices either a p/i/n or n/i/p doping profile can be used. The gate voltage modulates the band to band tunneling current. T-CNT-FETs benefit from a steep inverse subthreshold slope and a better controlled off-current. In this section the effect of symmetric and asymmetric doping on the device characteristics is discussed.

5.4.1 Symmetric and Asymmetric Doping

The operation of the device can be well understood by considering the spectrum of the electron density along the device (Fig. 5.17). At high negative gate voltages, due to strong band bending near the source contact, band to band tunneling contributes significantly to the total current. By increasing the gate voltage to positive values the band bending near the source contact decreases, and as a result band to band tunneling decreases.

On the other hand, the increase of the gate voltage results in strong band to band tunneling near

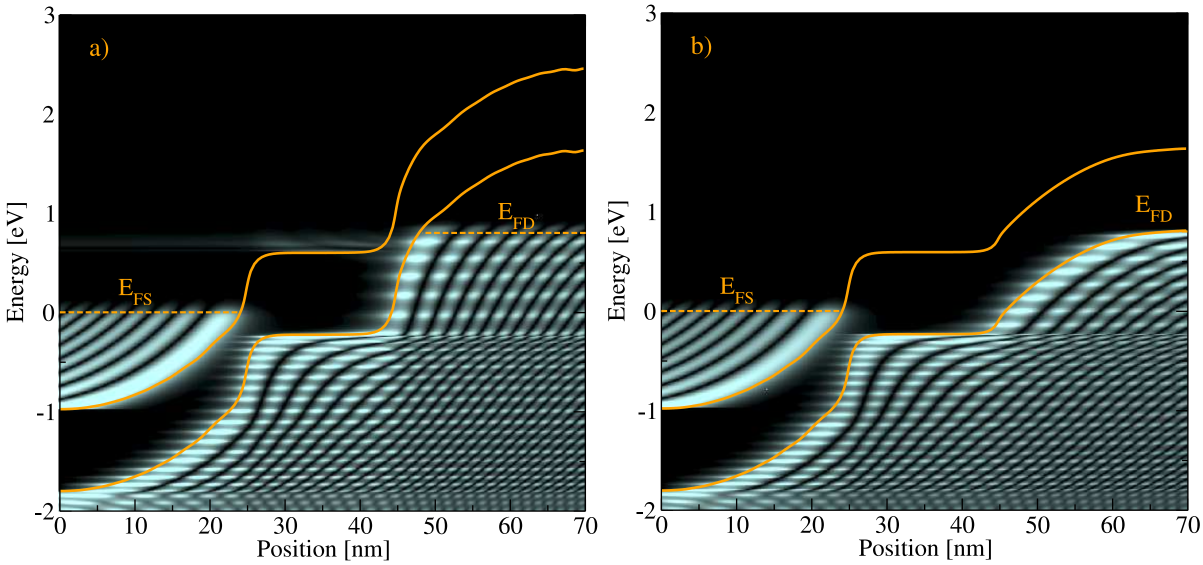

Figure 5.17: The electron density spectrum along the device with a) symmetric and b) asymmetric doping profile.

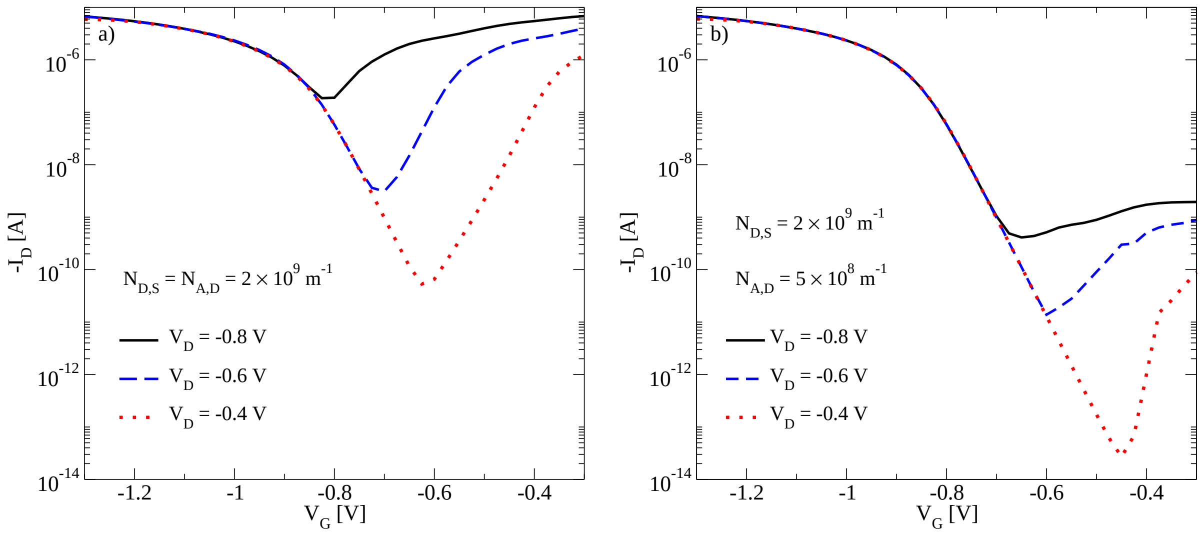

Figure 5.18: The transfer characteristics for a) symmetric and b) asymmetric doping.

the drain contact. As a result the total current increases in the off-regime (Fig. 5.18-a) which has a detrimental effect on the device performance. Fig. 5.19-a shows that the parasitic current increases if the drain voltage becomes much higher than the gate voltage. For the device with symmetric doping we assumed that the donor and acceptor concentrations at the source and drain contacts are $N_{\mathrm{D_S}} = N_{\mathrm{A_D}} = 2 \times 10^9$ m^{-1}. By decreasing the doping of the drain side, the band bending decreases for the same gate voltage (Fig. 5.17-b) and the band to band tunneling current near the drain contact decreases considerably (see Fig. 5.18-b and Fig. 5.19-b). For the device with asymmetric doping profile, $N_{\mathrm{D_S}} = 2 \times 10^9$ m^{-1} and $N_{\mathrm{A_D}} = 5 \times 10^8$ m^{-1}.

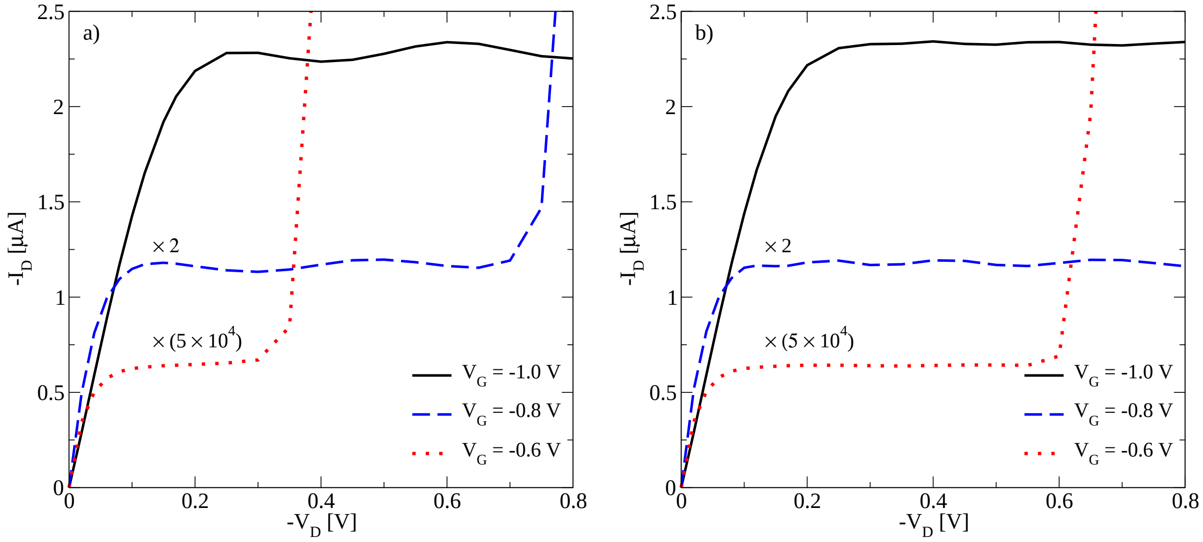

Figure 5.19: The output characteristics for a) symmetric and b) asymmetric doping.

5.5 The Effect of Electron-Phonon Interaction

The electron-phonon coupling strength and the phonon energy depend on the chirality and the diameter of the CNT (see Section 2.6.1). In this section the device response is studied for a wide range of electron-phonon interaction parameters.

5.5.1 Electron-Phonon Coupling Strength

Fig. 5.20-a shows the ballisticity as a function of the electron-phonon coupling strength. The ballisticity is defined as $I_{\mathrm{Sc}}/I_{\mathrm{Bl}}$, the ratio of the on-current in the presence of electron-phonon interaction to the current in the ballistic case [276]. With increasing electron-phonon coupling strength the self-energy increases.

The left part of Fig. 5.20-b illustrates an electron losing its kinetic energy by emitting a phonon. The electron will be scattered either forward or backward. In the case of backward scattering the electron faces a thick barrier near the source contact and will be reflected with high probability, such that its momentum will again be directed towards the drain contact.

Elastic scattering conserves the energy of carriers, but the current decreases due to elastic back-scattering of carriers. Fig. 5.21-a shows that for elastic scattering the source and drain current spectra are symmetric. As the electron-phonon coupling strength increases, resonances in the current spectrum are washed out and the total current decreases due to elastic back-scattering. In the case of inelastic scattering, carriers acquiring enough kinetic energy can emit a phonon and scatter into lower energy states. Therefore, as shown in Fig. 5.21-b, the source and drain current spectra are not symmetric.

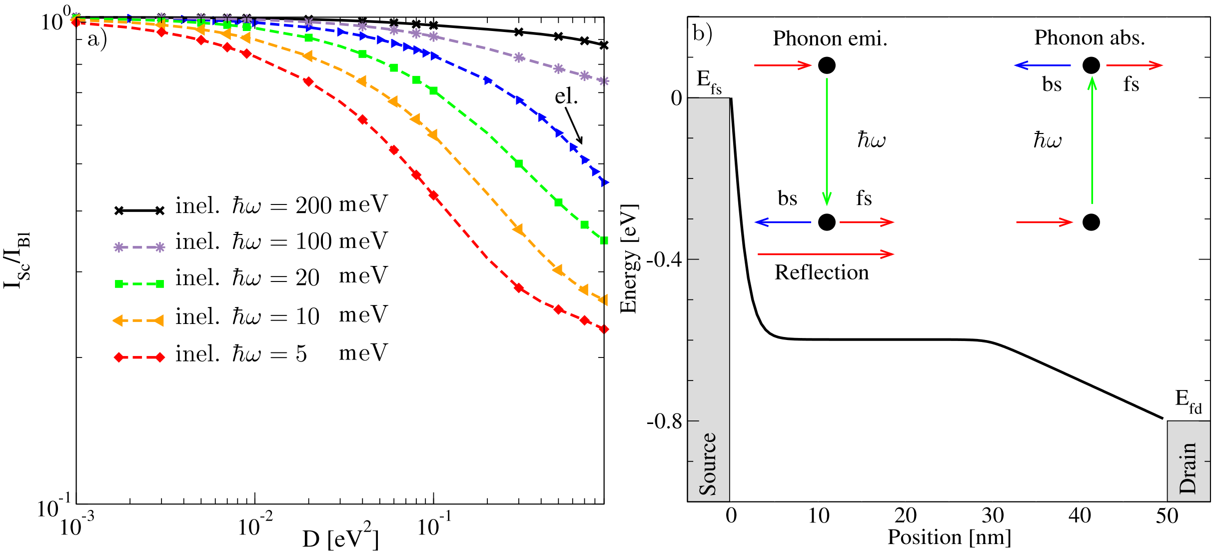

Figure 5.20: a) Ballisticity versus electron-phonon coupling strength for a CNT of 50 nm length. Results for both elastic and inelastic scattering with different phonon energies are shown. The operating point is $V_{\mathrm{G}} = V_{\mathrm{D}} = 1$ V. b) Sketch of phonon emission and absorption processes in the channel.

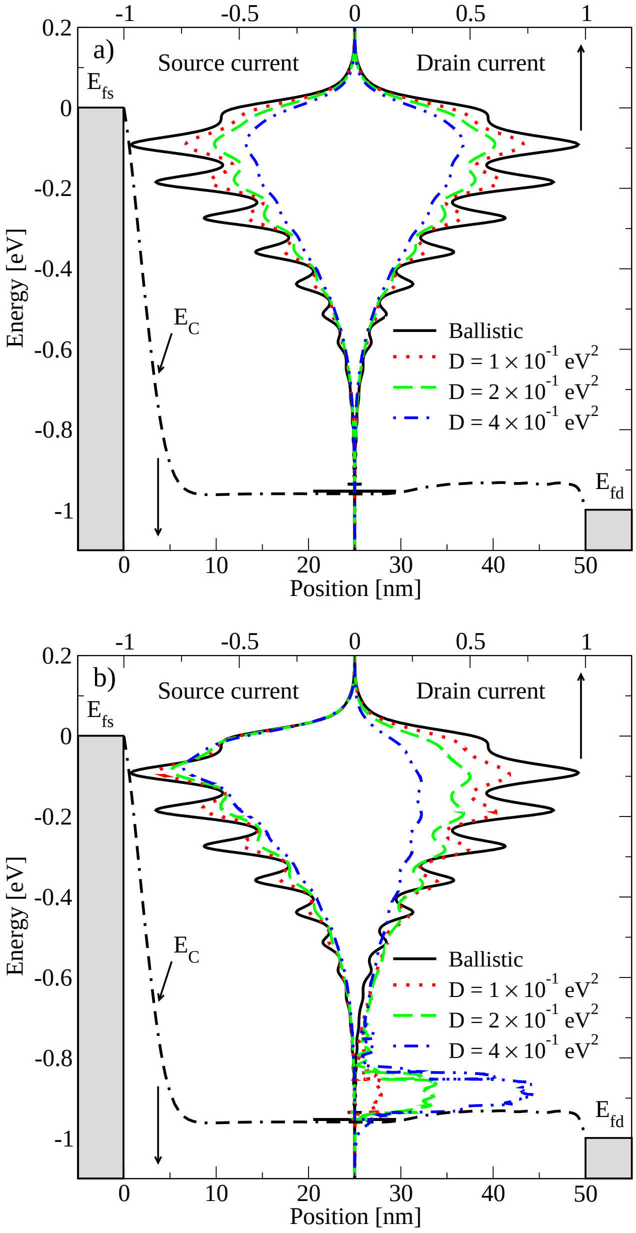

Figure 5.21: The spectra of the source and drain currents. a) The effect of elastic phonon scattering with different coupling strengths is shown. As the coupling strength increases resonances in the current spectrum wash out and the total current decreases due to elastic back-scattering. b) The effect of inelastic phonon scattering with different coupling strengths is shown. The phonon energy is $\hbar\omega = 100$ meV. Carriers acquiring enough kinetic energy can emit phonons and scatter into lower energy states. Since the energy of electrons is not conserved in this process, the source and drain current spectrum are not symmetric. As the coupling strength increases more electrons are scattered into lower energy states.

5.5.2 Phonon Energy

Figure 5.22-a shows the dependence of the ballisticity with respect to the phonon energy. With increasing phonon energy the effect of phonon scattering on the current is reduced, because scattered electrons lose more kinetic energy and the probability for traveling back to the source contact decreases. The considerable decrease of ballisticity for low energy phonons is due to the phonon absorption process.

The right part of Fig. 5.20-b shows an electron absorbing energy from a phonon and scattering into a higher energy state. In this case, the probability for arriving at the source contact increases. This process can severely reduce the total current.

Fig. 5.22-b separately shows the effects of the phonon emission and absorption processes on the ballisticity. As the phonon energy decreases, the phonon occupation number (C.18) increases exponentially, and the self-energy contributions of these two components increase. However, due to the higher probability for back-scattering of electrons in the case of phonon absorption, this component reduces the total current more effectively than the phonon emission process does.

Fig. 5.23-a shows the ratio of the gate-delay time (Section 5.3.1) in the presence of electron-phonon interaction to that in the ballistic case, $\tau_{\mathrm{Sc}}/\tau_{\mathrm{Bl}}$, as a function of the electron-phonon coupling strength. As the phonon energy increases the gate-delay time increases. This behavior can be attributed to the average electron velocity in the channel, which is high for ballistic electrons and low for electrons scattered to lower energy states.

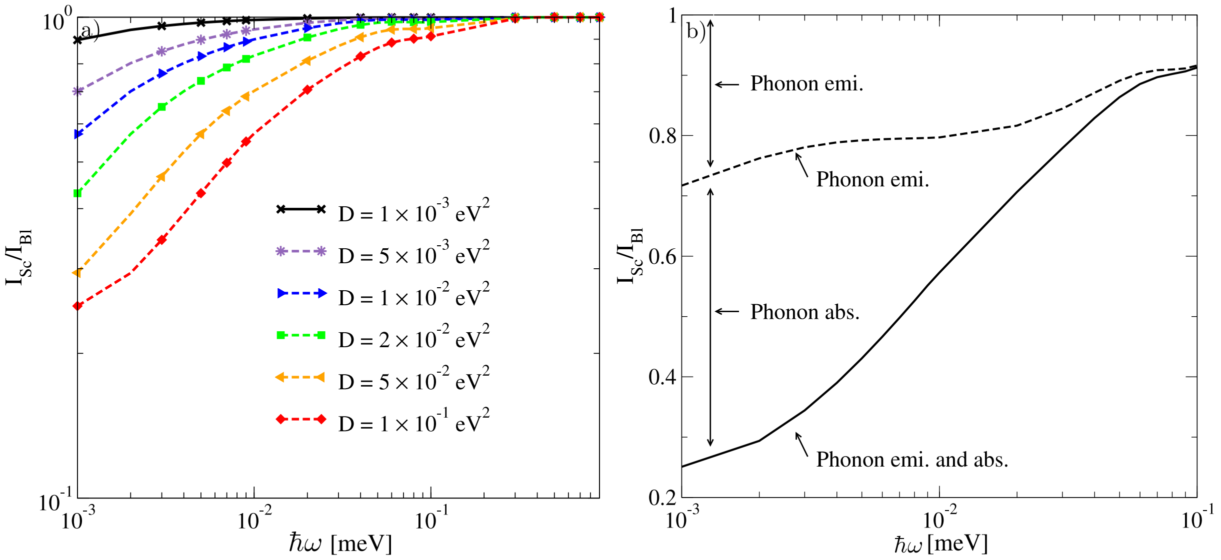

Figure 5.22: a) Ballisticity versus phonon energy for a CNT of 50 nm length. Results for inelastic scattering with different electron-phonon couplings are shown. $V_{\mathrm{G}} = V_{\mathrm{D}} = 1$ V. b) Ballisticity versus phonon energy with $D = 10^{-1}$ eV^2 at the bias point $V_{\mathrm{G}} = V_{\mathrm{D}} = 1$ V. The contributions due to phonon absorption and emission are shown.

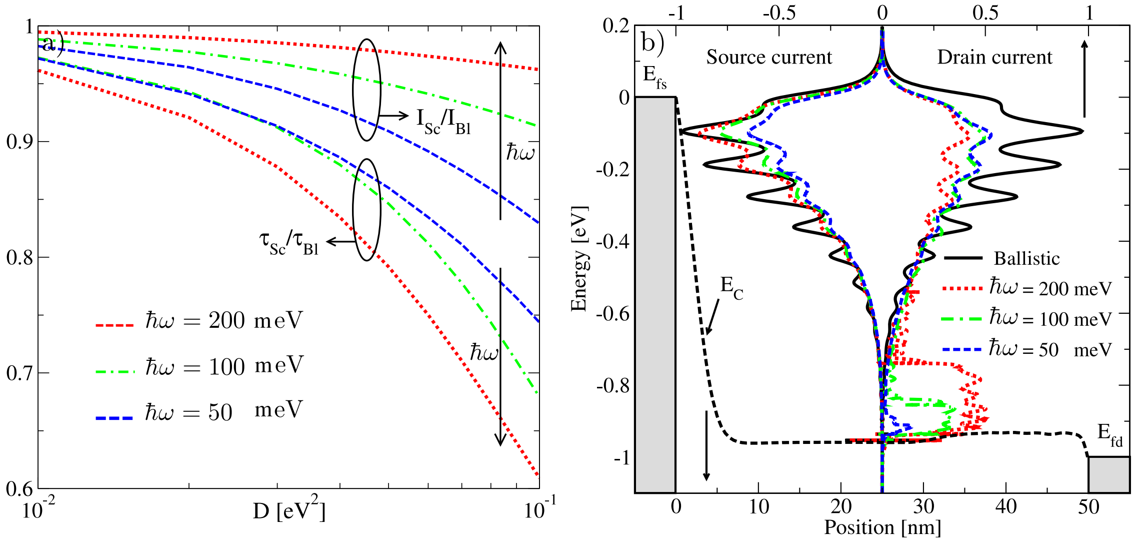

Figure 5.23: a) The ratio of the gate-delay time in the presence of electron-phonon interaction to the gate-delay time in the ballistic case, $\tau_{\mathrm{Sc}}/\tau_{\mathrm{Bl}}$, as a function of the electron-phonon coupling strength. For comparison, the ratio $I_{\mathrm{Sc}}/I_{\mathrm{Bl}}$ is also shown. As the phonon energy increases the gate-delay time increases. This behavior is due to the reduction of the electron velocity in the channel and the resulting charge pile up. b) The spectra of the source and drain currents. The effect of inelastic scattering with different phonon energies is shown. The electron-phonon coupling strength is $D = 2 \times 10^{-1}$ eV^2. The figure shows a considerable increase of the electron population close to the conduction band-edge as the phonon energy increases.

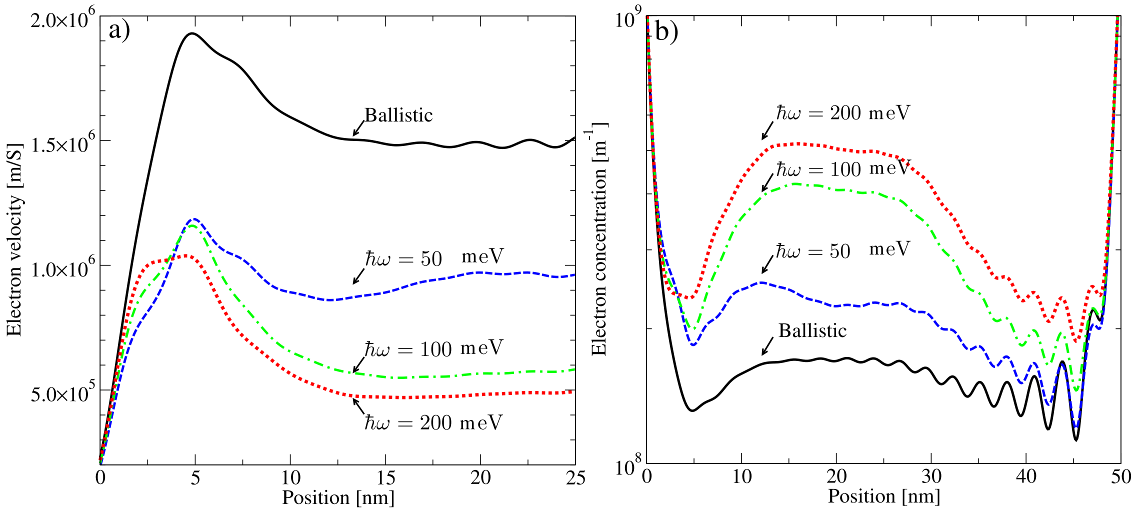

Figure 5.24: a) The profile of the electron velocity near the source contact. b) The profile of the electron concentration along the device. The results for the ballistic case and for electron-phonon interaction are shown. As the phonon energy increases the electrons scatter to lower energy states. Therefore, the electron velocity decreases and the carrier concentration increases. The electron-phonon coupling strength is $D = 10^{-1}$ eV^2 and the bias point is $V_{\mathrm{G}} = V_{\mathrm{D}} = 1$ V.

Fig. 5.23-b shows the spectra of the source and drain currents for different inelastic phonon energies. Electrons can emit a single phonon or a couple of phonons to reach lower energy states. The probability of multiple phonon emissions decreases as the number of interactions increases. Therefore, as the phonon energy increases, the occupation of electrons at lower energy states increases.

As shown in Fig. 5.23-b, the electron population close to the conduction band-edge considerably increases as the phonon energy increases. Therefore, as the phonon energy increases the mean velocity of electrons decreases and the carrier concentration in the channel increases (Fig. 5.24). The increased charge in the channel results in an increased gate-delay time.

5.5.3 Diffusive Limit

All the above discussed results were calculated for a device with a CNT length of 50 nm. In the case of ballistic transport the current is independent of the device length, but in the presence of scattering it decreases as the device length increases. Fig. 5.25-a shows the ballisticity as a function of the CNT length in the presence of elastic and inelastic electron-phonon interaction. An artificially large value for the electron-phonon coupling strength and a small value for the phonon energy is chosen to simulate the diffusive limit (see Fig. 5.25-b). In this case, the current is expected to be inversely proportional to the device length according to OHM's law.

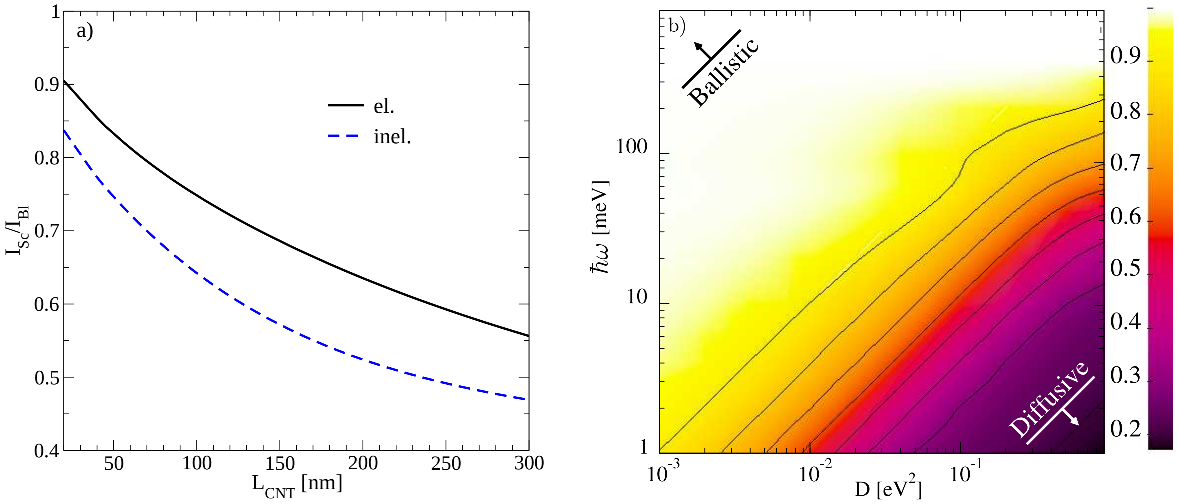

Figure 5.25: a) Ballisticity versus CNT length. The electron-phonon coupling strength for both elastic and inelastic scattering is $D = 10^{-1}$ eV^2, and $\hbar\omega = 25$ meV for inelastic scattering. These scattering parameters simulate the diffusive regime. In this case the ballisticity is inversely proportional to the device length [277]. b) Ballisticity as a function of the electron-phonon coupling strength and phonon energy for inelastic scattering. The scale of the ballisticity is shown in the color bar. The regions of ballistic and diffusive transport are shown. As the strength of the electron-phonon interaction increases transport of carriers deviates from the ballistic limit and becomes more diffusive.

5.5.4 Discussion

In general the electron-phonon interaction parameters depend on the diameter and the chirality of the CNT (see Section 2.6.1). CNTs with a diameter $d_{\mathrm{CNT}} > 2$ nm have a band gap $E_{\mathrm{G}} < 0.4$ eV (2.10), which render them unsuitable as channel for transistors. Since the fabrication of devices with a diameter $d_{\mathrm{CNT}} < 1$ nm is very difficult, we limit our study to zigzag CNTs with diameters in the range of $d_{\mathrm{CNT}} = 1 - 2$ nm.

Scattering with acoustic phonons is treated as an elastic process. The electron-phonon coupling is also weak for acoustic phonons ($D_{\mathrm{AP}} < 10^{-3}$ eV^2), which implies that elastic back-scattering of carriers is weak. Inelastic scattering is induced by OP, RBM, and K-point phonons (Section 2.5.2). Considering the class of CNTs discussed above, the energies of the these phonons are $\hbar\omega_{\mathrm{OP}} \approx 200$ meV, $\hbar\omega_{\mathrm{RBM}} \approx 25$ meV, and $\hbar\omega_{\mathrm{K}_1} \approx 160$ meV and $\hbar\omega_{\mathrm{K}_2} \approx 180$ meV [276, 279]. The corresponding coupling coefficients are $D_{\mathrm{OP}} \approx 40 \times 10^{-3}$ eV^2, $D_{\mathrm{RBM}} \approx 10^{-3}$ eV^2, and $D_{\mathrm{K}_1} \approx 10^{-4}$ eV^2, and $D_{\mathrm{K}_2} \approx 10^{-3}$ eV^2 [276].

As discussed in Section 5.5.2, high energy phonons such as OP and K-point phonons reduce the on-current only weakly, but can increase the gate-delay time considerably due to charge pileup in the channel. Low energy phonons such as the RBM phonon can reduce the on-current more effectively, but have a weaker effect on the gate-delay time. However, due to strong coupling, scattering processes are mostly due to electron-phonon interaction with high energy phonons. Therefore, the on-current of short CNT-FETs can be close to the ballistic limit [278] (see Fig. 5.26), whereas the gate-delay time can be significantly below that limit [89, 280]. The intrinsic (without parasitic capacitances) gate-delay time for the ballistic case can be approximated as $\tau \approx 1.7$ ps/μm, or equivalently $f_T \approx 100$ GHz/μm [281]. The highest reported cutoff frequency for a device with a length of less than 1μm is $f_T \approx 10$ GHz [90], which is far below the ballistic limit. Apart from parasitic capacitances, inelastic electron-phonon interaction with high energy phonon has to be considered to explain the results.

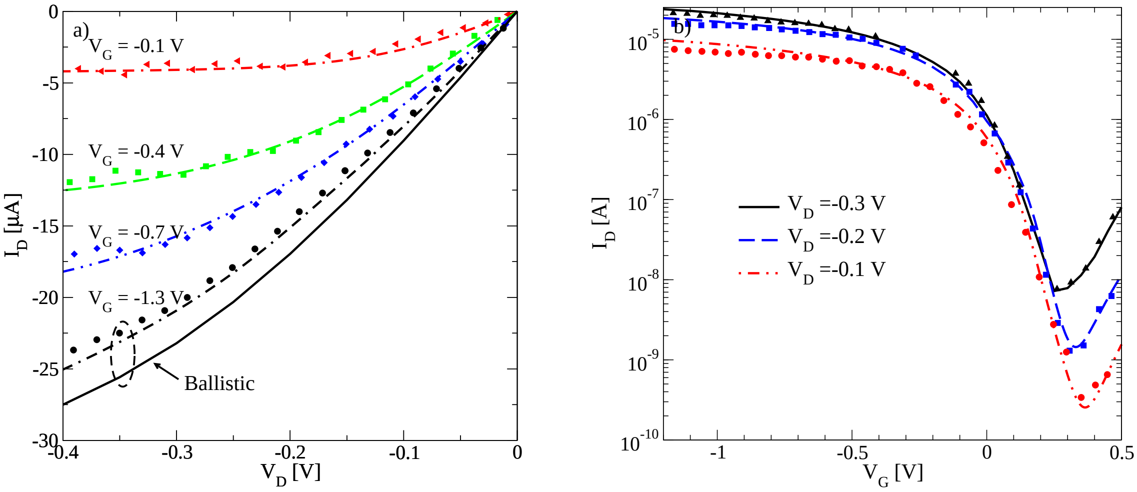

Figure 5.26: Comparison of the simulation results and experimental data for the a) output and b) transfer characteristics. Lines show the simulation results and symbols show experimental data. The result for $V_{\mathrm{G}} = -1.3$ V is compared with the ballistic limit. Experimental data have been adopted from [278].

Chapter 6

Summary and Conclusions

EVER SINCE the first demonstration of carbon nanotube FETs (CNT-FETs), their performance is improving very rapidly and the understanding of such devices is evolving. The one-dimensional nature of CNTs severely reduces the phase space for scattering, allowing CNTs to operate close to the ballistic limit even at room temperature. The low scattering probability and high mobility are responsible for high on-current of CNT-FETs.

Furthermore, the chemical stability and perfection of the CNT structure suggests that the carrier mobility at high gate fields may not be affected by processing and roughness scattering as it is the case in the conventional semiconductor channel. Electrostatic control is improved as well. The fact that there are no dangling bond states at the surface of CNTs allows for a much wider choice of gate insulators beyond the conventional SiO_2. Also, the strong one-dimensional electron confinement of the single-wall CNTs (typically $1 - 2$ nm diameter) should lead to a suppression of short-channel effects in transistor devices [5].

As far as integration is concerned, semiconducting CNTs benefit from their band structure which gives essentially the same effective mass for electrons and holes. This should enable similar mobilities and performance of n-type and p-type transistors, which is necessary for a complementary metal-oxide semiconductor (CMOS)-like technology. The most important appeal of this approach is the ability to fabricate one of the critical device dimensions (the CNT diameter) reproducibly using synthetic chemistry.

The purposes of this work are to develop a simulation approach and tools for CNT-FETs and apply them to understand device physics and explore device issues, which are crucial for improving device performance. We employed the non-equilibrium GREEN's function (NEGF) technique for modeling transport phenomena in CNT-FETs. The NEGF technique allow one to study the time evolution of a many-particle quantum system. Knowledge of the single-particle GREEN's function provides properties of the system and the excitation energies of the systems containing one more or one less particle. The many-particle information about the system is cast into self-energies, parts of the equations of motion for the GREEN's functions. GREEN's functions can be expressed as a perturbation expansion, which is the key to approximate the self-energies. GREEN's functions provide a very powerful technique for evaluating properties of many-particle systems both in thermodynamic equilibrium and also in non-equilibrium situations.

We solve the coupled system of transport and POISSON equations self-consistently. A tight-binding HAMILTONian is used to describe transport phenomena in CNT-FETs. The mode-space transformation used in this work reduces the computational cost considerably. The mode-space approach takes only a relatively small number of transverse modes into consideration. To reduce the computational cost even further, we used the local scattering approximation [112]. In this approximation the scattering self-energy terms are diagonal in coordinate representation. We show that the local approximation is well justified for electron-phonon scattering caused by deformation potential interaction.

The carrier concentration is related to the diagonal elements of the GREEN's function. The calculation of the current requires only the nearest off-diagonal elements of the GREEN's function. Furthermore, by using a nearest tight-binding HAMILTONian and assuming the local scattering approximation the achieved matrix is tridiagonal. Considering these factors we employed the efficient recursive GREEN's function method to calculate only the required elements of the GREEN's functions.

We also investigated methods of generating energy grids for numerical integration and their effects on the convergence behavior of the self-consistent iteration. Our results indicate that for accurate and fast convergent simulations the energy grid must be carefully adapted. All methods were implemented into the multi-purpose quantum-mechanical solver VSP.

Employing the described model, we investigated both the static and dynamic response of CNT-FETs. Based on the result we propose methods to improve the functionality and performance of such devices. The ambipolar conduction of CNT-FETs, which limits the performance, is studied in detail. We propose a double-gate structure to suppress this behavior. The first gate controls carrier injection at the source contact and the second one controls carrier injection at the drain contact, which can be used to suppress parasitic carrier injection.

We also considered single-gate devices. Scaling of the gate-source and gate-drain spacer length of single-gate CNT-FETs is studied in this work. By increasing the gate-drain spacer length the ambipolar conduction decreases and the $I_{\mathrm{on}}/I_{\mathrm{off}}$ ratio increases. Furthermore, the parasitic capacitances are reduced which results in a decrease of the switching time. By increasing the gate-source spacer length both the on-current and parasitic capacitances decrease. We show that by appropriately selecting this spacer length the performance of the device can be significantly enhanced. The results indicate that these effects can be very different from that in conventional MOSFETs.

Finally, the effect of electron-phonon interaction on the device characteristics is discussed in detail. In agreement with experimental data, our results indicate that electron phonon interaction affects the DC current of CNT-FETs only weakly, whereas the switching response of such devices can be significantly affected.

The implementation of these techniques allows the simulation and analysis of nano-electronic devices where quantum effects are either a parasitic effect or deliberately used as a part of the device functionality. Future work will concentrate on using these techniques to study transport in novel devices such as multiple gate MOSFETs, silicon nano-wires, and molecular devices. Furthermore, scattering processes can be more rigorously approximated. One can consider electron-electron interaction beyond the HARTREE approximation. Regarding electron-phonon interaction, one can relax the assumption of equilibrium phonons and calculate the renormalization of the phonon GREEN's function due to interaction with electrons.

Appendix A

First and Second Quantization

In condensed matter physics one is typically concerned with calculating physical observables from a microscopic description of the system under consideration. Such microscopic models are usually defined by the system HAMILTONian H. In many cases of interest the HAMILTONian takes the form

$$H \;=\; \sum_i H(\mathbf{r}_i) \;+\; \frac{1}{2}\sum_{i\neq j} V(\mathbf{r}_i - \mathbf{r}_j) \;, \tag{A.1}$$

where the first term contains a summation of single-particle HAMILTONians and V is the interaction potential between particles. The quantity $\mathbf{r}_i$ denotes the coordinate of the ith particle, including any discrete variables such as spin for a system of FERMIons. The summation of single-particle HAMILTONians by itself is just as simple to solve as each HAMILTONian alone. One solves the dynamics of one particle, and the total properties are the summation of the individual ones. The term which makes the HAMILTONian hard to solve is the particle-particle interaction $V(\mathbf{r}_i - \mathbf{r}_j)$. This term is multiplied by one-half since the double summation over (ij) counts each pair twice.

Together with an appropriate number of boundary conditions the basic problem is the solution of the many-particle SCHRÖDINGER equation

$$i\hbar\partial_t \Psi(\mathbf{r}_1, \mathbf{r}_2, \ldots, \mathbf{r}_N, t) \;=\; H\Psi(\mathbf{r}_1, \mathbf{r}_2, \ldots, \mathbf{r}_N, t) \;, \tag{A.2}$$

where $\Psi(\mathbf{r}_1, \mathbf{r}_2, \ldots, \mathbf{r}_N, t)$ is the many-particle wave function that in principle contains all relevant information about the state of the system. One can start by expanding the many-particle wave function Ψ in a complete set of symmetrized or anti-symmetrized products of time-independent single-particle wave functions for Bosons or FERMIons, respectively [189]. In principle, the N-body wave function contains all information, but a direct solution of the SCHRÖDINGER equation is impractical. Therefore, it is necessary to apply other techniques, and we shall rely on *second quantization*, *quantum field theory*, and the use of GREEN*'s functions*.

Historically, quantum physics first dealt only with the quantization of the motion of particles, leaving the electromagnetic field classical (SCHRÖDINGER, HEISENBERG, and DIRAC, 1925-26). Later also the electromagnetic field was quantized (DIRAC, 1927), and even the particles themselves got represented by quantized fields (JORDAN and WIGNER, 1927), resulting in the development of quantum electrodynamics and quantum field theory in general.

By convention, the original form of quantum mechanics is denoted first quantization, while quantum field theory is formulated in the language of second quantization. Second quantization greatly simplifies the discussion of many interacting particles. This approach merely reformulates the original SCHRÖDINGER equation. Nevertheless, it has the advantage that in second quantization operators incorporate the statistics, which contrasts with the more cumbersome approach of using symmetrized or anti-symmetrized products of single-particle wave functions.

In the second quantization formalism a quantum mechanical basis is used that describes the number of particles occupying each state in a complete set of single-particle states. For this purpose the time-independent abstract state vectors for an N-particle system are introduced

$$|n_1, n_2, \ldots\rangle \ , \ \text{where} \ \sum_j n_j \ = \ N \ . \tag{A.3}$$

The notation means that there are n_1 particles in the state 1, n_2 particles in the state 2, and so forth. It is therefore natural to define occupation number operators $\hat{n}_j$ which have the basis states $|n_j\rangle$ as eigenstates, and have the number n_j of particles occupying the state j as eigenvalues $\hat{n}_j|n_j\rangle = n_j|n_j\rangle$. For FERMIons n_j can be 0 or 1, while for Bosons it can be any non-negative number.

To connect first and second quantization, annihilation and creation operators c and $c^\dagger$ for FERMIons and b and $b^\dagger$ for Bosons are introduced. These operators satisfy either the commutation[1] or anti-commutation[2] rules

$$\begin{aligned}
[c_i, c_j]_+ &= 0 \ , & [b_i, b_j]_- &= 0 \\
[c_i, c_j^\dagger]_+ &= \delta_{i,j} \ , & [b_i, b_j^\dagger]_- &= \delta_{i,j} \\
[c_i^\dagger, c_j^\dagger]_+ &= 0 \ , & [b_i^\dagger, b_j^\dagger]_- &= 0 \ .
\end{aligned} \tag{A.4}$$

All of the properties of these operators follow directly from the commutation or anti-commutation rules. The annihilation operators, c_i and b_i, decrease the occupation number of the state i by 1, whereas the creation operators, $c_i^\dagger$ and $b_i^\dagger$, increase the occupation number of the state i by 1.

The HAMILTONian in (A.1) can be written in terms of annihilation and creation operators

$$\begin{aligned}
\hat{H} \ &= \ \sum_{ij} \langle i|H|j\rangle c_i^\dagger c_j \ + \ \frac{1}{2} \sum_{ijkl} \langle ij|V|kl\rangle c_i^\dagger c_j^\dagger c_l c_k \ , \\
\langle i|H|j\rangle &= \int d\mathbf{r} \phi_i^*(\mathbf{r}) H(\mathbf{r}) \phi_j(\mathbf{r}) \ , \\
\langle ij|V|kl\rangle \ &= \ \int d\mathbf{r} \int d\mathbf{r}' \phi_i^*(\mathbf{r}) \phi_j^*(\mathbf{r}') \ V(\mathbf{r} - \mathbf{r}') \phi_k(\mathbf{r}) \phi_l(\mathbf{r}') \ ,
\end{aligned} \tag{A.5}$$

where $\phi_i(\mathbf{r})$ are the single-particle wave functions and the circumflex denotes an operator in the abstract occupation-number Hilbert space. In this form, the matrix elements of the single-particle HAMILTONian and the interaction potential taken between the single-particle eigenstates of the SCHRÖDINGER equation in first quantization are merely complex numbers multiplying operators.

---

[1] The commutation relation for Bosons is defined by $[A, B]_- = [A, B] = AB - BA$.

[2] The anti-commutation relation for FERMIons is defined by $[A, B]_+ = \{A, B\} = AB + BA$.

It is often convenient to form a linear combination of the annihilation and creation operators

$$\begin{aligned}\hat{\psi}(\mathbf{r}) &= \sum_i \phi_i(\mathbf{r}) c_i \ , \\ \hat{\psi}^\dagger(\mathbf{r}) &= \sum_i \phi_i^\dagger(\mathbf{r}) c_i^\dagger \ ,\end{aligned} \tag{A.6}$$

where the sum is over the complete set of single-particle quantum numbers. The so-called *field operators* $\hat{\psi}(\mathbf{r})$ and $\hat{\psi}^\dagger(\mathbf{r})$ satisfy simple commutation or anti-commutation relations

$$\begin{aligned}[\hat{\psi}(\mathbf{r}), \hat{\psi}(\mathbf{r}')]_\pm &= 0 \ , \\ [\hat{\psi}(\mathbf{r}), \hat{\psi}^\dagger(\mathbf{r}')]_\pm &= \delta_{\mathbf{r},\mathbf{r}'} \ , \\ [\hat{\psi}^\dagger(\mathbf{r}), \hat{\psi}^\dagger(\mathbf{r}')]_\pm &= 0 \ ,\end{aligned} \tag{A.7}$$

where the plus (minus) sign refers to FERMIons (Bosons). The field operator $\hat{\psi}(\mathbf{r})$ annihilates and $\hat{\psi}^\dagger(\mathbf{r})$ creates a particle at place $\mathbf{r}$. The HAMILTONian operator can be rewritten in terms of these field operators as follows

$$\hat{H} = \int d\mathbf{r} \hat{\psi}^\dagger(\mathbf{r}) H(\mathbf{r}) \hat{\psi}(\mathbf{r}) + \frac{1}{2} \int d\mathbf{r} \int d\mathbf{r}' \hat{\psi}^\dagger(\mathbf{r}) \hat{\psi}^\dagger(\mathbf{r}') V(\mathbf{r} - \mathbf{r}') \hat{\psi}(\mathbf{r}') \hat{\psi}(\mathbf{r}) \ . \tag{A.8}$$

In this form, the HAMILTONian suggests the name *second quantization*, since the above expression looks like the expectation value of the HAMILTONian taken between wave functions. Both (A.5) and (A.8) are equivalent since the integration over spatial coordinates produces the single-particle matrix elements of the kinetic energy, potential and interaction potential energy, leaving a sum of these matrix elements multiplied by the appropriate annihilation and creation operators.

The methods of quantum field theory also allow us to concentrate on the few matrix elements of interest, thus avoiding the need for dealing directly with the many-particle wave function and the coordinates of all the remaining particles. Finally, the GREEN's functions contain the most important physical information such as the ground-state energy and other thermodynamic functions, the energy and life time of excited states, and the response to external perturbations. Unfortunately, the exact GREEN's functions are not easier to determine than the original wave function, and we therefore make use of perturbation theory which can be expressed in the systematic language of FEYNMAN rules and diagrams. These rules allow one to evaluate physical quantities to any perturbation order.

Appendix B

Time Evolution Pictures

The time evolution of operators and state vectors in quantum mechanics can be expressed in different representations. The SCHRÖDINGER, the interaction, and the HEISENBERG representations are useful in analyzing the second-quantized form of the SCHRÖDINGER equation. The HAMILTONian is assumed to be of the form (see (3.1))

$$\hat{H} \;=\; \hat{H}_0 \;+\; \hat{H}^{\mathrm{int}}, \tag{B.1}$$

where $\hat{H}_0$ is the non-interacting part, which is assumed to be exactly solvable. $\hat{H}^{\mathrm{int}}$ contains all the interactions, such as carrier-carrier, carrier-phonon, impurity scattering, and so forth.

B.1 SCHRÖDINGER Picture

In the SCHRÖDINGER picture the operators $\hat{O}_{\mathrm{S}}$ are time-independent

$$\hat{O}_{\mathrm{S}}(t) \;=\; \hat{O}_{\mathrm{S}}(t_0) \;=\; \hat{O}_{\mathrm{S}}\;, \tag{B.2}$$

where t_0 is assumed to be the time reference point. The time dependence of the state vector $\Psi_{\mathrm{S}}(t)$ is obtained from the SCHRÖDINGER equation

$$i\hbar\partial_t|\Psi_{\mathrm{S}}(t)\rangle \;=\; \hat{H}|\Psi_{\mathrm{S}}(t)\rangle\;, \tag{B.3}$$

which has the formal solution

$$|\Psi_{\mathrm{S}}(t)\rangle \;=\; e^{-i\hat{H}(t-t_0)/\hbar}|\Psi_{\mathrm{S}}(t_0)\rangle \tag{B.4}$$

B.2 Interaction Picture

In the interaction representation both the state vectors and the operators are time-dependent. The state vector in the interaction representation is given by

$$|\Psi_{\mathrm{I}}(t)\rangle \;=\; e^{i\hat{H}_0 t/\hbar}|\Psi_{\mathrm{S}}(t)\rangle \;, \tag{B.5}$$

which is merely a unitary transformation at the time t. The equation of motion of this state vector is found by taking the time derivative

$$\begin{aligned} i\hbar\partial_t|\Psi_{\mathrm{I}}(t)\rangle \;&=\; -\hat{H}_0 e^{i\hat{H}_0 t/\hbar}|\Psi_{\mathrm{S}}(t)\rangle + e^{i\hat{H}_0 t/\hbar} i\hbar\partial_t|\Psi_{\mathrm{S}}(t)\rangle \;, \\ &=\; e^{i\hat{H}_0 t/\hbar}[-\hat{H}_0 + \hat{H}_0 + \hat{H}^{\mathrm{int}}]e^{-i\hat{H}_0 t/\hbar}|\Psi_{\mathrm{I}}(t)\rangle \;. \end{aligned} \tag{B.6}$$

Therefore, one obtains the following set of equations in the interaction picture

$$\begin{aligned} i\hbar\partial_t|\Psi_{\mathrm{I}}(t)\rangle \;&=\; \hat{H}^{\mathrm{int}}(t)|\Psi_{\mathrm{I}}(t)\rangle \;, \\ \hat{H}^{\mathrm{int}}(t) \equiv \;& e^{i\hat{H}_0 t/\hbar}\hat{H}^{\mathrm{int}}e^{-i\hat{H}_0 t/\hbar} \;. \end{aligned} \tag{B.7}$$

An arbitrary matrix element in the Schrödinger picture can be written as

$$\langle\Psi'_{\mathrm{S}}(t)|\hat{O}_{\mathrm{S}}|\Psi_{\mathrm{S}}(t)\rangle \;=\; \langle\Psi'_{\mathrm{I}}(t)|e^{i\hat{H}_0 t/\hbar}\hat{O}_{\mathrm{S}}e^{-i\hat{H}_0 t/\hbar}|\Psi_{\mathrm{I}}(t)\rangle \;, \tag{B.8}$$

which suggests the following definition of an operator in the interaction picture

$$\hat{O}_{\mathrm{I}}(t) \;=\; e^{i\hat{H}_0 t/\hbar}\hat{O}_{\mathrm{S}}e^{-i\hat{H}_0 t/\hbar} \;. \tag{B.9}$$

B.3 Heisenberg Picture

In the Heisenberg representation state vectors are defined as

$$|\Psi_{\mathrm{H}}(t)\rangle \;=\; e^{i\hat{H}t/\hbar}|\Psi_{\mathrm{S}}(t)\rangle \;. \tag{B.10}$$

Its time derivative may be combined with (B.3) to yield $i\hbar\partial_t|\Psi_{\mathrm{H}}(t)\rangle = 0$, which shows that $|\Psi_{\mathrm{H}}(t)\rangle$ is time-independent. Since an arbitrary matrix element in the Schrödinger picture can be written as

$$\langle\Psi'_{\mathrm{S}}(t)|\hat{O}_{\mathrm{S}}|\Psi_{\mathrm{S}}(t)\rangle \;=\; \langle\Psi'_{\mathrm{H}}(t)|e^{i\hat{H}t/\hbar}\hat{O}_{\mathrm{S}}e^{-i\hat{H}t/\hbar}|\Psi_{\mathrm{H}}(t)\rangle \;, \tag{B.11}$$

a general operator in the Heisenberg picture is given by

$$\hat{O}_{\mathrm{H}}(t) \;=\; e^{i\hat{H}t/\hbar}\hat{O}_{\mathrm{S}}e^{-i\hat{H}t/\hbar} \;. \tag{B.12}$$

Equation (B.12) can be rewritten in terms of the interaction picture operators

$$\hat{O}_{\mathrm{H}}(t) \;=\; e^{i\hat{H}t/\hbar}e^{-i\hat{H}_0 t/\hbar}\hat{O}_{\mathrm{I}}(t)e^{i\hat{H}_0 t/\hbar}e^{-i\hat{H}t/\hbar} \;, \tag{B.13}$$

or in terms of the operator $\hat{S}$ derived in the next section

$$\hat{O}_{\mathrm{H}}(t) \;=\; \hat{S}(0,t)\hat{O}_{\mathrm{I}}(t)\hat{S}(t,0) \;. \tag{B.14}$$

B.4 The Evolution Operator $\hat{S}$

To solve the equations of motion in the interaction picture (B.7), a unitary operator $\hat{S}(t,t_0)$ that determines the state vector at time t in terms of the state vector at time t_0 is introduced

$$|\Psi_\mathrm{I}(t)\rangle \;=\; \hat{S}(t,t_0)|\Psi_\mathrm{I}(t_0)\rangle \;, \tag{B.15}$$

$\hat{S}$ satisfies the initial condition $\hat{S}(t_0,t_0) = 1$. For finite times $\hat{S}(t,t_0)$ can be constructed explicitly by employing the Schrödinger picture

$$\begin{aligned} |\Psi_\mathrm{I}(t)\rangle &= e^{i\hat{H}_0 t/\hbar}|\Psi_\mathrm{S}(t)\rangle \;, \\ &= e^{i\hat{H}_0 t/\hbar}e^{-i\hat{H}(t-t_0)/\hbar}|\Psi_\mathrm{S}(t_0)\rangle \;, \\ &= e^{i\hat{H}_0 t/\hbar}e^{-i\hat{H}(t-t_0)/\hbar}e^{-i\hat{H}_0 t_0/\hbar}|\Psi_\mathrm{I}(t_0)\rangle \;, \end{aligned} \tag{B.16}$$

which therefore identifies

$$\hat{S}(t,t_0) \;=\; e^{i\hat{H}_0 t/\hbar}e^{-i\hat{H}(t-t_0)/\hbar}e^{-i\hat{H}_0 t_0/\hbar} \;. \tag{B.17}$$

Since $\hat{H}$ and $\hat{H}_0$ do not commute with each other, the order of the operators must be carefully maintained. Equation (B.17) immediately yields several general properties of $\hat{S}$ [189]

- $\hat{S}^\dagger(t,t_0)\hat{S}(t,t_0) = \hat{S}(t,t_0)\hat{S}^\dagger(t,t_0) = 1$, implying that $\hat{S}$ is unitary $\hat{S}^\dagger(t,t_0) = \hat{S}^{-1}(t,t_0)$,
- $\hat{S}(t_1,t_2)\hat{S}(t_2,t_3) = \hat{S}(t_1,t_3)$, which shows that $\hat{S}$ has the group property, and
- $\hat{S}(t,t_0)\hat{S}(t_0,t) = 1$, implying that $\hat{S}(t_0,t) = \hat{S}^\dagger(t,t_0)$.

Although (B.17) is the formal solution to the problem posed by (B.15), it is not very useful for computational purposes. Instead one can construct an integral equation for $\hat{S}$, which can then be solved by iteration. It follows from (B.7) and (B.15) that $\hat{S}$ satisfies the differential equation

$$i\hbar\partial_t\hat{S}(t,t_0) \;= \hat{H}_\mathrm{I}^\mathrm{int}(t)\hat{S}(t,t_0) \;. \tag{B.18}$$

Integrating both sides of the (B.18) with respect to time with the initial condition $\hat{S}(t_0,t_0) = 1$ yields

$$\begin{aligned} \hat{S}(t,t_0) &= \hat{S}(t_0,t_0) \;-\; \frac{i}{\hbar}\int_{t_0}^{t} dt_1 \hat{H}_\mathrm{I}^\mathrm{int}(t_1)\hat{S}(t_1,t_0) \\ &= 1 \;-\; \frac{i}{\hbar}\int_{t_0}^{t} dt_1 \hat{H}_\mathrm{I}^\mathrm{int}(t_1)\hat{S}(t_1,t_0) \;. \end{aligned} \tag{B.19}$$

By iterating this equation repeatedly one gets

$$\begin{aligned}\hat{S}(t,t_0) &= 1 - \frac{i}{\hbar}\int_{t_0}^{t} dt_1 \hat{H}_{\mathrm{I}}^{\mathrm{int}}(t_1) + \left(\frac{-i}{\hbar}\right)^2 \int_{t_0}^{t} dt_1 \int_{t_0}^{t_1} dt_2 \hat{H}_{\mathrm{I}}^{\mathrm{int}}(t_1)\hat{H}_{\mathrm{I}}^{\mathrm{int}}(t_2) + \\ &\quad \ldots + \left(\frac{-i}{\hbar}\right)^n \int_{t_0}^{t} dt_1 \int_{t_0}^{t_1} dt_2 \ldots \int_{t_0}^{t_{n-1}} dt_n \hat{H}_{\mathrm{I}}^{\mathrm{int}}(t_1)\hat{H}_{\mathrm{I}}^{\mathrm{int}}(t_2)\ldots\hat{H}_{\mathrm{I}}^{\mathrm{int}}(t_n) \\ &= \sum_{n=0}^{\infty} \left(\frac{-i}{\hbar}\right)^n \int_{t_0}^{t} dt_1 \int_{t_0}^{t_1} dt_2 \ldots \int_{t_0}^{t_{n-1}} dt_n \hat{H}_{\mathrm{I}}^{\mathrm{int}}(t_1)\hat{H}_{\mathrm{I}}^{\mathrm{int}}(t_2)\ldots\hat{H}_{\mathrm{I}}^{\mathrm{int}}(t_n)\ .\end{aligned} \tag{B.20}$$

Equation (B.20) has the characteristic feature that the operator containing the latest time stands farthest to the left. At this point it is convenient to introduce the *time-ordering operator* denoted by the symbol T_{t}

$$T_{\mathrm{t}}\{\hat{A}(t_1)\hat{B}(t_2)\} = \theta(t_1 - t_2)\hat{A}(t_1)\hat{B}(t_2) + \theta(t_2 - t_1)\hat{B}(t_2)\hat{A}(t_1)\ . \tag{B.21}$$

where $\theta(t)$ is the step function[1]. Each time two FERMIons are interchanged, the resulting expression changes its sign. By rearranging the integral using T_{t}

$$\begin{aligned}&\frac{1}{2!}\int_{t_0}^{t} dt_1 \int_{t_0}^{t} dt_2 T_{\mathrm{t}}\{\hat{H}_{\mathrm{I}}^{\mathrm{int}}(t_1)\hat{H}_{\mathrm{I}}^{\mathrm{int}}(t_2)\} = \\ &\qquad \frac{1}{2!}\int_{t_0}^{t} dt_1 \int_{t_0}^{t_1} dt_2 \hat{H}_{\mathrm{I}}^{\mathrm{int}}(t_1)\hat{H}_{\mathrm{I}}^{\mathrm{int}}(t_2) + \frac{1}{2!}\int_{t_0}^{t} dt_2 \int_{t_0}^{t_1} dt_1 \hat{H}_{\mathrm{I}}^{\mathrm{int}}(t_2)\hat{H}_{\mathrm{I}}^{\mathrm{int}}(t_1)\ .\end{aligned} \tag{B.22}$$

The second term on the right hand-side is equal to the first, which is easy to see by just redefining the integration variables $t_1 \to t_2$, $t_2 \to t_1$. Thus one gets

$$\frac{1}{2!}\int_{t_0}^{t} dt_1 \int_{t_0}^{t} dt_2\ T_{\mathrm{t}}\{\hat{H}_{\mathrm{I}}^{\mathrm{int}}(t_1)\hat{H}_{\mathrm{I}}^{\mathrm{int}}(t_2)\} = \int_{t_0}^{t} dt_1 \int_{t_0}^{t_1} dt_2\ \hat{H}_{\mathrm{I}}^{\mathrm{int}}(t_1)\hat{H}_{\mathrm{I}}^{\mathrm{int}}(t_2)\ . \tag{B.23}$$

Thus for the expansion of the $\hat{S}(t,t_0)$ one obtains

$$\begin{aligned}\hat{S}(t,t_0) &= \sum_{n=0}^{\infty} \frac{1}{n!}\left(\frac{-i}{\hbar}\right)^n \int_{t_0}^{t} dt_1 \int_{t_0}^{t} dt_2 \ldots \int_{t_0}^{t} dt_n\ T_{\mathrm{t}}\{\hat{H}_{\mathrm{I}}^{\mathrm{int}}(t_1)\hat{H}_{\mathrm{I}}^{\mathrm{int}}(t_2)\ldots\hat{H}_{\mathrm{I}}^{\mathrm{int}}(t_n)\} \\ &= T_{\mathrm{t}}\{\exp\left(-\frac{i}{\hbar}\int_{t_0}^{t} dt' \hat{H}_{\mathrm{I}}^{\mathrm{int}}(t')\right)\}\ .\end{aligned} \tag{B.24}$$

---

[1] The step function is defined as $\theta(t) = \begin{cases} 1 & t > 0 \\ \frac{1}{2} & t = 0 \\ 0 & t < 0 \end{cases}$

B.5 Imaginary Time Operators

At finite temperature under thermodynamic equilibrium the state of a system is described by the equilibrium density operator $\hat{\rho}$. For a given $\hat{\rho}$ the ensemble average of any operator $\hat{O}$ can be calculated as (see (3.11))

$$\langle\hat{O}\rangle = \frac{\mathrm{Tr}[e^{-\beta\hat{K}}\hat{O}]}{\mathrm{Tr}[e^{-\beta\hat{K}}]} , \tag{B.25}$$

where $\hat{K} = \hat{H} - E_\mathrm{F}\hat{N}$ may be interpreted as a *grand canonical* Hamiltonian. For any Schrödinger operator $\hat{O}_\mathrm{S}$, the *so called* modified Heisenberg and interaction pictures can be introduced as

$$\begin{aligned} \hat{O}_\mathrm{K}(\tau) &\equiv e^{\hat{K}\tau/\hbar}\,\hat{O}_\mathrm{S}\,e^{-\hat{K}\tau/\hbar} , \\ \hat{O}_\mathrm{I}(\tau) &\equiv e^{\hat{K}_0\tau/\hbar}\,\hat{O}_\mathrm{S}\,e^{-\hat{K}_0\tau/\hbar} , \end{aligned} \tag{B.26}$$

where $\hat{K}_0$ includes only the non-interacting part of $\hat{K}$. It should be noticed that $\hat{O}^\dagger_\mathrm{K}(\tau) = e^{\hat{K}\tau/\hbar}\hat{O}^\dagger_\mathrm{S}e^{-\hat{K}\tau/\hbar}$ is not the adjoint of $\hat{O}_\mathrm{K}(\tau)$ as long as τ is real. If τ is interpreted as a complex variable, however, it may be analytically continued to a pure imaginary value $\tau = it$. The resulting expression $\hat{O}^\dagger_\mathrm{K}(\tau)$ then becomes the true adjoint of $\hat{O}_\mathrm{K}(\tau)$ and is formally identical with the original Heisenberg picture defined in (B.12), apart from the substitution of $\hat{K}$ for $\hat{H}$. For this reason (B.26) are sometimes called *imaginary-time* operators.

The modified Heisenberg and interaction pictures are related by (compare (B.13) and (B.14))

$$\begin{aligned} \hat{O}_\mathrm{K}(\tau) &= e^{\hat{K}\tau/\hbar}e^{-\hat{K}_0\tau/\hbar}\hat{O}_\mathrm{I}(\tau)e^{\hat{K}_0\tau/\hbar}e^{-i\hat{K}\tau/\hbar} , \\ &= \hat{\mathcal{S}}(0,\tau)\hat{O}_\mathrm{I}(\tau)\hat{\mathcal{S}}(\tau,0) , \end{aligned} \tag{B.27}$$

where the operator $\hat{\mathcal{S}}$ is defined by (compare (B.17))

$$\hat{\mathcal{S}}(\tau,\tau_0) = e^{\hat{K}_0\tau/\hbar}\,e^{-\hat{K}(\tau-\tau_0)/\hbar}\,e^{-\hat{K}_0\tau_0/\hbar} . \tag{B.28}$$

Note that $\hat{\mathcal{S}}$ is not unitary, but it still satisfies the group property

$$\hat{\mathcal{S}}(\tau_1,\tau_2)\,\hat{\mathcal{S}}(\tau_2,\tau_3) = \hat{\mathcal{S}}(\tau_1,\tau_3) , \tag{B.29}$$

and the boundary condition

$$\hat{\mathcal{S}}(\tau_0,\tau_0) = 1 . \tag{B.30}$$

In addition, the equation of motion of $\hat{\mathcal{S}}$ is calculated as

$$\begin{aligned} \hbar\partial_\tau\hat{\mathcal{S}}(\tau,\tau_0) &= e^{\hat{K}_0\tau/\hbar}\,(\hat{K}_0 - \hat{K})\,e^{-\hat{K}(\tau-\tau_0)/\hbar}\,e^{-\hat{K}_0\tau_0/\hbar} , \\ &= e^{\hat{K}_0\tau/\hbar}\,(\hat{K}_0 - \hat{K})\,e^{-\hat{K}_0\tau/\hbar}\hat{\mathcal{S}}(\tau,\tau_0) , \\ &= \hat{K}^\mathrm{int}(\tau)\hat{\mathcal{S}}(\tau,\tau_0) , \end{aligned} \tag{B.31}$$

where

$$\hat{K}^{\mathrm{int}}(\tau) \;\equiv\; e^{\hat{K}_0\tau/\hbar}\hat{K}^{\mathrm{int}}e^{-\hat{K}_0\tau/\hbar} \; . \tag{B.32}$$

It follows that the operator $\hat{\mathcal{S}}$ obeys essentially the same differential equation as the unitary operator introduced in (B.15), and one may immediately write down the solution (compare (B.24))

$$\begin{aligned} \hat{\mathcal{S}}(\tau,\tau_0) \;&=\; \sum_{n=0}^{\infty}\frac{1}{n!}\left(\frac{-1}{\hbar}\right)^n \int\limits_{\tau_0}^{\tau} d\tau_1 \int\limits_{\tau_0}^{\tau} d\tau_2 \ldots \int\limits_{\tau_0}^{\tau} d\tau_n \; T_\tau\{\hat{K}_{\mathrm{I}}^{\mathrm{int}}(\tau_1)\hat{K}_{\mathrm{I}}^{\mathrm{int}}(\tau_2)\ldots\hat{K}_{\mathrm{I}}^{\mathrm{int}}(\tau_n)\} \; , \\ &=\; T_\tau\{\exp\left(-\frac{1}{\hbar}\int\limits_{\tau_0}^{\tau} d\tau'\hat{K}_{\mathrm{I}}^{\mathrm{int}}(\tau')\right)\} \; . \end{aligned} \tag{B.33}$$

If τ is set equal to $\beta\hbar$, (B.28) may be rewritten as

$$e^{-\beta\hat{K}} \;=\; e^{-\beta\hat{K}_0}\hat{\mathcal{S}}(\beta\hbar,0) \; , \tag{B.34}$$

which relates the many particle density operator to the single-particle density operator by means of an imaginary time-evolution operator.

Appendix C

Review of Thermodynamics and Statistical Mechanics

The fundamental thermodynamic identity

$$dE \;=\; TdS \;-PdV \;+\; E_{\mathrm{F}}dN \;, \tag{C.1}$$

specifies the change in the internal energy E arising from small independent changes in the entropy S, the volume V, and the number of particles N. Equation (C.1) shows that the internal energy is a function of these three variables, $E = E(S, V, N)$, and that the temperature T, the pressure P, and the FERMI energy E_{F} (also called the chemical potential) are related to the partial derivatives of E

$$T \;=\; \left(\frac{\partial E}{\partial S}\right)_{VN} \;, \qquad P \;=\; -\left(\frac{\partial E}{\partial V}\right)_{SN} \;, \qquad E_{\mathrm{F}} \;=\; \left(\frac{\partial E}{\partial N}\right)_{SV} \;. \tag{C.2}$$

In practice, however, experiments are usually performed at fixed T and it is convenient to make LEGENDRE transformation to the variables (T, V, N) or (T, P, N). The resulting functions are known as HELMHOLTZ *free energy* $F(T, V, N)$ and GIBBS *free energy* $G(T, P, N)$. It is often important to consider the set of independent variables (T, V, E_{F}), which is appropriate for variable N. A further LEGENDRE transformation leads to the *thermodynamic potential*

$$\Omega(T, V, E_{\mathrm{F}}) \;=\; F \;-\; E_{\mathrm{F}}N \;=\; E \;-\; TS \;-\; E_{\mathrm{F}}N \;, \tag{C.3}$$

with the corresponding differential and coefficients

$$d\Omega(T, V, E_{\mathrm{F}}) \;=\; -\,SdT \;-\; PdV \;-NdE_{\mathrm{F}} \;, \tag{C.4}$$

$$S \;=\; -\left(\frac{\partial \Omega}{\partial T}\right)_{VE_{\mathrm{F}}} \;, \qquad P \;=\; -\left(\frac{\partial \Omega}{\partial V}\right)_{TE_{\mathrm{F}}} \;, \qquad N \;=\; -\left(\frac{\partial \Omega}{\partial E_{\mathrm{F}}}\right)_{TV} \;. \tag{C.5}$$

Although E, F, G, and Ω represent equivalent ways of describing the same system, their natural independent variables differ in one important way. In particular, the set (S, V, N) consists entirely of extensive variables, proportional to the actual amount of matter present. The transformation to F and then to G or Ω may be interpreted as reducing the number of extensive variables in favor of intensive ones that are independent of the total amount of matter.

To this point, only macroscopic thermodynamics has been discussed. The microscopic content of the theory must be added separately through statistical mechanics, which relates the thermodynamic functions to the HAMILTONian of the many-particle system. The elementary discussions of statistical mechanics usually consider systems containing a fixed number of particles. This approach, which is refereed to as *canonical ensemble*, is too restricted for our purposes. To include the possibility of a variable number of particles the *grand canonical ensemble* can be employed. For a grand canonical ensemble at FERMI energy E_F and temperature T, the grand partition function Z is defined as

$$\begin{aligned} Z &\equiv \sum_N \sum_i e^{-\beta(E_i - E_\mathrm{F} N)} \ , \\ &= \sum_N \sum_i \langle N_i | e^{-\beta(\hat{H} - E_\mathrm{F}\hat{N})} | N_i \rangle \ \equiv \ \mathrm{Tr}[e^{-\beta(\hat{H} - E_\mathrm{F}\hat{N})}] \ , \end{aligned} \tag{C.6}$$

where i denotes the set of all states for a fixed number of particles N, and the sum implied in the trace is over both i and N. Short-hand notation $\beta = 1/k_\mathrm{B}T$ has been introduced, where k_B is the BOLTZMANN constant. A fundamental result from statistical mechanics states that

$$\Omega(T, V, E_\mathrm{F}) \ = \ -k_\mathrm{B}T \ \ln(Z) \ , \tag{C.7}$$

which allows one to compute all the macroscopic equilibrium thermodynamics from the grand partition function. The statistical operator ρ corresponding to (C.6) is given by

$$\rho \ = \frac{e^{-\beta(\hat{H} - E_\mathrm{F}\hat{N})}}{Z} \ . \tag{C.8}$$

For any operator $\hat{O}$, the ensemble average $\langle \hat{O} \rangle$ is achieved with the prescription

$$\begin{aligned} \langle \hat{O} \rangle &= \mathrm{Tr}[\rho \hat{O}] \ , \\ &= \frac{\mathrm{Tr}[e^{-\beta(\hat{H} - E_\mathrm{F}\hat{N})}\hat{O}]}{\mathrm{Tr}[e^{-\beta(\hat{H} - E_\mathrm{F}\hat{N})}]} \ . \end{aligned} \tag{C.9}$$

By applying these results the properties of a gas of non-interacting Bosons or FERMIons can be studied. If (C.6) is written out in detail with the complete set of states in the abstract occupation number HILBERT space, one gets

$$\begin{aligned} Z &= \mathrm{Tr}[e^{-\beta(\hat{H} - E_\mathrm{F}\hat{N})}] \ , \\ &= \sum_{n_1 \ \dots \ n_\infty} \langle n_1 \dots n_\infty | e^{-\beta(\hat{H} - E_\mathrm{F}\hat{N})} | n_1 \dots n_\infty \rangle \ . \end{aligned} \tag{C.10}$$

Since these states are eigen-states of the non-interacting HAMILTONian $\hat{H}_0$ and the number operator $\hat{N}$, both operators can be replaced by their eigen-values

$$Z \ = \sum_{n_1 \dots n_\infty} \langle n_1 \dots n_\infty | \exp\left[-\beta \left(\sum_i E_i n_i - E_\mathrm{F} \sum_i n_i \right) \right] | n_1 \dots n_\infty \rangle \ . \tag{C.11}$$

The exponential is now a number and is equivalent to a product of exponentials. Therefore, the sum over expectation values factor into a product of traces

$$\begin{aligned} Z &= \sum_{n_1} \langle n_1 | e^{-\beta(E_1 n_1 - E_\mathrm{F} n_1)} | n_1 \rangle \ \dots \ \sum_{n_\infty} \langle n_\infty | e^{-\beta(E_\infty n_\infty - E_\mathrm{F} n_\infty)} | n_\infty \rangle \ , \\ &= \prod_{i=1}^{\infty} \sum_{n_i} e^{-\beta(E_i - E_\mathrm{F}) n_i} \ . \end{aligned} \tag{C.12}$$

C.1 FERMI-DIRAC Statistics

For FERMIons the occupation numbers are either 0 or 1, and the sum in (C.12) is restricted to these values

$$\begin{aligned} Z_{\mathrm{F}} &= \prod_{i=1}^{\infty} \sum_{n_i=0}^{1} \left(e^{-\beta(E_i-E_{\mathrm{F}})}\right)^{n_i} , \\ &= \prod_{i=1}^{\infty} \left(1+e^{-\beta(E_i-E_{\mathrm{F}})}\right) . \end{aligned} \tag{C.13}$$

Taking the logarithm of both sides, one gets

$$\Omega_{\mathrm{F}}(T,V,E_{\mathrm{F}}) = \; k_{\mathrm{B}}T \sum_{i=1}^{\infty} \ln\left(1+e^{-\beta(E_i-E_{\mathrm{F}})}\right) , \tag{C.14}$$

while the mean number of FERMIons is given by the FERMI-DIRAC distribution function

$$n_{\mathrm{F}} \; \equiv \; \sum_{i=1}^{\infty} n_i \; = \; \sum_{i=1}^{\infty} \frac{1}{e^{\beta(E_i-E_{\mathrm{F}})}+1} . \tag{C.15}$$

C.2 Bose-EINSTEIN Statistics

For Bosons the occupation number is not restricted, so one must sum n_i over all integers in (C.12)

$$\begin{aligned} Z_{\mathrm{B}} &= \prod_{i=1}^{\infty} \sum_{n_i=0}^{\infty} \left(e^{-\beta(E_i-E_{\mathrm{F}})}\right)^{n_i} , \\ &= \prod_{i=1}^{\infty} \left(1-e^{-\beta(E_i-E_{\mathrm{F}})}\right)^{-1} . \end{aligned} \tag{C.16}$$

The logarithm of (C.16) yields the thermodynamic potential

$$\begin{aligned} \Omega_{\mathrm{B}}(T,V,E_{\mathrm{F}}) &= \; - \; k_{\mathrm{B}}T \ln\left(\prod_{i=1}^{\infty} \left(1-e^{-\beta(E_i-E_{\mathrm{F}})}\right)^{-1}\right) , \\ &= \; k_{\mathrm{B}}T \sum_{i=1}^{\infty} \ln\left(1-e^{-\beta(E_i-E_{\mathrm{F}})}\right) . \end{aligned} \tag{C.17}$$

The mean number of particles is obtained from Ω_0 by differentiating with respect to the FERMI energy, as in (C.5), by keeping T and V (equivalently the E_i) fixed. As a result, the mean number of Bosons is given by the Bose-EINSTEIN distribution function

$$n_{\mathrm{B}} \; \equiv \; \sum_{i=1}^{\infty} n_i \; = \; \sum_{i=1}^{\infty} \frac{1}{e^{\beta(E_i-E_{\mathrm{F}})}-1} , \tag{C.18}$$

where n_i is the mean occupation number in the ith state.

Appendix D

Non-Interacting GREEN's Functions

The non-interacting or free GREEN's function is used in the perturbation expansions described in Section 3.4. In this appendix real-time GREEN's functions for both electrons and phonons are derived.

D.1 Non-Interacting FERMIons

The HAMILTONian for non-interacting electrons (FERMIons) in momentum representation is

$$H_0 \;=\; \sum_{\mathbf{k}} \xi_{\mathbf{k}} c_{\mathbf{k}}^{\dagger} c_{\mathbf{k}} \;, \tag{D.1}$$

where $\xi_{\mathbf{k}} = E_{\mathbf{k}} - E_{\mathrm{F}}$ is the single-particle energy measured with respect to the FERMI energy $c_{\mathbf{k}}$ and $c_{\mathbf{k}}^{\dagger}$ are the FERMIon annihilation and creation operators, respectively (Appendix A). The time-evolution of the annihilation operator in the HEISENBERG picture is (Appendix B)

$$c_{\mathbf{k}}(t) \;=\; e^{iH_0 t/\hbar}\; c_{\mathbf{k}}\; e^{-iH_0 t/\hbar} \;, \tag{D.2}$$

so the operator obeys the equation

$$i\hbar \partial_t c_{\mathbf{k}}(t) \;=\; [c_{\mathbf{k}}(t), H_0] \;=\; \xi_{\mathbf{k}} c_{\mathbf{k}}(t) \;, \tag{D.3}$$

which has the solution

$$c_{\mathbf{k}}(t) \;=\; e^{-i\xi_{\mathbf{k}} t/\hbar}\; c_{\mathbf{k}} \;. \tag{D.4}$$

The creation operator for FERMIons is the just the HERMITian conjugate of $c_{\mathbf{k}}$, i.e.

$$c_{\mathbf{k}}^{\dagger}(t) \;=\; e^{i\xi_{\mathbf{k}} t/\hbar}\; c_{\mathbf{k}}^{\dagger} \;. \tag{D.5}$$

The non-interacting real-time GREEN's functions (Section 3.7.1) for FERMIons in momentum representation are now given by

$$\begin{aligned}
G_0^<(\mathbf{k},t;\mathbf{k}',t') &\equiv +i\hbar^{-1}\langle c_{\mathbf{k}'}^\dagger(t')c_\mathbf{k}(t)\rangle_0 \ ,\\
&= +i\hbar^{-1}e^{-i\xi_\mathbf{k}(t-t')/\hbar}n_\mathbf{k}\delta_{\mathbf{k},\mathbf{k}'} \ ,\\
G_0^>(\mathbf{k},t;\mathbf{k}',t') &\equiv -i\hbar^{-1}\langle c_\mathbf{k}(t)c_{\mathbf{k}'}^\dagger(t')\rangle_0 \ ,\\
&= -i\hbar^{-1}e^{-i\xi_\mathbf{k}(t-t')/\hbar}[1-n_\mathbf{k}]\delta_{\mathbf{k},\mathbf{k}'} \ ,\\
G_0^\mathrm{r}(\mathbf{k},t;\mathbf{k}',t') &\equiv -i\hbar^{-1}\theta(t-t')\langle c_\mathbf{k}(t)c_{\mathbf{k}'}^\dagger(t')+c_{\mathbf{k}'}^\dagger(t')c_\mathbf{k}(t)\rangle_0 \ ,\\
&= -i\hbar^{-1}\theta(t-t')e^{-i\xi_\mathbf{k}(t-t')/\hbar}\delta_{\mathbf{k},\mathbf{k}'} \ ,\\
G_0^\mathrm{a}(\mathbf{k},t;\mathbf{k}',t') &\equiv +i\hbar^{-1}\theta(t'-t)\langle c_\mathbf{k}(t)c_{\mathbf{k}'}^\dagger(t')+c_{\mathbf{k}'}^\dagger(t')c_\mathbf{k}(t)\rangle_0 \ ,\\
&= +i\hbar^{-1}\theta(t'-t)e^{-i\xi_\mathbf{k}(t'-t)/\hbar}\delta_{\mathbf{k},\mathbf{k}'} \ ,
\end{aligned} \tag{D.6}$$

where $n_\mathbf{k} = \langle c_\mathbf{k}^\dagger c_\mathbf{k}\rangle$ is the average occupation number of the state $\mathbf{k}$. The GREEN's functions depend only on time differences. One usually Fourier transforms the time difference coordinate, $t-t'$, to energy

$$\begin{aligned}
G_0^<(\mathbf{k},E) &= +2\pi i n_\mathbf{k}\delta(E-\xi_\mathbf{k}) \ ,\\
G_0^>(\mathbf{k},E) &= +2\pi i[1-n_\mathbf{k}]\delta(E-\xi_\mathbf{k}) \ ,\\
G_0^\mathrm{r}(\mathbf{k},E) &= \frac{1}{E-\xi_\mathbf{k}+i\eta} \ ,\\
G_0^\mathrm{a}(\mathbf{k},E) &= \frac{1}{E-\xi_\mathbf{k}-i\eta} \ ,
\end{aligned} \tag{D.7}$$

where $\eta = 0^+$ is a small positive number. Assuming that the particles are in thermal equilibrium one obtains $n_\mathbf{k} = n_\mathrm{F}(\xi_\mathbf{k})$, where n_F is the FERMI-DIRAC distribution function (Appendix C.1). The result (D.7) shows that $G^<$ and $G^>$ provide information about the statistics, such as occupation $n_\mathbf{k}$ or un-occupation $1-n_\mathbf{k}$ of the states, and G^r and G^a provide information about the states regardless of their occupation. The spectral function $A_0(\mathbf{k},E)$ for FERMIons is therefore defined as

$$\begin{aligned}
A_0(\mathbf{k},E) &= +i[G_0^\mathrm{r}(\mathbf{k},E)-G_0^\mathrm{a}(\mathbf{k},E)] = -2\Im\mathrm{m}[G_0^\mathrm{r}(\mathbf{k},E)] \ ,\\
&= +2\pi\delta(E-\xi_\mathbf{k}) \ ,
\end{aligned} \tag{D.8}$$

where the following relation is used

$$\frac{1}{x\pm i\eta} = \mathcal{P}\left(\frac{1}{x}\right) \mp i\pi\delta(x) \ , \tag{D.9}$$

where $\mathcal{P}$ indicates the principal value. Under equilibrium the lesser and greater GREEN's functions can be rewritten as

$$\begin{aligned}
G_0^<(\mathbf{k},E) &= i n_\mathrm{F} A_0(\mathbf{k},E) \ ,\\
G_0^>(\mathbf{k},E) &= i[1-n_\mathrm{F}]A_0(\mathbf{k},E) \ .
\end{aligned} \tag{D.10}$$

D.2 Non-Interacting Bosons

The HAMILTONian for non-interacting phonons (Bosons) in momentum representation is

$$H_0 \;=\; \sum_{\mathbf{q},\lambda} \hbar\omega_{\mathbf{q},\lambda} \left(b^\dagger_{\mathbf{q},\lambda} b_{\mathbf{q},\lambda} \;+\; \frac{1}{2} \right) \;, \tag{D.11}$$

where $\hbar\omega_{\mathbf{q},\lambda}$ is the energy of mode $\mathbf{q}$ with the polarization λ, $b_{\mathbf{q},\lambda}$, and $b^\dagger_{\mathbf{q},\lambda}$ are the Bosons annihilation and creation operators. The time-evolution of the annihilation operator in the HEISENBERG picture is

$$b_{\mathbf{q},\lambda}(t) \;=\; e^{iH_0 t/\hbar}\, b_{\mathbf{q},\lambda}\, e^{-iH_0 t/\hbar} \;, \tag{D.12}$$

so the operator obeys the equation

$$i\hbar\partial_t b_{\mathbf{q},\lambda}(t) \;=\; [b_{\mathbf{q},\lambda}(t), H_0] \;=\; \hbar\omega_{\mathbf{q},\lambda} b_{\mathbf{q},\lambda}(t) \;, \tag{D.13}$$

which has the solution

$$b_{\mathbf{q},\lambda}(t) \;=\; e^{-i\omega_{\mathbf{q},\lambda} t}\, b_{\mathbf{q},\lambda} \;. \tag{D.14}$$

The creation operator for Bosons is the just the HERMITian conjugate of $b_{\mathbf{q}}$, i.e.

$$b^\dagger_{\mathbf{q},\lambda}(t) \;=\; e^{+i\omega_{\mathbf{q},\lambda} t}\, b^\dagger_{\mathbf{q},\lambda} \;. \tag{D.15}$$

The non-interacting real-time GREEN's functions for Bosons in momentum representation are now given by

$$\begin{aligned}
D^<_{\lambda_0}(\mathbf{q},t;\mathbf{q}',t') \;&\equiv\; -i\hbar^{-1}\langle \hat{A}^\dagger_{\mathbf{q}',\lambda}(t')\hat{A}_{\mathbf{q},\lambda}(t)\rangle_0 \;, \\
&=\; -i\hbar^{-1}\langle b^\dagger_{\mathbf{q}',\lambda}(t') b_{\mathbf{q},\lambda}(t) \;+\; b_{-\mathbf{q}',\lambda}(t') b^\dagger_{-\mathbf{q},\lambda}(t)\rangle_0 \;, \\
&=\; -i\hbar^{-1}\left[e^{-i(\omega_{\mathbf{q},\lambda}t-\omega_{\mathbf{q}',\lambda}t')}\langle b^\dagger_{\mathbf{q}',\lambda} b_{\mathbf{q},\lambda}\rangle_0 \;+\; e^{-i(\omega_{\mathbf{q}',\lambda}t'-\omega_{\mathbf{q},\lambda}t)}\langle b_{-\mathbf{q}',\lambda} b^\dagger_{-\mathbf{q},\lambda}\rangle_0 \right]\delta_{\mathbf{q},\mathbf{q}'} \;, \\
&=\; -i\hbar^{-1}\left[e^{-i\omega_{\mathbf{q},\lambda}(t-t')} n_{\mathbf{q},\lambda} \;+\; e^{+i\omega_{\mathbf{q},\lambda}(t-t')}(n_{\mathbf{q},\lambda}+1) \right]\delta_{\mathbf{q},\mathbf{q}'} \;, \\
&\equiv D^<_{\lambda_0}(\mathbf{q};t,t') \;, \\
D^>_{\lambda_0}(\mathbf{q};t,t') \;&=\; D^<_{\lambda_0}(\mathbf{q};t',t) \;, \\
&=\; -i\hbar^{-1}\left[e^{+i\omega_{\mathbf{q},\lambda}(t-t')} n_{\mathbf{q},\lambda} \;+\; e^{-i\omega_{\mathbf{q},\lambda}(t-t')}(n_{\mathbf{q},\lambda}+1) \right] \;, \\
D^{\mathrm{r}}_{\lambda_0}(\mathbf{q};t,t') \;&\equiv\; -i\hbar^{-1}\theta(t-t')\langle \hat{A}^\dagger_{\mathbf{q},\lambda}(t')\hat{A}_{\mathbf{q},\lambda}(t) \;+\; \hat{A}_{\mathbf{q},\lambda}(t)\hat{A}^\dagger_{\mathbf{q},\lambda}(t')\rangle_0 \;, \\
&=\; -i\hbar^{-1}\theta(t-t')\left[e^{-i\omega_{\mathbf{q},\lambda}(t-t')} \;-\; e^{+i\omega_{\mathbf{q},\lambda}(t-t')} \right] \;, \\
D^{\mathrm{a}}_{\lambda_0}(\mathbf{q};t,t') \;&=\; -i\hbar^{-1}\theta(t'-t)\left[e^{+i\omega_{\mathbf{q},\lambda}(t-t')} \;-\; e^{-i\omega_{\mathbf{q},\lambda}(t-t')} \right] \;,
\end{aligned} \tag{D.16}$$

where $\hat{A}_{\mathbf{q},\lambda}(t) = b_{\mathbf{q},\lambda}(t) + b^{\dagger}_{-\mathbf{q},\lambda}(t)$, $\hat{A}^{\dagger}_{\mathbf{q},\lambda}(t) = \hat{A}^{\dagger}_{-\mathbf{q},\lambda}(t)$, $\omega_{-\mathbf{q},\lambda} = \omega_{\mathbf{q},\lambda}$, and $n_{\mathbf{q},\lambda} = \langle b^{\dagger}_{\mathbf{q},\lambda} b_{\mathbf{q},\lambda}\rangle$ is the occupation number of the state $(\mathbf{q}, \lambda)$, where under thermal equilibrium one obtains $n_{\mathbf{q},\lambda} = n_{\mathrm{B}}(\hbar\omega_{\mathbf{q},\lambda})$, with n_{B} denoting the Bose-EINSTEIN distribution function (Appendix C.2). The GREEN's functions depend only on time differences. One usually Fourier transforms the time difference coordinate, $t - t'$, to energy

$$\begin{aligned}
D^{<}_{\lambda_0}(\mathbf{q}, E) &= -2\pi i \left[n_{\mathbf{q},\lambda}\delta(E - \hbar\omega_{\mathbf{q},\lambda}) + (n_{\mathbf{q},\lambda} + 1)\delta(E + \hbar\omega_{\mathbf{q},\lambda})\right] \ , \\
D^{>}_{\lambda_0}(\mathbf{q}, E) &= -2\pi i \left[n_{\mathbf{q},\lambda}\delta(E + \hbar\omega_{\mathbf{q},\lambda}) + (n_{\mathbf{q},\lambda} + 1)\delta(E - \hbar\omega_{\mathbf{q},\lambda})\right] \ , \\
D^{\mathrm{r}}_{\lambda_0}(\mathbf{q}, E) &= \frac{1}{E - \hbar\omega_{\mathbf{q},\lambda} + i\eta} - \frac{1}{E + \hbar\omega_{\mathbf{q},\lambda} + i\eta} \ , \\
D^{\mathrm{a}}_{\lambda_0}(\mathbf{q}, E) &= \frac{1}{E - \hbar\omega_{\mathbf{q},\lambda} - i\eta} - \frac{1}{E + \hbar\omega_{\mathbf{q},\lambda} - i\eta},
\end{aligned} \tag{D.17}$$

Appendix E

FEYNMAN Diagrams

The WICK theorem allows us to evaluate the exact GREEN's functions as a perturbation expansion involving expressions of free GREEN's functions G_0 and the perturbation potential V (see Section 3.4.1). This expression can be analyzed directly in coordinate or momentum space, in time or energy domain. FEYNMAN introduced the idea of representing different contributions obtained from the WICK decomposition by drawings. These drawings, called diagrams, are very useful for providing an insight into the physical process which these terms represent. The FEYNMAN diagrams provide an illustrative way to solve the many-particle problems and the perturbation expansion of the GREEN's functions.

A diagram dictionary for electrons, which are FERMIons, and phonons, which are Bosons, are shown in Table E. Diagrams for electrons are in coordinate-time space, while phonon diagrams are in momentum-energy space. As described in Section 3.1.1, the GREEN's function can be interpreted as the creation of a particle at $(\mathbf{r}', t')$ in space-time, the propagation of the corresponding perturbation to the point $(\mathbf{r}, t)$ in space-time, where the particle is annihilated. Hence, the full GREEN's function is represented by a double line joining these two points. The free GREEN's function is characterized by a single line.

The COULOMB potential is represented by a wavy line with two inputs and outputs which can be coupled together to describe a self-interaction. The COULOMB interaction is assumed to be instantaneous. It is convenient to consider the inter-particle potential as a static instantaneous potential proportional to a delta function δ_{t_1,t_2}.

Intermediate variables describe events taking place between the two space-time arguments of the GREEN's function, but without any constraints for exact time or place. The overall amplitude involves an integration over these variables. Each time a FERMIon loop appears, the perturbation expression corresponding to this FEYNMAN diagram must be multiplied by a factor -1.

Electrons can also interact with phonons. For phonons it is more convenient to work in the momentum-energy rather than in the space-time domain. Diagrams concerning a free phonon GREEN's functions and the interaction between electrons and phonons are also shown in Table E. The factor $M_{\mathbf{q}}$ refers to the electron-phonon interaction matrix elements.

Expression	Description	Diagram
$i\hbar G(\mathbf{r},t;\mathbf{r}',t')$	Full Green's function	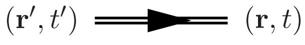
$i\hbar G_0(\mathbf{r},t;\mathbf{r}',t')$	Free Green's function	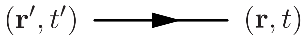
$-iV(\mathbf{r_1},\mathbf{r_2})/\hbar$	Coulomb interaction	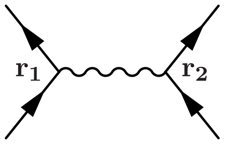
$\int \mathbf{r_1} \int t_1$	Intermediate variable(s)	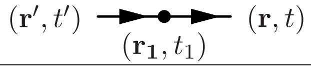
Factor -1	Any Fermion loop	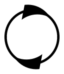
$i\hbar D_0(\mathbf{q};\omega)$	Free phonons	
$-iM_q/\hbar$	Electron-phonon interaction	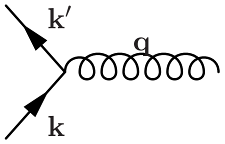

Table E.1: Feynman Diagrams for electrons (Fermions) and phonons (Bosons).

Appendix F

Variational Derivation of Self-Energies

We consider the time evolution of the GREEN's function under the action of the time-independent HAMILTONian $\hat{H} = \hat{H}_0 + \hat{H}^{\rm int}$ and the time-dependent external perturbation $\hat{H}^{\rm ext}$. The latter is included through the evolution operator $\hat{S}^{\rm ext}_{\rm C}$

$$G(12) \;=\; -\frac{i}{\hbar}\langle T_{\rm C}\{\hat{S}^{\rm ext}_{\rm C}\;\hat{\psi}_{\rm H}(1)\;\hat{\psi}^{\dagger}_{\rm H}(2)\}\rangle_0 \;, \tag{F.1}$$

where the abbreviation $1 \equiv (\mathbf{r_1}, t_1)$ is used. To obtain the equation of motion, one can take the derivative of the GREEN's function with respect to time

$$\begin{aligned} i\hbar\partial_t G(12) \;=\;& \delta_{t_1,t_2}\;\langle\hat{\psi}_{\rm H}(1)\;\hat{\psi}^{\dagger}_{\rm H}(2) + \hat{\psi}^{\dagger}_{\rm H}(2)\;\hat{\psi}_{\rm H}(1)\rangle_0 \\ &+ \langle T_{\rm C}\{\hat{S}^{\rm ext}_{\rm C}\;[\hat{\psi}_{\rm H}(1), \hat{H}]_-\;\hat{\psi}^{\dagger}_{\rm H}(2)\}\rangle_0 \\ &+ \langle T_{\rm C}\{\hat{S}^{\rm ext}_{\rm C}\;U(1)\;\hat{\psi}_{\rm H}(1)\;\hat{\psi}^{\dagger}_{\rm H}(2)\}\rangle_0 \;. \end{aligned} \tag{F.2}$$

The first contribution results from $\partial_t\theta(t_1, t_2)$ (see Section 3.7.1). Because of the anti-commutation relation of the field operators it can be reduced to $\delta_{1,2} = \delta_{\mathbf{r_1},\mathbf{r_2}}\delta_{t_1,t_2}$. The equation of motion for the field operator, $i\hbar\partial_{t_1}\hat{\psi}_{\rm H}(1) = [\hat{\psi}_{\rm H}(1), \hat{H}]_-$, has been used in the second term, and the third contribution results from $\partial_t\hat{S}^{\rm ext}_{\rm C}$. Inserting the commutator with the HAMILTONian, one obtains

$$\Big[i\hbar\partial_{t_1} \;-\; \hat{H}_0(1)\Big]\,G(12) \;=\; \delta_{1,2} \;-i\hbar\int\limits_{\rm C} d3\;V(1-3)\;G(1323)\;, \tag{F.3}$$

where the two-particle GREEN's function $G(1234)$ is defined by

$$G(1234) \;=\; \left(-\frac{i}{\hbar}\right)^2\;\langle T_{\rm C}\{\hat{S}^{\rm ext}_{\rm C}\;\hat{\psi}_{\rm H}(1)\;\hat{\psi}_{\rm H}(2)\;\hat{\psi}^{\dagger}_{\rm H}(4)\;\hat{\psi}^{\dagger}_{\rm H}(3)\}\rangle_0 \;. \tag{F.4}$$

To evaluate the two-particle GREEN's functions, one can express it as products of single-particle GREEN's functions $G(12)$, yielding an infinite perturbation expansion [203, 205, 282]. This can be accomplished by utilizing the Green's functions as generating functional. The two-particle Green's function can be expressed by means of functional derivatives of the single-particle Green's functions with respect to the external potential. Based on the variational method, the electron-electron and electron-phonon self-energies are derived next.

F.1 Electron-Electron Interaction

By taking the functional derivative of (F.4) with respect to U one obtains

$$\begin{aligned}
\frac{\delta G(12)}{\delta U(3)} &= -\frac{i}{\hbar}\frac{1}{\langle T_{\mathrm{C}}\hat{S}_{\mathrm{C}}^{\mathrm{ext}}\rangle_0}\langle T_{\mathrm{C}}\{\frac{\delta \hat{S}_{\mathrm{C}}^{\mathrm{ext}}}{\delta U(3)}\ \hat{\psi}_{\mathrm{H}}(1)\ \hat{\psi}_{\mathrm{H}}^{\dagger}(2)\}\rangle_0 \\
&\quad +\frac{i}{\hbar}\frac{\langle T_{\mathrm{C}}\{\hat{S}_{\mathrm{C}}^{\mathrm{ext}}\ \hat{\psi}_{\mathrm{H}}(1)\ \hat{\psi}_{\mathrm{H}}^{\dagger}(2)\}\rangle_0}{\langle T_{\mathrm{C}}\hat{S}_{\mathrm{C}}^{\mathrm{ext}}\rangle_0{}^2}\langle T_{\mathrm{C}}\ \frac{\delta \hat{S}_{\mathrm{C}}^{\mathrm{ext}}}{\delta U(3)}\rangle_0\ , \\
&= -\left(-\frac{i}{\hbar}\right)^2\frac{\langle T_{\mathrm{C}}\{\hat{S}_{\mathrm{C}}^{\mathrm{ext}}\ \hat{\psi}(1)\ \hat{\psi}_{\mathrm{H}}(3)\ \hat{\psi}_{\mathrm{H}}^{\dagger}(3)\ \hat{\psi}_{\mathrm{H}}^{\dagger}(2)\}\rangle_0}{\langle T_{\mathrm{C}}\hat{S}_{\mathrm{C}}^{\mathrm{ext}}\rangle_0} \\
&\quad +G(12)\left(-\frac{i}{\hbar}\right)\frac{\langle T_{\mathrm{C}}\{\hat{S}_{\mathrm{C}}^{\mathrm{ext}}\ \hat{\psi}_{\mathrm{H}}(3)\ \hat{\psi}_{\mathrm{H}}^{\dagger}(3)\}\rangle_0}{\langle T_{\mathrm{C}}\hat{S}_{\mathrm{C}}^{\mathrm{ext}}\rangle_0}\ , \\
&= -G(121'2)+G(12)G(33)\ ,
\end{aligned} \tag{F.5}$$

Equation (F.5) relates the two-particle Green's function to the functional derivative of the single-particle Green's function, which allows one to write the equation of motion (F.3) as

$$\left(i\hbar\partial_{t_1}+\frac{\hbar^2}{2m}\nabla_1^2-U_{\mathrm{eff}}(1)\right)G(12)\ =\delta_{1,2}+\ i\hbar\int\limits_{\mathrm{C}} d3\ V(1-3)\ \frac{\delta G(12)}{\delta U(3)}\ , \tag{F.6}$$

where $H_0(1)=-\frac{\hbar^2}{2m}\nabla_1^2+U(1)$ and the effective potential is given by

$$U_{\mathrm{eff}}(1)\ =\ U(1)-i\hbar\int\limits_{\mathrm{C}} d2\ V(1-2)\ G(22)\ . \tag{F.7}$$

Since $-i\hbar G(22)$ is nothing but the electron density, the second term in (F.7) can be easily identified as the Hartree potential. Exchange and correlation effects are described by the functional derivative contribution, which still requires the calculation of a two-particle Green's function. In order to decouple the hierarchy formally, one can introduce the single-particle self-energy. This is accomplished by the identity

$$G(12)\ =\ \int\limits_{\mathrm{C}} d4\int\limits_{\mathrm{C}} d5\ G(14)\ G^{-1}(45)\ G(52)\ , \tag{F.8}$$

Differentiating with respect to U, one obtains

$$\frac{\delta G(12)}{\delta U(3)}\ =\ \int\limits_{\mathrm{C}} d4\int\limits_{\mathrm{C}} d5\ G(14)\ \frac{\delta G^{-1}(45)}{\delta U(3)}\ G(52)\ , \tag{F.9}$$

where the following relation was used

$$\begin{aligned}\frac{\delta}{\delta U_{\mathrm{eff}}(4)} \int\limits_{\mathrm{C}} d3\; G(13) G^{-1}(32) \;&=\; \frac{\delta_{1,2}}{U(4)} \;=\; 0 \;, \\ &=\; \int\limits_{\mathrm{C}} d3\; \frac{G(13)}{U(4)}\; G^{-1}(32) + \int\limits_{\mathrm{C}} d3\; G(13)\; \frac{G(32)}{U(4)} \;,\end{aligned} \tag{F.10}$$

which allows us to express the functional derivative of G by means of the functional derivative of G^{-1}. Therefore, the equations of motion can be cast into a closed form

$$\left(i\hbar \partial_{t_1} + \frac{\hbar^2}{2m} \nabla_1^2 - U_{\mathrm{eff}}(1) \right) G(12) - \int\limits_{\mathrm{C}} d3\; G(13)\; \Sigma(32) \;=\; \delta_{1,2} \;, \tag{F.11}$$

where the self-energy is defined as

$$\Sigma(12) \;=\; -i\hbar \int\limits_{\mathrm{C}} d3 \int\limits_{\mathrm{C}} d4\; V(1-3)\; G(14)\; \frac{\delta G^{-1}(42)}{\delta U(3)} \;. \tag{F.12}$$

F.1.1 Screened Interaction, Polarization, and Vertex Function

The equation (F.12) can be used as a starting point for a diagrammatic expansion. One possible way is to iterate $G(12)$ in the functional derivative with respect to $U(3)$, starting from the non-interacting GREEN's function G_0. This procedure is described e.g. in [93], and specifically for the KELDYSH formalism, in [203]. This expansion scheme is based on the non-interacting GREEN's function. In order to avoid the appearance of non-interacting GREEN's functions in the diagrammatic expansion without simultaneously complicating the rules for constructing the diagrams, one has to extend the equations for $G(12)$. Technically, this extension is based on the repeated change of variables and the consequent application of the chain-rule in the evaluation of the functional derivatives. One usually generates the following additional function

- the self-energy $\Sigma(12)$, which contains information on both the renormalization of the single-particle energies and the scattering rates.
- the longitudinal polarization function $\Pi(21)$, which describes the possible single-particle transitions as a result of a longitudinal electric field (which can either be an external field or the result of charge density fluctuations in the system),
- the screened COULOMB potential $W(12)$, which differs from the bare COULOMB potential because of the possibility of single-particle transitions as described by Π, brought about by charge density fluctuations, and because of the related possibility of collective excitations,
- the vertex function $\Gamma(123)$, which serves to formally complete the set of equations.

Although the expanded set of functions still does not lead to a closed set of equations (an additional function, $\delta\Sigma/\delta G$, occurs), it allows for a perturbative solution by means of iterating

Σ in the derivative $\delta\Sigma/\delta G$. The formal structure of these equations will turn out to be essentially

$$\begin{aligned} \Sigma &= W\, G\, \Gamma\ , \\ \Pi &= G\, \Gamma\, G\ , \\ W &= V\ +\ V\, \Pi\, W\ , \\ \Gamma &= 1\ +\ \frac{\delta\Sigma}{\delta G}\, G\, \Gamma\, G\ . \end{aligned} \tag{F.13}$$

By applying the chain rule for functional derivatives, one can introduce the derivative with respect to the effective potential. This allows one to write the self-energy (F.12) as [203]

$$\begin{aligned} \Sigma(12) &= -i\hbar \int\limits_{C} d3 \int\limits_{C} d4\ V(1-3)\ G(14)\ \frac{\delta G^{-1}(42)}{\delta U(3)}\ , \\ &= -i\hbar \int\limits_{C} d3 \int\limits_{C} d4 \int\limits_{C} d5\ V(1-3)\ G(14)\ \frac{\delta G^{-1}(42)}{\delta U_{\text{eff}}(5)} \frac{U_{\text{eff}}(5)}{U(3)}\ , \\ &= -i\hbar \int\limits_{C} d3 \int\limits_{C} d4\ W(51)\ G(14)\ \Gamma(425)\ , \end{aligned} \tag{F.14}$$

where the *screened* interaction is defined as

$$W(12) = \int\limits_{C} d3\ V(2-3)\ \frac{\delta U_{\text{eff}}(1)}{\delta U(3)}\ , \tag{F.15}$$

and the vertex function

$$\Gamma(123) = \frac{\delta G^{-1}(12)}{\delta U_{\text{eff}}(3)}\ . \tag{F.16}$$

Using the definition of the effective potential (F.7) together with (F.9) and the chain rule, the screened COULOMB potential, or equivalently, the inverse dielectric function[1]

$$\epsilon^{-1}(12) = \frac{\delta U_{\text{eff}}(1)}{\delta U(2)}\ , \tag{F.17}$$

can be written in terms of the polarization function

$$\Pi(12) = -i\hbar \frac{\delta G(11)}{\delta U_{\text{eff}}(2)}\ , \tag{F.18}$$

in the following way

$$\begin{aligned} \frac{\delta U_{\text{eff}}(1)}{\delta U(2)} &= \frac{\delta U(1)}{\delta U(2)}\ -\ i\hbar \int\limits_{C} d3 \int\limits_{C} d4\ V(1-3)\ \frac{\delta G(33)}{\delta U_{\text{eff}}(4)}\ \frac{\delta U_{\text{eff}}(4)}{\delta U(2)}\ , \\ &= \delta_{1,2}\ +\ \int\limits_{C} d3 \int\limits_{C} d4\ V(1-3)\ \Pi(34)\ \frac{\delta U_{\text{eff}}(4)}{\delta U(2)}\ . \end{aligned} \tag{F.19}$$

---

[1] Screening is defined by the inverse dielectric function. An external potential induces a charge density in the system. This induced charge density gives rise to a change in the potential via the COULOMB interaction, which in turn yields an induced charge density and so forth. The result of this infinite series of charge redistribution process is the screening of the external potential.

In this way, one obtains

$$\epsilon^{-1}(12) \;=\; \delta_{1,2} \;+\; \int\limits_{C} d3 \int\limits_{C} d4\; V(1-3)\; \Pi(34)\; \epsilon^{-1}(42)\;. \tag{F.20}$$

and from (F.15)

$$W(12) \;=\; V(2-1) \;+\; \int\limits_{C} d3 \int\limits_{C} d4\; V(1-3)\; \Pi(34)\; W(42)\;. \tag{F.21}$$

By using the relation (F.10) one can express the polarization in terms of the vertex function

$$\begin{aligned}
\Pi(12) \;&=\; -i\hbar\, \frac{\delta G(11)}{\delta U_{\rm eff}(2)}\;, \\
&=\; -i\hbar \int\limits_{C} d3 \int\limits_{C} d4\; G(13)\, \frac{\delta G^{-1}(34)}{\delta U_{\rm eff}(2)}\, G(41)\;, \\
&=\; -i\hbar \int\limits_{C} d3 \int\limits_{C} d4\; G(13)\; \Gamma(342)\; G(41)\;.
\end{aligned} \tag{F.22}$$

The system of equations defining the self-energy is closed by the equation for the vertex functions. For that purpose one needs an explicit expression for G^{-1} in terms of G. One can multiply and integrate both sides of the equation of motion (F.11) by $G_0^{-1}(32)$ and $G^{-1}(32)$, where $G_0^{-1}(12) = (i\hbar\partial_{t_1} + \frac{\hbar^2}{2m}\nabla_1^2 - U_{\rm eff}(1))\delta_{1,2}$. Finally, one obtains $G^{-1}(12) = G_0^{-1}(12) - \Sigma(12)$, which can be used to rewrite the vertex function (F.16) as

$$\begin{aligned}
\Gamma(123) \;&=\; \frac{\delta G^{-1}(12)}{\delta U_{\rm eff}(3)} \;=\; \frac{\delta G_0^{-1}(12)}{\delta U_{\rm eff}(3)} \;-\; \frac{\delta \Sigma(12)}{\delta U_{\rm eff}(3)}\;, \\
&=\; -\delta_{1,2}\delta_{1,3} \;-\; \int\limits_{C} d4 \int\limits_{C} d5\; \frac{\delta \Sigma(12)}{\delta G(45)}\, \frac{\delta G(45)}{\delta U_{\rm eff}(3)}\;, \\
&=\; -\delta_{1,2}\delta_{1,3} \;+\; \int\limits_{C} d4 \int\limits_{C} d5\; \frac{\delta \Sigma(12)}{\delta G(45)} \int\limits_{C} d6 \int\limits_{C} d7\; G(46)\, \frac{\delta G^{-1}(67)}{\delta U_{\rm eff}(3)}\, G(75)\;, \\
&=\; -\delta_{1,2}\delta_{1,3} \;+\; \int\limits_{C} d4 \int\limits_{C} d5 \int\limits_{C} d6 \int\limits_{C} d7\; \frac{\delta \Sigma(12)}{\delta G(45)}\, G(46)\; \Gamma(673)\; G(75)\;,
\end{aligned} \tag{F.23}$$

where the relation (F.10) has been used. Contributions proportional to $\delta\Sigma/\delta G$ are referred to as *vertex corrections* and describe interaction processes at the two-particle level.

F.2 Electron-Phonon Interaction

The coupling of electrons and nuclei in the lattice to the external sources is given by

$$\hat{H}^{\text{ext}} = \int d\mathbf{r}\; U(\mathbf{r},t)\left(\rho_{\text{el}}(\mathbf{r}) + \rho_{\text{n}}(\mathbf{r})\right) \; + J(\mathbf{r},t)\rho_{\text{n}}(\mathbf{r}) \;, \tag{F.24}$$

where $\langle\rho_{\text{el}}(\mathbf{r})\rangle = i\text{q}\hbar G^{<}(\mathbf{r},t;\mathbf{r},t)$ is the density of electrons. The density of the nuclei in the lattice $\langle\rho_{\text{n}}(\mathbf{r})\rangle$ is represented as a sum of local charge densities ρ_κ

$$\rho_{\text{n}}(\mathbf{r},t) = \sum_{\mathbf{L}\kappa} \rho_\kappa(\mathbf{r} - \mathbf{R}(\mathbf{L}\kappa)) \;, \tag{F.25}$$

where the actual positions of the nuclei $\mathbf{R}(\mathbf{L}\kappa) = \mathbf{L} + \kappa + \mathbf{u}(\mathbf{L}\kappa)$, is defined in terms of the equilibrium lattice vector $\mathbf{L}$, the basis vector within the unit cell κ, and the lattice displacement $\mathbf{u}(\mathbf{L}\kappa)$. In case of bare nuclei, ρ_κ would approximately be δ functions. However, it is more convenient to consider rigid ion cores instead of bare nuclei. In this case ρ_κ denotes the charge density of the ion cores.

For a simple derivation of the electron-phonon interaction, one has to add an additional external source $J(\mathbf{r},t)$ in (F.24) [203], which couples to the charge density of the nuclei and is merely a mathematical trick, see (F.32)-(F.35). With similar steps for deriving (F.7), one can show that under the HAMILTONian in (F.24) the effective potential can be written as

$$\begin{aligned} U_{\text{eff}}(1) &= U(1) \; - \; i\hbar \int\limits_{\text{C}} d2\; V(1-2)\; G(22) + \int\limits_{\text{C}} d2\; V(1-2)\; \langle\rho_{\text{n}}(2)\rangle \;, \\ &= U(1) \; + \int\limits_{\text{C}} d2\; V(1-2)\left(\langle\rho_{\text{el}}(2)\rangle + \langle\rho_{\text{n}}(2)\rangle\right) \;. \end{aligned} \tag{F.26}$$

The aim is the calculation of the total linear response of the system, including the contribution from the nuclei, i.e. the variation of the total electrostatic potential with the external potential [205]

$$\begin{aligned} \frac{\delta U_{\text{eff}}(1)}{\delta U(2)} &= \frac{\delta U(1)}{\delta U(2)} \; - \; i\hbar \int\limits_{\text{C}} d3\; V(1-3)\left(\frac{\delta\langle\rho_{\text{el}}(3)\rangle}{\delta U(2)} + \frac{\delta\langle\rho_{\text{n}}(3)\rangle}{\delta U(2)}\right) \;, \\ &= \delta_{1,2} \; + \int\limits_{\text{C}} d3 \int\limits_{\text{C}} d4\; V(1-3)\; \frac{\delta\langle\rho_{\text{el}}(3)\rangle}{\delta U_{\text{eff}}(4)} \frac{\delta U_{\text{eff}}(4)}{\delta U(2)} \; + \int\limits_{\text{C}} d3\; V(1-3)\; \frac{\delta\langle\rho_{\text{n}}(3)\rangle}{\delta U(2)} \;. \end{aligned} \tag{F.27}$$

Solving with respect to $\delta U_{\text{eff}}/\delta U$, one obtains

$$\frac{\delta U_{\text{eff}}(1)}{\delta U(2)} = \epsilon^{-1}(12) \; + \int\limits_{\text{C}} d3\; W(13) \frac{\delta\langle\rho_{\text{n}}(3)\rangle}{\delta U(2)} \;, \tag{F.28}$$

where the *dielectric function* is

$$\epsilon(12) = \delta_{1,2} \; + \int\limits_{\text{C}} d3\; V(1-3)\; \frac{\delta\langle\rho_{\text{el}}(3)\rangle}{\delta U_{\text{eff}}(2)} \;, \tag{F.29}$$

and W is the screened interaction. The derivative $\delta\langle\rho_{\mathrm{el}}\rangle/\delta U_{\mathrm{eff}}$ differs from the purely electronic polarization which is introduced in Appendix F.1.1, owing to the phonon contribution to the total potential. Neglecting this phonon contribution to the polarization function is one of the ingredients of the *adiabatic approximation* [246]. This approximation reduces the dielectric function and the screened interaction in (F.28) to the purely electronic quantities which are introduced in (F.20) and (F.21). The next step is the calculation of the lattice contribution. Similar to the Green's function for electrons, one can consider the expectation value of the density of nuclei

$$\langle\rho_{\mathrm{n}}(1)\rangle \;=\; \frac{\langle T_{\mathrm{C}}\{\hat{S}_{\mathrm{C}}^{\mathrm{ext}}\;\rho_{\mathrm{n}}(1)\}\rangle}{\langle T_{\mathrm{C}}\hat{S}_{\mathrm{C}}^{\mathrm{ext}}\rangle}\;. \tag{F.30}$$

With similar steps for deriving (F.5), the density response of the nuclei under the action of $\hat{H}^{\mathrm{ext}}$ can be calculated as

$$\begin{aligned}\frac{\delta\langle\rho_{\mathrm{n}}(1)\rangle}{\delta U(2)} \;&=\; -\frac{i}{\hbar}\frac{\langle T_{\mathrm{C}}\{\hat{S}_{\mathrm{C}}^{\mathrm{ext}}[\rho_{\mathrm{el}}(2)+\rho_{\mathrm{n}}(2)]\rho_{\mathrm{n}}(1)\}\rangle}{\langle T_{\mathrm{C}}\hat{S}_{\mathrm{C}}^{\mathrm{ext}}\rangle}\\ &\quad+\frac{i}{\hbar}\frac{\langle T_{\mathrm{C}}\{\hat{S}_{\mathrm{C}}^{\mathrm{ext}}\rho_{\mathrm{n}}(1)\}\rangle\langle T_{\mathrm{C}}\{\hat{S}_{\mathrm{C}}^{\mathrm{ext}}[\rho_{\mathrm{el}}(2)+\rho_{\mathrm{n}}(2)]\}\rangle}{\langle T_{\mathrm{C}}\hat{S}_{\mathrm{C}}^{\mathrm{ext}}\rangle^{2}}\;,\\ &=\; -\frac{i}{\hbar}\frac{\langle T_{\mathrm{C}}\{\hat{S}_{\mathrm{C}}^{\mathrm{ext}}[\Delta\rho_{\mathrm{el}}(2)+\Delta\rho_{\mathrm{n}}(2)]\Delta\rho_{\mathrm{n}}(1)\}\rangle}{\langle T_{\mathrm{C}}\hat{S}_{\mathrm{C}}^{\mathrm{ext}}\rangle}\;.\end{aligned} \tag{F.31}$$

In the last step, the deviation operator $\Delta\rho = \rho - \langle\rho\rangle$ is introduced. Furthermore, the relation $\langle AB\rangle - \langle A\rangle\langle B\rangle = \langle(A-\langle A\rangle)(B-\langle B\rangle)\rangle$ is used. Now the additional external field J comes into play, which allows us to eliminate the mixed electron-nuclei contribution. By steps completely analogous to those used before, one finds

$$\frac{\delta\langle\rho_{\mathrm{el}}(1)\rangle}{\delta J(2)} \;=\; -\frac{i}{\hbar}\frac{\langle T_{\mathrm{C}}\{\hat{S}_{\mathrm{C}}^{\mathrm{ext}}\;\Delta\rho_{\mathrm{el}}(1)\;\Delta\rho_{\mathrm{n}}(2)\}\rangle}{\langle T_{\mathrm{C}}\hat{S}_{\mathrm{C}}^{\mathrm{ext}}\rangle}\;, \tag{F.32}$$

which together with (F.31), yields the result

$$\begin{aligned}\frac{\delta\langle\rho_{\mathrm{n}}(1)\rangle}{\delta U(2)} \;&=\; \frac{\delta\langle\rho_{\mathrm{el}}(1)+\rho_{\mathrm{n}}(1)\rangle}{\delta J(2)}\;,\\ &=\; D(12)\;+\;\frac{\delta\langle\rho_{\mathrm{el}}(1)\rangle}{\delta J(2)}\;,\end{aligned} \tag{F.33}$$

where the density-density correlation function of the nuclei is defined as

$$\begin{aligned}D(12) \;&=\; -\frac{i}{\hbar}\frac{\langle T_{\mathrm{C}}\{\hat{S}_{\mathrm{C}}^{\mathrm{ext}}\;\Delta\rho_{\mathrm{n}}(2)\Delta\rho_{\mathrm{n}}(1)\}\rangle}{\langle T_{\mathrm{C}}^{\mathrm{ext}}\hat{S}_{\mathrm{C}}\rangle}\;,\\ &=\; \frac{\delta\langle\rho_{\mathrm{n}}(1)\rangle}{\delta J(2)}\;.\end{aligned} \tag{F.34}$$

One can again apply the chain rule to (F.33) to eliminate the $\delta\langle\rho_{\mathrm{el}}\rangle/\delta J$ contribution.

$$\frac{\delta\langle\rho_{\mathrm{n}}(1)\rangle}{\delta U(2)} \;=\; D(12) \;+\; \int\limits_{\mathrm{C}} d3 \int\limits_{\mathrm{C}} d4\; \frac{\delta\langle\rho_{\mathrm{el}}(2)\rangle}{\delta U_{\mathrm{eff}}(3)}\; V(3-4)\; \frac{\delta\langle\rho_{\mathrm{el}}(4)+\rho_{\mathrm{n}}(4)\rangle}{\delta J(1)}\;. \tag{F.35}$$

Making use of the relation (F.33) once more, one can solve the resulting equation with respect to $\delta\langle\rho_{\mathrm{n}}\rangle/\delta U$ and express the solution in terms of the dielectric function. After insertion in (F.28), this yields the total dielectric screening function as

$$\frac{\delta U_{\mathrm{eff}}(1)}{\delta U(2)} \;=\; \epsilon^{-1}(12) \;+\; \int\limits_{\mathrm{C}} d3 \int\limits_{\mathrm{C}} d4\; W(13)\; D(34)\; \epsilon^{-1}(42)\;. \tag{F.36}$$

The desired effective electron-electron interaction induced by lattice vibrations is thus finally given by [205]

$$W_{\mathrm{eff}}(12) \;=\; W(12) \;+\; \underbrace{\int\limits_{\mathrm{C}} d3 \int\limits_{\mathrm{C}} d4\; W(13)\; D(34)\; W(42)}_{W_{\mathrm{ph}}}\;. \tag{F.37}$$

Therefore, the problem of electron-phonon interaction is reduced to the replacement of the electronically screened interaction introduced in Appendix F.1.1 by the effective interaction (F.37).

F.2.1 The Phonon GREEN's Function

The density-density correlation function of the nuclei is reduced in the following to a quantity of more practical interest, namely the phonon GREEN's function within the harmonic approximation. One can expand the ionic charge density up to first-order in the lattice displacement $\mathbf{u}_\alpha(\mathbf{L}\kappa)$ with respect to the equilibrium positions of ions (see (F.25)) [205]

$$\rho_{\mathrm{n}}(\mathbf{r},t) \;=\; \sum_{\mathbf{L}\kappa} \rho_\kappa(\mathbf{r}-\mathbf{L}-\kappa) \;+\; \sum_{\mathbf{L}\kappa\alpha} \nabla_\alpha\; \rho_\kappa(\mathbf{r}-\mathbf{L}-\kappa) u_\alpha(\mathbf{L}\kappa,t)\;, \tag{F.38}$$

where α denotes the Cartesian components. This expansion reduces the density-density correlation function (F.34) to

$$D_{\alpha\beta}(\mathbf{r},t;\mathbf{r}',t') \;=\; \sum_{\mathbf{L}\kappa\alpha,\mathbf{L}'\kappa'\beta} \nabla_\alpha\; \rho_\kappa(\mathbf{r}-\mathbf{L}-\kappa)\; D_{\alpha\beta}(\mathbf{L}\kappa,t;\mathbf{L}'\kappa',t')\; \nabla_\beta\; \rho_{\kappa'}(\mathbf{r}'-\mathbf{L}'-\kappa')\;, \tag{F.39}$$

where the phonon GREEN's function in real space is

$$D_{\alpha\beta}(\mathbf{L}\kappa,t;\mathbf{L}'\kappa',t') \;=\; -\frac{i}{\hbar}\langle T_{\mathrm{C}}\{\; u_\alpha(\mathbf{L}\kappa,t)\; u_\beta(\mathbf{L}'\kappa',t')\;\}\rangle\;. \tag{F.40}$$

Owing to the lattice periodicity of the ionic charge densities, the spatial FOURIER transformation of (F.39) takes the form

$$\begin{aligned} &D_{\alpha\beta}(\mathbf{G}+\mathbf{q},\mathbf{G}'+\mathbf{q};t,t') \;=\; \\ &\quad \sum_{\kappa\alpha,\kappa'\beta} (G_\alpha+q_\alpha)\; \rho_\kappa(\mathbf{G}+\mathbf{q})\; e^{i\mathbf{G}\kappa}\; \frac{D_{\alpha\kappa,\beta\kappa'}(\mathbf{q};t,t')}{\sqrt{M_\kappa M_{\kappa'}}}\; \rho_{\kappa'}(G'_\beta+q_\beta)\; e^{i\mathbf{G}'\kappa'}\;. \end{aligned} \tag{F.41}$$

The Fourier expansion of the lattice displacement can be written as

$$u_\alpha(\mathbf{L}\kappa, t) \;=\; \frac{1}{\sqrt{NM_\kappa}} \sum_{\mathbf{q}} e^{i\mathbf{q}(\mathbf{L}+\kappa)} u_{\alpha\kappa}(\mathbf{q}, t) \;, \tag{F.42}$$

where M_κ are the mass of the atoms and N is the number of atoms in the unit cell. By means of (F.42), the Fourier transformation of (F.40) is given by

$$D_{\alpha\kappa,\beta\kappa'}(\mathbf{q}, t; \mathbf{q}', t') \;=\; -\frac{i}{\hbar} \langle T_{\mathrm{C}}\{\; \hat{u}_{\alpha\kappa}(\mathbf{q}, t)\; \hat{u}^{\dagger}_{\beta,\kappa'}(\mathbf{q}', t')\; \}\rangle \delta_{\mathbf{q},\mathbf{q}'} \;. \tag{F.43}$$

By diagonalizing the dynamical matrix [283], one obtains the eigen-modes $e_{\alpha\kappa\lambda}(\mathbf{q})$ and eigen-frequencies $\omega_{\lambda,\mathbf{q}}$ of the lattice vibrations. These eigen-vectors can be used to expand the Fourier components of the displacement in terms of phonon operators

$$\hat{u}_{\alpha\kappa}(\mathbf{q}, t) \;=\; \sum_{\lambda} \sqrt{\frac{\hbar}{2\omega_{\lambda,\mathbf{q}}}} e_{\alpha\kappa\lambda}(\mathbf{q}) \left(b_{\lambda,\mathbf{q}}(t) + b^{\dagger}_{\lambda,-\mathbf{q}}(t) \right) \;, \tag{F.44}$$

where these operators have the time dependence

$$b_{\lambda,\mathbf{q}}(t) \;=\; b_{\lambda,\mathbf{q}} e^{-i\omega_{\lambda,\mathbf{q}} t} \;. \tag{F.45}$$

This eigen-vector expansion allows one to factorize (F.43) for each phonon mode according to

$$D_{\alpha\kappa,\beta\kappa'}(\mathbf{q}; t, t') \;=\; \sum_{\lambda} d_{\alpha\kappa,\beta\kappa'}(\mathbf{q}; t, t') D_\lambda(\mathbf{q}; t, t') \;. \tag{F.46}$$

into a weight factor

$$d_{\alpha\kappa,\beta\kappa'}(\mathbf{q}, \lambda) \;=\; \frac{e_{\alpha\kappa\lambda}(\mathbf{q}) e_{\beta\kappa'\lambda}(\mathbf{q})}{2\omega_{\lambda,\mathbf{q}}} \tag{F.47}$$

and the phonon Green's function (Appendix D.2)

$$D_\lambda(\mathbf{q}; t, t') \;=\; -\frac{i}{\hbar} \langle T_{\mathrm{C}}\{\; \hat{A}_{\lambda,\mathbf{q}}(t)\; \hat{A}^{\dagger}_{\lambda,\mathbf{q}}(t')\}\rangle \;, \tag{F.48}$$

where $\hat{A}_{\lambda,\mathbf{q}}(t) \;=\; b_{\lambda,\mathbf{q}}(t) + b^{\dagger}_{\lambda,-\mathbf{q}}(t)$, b, and $b^{\dagger}$ are the annihilation and creation operators for Bosons. This factorization allows one to evaluate the coupling for any combination of phonon branch indices.

F.2.2 The Phonon Self-Energy

In the previous sections helpful forms of the electron-phonon interaction are derived. One can link up with the many-particle theory and introduce phonon contributions into the quantum kinetic equations. As shown in the derivation of the general result (F.37), one has to add the phonon induced contribution to the electronically screened interaction. Together with (F.14), this defines the phonon self-energies which enters the quantum kinetic equations. As the phonon induced interaction is not a functional of the single-particle GREEN's function, the problem is slightly less complicated than the electron-electron interaction. As in the purely electronic case, one is dependent on approximation schemes. An expansion of the self-energy in powers of the phonon-induced interaction is easily generated by means of (F.14). The contribution linear in the phonon induced interaction, i.e. the single-phonon self-energy takes the form

$$\Sigma_1(12) \;=\; i\hbar\, W_{\mathrm{ph}}(21)\; G(12)\ . \tag{F.49}$$

By performing eigen-function expansion (see Appendix F.2.1) one obtains

$$\Sigma_1(\mathbf{k};t_1,t_2) \;=\; -i\hbar\sum_{\mathbf{q}} W_{\mathrm{ph}}(\mathbf{q};t_1,t_2)\; G(\mathbf{k}+\mathbf{q};t_1,t_2)\ , \tag{F.50}$$

where

$$W_{\mathrm{ph}}(\mathbf{q};t_1,t_2) \;=\; \sum_{\lambda} M^2_{\lambda}(\mathbf{q})\; D_{\lambda}(\mathbf{q};t_1,t_2)\ , \tag{F.51}$$

$$M^2_{\lambda}(\mathbf{q}) \;=\; \sum_{\alpha\beta\kappa\kappa'} F_{\alpha\kappa}(\mathbf{q})\frac{d_{\alpha\kappa,\beta\kappa'}(\mathbf{q},\lambda)}{\sqrt{M_{\kappa}M_{\kappa'}}}F_{\beta\kappa'}(\mathbf{q})\ , \tag{F.52}$$

$$F_{\alpha\kappa}(\mathbf{q}) \;=\; \sum_{\mathbf{G}} W(\mathbf{q},\mathbf{G}+\mathbf{q};t_1,t_2)(G_{\alpha}+q_{\alpha})\; \rho_{\kappa}(\mathbf{G}+\mathbf{q})\; e^{i\mathbf{G}\kappa}\ . \tag{F.53}$$

The phonon GREEN's functions entering (F.51) are discussed in Appendix F.2.1.

F.3 Approximation of the Self-Energy

Depending on the problem, one can either attempt a summation of a selected class of dominant contributions or perform an expansion with respect to the screened interaction. As shown in Appendix F.1.1, the self-energy itself and the polarization propagator, which determines the screened interaction, depend sensitively on the vertex corrections. Thus there is a complicated functional dependence of single-particle properties on two-particle properties and vice versa, and one has to consider the consistence of approximations at the single-particle and two-particle levels. In principle, there are two different approaches to attack the coupled system of equations derived in Appendix F.1.1 An *iterative procedure* and *self-consistent approximations*.

Starting such an iterative solution, one can first neglect vertex corrections in (F.23) and obtain an approximation for the self-energy by means of (F.14) together with (F.21) and (F.22). Making use of this approximation, one calculates $\delta\Sigma/\delta G$, and includes vertex corrections in the next step. The iteration of such a procedure generates an expansion in terms of the screened interaction and the GREEN's function defined as a self-consistent solution of the DYSON equation.

For the iterative procedure, the sequence of steps can be defined by the vertex function (F.23), which yields by means of the chain rule the recurrence relation

$$\Gamma_{n+1}(123) \;=\; -\delta_{1,2}\delta_{1,3} \;-\; \frac{\delta\Sigma_n(12)}{\delta U_{\mathrm{eff}}(3)}\;. \tag{F.54}$$

One starts with the HARTREE-approximation, i.e. $\Sigma_0 = 0$, which delivers G_0, $\Gamma_1 = -\delta_{1,2}\delta_{1,3}$ and the screened interaction W_1. In the subsequent step one obtains Σ_1, G_1 and Γ_2 and so forth. The effect of this interaction is two-fold. In the n-th step, the GREEN's functions contributing to $\Sigma_n[G_{n-1}]$ become dressed by an additional interaction line and additionally new types of diagrams are generated.

For the *Self-consistent approximations*, one selects a certain class of self-energy diagrams $\Sigma[G]$. The DYSON equation becomes a non-linear functional equation of the GREEN's functions, which has to be solved self-consistently. The selection corresponds to the summation of a certain class of diagrams up to infinite-order in the interaction, whereas others which contribute even in lower order are neglected. The difficulty is in finding the correct way to choose a subset of diagrams for each order. In order to deliver physically meaningful results, any approximation should guarantee certain macroscopic conservation laws. This condition can be imposed by the postulate that all diagrams contributing to the self-energy are obtained from the functional derivative of a functional $\Phi[G]$ with respect to G. Solving the DYSON equation self-consistently with a Φ-*derivable self-energy* yields a GREEN's function which conserves particle number, energy, and momentum [93].

Appendix G

Treatment of Contacts

In order to solve the transport equations, boundary conditions have to be specified. An important point is the treatment of contacts, which act as a source or drain for the carriers [8, 97, 116, 181, 284, 285]. Here, the method described in [285] is followed.

One can partition the layered structure into left contact with index L, device with index D, and right contact with index R (Fig. G.1). The device corresponds to the region where one solves the transport equations and the contacts are the highly conducting regions connected to the device.

While the device region consists of only N layers, the matrices corresponding to the GREEN's functions (4.11) and (4.12) are infinite dimensional due to the semi-infinite contacts. It is shown next, that the influence of the semi-infinite contacts can be folded into the device region, where the semi-infinite contacts only affect layers 1 and N of the device region.

As shown next, the influence of the semi-infinite contacts can be folded into the device region by adding a self-energy to the device region. This can be viewed as an additional self-energy, due to the transitions between the device and the contacts.

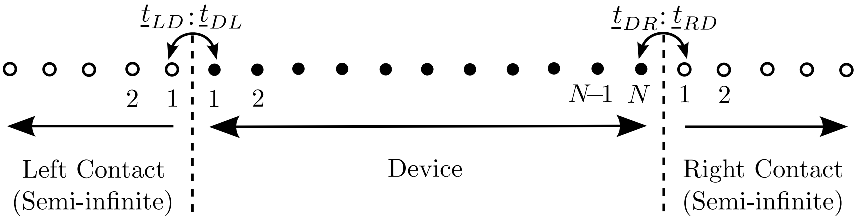

Figure G.1: Partitioning of the simulation domain into device region and left and right contacts.

G.1 Matrix Truncation

By defining

$$\underline{A} \;=\; [E\underline{I} - \underline{H} - \Sigma_{\text{Scat}}]\;, \tag{G.1}$$

the equation (4.11) ($\underline{A}\underline{G}^{\text{r}} = \underline{I}$) can be written as,

$$\begin{bmatrix} \underline{A}_{LL} & \underline{A}_{LD} & \\ \underline{A}_{DL} & \underline{A}_{DD} & \underline{A}_{DR} \\ & \underline{A}_{RD} & \underline{A}_{RR} \end{bmatrix} \begin{bmatrix} \underline{G}^{\text{r}}_{LL} & \underline{G}^{\text{r}}_{LD} & \underline{G}^{\text{r}}_{LR} \\ \underline{G}^{\text{r}}_{DL} & \underline{G}^{\text{r}}_{DD} & \underline{G}^{\text{r}}_{DR} \\ \underline{G}^{\text{r}}_{RL} & \underline{G}^{\text{r}}_{RD} & \underline{G}^{\text{r}}_{RR} \end{bmatrix} = \begin{bmatrix} \underline{I} & & \\ & \underline{I} & \\ & & \underline{I} \end{bmatrix}, \tag{G.2}$$

where

$$\underline{A}_{LL} \;=\; \begin{bmatrix} \bullet & \bullet & \bullet & & & \\ & \bullet & \bullet & \bullet & & \\ & & -\underline{t}^{\dagger}_{L_{4,3}} & \underline{A}_{L_3} & -\underline{t}_{L_{3,2}} & \\ & & & -\underline{t}^{\dagger}_{L_{3,2}} & \underline{A}_{L_2} & -\underline{t}_{L_{2,1}} \\ & & & & -\underline{t}^{\dagger}_{L_{2,1}} & \underline{A}_{L_1} \end{bmatrix}, \tag{G.3}$$

corresponds to the left semi-infinite contact,

$$\underline{A}_{RR} \;=\; \begin{bmatrix} \underline{A}_{R_1} & -\underline{t}_{R_{12}} & & & & \\ -\underline{t}^{\dagger}_{R_{12}} & \underline{A}_{R_2} & -\underline{t}_{R_{23}} & & & \\ & -\underline{t}^{\dagger}_{R_{23}} & \underline{A}_{R_3} & -\underline{t}_{R_{34}} & & \\ & & \bullet & \bullet & \bullet & \\ & & & \bullet & \bullet & \bullet \end{bmatrix}, \tag{G.4}$$

corresponds to the right semi-infinite contact, and

$$\underline{A}_{DD} \;=\; \begin{bmatrix} \underline{A}_1 & -\underline{t}_{12} & & & & & \\ -\underline{t}^{\dagger}_{12} & \underline{A}_2 & -\underline{t}_{2,3} & & & & \\ & \bullet & \bullet & \bullet & & & \\ & & & \bullet & \bullet & \bullet & \\ & & & & -\underline{t}^{\dagger}_{N-2,N-1} & \underline{A}_{N-1} & -\underline{t}_{N-1,N} \\ & & & & & -\underline{t}^{\dagger}_{N-1,N} & \underline{A}_N \end{bmatrix}, \tag{G.5}$$

corresponds to the device region.

The coupling between the left and right contacts and device are respectively given by

$$\underline{A}_{LD} \;=\; \begin{bmatrix} 0 & 0 & \bullet & \bullet & 0 & 0 \\ 0 & 0 & \bullet & \bullet & 0 & 0 \\ 0 & 0 & \bullet & \bullet & 0 & 0 \\ 0 & 0 & \bullet & \bullet & 0 & 0 \\ -\underline{t}_{LD} & 0 & \bullet & \bullet & 0 & 0 \end{bmatrix}, \tag{G.6}$$

and

$$\underline{A}_{RD} \;=\; \begin{bmatrix} 0 & 0 & \bullet & \bullet & 0 & -\underline{t}_{RD} \\ 0 & 0 & \bullet & \bullet & 0 & 0 \\ 0 & 0 & \bullet & \bullet & 0 & 0 \\ 0 & 0 & \bullet & \bullet & 0 & 0 \\ 0 & 0 & \bullet & \bullet & 0 & 0 \end{bmatrix} . \tag{G.7}$$

It should be noted that $\underline{A}_{DL} = \underline{A}^{\dagger}_{LD}$, $\underline{A}_{DR} = \underline{A}^{\dagger}_{RD}$, and $\underline{A}_{LD}$ and $\underline{A}_{DL}$ ($\underline{A}_{RD}$, and $\underline{A}_{DR}$) are sparse matrices. Their only non-zero entry represents the coupling of the left (right) contact and device. From (G.2), one obtains

$$\underline{G}^{\mathrm{r}}_{LD} \;=\; -\underline{A}^{-1}_{LL}\, \underline{A}_{LD}\, \underline{G}^{\mathrm{r}}_{DD} \;, \tag{G.8}$$

$$\underline{G}^{\mathrm{r}}_{RD} \;=\; -\underline{A}^{-1}_{RR}\, \underline{A}_{RD}\, \underline{G}^{\mathrm{r}}_{DD} \;, \tag{G.9}$$

$$\underline{A}_{DL}\, \underline{G}^{\mathrm{r}}_{LD} \;+\; \underline{A}_{DD}\, \underline{G}^{\mathrm{r}}_{DD} \;+\; \underline{A}_{DR}\, \underline{G}^{\mathrm{r}}_{RD} \;=\; \underline{I} \;. \tag{G.10}$$

Substituting (G.8) and (G.9) in (G.10), one obtains a matrix equation with a dimension corresponding to the total number of grid points in device layers,

$$[\underline{A}_{DD} \;-\; \underline{A}_{DL}\, \underline{A}^{-1}_{LL}\, \underline{A}_{LD} \;-\; \underline{A}_{DR}\, \underline{A}^{-1}_{RR}\, \underline{A}_{RD}]\, \underline{G}^{\mathrm{r}}_{DD} \;=\; \underline{I} \;. \tag{G.11}$$

The second and third terms of (G.11) are self-energies due to coupling of the device region to left and right contacts, respectively.

The Green's functions of the isolated semi-infinite contacts are defined as

$$\begin{aligned} \underline{A}_{LL}\, \underline{g}^{\mathrm{r}}_{L} &= \underline{I} \;, \\ \underline{A}_{RR}\, \underline{g}^{\mathrm{r}}_{R} &= \underline{I} \;. \end{aligned} \tag{G.12}$$

The *surface* Green*'s function* of the left and right contacts are the Green's function elements corresponding to the first edge layer of the respective contact

$$\begin{aligned} \underline{g}^{\mathrm{r}}_{L_{1,1}} &= \underline{A}^{-1}_{LL_{1,1}} \;, \\ \underline{g}^{\mathrm{r}}_{R_{1,1}} &= \underline{A}^{-1}_{RR_{1,1}} \;. \end{aligned} \tag{G.13}$$

G.2 Contact Self-Energies

The surface Green's functions defined in (G.13) enable us to rewrite (G.11) in a form very similar to (4.11),

$$[E\underline{I} - \underline{H} - \underline{\Sigma}^{\mathrm{r}}_{\mathrm{Scat}} - \underline{\Sigma}^{\mathrm{r}}_{\mathrm{C}}]\; \underline{G}^{\mathrm{r}}_{DD} \;=\; \underline{I}\;, \tag{G.14}$$

where,

$$\begin{aligned} \underline{\Sigma}^{\mathrm{r}}_{C_{1,1}} &= \underline{t}_{DL}\, \underline{g}^{\mathrm{r}}_{L_{1,1}}\, \underline{t}_{LD} &= \underline{\Sigma}^{\mathrm{r}}_{L}\;, \\ \underline{\Sigma}^{\mathrm{r}}_{C_{N,N}} &= \underline{t}_{DR}\, \underline{g}^{\mathrm{r}}_{R_{1,1}}\, \underline{t}_{RD} &= \underline{\Sigma}^{\mathrm{r}}_{R}\;. \end{aligned} \tag{G.15}$$

All other elements of $\underline{\Sigma}^{\mathrm{r}}_{\mathrm{C}}$ are zero. $\underline{\Sigma}^{\mathrm{r}}_{L}$ and $\underline{\Sigma}^{\mathrm{r}}_{R}$ are *self-energies* due to the left and right contacts, respectively, and $\underline{t}_{DL} = \underline{t}^{\dagger}_{LD}$ and $\underline{t}_{DR} = \underline{t}^{\dagger}_{RD}$. By following the same procedure one obtains the equation of motion for the lesser and greater Green's functions as [116]

$$\underline{G}^{\gtrless}_{DD} \;=\; \underline{G}^{\mathrm{r}}_{DD}\, \left[\underline{\Sigma}^{\lessgtr}_{\mathrm{Scat}} \;+\; \underline{\Sigma}^{\mathrm{r}}_{\mathrm{C}}\right]\, \underline{G}^{\mathrm{a}}_{DD}\;, \tag{G.16}$$

where,

$$\begin{aligned} \underline{\Sigma}^{\gtrless}_{C_{1,1}} &= \underline{t}_{DL}\, \underline{g}^{\gtrless}_{L_{1,1}}\, \underline{t}_{LD} &= \underline{\Sigma}^{\gtrless}_{L}\;, \\ \underline{\Sigma}^{\gtrless}_{C_{N,N}} &= \underline{t}_{DR}\, \underline{g}^{\gtrless}_{R_{1,1}}\, \underline{t}_{RD} &= \underline{\Sigma}^{\gtrless}_{R}\;. \end{aligned} \tag{G.17}$$

Since the contacts are by definition in equilibrium, one obtains (Appendix D.1)

$$\begin{aligned} \underline{g}^{<}_{1,1} &= i\, \underline{a}_{1,1}\, f_L\;, \\ \underline{g}^{<}_{1,1} &= i\, \underline{a}_{1,1}\, f_R\;, \end{aligned} \tag{G.18}$$

where $\underline{a} = i(\underline{g}^{\mathrm{r}} - \underline{g}^{\mathrm{a}}) = -2\Im\mathrm{m}[\underline{g}^{\mathrm{r}}]$ is the spectral function and $f_{L(R)}$ is the Fermi factor of the left (right) contact. By defining the broadening function as

$$\begin{aligned} \underline{\Gamma}_{C_{1,1}} &= i\,(\underline{\Sigma}^{\mathrm{r}}_{1,1} \;-\; \underline{\Sigma}^{\mathrm{a}}_{1,1}) &= \underline{t}_{DL}\, \underline{a}_{1,1}\, \underline{t}_{LD} &= \underline{\Gamma}_{L}\;, \\ \underline{\Gamma}_{C_{1,1}} &= i\,(\underline{\Sigma}^{\mathrm{r}}_{1,1} \;-\; \underline{\Sigma}^{\mathrm{a}}_{1,1}) &= \underline{t}_{DR}\, \underline{a}_{1,1}\, \underline{t}_{RD} &= \underline{\Gamma}_{R}\;, \end{aligned} \tag{G.19}$$

equation (G.17) can be rewritten as

$$\begin{aligned} \underline{\Sigma}^{<}_{L} &= +i\, \underline{\Gamma}_{L}\, f_L\;, \\ \underline{\Sigma}^{<}_{R} &= +i\, \underline{\Gamma}_{R}\, f_R\;. \end{aligned} \tag{G.20}$$

In a similar manner one can show that

$$\begin{aligned} \underline{\Sigma}^{>}_{L} &= -i\, \underline{\Gamma}_{L}\, (1 - f_L)\;, \\ \underline{\Sigma}^{>}_{R} &= -i\, \underline{\Gamma}_{R}\, (1 - f_R)\;. \end{aligned} \tag{G.21}$$

G.3 Surface GREEN's Function

The main information needed to solve (G.14) are the surface GREEN's functions of $\underline{g}_L^{\mathrm{r}}$ and $\underline{g}_R^{\mathrm{r}}$. Using the recursive relation (H.10), equation (G.12) can be written as

$$\begin{aligned}
[\underline{A}_{L_i} \; - \; \underline{t}_{L_{i,i+1}} \; \underline{g}^{\mathrm{r}}_{L_{i+1,i+1}} \underline{t}^{\dagger}_{L_{i+1,i}}] \; \underline{g}^{\mathrm{r}}_{L_{i,i}} \quad &= \; \underline{I} \; , \\
[\underline{A}_{R_i} \; - \; \underline{t}^{\dagger}_{R_{i,i-1}} \; \underline{g}^{\mathrm{r}}_{R_{i-1,i-1}} \underline{t}_{R_{i-1,i}}] \; \underline{g}^{\mathrm{r}}_{R_{i,i}} \quad &= \; \underline{I} \; .
\end{aligned} \tag{G.22}$$

If the potential does not vary in the left and right contacts and if the coupling between different layers are equal, then $\underline{A}_{LL}$ and $\underline{A}_{RR}$ become semi-infinite periodic matrices with

$$\begin{aligned}
\underline{A}_{L_1} &= \underline{A}_{L_2} = \underline{A}_{L_3} = \ldots = \underline{A}_L \; , \\
\underline{A}_{R_1} &= \underline{A}_{R_2} = \underline{A}_{R_3} = \ldots = \underline{A}_R \; , \\
\underline{t}_{L_{1,2}} &= \underline{t}_{L_{2,3}} = \underline{t}_{L_{3,4}} = \ldots = \underline{t}_L \; , \\
\underline{t}_{R_{1,2}} &= \underline{t}_{R_{2,3}} = \underline{t}_{R_{3,4}} = \ldots = \underline{t}_R \; .
\end{aligned} \tag{G.23}$$

Under this condition one obtains

$$\begin{aligned}
\underline{g}^{\mathrm{r}}_{L_{1,1}} &= \underline{g}^{\mathrm{r}}_{R_{2,2}} = \ldots = \underline{g}^{\mathrm{r}}_{L} \; , \\
\underline{g}^{\mathrm{r}}_{R_{1,1}} &= \underline{g}^{\mathrm{r}}_{R_{2,2}} = \ldots = \underline{g}^{\mathrm{r}}_{R} \; .
\end{aligned} \tag{G.24}$$

Therefore, the surface GREEN's functions can be obtained by solving the quadratic matrix equations

$$\begin{aligned}
[\underline{A}_L - \underline{t}_L \; \underline{g}^{\mathrm{r}}_L \; \underline{t}^{\dagger}_L] \; \underline{g}^{\mathrm{r}}_L \quad &= \; \underline{I} \; , \\
[\underline{A}_R - \underline{t}^{\dagger}_R \; \underline{g}^{\mathrm{r}}_R \; \underline{t}_R] \; \underline{g}^{\mathrm{r}}_R \quad &= \; \underline{I} \; .
\end{aligned} \tag{G.25}$$

These equations can be solved iteratively by

$$\begin{aligned}
[\underline{A}_L - \underline{t}_L \; \underline{g}^{\mathrm{r}\,\langle m-1\rangle}_L \; \underline{t}^{\dagger}_L] \; \underline{g}^{\mathrm{r}\,\langle m\rangle}_L \quad &= \; \underline{I} \; , \\
[\underline{A}_R - \underline{t}^{\dagger}_R \; \underline{g}^{\mathrm{r}\,\langle m-1\rangle}_R \; \underline{t}_R] \; \underline{g}^{\mathrm{r}\,\langle m\rangle}_R \quad &= \; \underline{I} \; ,
\end{aligned} \tag{G.26}$$

where m represents the iteration number. It should be noted that the solution to (G.25) is analytic if the dimension of $\underline{A}_R$ is one.

Appendix H

Recursive GREEN's Function Method

As discussed in Section 4.2, the matrix representation of the kinetic equations is given by

$$\underline{A}\,\underline{G}^{\mathrm{r}} \;=\; \underline{I}\ , \tag{H.1}$$

$$\underline{A}\,\underline{G}^{<} \;=\; \underline{\Sigma}^{<}\,[\underline{G}^{\mathrm{r}}]^{\dagger}\ , \tag{H.2}$$

$$\underline{A} \;=\; [E\underline{I} - \underline{H} - \underline{\Sigma}^{\mathrm{r}}]\ , \tag{H.3}$$

where $\underline{\Sigma}$ is the total self-energy. To calculate the GREEN's functions, matrix inversion is required. However, since the matrices are block tridiagonal and also most of the observables are related to the diagonal blocks of the GREEN's functions, one can employ a recursive method to calculate the observables efficiently [8, 116]. We follow here the method proposed in [8].

H.1 Recursive Algorithm to Calculate G^{r}

The DYSON equation for the retarded GREEN's function and the left-connected GREEN's function [116] are employed to calculate the diagonal blocks of the full GREEN's function recursively. The solution to the matrix equation

$$\begin{bmatrix} \underline{A}_{Z,Z} & \underline{A}_{Z,Z'} \\ \underline{A}_{Z',Z} & \underline{A}_{Z',Z'} \end{bmatrix} \begin{bmatrix} \underline{G}^{\mathrm{r}}_{Z,Z} & \underline{G}^{\mathrm{r}}_{Z,Z'} \\ \underline{G}^{\mathrm{r}}_{Z',Z} & \underline{G}^{\mathrm{r}}_{Z',Z'} \end{bmatrix} = \begin{bmatrix} \underline{I} & 0 \\ 0 & \underline{I} \end{bmatrix}\ , \tag{H.4}$$

is

$$\begin{aligned} \underline{G}^{\mathrm{r}} &= \underline{G}^{\mathrm{r}0} + \underline{G}^{\mathrm{r}0}\,\underline{U}\,\underline{G}^{\mathrm{r}}\ , \\ &= \underline{G}^{r0} + \underline{G}^{\mathrm{r}}\,\underline{U}\,\underline{G}^{\mathrm{r}0}\ , \end{aligned} \tag{H.5}$$

where,

$$\underline{G}^{\mathrm{r}} \;=\; \begin{bmatrix} \underline{G}^{\mathrm{r}}_{Z,Z} & \underline{G}^{\mathrm{r}}_{Z,Z'} \\ \underline{G}^{\mathrm{r}}_{Z',Z} & \underline{G}^{\mathrm{r}}_{Z',Z'} \end{bmatrix}\ , \tag{H.6}$$

$$\underline{G}^{\mathrm{r}0} = \begin{bmatrix} \underline{G}^{\mathrm{r}0}_{Z,Z} & 0 \\ 0 & \underline{G}^{\mathrm{r}0}_{Z',Z'} \end{bmatrix} = \begin{bmatrix} \underline{A}^{-1}_{Z,Z} & 0 \\ 0 & \underline{A}^{-1}_{Z',Z'} \end{bmatrix} , \tag{H.7}$$

$$\underline{U} \;=\; \begin{bmatrix} 0 & -\underline{A}_{Z,Z'} \\ -\underline{A}_{Z',Z} & 0 \end{bmatrix} . \tag{H.8}$$

The *left-connected* retarded GREEN's function $\underline{g}^{\mathrm{r}}_{L_q}$ is defined by the first q blocks of (H.1) by

$$\underline{A}_{1:q,1:q}\; \underline{g}^{\mathrm{r}}_{L_q} = \underline{I}_{1:q,1:q} . \tag{H.9}$$

$\underline{g}^{\mathrm{r}}_{L_{q+1}}$ is defined in a manner identical to $\underline{g}^{\mathrm{r}}_{L_q}$ except that the left-connected system is comprised of the first $q+1$ blocks of (H.1). In terms of (H.4), the equation governing $\underline{g}^{\mathrm{r}}_{L_{q+1}}$ follows by setting $Z = 1:q$ and $Z' = q+1$. Using the DYSON equation [(H.5)], one obtains

$$\underline{g}^{\mathrm{r}}_{L_{q+1,q+1}} = \left(\underline{A}_{q+1,q+1} \;-\; \underline{A}_{q+1,q} \underline{g}^{\mathrm{r}}_{L_{q,q}} \; \underline{A}_{q,q+1} \right)^{-1} . \tag{H.10}$$

It should be noted that the last block $\underline{g}^{\mathrm{r}}_{L_{N,N}}$ is equal to the fully connected GREEN's function $\underline{G}^{\mathrm{r}}_{L_{N,N}}$, which is the solution to (H.1). The full GREEN's function can be expressed in terms of the left-connected GREEN's function by considering (H.4) such that $\underline{A}_{Z,Z} = \underline{A}_{1:q,1:q}$, $\underline{A}_{Z',Z'} = \underline{A}_{q+1:N,q+1:N}$ and $\underline{A}_{Z,Z'} = \underline{A}_{1:q,q+1:N}$. By noting that the only non-zero block of $\underline{A}_{1:q,q+1:N}$ is $\underline{A}_{q,q+1}$ and using (H.5), one obtains

$$\begin{aligned} \underline{G}^{\mathrm{r}}_{q,q} \;&=\; \underline{g}^{\mathrm{r}}_{L_{q,q}} \;+\; \underline{g}^{\mathrm{r}}_{L_{q,q}} \left(\underline{A}_{q,q+1} \; \underline{G}^{\mathrm{r}}_{q+1,q+1} \; \underline{A}_{q+1,q} \right) \underline{g}^{\mathrm{r}}_{L_{q,q}} , \\ &=\; \underline{g}^{\mathrm{r}}_{L_{q,q}} \;-\; \underline{g}^{\mathrm{r}}_{L_{q,q}} \; \underline{A}_{q,q+1} \; \underline{G}^{\mathrm{r}}_{q+1,q} , \end{aligned} \tag{H.11}$$

Both $G^{\mathrm{r}}_{q,q}$ and $G^{\mathrm{r}}_{q+1,q}$ are used for the calculation of the electron density, and so storing both sets of matrices will be useful. In view of the above equations, the algorithm to compute the diagonal blocks $G^{\mathrm{r}}_{q,q}$ is given by the following steps

- $g^{\mathrm{r}}_{L_{1,1}} \;=\; \underline{A}^{-1}_{1}$,
- For $q \;=\; 1,\; 2,\; \ldots,\; N-1$, (H.10) is computed,
- For $q \;=\; N-1,\; N-2,\; \ldots,\; 1$, (H.11) is computed.

H.2 Recursive Algorithm to Calculate $G^<$

Following Appendix H.1, the algorithm to calculate the electron density (diagonal elements of $G^<$) is discussed in terms of the Dyson equation for the lesser and the left-connected Green's functions. The solution to the matrix equation

$$\begin{bmatrix} \underline{A}_{Z,Z} & \underline{A}_{Z,Z'} \\ \underline{A}_{Z',Z} & \underline{A}_{Z',Z'} \end{bmatrix} \begin{bmatrix} \underline{G}^<_{Z,Z} & \underline{G}^<_{Z,Z'} \\ \underline{G}^<_{Z',Z} & \underline{G}^<_{Z',Z'} \end{bmatrix} = \begin{bmatrix} \underline{\Sigma}^<_{Z,Z} & \underline{\Sigma}^<_{Z,Z'} \\ \underline{\Sigma}^<_{Z',Z} & \underline{\Sigma}^<_{Z',Z'} \end{bmatrix} \begin{bmatrix} \underline{G}^{\mathrm{a}}_{Z,Z} & \underline{G}^{\mathrm{a}}_{Z,Z'} \\ \underline{G}^{\mathrm{a}}_{Z',Z} & \underline{G}^{\mathrm{a}}_{Z',Z'} \end{bmatrix} , \tag{H.12}$$

can be written as

$$\underline{G}^< \;=\; \underline{G}^{\mathrm{r}0}\, \underline{U}\, \underline{G}^< \;+\; \underline{G}^{\mathrm{r}0}\, \underline{\Sigma}^<\, \underline{G}^{\mathrm{a}} , \tag{H.13}$$

where $\underline{G}^{\mathrm{r}0}$ and $\underline{U}$ have been defined in (H.7) and (H.8), and $\underline{G}^<$ and $\underline{G}^a$ are readily identifiable from (H.12). Using the relation $\underline{G}^{\mathrm{a}} = \underline{G}^{\mathrm{r}\dagger} = \underline{G}^{\mathrm{a}0} + \underline{G}^{\mathrm{a}0}\underline{U}^\dagger\underline{G}^{\mathrm{a}}$, (H.13) can be written as

$$\begin{aligned} \underline{G}^< \;&=\; \underline{G}^{<0} \;+\; \underline{G}^{<0}\, \underline{U}^\dagger\, \underline{G}^a \;+\; \underline{G}^{r0}\, \underline{U}\, \underline{G}^< , \\ &=\; \underline{G}^{<0} \;+\; \underline{G}^{\mathrm{r}}\, \underline{U}\, \underline{G}^{<0} \;+\; \underline{G}^<\, \underline{U}^\dagger\, \underline{G}^{\mathrm{a}0} , \end{aligned} \tag{H.14}$$

where

$$\underline{G}^{<0} \;=\; \underline{G}^{r0}\, \underline{\Sigma}^<\, \underline{G}^{a0} . \tag{H.15}$$

The *left-connected* lesser Green's function $\underline{g}^<_{L_q}$ is defined by the first q blocks of (H.2)

$$\underline{A}_{1:q,1:q}\, \underline{g}^<_{L_q} \;=\; \underline{\Sigma}^<_{1:q,1:q}\, \underline{g}^{\mathrm{a}}_{L_{1:q,1:q}} . \tag{H.16}$$

$\underline{g}^<_{L_{q+1}}$ is defined in a manner identical to $\underline{g}^<_{L_q}$ except that the left-connected system is comprised of the first $q+1$ blocks of (H.2). In terms of (H.12), the equation governing $\underline{g}^<_{L_{q+1}}$ follows by setting $Z = 1:q$ and $Z' = q+1$. Using the Dyson equations for $\underline{G}^{\mathrm{r}}$ and $\underline{G}^<$, $\underline{g}^<_{L_{q+1,q+1}}$ can be recursively obtained as [8]

$$\underline{g}^<_{L_{q+1,q+1}} = \underline{g}^{\mathrm{r}}_{L_{q+1,q+1}} \left[\underline{\Sigma}^<_{q+1,q+1} + \underline{\sigma}^<_{q+1}\right] \underline{g}^{\mathrm{a}}_{L_{q+1,q+1}} + \underline{g}^{\mathrm{r}}_{L_{q+1,q+1}} \underline{\Sigma}^<_{q+1,q} \underline{g}^{\mathrm{a}}_{L_{q,q+1}} + \underline{g}^{\mathrm{r}}_{L_{q+1,q}} \underline{\Sigma}^<_{q,q+1} \underline{g}^{\mathrm{a}}_{L_{q+1,q+1}} , \tag{H.17}$$

which can be written in a more intuitive form as

$$\underline{g}^<_{L_{q+1,q+1}} = \underline{g}^{\mathrm{r}}_{L_{q+1,q+1}} \left[\underline{\Sigma}^<_{q+1,q+1} + \underline{\sigma}^<_{q+1} - \underline{\Sigma}^<_{q+1,q} \underline{g}^{\mathrm{a}}_{L_{q,q}} \underline{A}^\dagger_{q,q+1} - \underline{A}_{q+1,q} \underline{g}^{\mathrm{r}}_{L_{q,q}} \underline{\Sigma}^<_{q,q+1}\right] \underline{g}^{\mathrm{a}}_{L_{q+1,q+1}} , \tag{H.18}$$

where $\underline{\sigma}^<_{q+1} = \underline{A}_{q+1,q} \underline{g}^<_{L_{q,q}} \underline{A}^\dagger_{q,q+1}$. Equation (H.18) has the physical meaning that $\underline{g}^<_{L_{q+1,q+1}}$ has contributions due to four injection functions: (i) an effective self-energy due to the left-connected structure that ends at q, which is represented by $\underline{\sigma}^<_{q+1}$, (ii) the diagonal self-energy component at grid point $q+1$ that enters (H.2), and (iii) the two off-diagonal self-energy components involving grid points q and $q+1$.

To express the *full* lesser GREEN's function in terms of the left-connected GREEN's function, one can consider (H.12) such that $\underline{A}_{Z} = \underline{A}_{1:q,1:q}$, $\underline{A}'_{Z} = \underline{A}_{q+1:N,q+1:N}$ and $\underline{A}_{Z,Z'} = \underline{A}_{1:q,q+1:N}$. Noting that the only non-zero block of $\underline{A}_{1:q,q+1:N}$ is $\underline{A}_{q,q+1}$ and using (H.14), one obtains

$$\underline{G}^{<}_{q,q} = \underline{g}^{<}_{L_{q,q}} - \underline{g}^{<}_{L_{q,q}}\underline{A}^{\dagger}_{q,q+1}\underline{G}^{\mathrm{a}}_{q+1,q} - \underline{g}^{<0}_{q,q+1}\underline{A}^{\dagger}_{q+1,q}\underline{G}^{\mathrm{a}}_{q,q} - \underline{g}^{\mathrm{r}}_{L_{q,q}}\underline{A}_{q,q+1}\underline{G}^{<}_{q+1,q} \;. \tag{H.19}$$

Using (H.14), $\underline{G}^{<}_{q+1,q}$ can be written in terms of $\underline{G}^{<}_{q+1,q+1}$ and other known GREEN's functions as

$$\underline{G}^{<}_{q+1,q} = \underline{g}^{<0}_{q+1,q} - \underline{G}^{\mathrm{r}}_{q+1,q}\underline{A}_{q,q+1}\underline{g}^{<0}_{q+1,q} - \underline{G}^{\mathrm{r}}_{q+1,q+1}\underline{A}_{q+1,q}\underline{g}^{<}_{L_{q,q}} - \underline{G}^{<}_{q+1,q+1}\underline{A}^{\dagger}_{q,q+1}\underline{g}^{\mathrm{a}}_{L_{q,q}} \;. \tag{H.20}$$

Substituting (H.20) in (H.19) and using (H.5), one obtains

$$\begin{aligned} \underline{G}^{<}_{q,q} \;=\;& \underline{g}^{<}_{L_{q,q}} + \underline{g}^{\mathrm{r}}_{L_{q,q}}\left(\underline{A}_{q,q+1}\underline{G}^{<}_{q+1,q+1}\underline{A}^{\dagger}_{q+1,q}\right)\underline{g}^{\mathrm{a}}_{L_{q,q}} - \left[\underline{g}^{<}_{L_{q,q}}\underline{A}^{\dagger}_{q,q+1}\underline{G}^{\mathrm{a}}_{q+1,q} + \underline{G}^{\mathrm{r}}_{q,q+1}\underline{A}_{q+1,q}\underline{g}^{<}_{L_{q,q}}\right] \\ & - \left[\underline{g}^{<0}_{q,q+1}\underline{A}^{\dagger}_{q+1,q}\underline{G}^{\mathrm{a}}_{q,q} + \underline{G}^{\mathrm{r}}_{q,q}\underline{A}_{q,q+1}\underline{g}^{<0}_{q+1,q}\right] \;, \end{aligned} \tag{H.21}$$

where

$$\begin{aligned} \underline{g}^{<0}_{q,q+1} &= \underline{g}^{\mathrm{r}0}_{q,q}\;\underline{\Sigma}^{<}_{q,q+1}\;\underline{g}^{\mathrm{a}0}_{q+1,q+1} \\ \underline{g}^{<0}_{q+1,q} &= \underline{g}^{\mathrm{r}0}_{q+1,q+1}\;\underline{\Sigma}^{<}_{q+1,q}\;\underline{g}^{\mathrm{a}0}_{q,q} \;. \end{aligned} \tag{H.22}$$

The terms inside the square brackets of (H.21) are HERMITian conjugates of each other. In view of the above equations, the algorithm to compute the diagonal blocks of $\underline{G}^{<}$ is given by the following steps:

- $\underline{g}^{<}_{L_{1,1}} = \underline{g}^{\mathrm{r}0}_{1,1}\;\underline{\Sigma}^{<}_{L}\;\underline{g}^{\mathrm{a}0}_{1,1}$,
- For $q = 1,\ 2,\ \ldots,\ N-1$, (H.18) is computed,
- For $q = \ N-1,\ N-2,\ \ldots,\ 1$, (H.21) and (H.22) are computed.

Bibliography

[1] "International Technology Roadmap for Semiconductors - 2005 Edition," tech. rep., Semiconductor Industry Association, 2005.
URL: `http://public.itrs.net`.

[2] S. Iijima, "Helical Microtubules of Graphitic Carbon," *Nature (London)*, vol. 354, no. 6348, pp. 56–58, 1991.

[3] R. Martel, T. Schmidt, H. Shea, T. Hertel, and P. Avouris, "Single- and Multi-Wall Carbon Nanotube Field-Effect Transistors," *Appl.Phys.Lett.*, vol. 73, no. 17, pp. 2447–2449, 1998.

[4] S. J. Tans, A. R. M. Verschueren, and C. Dekker, "Room-Temperature Transistor Based on a Single Carbon Nanotube," *Nature (London)*, vol. 393, no. 6680, pp. 49–52, 1998.

[5] J. Guo, S. Datta, and M. Lundstrom, "A Numerical Study of Scaling Issues for Schottky Barrier Carbon Nanotube Transistors," *IEEE Trans. Electron Devices*, vol. 51, no. 2, pp. 172–177, 2004.

[6] M. Freitag, Y. Martin, J. Misewich, R. Martel, and P. Avouris, "Photoconductivity of Single Carbon Nanotubes," *Nano Lett.*, vol. 3, no. 8, pp. 1067–1071, 2003.

[7] M. Freitag, J. Chen, J. Tersoff, J. Tsang, Q. Fu, J. Liu, and P. Avouris, "Mobile Ambipolar Domain in Carbon-Nanotube Infrared Emitters," vol. 93, p. 076803, 2004.

[8] A. Svizhenko, M. P. Anantram, T. R. Govindan, B. Biegel, and R. Venugopal, "Two-Dimensional Quantum Mechanical Modeling of Nanotransistors," *J.Appl.Phys.*, vol. 91, no. 4, pp. 2343–2354, 2002.

[9] R. Venugopal, Z. Ren, S. Datta, M. Lundstrom, and D. Jovanovic, "Simulating Quantum Transport in Nanoscale Transistors: Real Versus Mode-Space Approaches," *J.Appl.Phys.*, vol. 92, no. 7, pp. 3730–3739, 2002.

[10] A. Svizhenko and M. Anantram, "Effect of Scattering and Contacts on Current and Electrostatics in Carbon Nanotubes," *Phys.Rev.B*, vol. 72, p. 085430, 2005.

[11] Y. Xue, S. Datta, and M. A. Ratner, “First-Principles Based Matrix Green’s Function Approach to Molecular Electronic Devices: General Formalism,” *Chem.Phys.*, vol. 281, no. 2-3, pp. 151–170, 2002.

[12] R. Saito, G. Dresselhaus, and M. Dresselhaus, *Physical Properties of Carbon Nanotubes*. London: Imperial College Press, 1998.

[13] M. Endo, *Mecanisme de Croissance en Phase Vapeur de Fibres de Carbone (The Growth Mechanism of Vapor-Grown Carbon Fibers)*. Dissertation, University of Orleans, Orleans, France, 1975.

[14] A. Oberlin, M. Endo, and T. Koyama, “Filamentous Growth of Carbon through Benzene Decomposition,” *J.Cryst.Growth*, vol. 32, no. 3, pp. 335–349, 1976.

[15] S. Iijima, “Direct Observation of the Tetrahedral Bonding in Graphitized Carbon Black by High Resolution Electron Microscopy,” *J.Cryst.Growth*, vol. 55, no. 3, pp. 675–683, 1980.

[16] M. S. Dresselhaus, G. Dresselhaus, and R. Saito, “Carbon Fibers Based on C60 and Their Symmetry ,” *Phys.Rev.B*, vol. 45, no. 11, pp. 6234–6242, 1992.

[17] J. W. Mintmire, B. I. Dunlap, and C. T. White, “Are Fullerene Tubules Metallic?,” *Phys.Rev.Lett.*, vol. 68, no. 5, pp. 631–634, 1992.

[18] N. Hamada, S. Sawada, and A. Oshiyama, “New One-Dimensional Conductors: Graphitic Microtubules ,” *Phys.Rev.Lett.*, vol. 68, no. 10, pp. 1579–1581, 1992.

[19] J. W. G. Wildöer, L. C. Venema, A. G. Rinzler, R. E. Smalley, and C. Dekker, “Electronic Structure of Atomically Resolved Carbon Nanotubes,” *Nature (London)*, vol. 391, no. 6662, pp. 59–62, 1998.

[20] T. W. Odom, J. L. Huang, P. Kim, and C. M. Lieber, “Atomic Structure and Electronic Properties of Single-Walled Carbon Nanotubes,” *Nature (London)*, vol. 391, no. 6662, pp. 62–64, 1998.

[21] R. Saito, M. Fujita, G. Dresselhaus, and M. S. Dresselhaus, “Electronic Structure of Chiral Graphene Tubules,” *Appl.Phys.Lett.*, vol. 60, no. 18, pp. 2240–2206, 1992.

[22] S. Reich, , C. Thomsen, and J. Maultzsch, *Carbon Nanotubes: Basic Concepts and Physical Properties*. Weinheim, Cambridge: Wiley-VCH, 2004.

[23] D. S. Bethune, C. H. Kiang, M. S. de Vries, G. Gorman, R. Savoy, J. Vazquez, and R. Beyers, “Cobalt-Catalysed Growth of Carbon Nanotubes with Single-Atomic-Layer Walls,” *Nature (London)*, vol. 363, no. 6430, pp. 605–607, 1993.

[24] A. Thess, R. Lee, P. Nikolaev, H. J. Dai, P. Petit, J. Robert, C. H. Xu, Y. H. Lee, S. G. Kim, A. G. Rinzler, D. T. Colbert, G. E. Scuseria, D. Tomanek, J. E. Fischer, and R. E. Smalley, “Crystalline Ropes of Metallic Carbon Nanotubes,” *Science*, vol. 273, no. 5274, pp. 483–487, 1996.

[25] H. Dai, J. Kong, C. Zhou, N. Franklin, T. Tombler, A. Cassell, S. Fan, and M. Chapline, “Controlled Chemical Routes to Nanotube Architectures, Physics, and Devices,” *J.Phys.Chem.B*, vol. 103, no. 51, pp. 11246–11255, 1999.

[26] S. Fan, M. Chapline, F. Franklin, T. Tombler, A. Cassell, and H. Dai, “Self-Oriented Regular Arrays of Carbon Nanotubes and Their Field Emission Properties,” *Science*, vol. 283, no. 5401, pp. 512–514, 1999.

[27] A. M. Cassell, N. R. Franklin, T. W. Tombler, E. M. Chan, J. Han, and H. Dai, “Directed Growth of Free-Standing Single-Walled Carbon Nanotubes,” *J.Am.Chem.Soc.*, vol. 121, no. 34, pp. 7975–7976, 1999.

[28] N. Franklin and H. Dai, “An Enhanced CVD Approach to Extensive Nanotube Networks with Directionality,” *Adv.Mater.*, vol. 12, no. 12, pp. 890–894, 2000.

[29] R. A. Jishi, D. Inomata, K. Nakao, M. S. Dresselhaus, and G. Dresselhaus, “Electronic and Lattice Properties of Carbon Nanotubes,” *J.Phys.Soc.Jap.*, vol. 63, no. 6, pp. 2252–2260, 1994.

[30] V. Popov, “Curvature Effects on the Structural, Electronic and Optical Properties of Isolated Single-Walled Carbon Nanotubes within a Symmetry-Adapted Non-Orthogonal Tight-Binding Model,” *New J.Phys.*, vol. 6, no. 17, pp. 1–17, 2004.

[31] S. Reich and C. T. S. P. Ordejón, “Electronic Band Structure of Isolated and Bundled Carbon Nanotubes,” *Phys.Rev.B*, vol. 65, p. 155411, 2002.

[32] V. Zólyomi and J. Kürti, “First-Principles Calculations for the Electronic Band Structures of Small Diameter Single-Wall Carbon Nanotubes,” *Phys.Rev.B*, vol. 70, p. 085403, 2004.

[33] S. Datta, *Quantum Transport: From Atoms to Transistors*. Cambridge, New York: Cambridge University Press, 2005.

[34] J. W. Mintmire and C. White, “Universal Density of States for Carbon Nanotubes,” *Phys.Rev.Lett.*, vol. 81, no. 12, pp. 2506–2509, 1998.

[35] A. Kasuya, Y. Sasaki, Y. Saito, K. Tohji, and Y. Nishina, “Evidence for Size-Dependent Discrete Dispersions in Single-Wall Nanotubes,” *Phys.Rev.Lett.*, vol. 78, no. 23, pp. 4434–4437, 1997.

[36] S. Kazaoui, N. Minami, R. Jacquemin, and H. Kataura, “Amphoteric Doping of Single-Wall Carbon-Nanotube Thin Films as Probed by Optical Absorption Spectroscopy,” *Phys.Rev.B*, vol. 60, no. 19, pp. 13339–13342, 1999.

[37] R. A. Jishi, L. Venkataraman, M. S. Dresselhaus, and G. Dresselhaus, “Phonon Modes in Carbon Nanotubules,” *Chem.Phys.Lett.*, vol. 209, no. 1-2, pp. 77–82, 1993.

[38] P. C. Eklunda, J. M. Holdena, and R. A. Jishi, “Vibrational Modes of Carbon Nanotubes; Spectroscopy and theory,” *Carbon*, vol. 33, no. 7, pp. 959–972, 1995.

[39] J. Yu, R. K. Kalia, and P. Vashishta, “Phonons in Graphitic Tubules: A Tight-Binding Molecular Dynamics Study,” *J.Chem.Phys*, vol. 103, no. 15, pp. 6697–6705, 1995.

[40] M. Menon, E. Richter, and K. R. Subbaswamy, “Structural and Vibrational Properties of Fullerenes and Nanotubes in a Nonorthogonal Tight-Binding Scheme,” *J.Chem.Phys*, vol. 104, no. 15, pp. 5875–5882, 1995.

[41] J. Kürti, G. Kresse, and H. Kuzmany, “First-Principles Calculations of the Radial Breathing Mode of Single-Wall Carbon Nanotubes,” *Phys.Rev.B*, vol. 58, no. 14, pp. 8869–8872, 1998.

[42] D. Sánchez-Portal, E. Artacho, J. M. Soler, A. Rubio, and P. Ordejón, “Ab Initio Structural, Elastic, and Vibrational Properties of Carbon Nanotubes,” *Phys.Rev.B*, vol. 59, no. 19, pp. 12678–12688, 1999.

[43] O. Dubay, G. Kresse, and H. Kuzmany, “Phonon Softening in Metallic Nanotubes by a Peierls-like Mechanism,” *Phys.Rev.Lett.*, vol. 88, p. 235506, 2002.

[44] O. Dubay and G. Kresse, “Accurate Density Functional Calculations for the Phonon Dispersion Relations of Graphite Layer and Carbon Nanotubes,” *Phys.Rev.B*, vol. 67, p. 035401, 2003.

[45] L.-H. Ye, B.-G. Liu, D.-S. Wang, and R. Han, “Ab Initio Phonon Dispersions of Single-Wall Carbon Nanotubes,” *Phys.Rev.B*, vol. 69, p. 235409, 2004.

[46] J. Maultzsch, S. Reich, C. Thomsen, H. Requardt, and P. Ordejón, “Phonon Dispersion in Graphite,” *Phys.Rev.B*, vol. 92, p. 075501, 2004.

[47] S. Piscanec, M. Lazzeri, F. Mauri, A. C. Ferrari, and J. Robertson, “Kohn Anomalies and Electron-Phonon Interactions in Graphite,” *Phys.Rev.B*, vol. 93, p. 185503, 2004.

[48] K.-P. Bohnen, R. Heid, H. J. Liu, and C. T. Chan, “Lattice Dynamics and Electron-Phonon Interaction in (3,3) Carbon Nanotubes,” *Phys.Rev.Lett.*, vol. 93, p. 245501, 2004.

[49] D. Connétable, G.-M. Rignanese, J.-C. Charlier, and X. Blase, “Room Temperature Peierls Distortion in Small Diameter Nanotubes,” *Phys.Rev.Lett.*, vol. 94, p. 015503, 2005.

[50] V. N. Popov, V. E. V. Doren, and M. Balkanski, “Lattice Dynamics of Single-Walled Carbon Nanotubes,” *Phys.Rev.B*, vol. 59, no. 13, pp. 8355–8358, 1999.

[51] Z. M. Li, V. N. Popov, and Z. K. Tang, “A Symmetry-Adapted Force-Constant Lattice-Dynamical Model for Single-Walled Carbon Nanotubes,” *Solid-State Communications*, vol. 130, no. 10, pp. 657–661, 2004.

[52] I. Milošević, E. Dobardžić, and M. Damnjanović, “Phonons in Narrow Carbon Nanotubes,” *Phys.Rev.B*, vol. 72, p. 085426, 2005.

[53] C. Mapelli, C. Castiglioni, G. Zerbi, and K. Müllen, “Common Force Field for Graphite and Polycyclic Aromatic Hydrocarbons ,” *Phys.Rev.B*, vol. 60, no. 18, pp. 12710–12725, 1999.

[54] V. N. Popov and P. Lambin, “Radius and Chirality Dependence of the Radial Breathing Mode and the G-band Phonon Modes of Single-Walled Carbon Nanotubes,” *Phys.Rev.B*, vol. 73, p. 085407, 2006.

[55] S. O. Koswatta, S. Hasan, M. Lundstrom, M. P. Anantram, and D. E. Nikonov, “Non-Equilibrium Green’s Function Treatment of Phonon Scattering in Carbon Nanotube Transistors,” *cond-mat/0702496*, 2007.

[56] V. N. Popov and P. Lambin, “Intraband Electron-Phonon Scattering in Single-Walled Carbon Nanotubes,” *Phys.Rev.B*, vol. 74, p. 075415, 2006.

[57] G. D. Mahan, “Electron-Optical Phonon Interaction in Carbon Nanotubes,” *Phys.Rev.B*, vol. 68, p. 125409, 2003.

[58] J. Jiang, R. Saito, G. G. Samsonidze, S. G. Chou, A. Jorio, G. Dresselhaus, and M. S. Dresselhaus, “Electron-Phonon Matrix Elements in Single-Wall Carbon Nanotubes,” *Phys.Rev.B*, vol. 72, p. 235408, 2005.

[59] V. N. Popov, V. E. V. Doren, and M. Balkanski, “Elastic Properties of Single-Walled Carbon Nanotubes,” *Phys.Rev.B*, vol. 61, no. 4, pp. 3078–3084, 2000.

[60] S. Datta, *Electronic Transport in Mesoscopic Systems*. New York: Cambridge University Press, 1995.

[61] B. J. Wees, H. van Houten, C. W. J. Beenakker, J. G. Williamson, L. P. Kouwenhoven, D. van der Marel, and C. T. Foxon, “Quantized Conductance of Point Contacts in a Two-Dimensional Electron Gas,” *Phys.Rev.Lett.*, vol. 60, no. 9, pp. 848–850, 1988.

[62] W. Hoenlein, F. Kreupl, G. Duesberg, A. Graham, M. Liebau, R. Seidel, and E. Unger, “Carbon Nanotube Applications in Microelectronics,” *IEEE Trans.Components and Packaging Technologies*, vol. 27, no. 4, pp. 629–634, 2004.

[63] H. T. Soh, C. F. Quate, A. F. Morpurgo, C. Marcus, J. Kong, and H. Dai, “Integrated Nanotube Circuits: Controlled Growth and Ohmic Contacting of Single-Walled Carbon Nanotubes,” *Appl.Phys.Lett.*, vol. 75, no. 5, pp. 627–629, 1999.

[64] R. Martel, V. Derycke, C. Lavoie, J. Appenzeller, K. K. Chan, J. Tersoff, and P. Avouris, “Ambipolar Electrical Transport in Semiconducting Single-Wall Carbon Nanotubes,” *Phys.Rev.Lett.*, vol. 87, p. 256805, 2001.

[65] R. Seidel, M. Liebau, G. Duesberg, F. Kreupl, E. Unger, A. Graham, W. Hoenlein, and W. Pompe, “In-Situ Contacted Single-Walled Carbon Nanotubes and Contact Improvement by Electroless Deposition,” *Nano Lett.*, vol. 3, no. 7, pp. 965–968, 2003.

[66] A. Javey, J. Guo, Q. Wang, M. Lundstrom, and H. Dai, “Ballistic Carbon Nanotube Field-Effect Transistors,” *Nature (London)*, vol. 424, no. 6949, pp. 654–657, 2003.

[67] V. Derycke, R. Martel, J. Appenzeller, and P. Avouris, “Carbon Nanotube Inter- and Intramolecular Logic Gates,” *Nano Lett.*, vol. 1, no. 9, pp. 453–465, 2001.

[68] S. Wind, J. Appenzeller, R. Martel, V. Derycke, and P. Avouris, “Vertical Scaling of Carbon Nanotube Field-Effect Transistors using Top Gate Electrodes,” vol. 80, no. 20, pp. 3817–3819, 2002.

[69] J. Appenzeller, J. Knoch, R. Martel, V. Derycke, S. Wind, and P. Avouris;, “Carbon Nanotube Electronics,” *IEEE Trans.Nanotechnology*, vol. 1, no. 4, pp. 184–189, 2002.

[70] A. Javey, H. Kim, M. Brink, Q. Wang, A. Ural, J. Guo, P. McIntyre, P. McEuen, M. Lundstrom, and H. Dai, “High-κ Dielectrics for Advanced Carbon Nanotube Transistors and Logic Gates,” *Nature Materials*, vol. 1, no. 4, pp. 241–246, 2002.

[71] M. Radosavljevic, J. Appenzeller, P. Avouris, and J. Knoch, “High Performance of Potassium n-Doped Carbon Nanotube Field-Effect Transistors,” *Appl.Phys.Lett.*, vol. 84, no. 18, pp. 3693–3695, 2004.

[72] F. Leonard and J. Tersoff, “Novel Length Scales in Nanotube Devices,” *Phys.Rev.Lett.*, vol. 83, no. 24, pp. 5174–5177, 1999.

[73] F. Leonard and J. Tersoff, “Role of Fermi-Level Pinning in Nanotube Schottky Diodes,” *Phys.Rev.Lett.*, vol. 84, no. 20, pp. 4693–4696, 2000.

[74] J. Appenzeller, M. Radosavljevic, J. Knoch, and P. Avouris, “Tunneling Versus Thermionic Emission in One-Dimensional Semiconductors,” *Phys.Rev.Lett.*, vol. 92, p. 048301, 2004.

[75] R. V. Seidel, A. P. Graham, J. Kretz, B. Rajasekharan, G. S. Duesberg, M. Liebau, E. Unger, F. Kreupl, and W. Hoenlein, “Sub-20 nm Short Channel Carbon Nanotube Transistors,” *Nano Lett.*, vol. 5, no. 1, pp. 147–150, 2005.

[76] M. H. Yang, K. B. K. Teo, L. Gangloff, W. I. Milne, D. G. Hasko, Y. Robert, and P. Legagneux, “Advantages of Top-Gate, High-k Dielectric Carbon Nanotube Field-Effect Transistors,” *Appl.Phys.Lett.*, vol. 85, p. 113507, 2006.

[77] J. Appenzeller, J. Knoch, V. Derycke, R. Martel, S. Wind, and P. Avouris, “Field-Modulated Carrier Transport in Carbon Nanotube Transistors,” *Phys.Rev.Lett.*, vol. 89, p. 126801, 2002.

[78] S. Heinze, J. Tersoff, R. Martel, V. Derycke, J. Appenzeller, and P. Avouris, “Carbon Nanotubes as Schottky Barrier Transistors,” *Phys.Rev.Lett.*, vol. 89, p. 106801, 2002.

[79] M. Freitag, M. Radosavljevic, Y. X. Zhou, A. T. Johnson, and W. F. Smith, “Controlled Creation of a Carbon Nanotube Diode by a Scanned Gate,” *Appl.Phys.Lett.*, vol. 79, no. 20, pp. 3326–3328, 2001.

[80] S. Wind, J. Appenzeller, and P. Avouris, “Lateral Scaling in Carbon-Nanotube Field-Effect Transistors,” *Phys.Rev.Lett.*, vol. 91, p. 058301, 2003.

[81] Z. Chen, J. Appenzeller, J. Knoch, Y.-M. Lin, and P. Avouris, “The Role of Metal-Nanotube Contact in the Performance of Carbon Nanotube Field-Effect Transistors,” *Nano Lett.*, vol. 5, no. 6, pp. 1497–1502, 2005.

[82] P. G. Collins, K. Bradley, M. Ishigami, and A. Zettl, “Extreme Oxygen Sensitivity of Electronic Properties of Carbon Nanotubes,” *Science*, vol. 287, no. 5459, pp. 1801–1803, 2000.

[83] V. Derycke, R. Martel, J. Appenzeller, and P. Avouris, “Controlling Doping and Carrier Injection in Carbon Nanotube Transistors,” vol. 80, no. 15, pp. 2773–2775, 2002.

[84] T. Nakanishi, A. Bachtold, and C. Dekker, “Transport Through the Interface Between a Semiconducting Carbon Nanotube and a Metal Electrode,” *Phys.Rev.B*, vol. 66, p. 073307, 2002.

[85] T. Rueckes, K. Kim, E. Joselevich, G. Y. Tseng, C. L. Cheung, and C. M. Lieber, “Carbon Nanotube-Based Nonvolatile Random Access Memory for Molecular Computing,” *Science*, vol. 289, no. 5476, pp. 94–97, 2000.

[86] J. Kong, N. R. Franklin, C. W. Zhou, M. G. Chapline, S. Peng, K. J. Cho, and H. J. Dai, "Nanotube Molecular Wires as Chemical Sensors," *Science*, vol. 287, no. 5453, pp. 622–625, 2000.

[87] A. Bachtold, P. Hadley, T. Nakanishi, and C. Dekker, "Logic Circuits with Carbon Nanotube Transistors," *Science*, vol. 294, no. 5545, pp. 1317–1320, 2001.

[88] Z. Chen, J. Appenzeller, Y.-M. Lin, J. Sippel-Oakley, A. G. Rinzler, J. Tang, S. J. Wind, P. M. Solomon, and P. Avouris, "An Integrated Logic Circuit Assembled on a Single Carbon Nanotube," *Science*, vol. 311, no. 5768, p. 1735, 2006.

[89] D. Frank and J. Appenzeller, "High-Frequency Response in Carbon Nanotube Field-Effect Transistors," *IEEE Trans. Electron Devices*, vol. 25, no. 1, pp. 34–36, 2004.

[90] X. Huo, M. Zhang, P. C. H. Chan, Q. Liang, and Z. K. Tang, "High Frequency S parameters Characterization of Back-Gate Carbon Nanotube Field-Effect Transistors," in *IEDM Tech.Dig.*, (San Francisco), pp. 691–694, IEEE, 2004.

[91] S. Rosenblatt, H. Lin, V. Sazonova, S. Tiwari, and P. L. McEuen, "Mixing at 50 GHz Using a Single-Walled Carbon Nanotube Transistor," *Appl.Phys.Lett.*, vol. 87, p. 153111, 2005.

[92] J. Schwinger, "Brownian Motion of a Quantum Oscillator," *J.Math.Phys.*, vol. 2, no. 3, pp. 407–432, 1961.

[93] L. P. Kadanoff and G. Baym, *Quantum Statistical Mechanics: Green's Function Methods in Equilibrium and Non-Equilibrium Problems.* New York: W.A. Benjamin, 1962.

[94] C. B. Duke, *Tunneling in Solids.* New York: Academic Press, 1969.

[95] G. Kim and G. B. Arnold, "Theoretical Study of Tunneling Phenomena in Double-Barrier Quantum-Well Heterostructures," *Phys.Rev.B*, vol. 38, no. 5, pp. 3252–3262, 1988.

[96] C. Caroli, R. Combescot, P. Nozieres, and D. Saint-James, "Direct Calculation of the Tunneling Current," *J.Phys.C:Solid State Phys.*, vol. 4, no. 8, pp. 916–929, 1971.

[97] C. Caroli, R. Combescot, D. Lederer, P. Nozieres, and D. Saint-James, "A Direct Calculation of the Tunnelling Current. II. Free Electron Description," *J.Phys.C:Solid State Phys.*, vol. 4, no. 16, pp. 2598–2610, 1971.

[98] R. Combescot, "A Direct Calculation of the Tunnelling Current. III. Effect of Localized Impurity States in the Barrier," *J.Phys.C:Solid State Phys.*, vol. 4, no. 16, pp. 2611–2622, 1971.

[99] C. Caroli, R. Combescot, P. Nozieres, and D. Saint-James, "A Direct Calculation of the Tunnelling Current: IV. Electron-Phonon Interaction Effects," *J.Phys.C:Solid State Phys.*, vol. 5, no. 1, pp. 21–42, 1972.

[100] W. R. Bandy and A. J. Glick, "Tight-Binding Green's-Function Calculation of Electron Tunneling. I. One-Dimensional Two-Band Model," *Phys.Rev.B*, vol. 13, no. 8, pp. 3368–3380, 1976.

[101] W. R. Bandy and A. J. Glick, “Tight-Binding Green’s-Function Calculations of Electron Tunneling. II. Diagonal Disorder in the One-Dimensional Two-Band Model,” *Phys.Rev.B*, vol. 16, no. 6, pp. 2346–2349, 1977.

[102] M. Cini, “Time-Dependent Approach to Electron Transport through Junctions: General Theory and Simple Applications,” *Phys.Rev.B*, vol. 22, no. 12, pp. 5887–5899, 1980.

[103] H. Haug, ed., *Optical Nonlinearities and Instabilities in Semiconductors.* Boston: Academic Press, 1988.

[104] A. P. Jauho and J. W. Wilkins, “Theory of High-Electric-Field Quantum Transport for Electron-Resonant Impurity Systems,” *Phys.Rev.B*, vol. 29, no. 4, pp. 1919–1938, 1984.

[105] G. D. Mahan, “Quantum Transport Equation for Electric and Magnetic Fields,” *Physics Reports*, vol. 145, no. 5, pp. 251–318, 1987.

[106] R. Bertoncini and A.-P. Jauho, “Quantum Transport Theory for Electron-Phonon Systems in Strong Electric Fields,” *Phys.Rev.Lett.*, vol. 68, no. 18, pp. 2826–2829, 1992.

[107] E. V. Anda and F. Flores, “The Role of Inelastic Scattering in Resonant Tunnelling Heterostructures,” *J.Phys.:Condensed Matter*, vol. 3, no. 46, pp. 9087–9101, 1991.

[108] L. Y. Chen and C. S. Ting, “AC Conductance of a Double-Barrier Resonant Tunneling System Under a DC-Bias Voltage,” *Phys.Rev.Lett.*, vol. 64, no. 26, pp. 3159–3162, 1990.

[109] J. Zang and J. L. Birman, “Theory of Intrinsic Bistability in Double-Barrier Resonant-Tunneling Structures,” *Phys.Rev.B*, vol. 46, no. 8, pp. 5020–5023, 1992.

[110] R. K. Lake and S. Datta, “High-Bias Quantum Electron Transport,” *Superlattices & Microstructures*, vol. 11, no. 1, pp. 83–87, 1992.

[111] C. H. Grein, E. Runge, and H. Ehrenreich, “Phonon-Assisted Transport in Double-Barrier Resonant-Tunneling Tructures,” *Phys.Rev.B*, vol. 47, no. 19, pp. 12590–12597, 1993.

[112] R. Lake and S. Datta, “Nonequilibrium Green’s-Function Method Applied to Double-Barrier Resonant-Tunneling Diodes,” *Phys.Rev.B*, vol. 45, no. 12, pp. 6670–6685, 1992.

[113] A. L. Yeyati, F. Flores, and E. V. Anda, “Model Calculation of the Noise Characteristic in Double-Barrier Heterostructures,” *Phys.Rev.B*, vol. 47, no. 16, pp. 10543–10547, 1993.

[114] R. Lake, G. Klimeck, R. C. Bowen, C. Fernando, M. Leng, T. Moise, and Y. C. Kao, “Interface Roughness, Polar Optical Phonons, and the Valley Current of a Resonant Tunneling Diode,” *Superlattices & Microstructures*, vol. 20, no. 3, pp. 279–285, 1996.

[115] R. Lake, G. Klimeck, R. C. Bowen, C. L. Fernando, D. Jovanovic, D. Blanks, T. S. Moise, Y. C. Kao, M. Leng, and W. R. Frensley, “Experimentally Verified Quantum Device Simulations Based on Multiband Models, Hartree Self-Consistency, and Scattering Assisted Charging,” in *54th Annual Device Research Conference Digest*, (Santa Barbara), pp. 174–175, IEEE, 1996.

[116] R. Lake, G. Klimeck, R. C. Bowen, and D. Jovanovic, “Single and Multiband Modeling of Quantum Electron Transport Through Layered Semiconductor Devices,” *J.Appl.Phys.*, vol. 81, no. 12, pp. 7845–7869, 1997.

[117] G. Kim, H. Suh, and E. Lee, “Green’s-Function Study of the Electron Tunneling in a Double-Barrier Heterostructure,” *Phys.Rev.B*, vol. 52, no. 4, pp. 2632–2639, 1995.

[118] G. Klimeck, R. C. Bowen, T. Boykin, R. L. D. Blanks, T. S. Moise, Y. C. Kao, and W. R. Frensley, “Quantitative Simulation of Strained and Unstrained InP-Based Resonant Tunneling Diodes,” in *55th Annual Device Research Conference Digest*, (Fort Collins), pp. 92–93, IEEE, 1997.

[119] L. Y. Chen and C. S. Ting, “Theoretical Investigation of Noise Characteristics of Double-Barrier Resonant-Tunneling Systems,” *Phys.Rev.B*, vol. 43, no. 5, pp. 4534–4537, 1991.

[120] R. Lake and S. Datta, “Energy Balance and Heat Exchange in Mesoscopic Systems,” *Phys.Rev.B*, vol. 46, no. 8, pp. 4757–4763, 1992.

[121] G. Klimeck, R. Lake, R. C. Bowen, and W. R. Frensley, “Quantum Device Simulation with a Generalized Tunneling Formula,” *Appl.Phys.Lett.*, vol. 67, no. 17, pp. 2539–2541, 1995.

[122] R. C. Bowen, G. Klimeck, R. K. Lake, W. R. Frensley, and T. Moise, “Quantitative Simulation of a Resonant Tunneling Diode,” *J.Appl.Phys.*, vol. 81, no. 7, pp. 3207–3213, 1997.

[123] M. J. McLennan, Y. Lee, and S. Datta, “Voltage Drop in Mesoscopic Systems: A Numerical Study Using a Quantum Kinetic Equation,” *Phys.Rev.B*, vol. 43, no. 17, pp. 13846–13884, 1991.

[124] S.-C. Lee and A. Wacker, “Nonequilibrium Green’s Function Theory for Transport and Gain Properties of Quantum Cascade Structures,” *Phys.Rev.B*, vol. 66, no. 24, p. 245314, 2002.

[125] C. Rivas, R. Lake, G. Klimeck, W. R. Frensley, M. V. Fischetti, P. E. Thompson, S. L. Rommel, and P. R. Berger, “Full-Band Simulation of Indirect Phonon Assisted Tunneling in a Silicon Tunnel Diode with Delta-Doped Contacts,” *Appl.Phys.Lett.*, vol. 78, no. 8, pp. 814–916, 2001.

[126] C. Rivas, R. Lake, W. R. Frensley, G. Klimeck, P. E. Thompson, S. L. Rommel, and P. R. Berger, “Full Band Modeling of the Excess Current in a Delta-Doped Silicon Tunnel Diode,” *J.Appl.Phys.*, vol. 94, no. 8, pp. 5005–5013, 2003.

[127] D. Jovanovic and R. Venugopal, “Computational Techniques for the Nonequilibrium Quantum Field Theory Simulation of MOSFETs,” in *7th International Workshop on Computational Electronics. Book of Abstracts*, (Glasgow), pp. 30–31, IWCE, 2000.

[128] R. Lake, D. Jovanovic, and C. Rivas, “Nonequilibrium Green’s Functions in Semiconductor Device Modeling,” in *Progress in Nonequilibrium Green Functions*, (NewJersey), pp. 143–158, World Scientific, 2003.

[129] A. Svizhenko and M. P. Anantram, “Role of Scattering in Nanotransistors,” *IEEE Trans. Electron Devices*, vol. 50, no. 6, pp. 1459–1466, 2003.

[130] R. Venugopal, M. Paulsson, S. Goasguen, S. Datta, and M. S. Lundstrom, "A Simple Quantum Mechanical Treatment of Scattering in Nanoscale Transistors," *J.Appl.Phys.*, vol. 93, no. 9, pp. 5613–5625, 2003.

[131] Y.-J. Ko, M. Shin, S. Lee, and K. W. Park, "Effects of Atomistic Defects on Coherent Electron Transmission in Si Nanowires: Full Band Calculations," *J.Appl.Phys.*, vol. 89, no. 1, pp. 374–379, 2001.

[132] C. R. R. Lake, "Three-Dimensional, Full-Band, Quantum Modeling of Electron and Hole Transport through Si / SiGe Nano-Structures," in *Technical Proceedings of the 2003 Nanotechnology Conference and Trade Show*, vol. 2, (San Francisco), pp. 137–140, Computational Publications, 2003.

[133] C. Rivas and R. Lake, "Non-equilibrium Green Function Implementation of Boundary Conditions for Full Band Simulations of Substrate-Nanowire Structures," *Phys.stat.sol.(b)*, vol. 239, no. 1, pp. 94–102, 2003.

[134] M. B. Nardelli99, "Electronic Transport in Extended Systems: Application to Carbon Nanotubes," *Phys.Rev.B*, vol. 60, no. 11, pp. 7828–7833, 1999.

[135] J. Taylor, H. Guo, and J. Wang, "Ab Initio Modeling of Quantum Transport Properties of Molecular Electronic Devices," *Phys.Rev.B*, vol. 63, p. 245407, 2001.

[136] H. Mehrez, J. Taylor, H. Guo, J. Wang, and C. Roland, "Carbon Nanotube Based Magnetic Tunnel Junctions," *Phys.Rev.Lett.*, vol. 84, no. 12, pp. 2682–2685, 2000.

[137] D. Orlikowski, H. Mehrez, J. Taylor, H. Guo, J. Wang, and C. Roland, "Resonant Transmission Through Finite-Sized Carbon Nanotubes," *Phys.Rev.B*, vol. 63, p. 155412, 2001.

[138] J. Taylor, H. Guo, and J. Wang, "Ab Initio Modeling of Open Systems: Charge Transfer, Electron Conduction, and Molecular Switching of a C_{60} Device," *Phys.Rev.B*, vol. 63, p. 121104, 2001.

[139] M. P. Anantram, "Which Nanowire Couples Better Electrically to a Metal Contact: Armchair or Zigzag Nanotube?," *Appl.Phys.Lett.*, vol. 78, no. 14, pp. 2055–2057, 2001.

[140] A. Maiti, A. Svizhenko, and M. P. Anantram, "Electronic Transport through Carbon Nanotubes: Effects of Structural Deformation and Tube Chirality," *Phys.Rev.Lett.*, vol. 88, p. 126805, 2002.

[141] C.-C. Kaun, B. Larade, H. Mehrez, J. Taylor, and H. Guo, "Current-Voltage Characteristics of Carbon Nanotubes with Substitutional Nitrogen," *Phys.Rev.B*, vol. 65, p. 205416, 2002.

[142] G. Cuniberti, R. Gutiérrez, G. Fagas, F. Grossmann, K. Richter, and R. Schmidt, "Fullerene Based Devices for Molecular Electronics," *Physica E*, vol. 12, no. 1-4, pp. 749–752, 2002.

[143] J. J. Palacios, A. J. P. Jimenez, E. Louis, E. SanFabioa, and J. Verges, "First-Principles Phase-Coherent Transport in Metallic Nanotubes with Realistic Contacts," *Phys.Rev.Lett.*, vol. 90, p. 106801, 2003.

[144] Y. Xue and M. A. Ratner, “Schottky Barriers at Metal-Finite Semiconducting Carbon Nanotube Interfaces,” *Appl.Phys.Lett.*, vol. 83, no. 12, pp. 2429–2431, 2003.

[145] T.-S. Xia, L. F. Register, and S. K. Banerjee, “Quantum Transport in Carbon Nanotube Transistors: Complex Band Structure Effects,” *J.Appl.Phys.*, vol. 95, no. 3, pp. 1597–1599, 2004.

[146] M. Brandbyge, J.-L. Mozos, P. Ordejón, J. Taylor, and K. Stokbro, “Density-Functional Method for Nonequilibrium Electron Transport,” *Phys.Rev.B*, vol. 65, p. 165401, 2002.

[147] E. Louis, J. A. Vergés, J. J. Palacios, A. J.Pérez-Jiménez, and E. SanFabián, “Implementing the Keldysh Formalism into Ab Initio Methods for the Calculation of Quantum Transport: Application to Metallic Nanocontacts,” *Phys.Rev.B*, vol. 67, p. 155321, 2003.

[148] W. Tian, S. Datta, S. Hong, R. Reifenberger, J. I. Henderson, and C. P. Kubiak, “Conductance Spectra of Molecular Wires,” *J.Chem.Phys*, vol. 109, no. 7, pp. 2874–2882, 1998.

[149] P. A. Derosa and J. M. Seminario, “Electron Transport through Single Molecules: Scattering Treatment Using Density Functional and Green Function Theories,” *J.Phys.Chem.B*, vol. 105, no. 2, pp. 471–481, 2001.

[150] Y. Xue, S. Datta, and M. A. Ratner, “Charge Transfer and ”Band Lineup” in Molecular Electronic Devices: A Chemical and Numerical Interpretation,” *J.Chem.Phys*, vol. 115, no. 9, pp. 4292–4299, 2001.

[151] Y. Xue, *Molecular Electronic Devices: Electronic Structure and Transport Properties*. Dissertation, Purdue University, 2000.

[152] P. S. Damle, A. W. Ghosh, and S. Datta, “Unified Description of Molecular Conduction: From Molecules to Metallic Wires,” *Phys.Rev.B*, vol. 64, p. 201403, 2001.

[153] J. M. Seminario, A. G. Zacarias, and P. A. Derosa, “Theoretical Analysis of Complementary Molecular Memory Devices,” *J.Phys.Chem.A*, vol. 105, no. 5, pp. 791–795, 2001.

[154] J. M. Seminario and P. A. Derosa, “Molecular Gain in a Thiotolane System,” *J.Am.Chem.Soc.*, vol. 123, no. 49, pp. 12418–12419, 2001.

[155] J. Taylor, M. Brandbyge, and K. Stokbro, “Theory of Rectification in Tour Wires: The Role of Electrode Coupling,” *Phys.Rev.Lett.*, vol. 89, no. 13, p. 138301, 2002.

[156] J. Palacios, E. Louis, A. J. Pérez-Jiménez, E. S. Fabián, and J. Vergés, “An Ab Initio Approach to Electrical Transport in Molecular Devices,” *Nanotechnology*, vol. 13, no. 3, pp. 378–381, 2002.

[157] J. Heurich, J. C. Cuevas, W. Wenzel, and G. Schön, “Electrical Transport through Single-Molecule Junctions: From Molecular Orbitals to Conduction Channels,” *Phys.Rev.Lett.*, vol. 88, p. 256803, 2002.

[158] Y. Xue and M. A. Ratner, “Microscopic Study of Electrical Transport through Individual Molecules with Metallic Contacts. I. Band Lineup, Voltage Drop, and High-Field Transport,” *Phys.Rev.B*, vol. 68, p. 115406, 2003.

[159] J. M. Seminario, L. E. Cordova, and P. A. Derosa, “An Ab Initio Approach to the Calculation of Current-Voltage Characteristics of Programmable Molecular Devices,” *Proc.IEEE*, vol. 91, no. 11, pp. 1958–1975, 2003.

[160] M. Galperin, A. Nitzan, S. Sek, and M. Majda, “Asymmetric Electron Transmission across Asymmetric Alkanethiol Bilayer Junctions,” *J. Electroanalytical Chem.*, vol. 550-551, no. 1, pp. 337–350, 2003.

[161] P. A. Derosa, S. Guda, and J. M. Seminario, “A Programmable Molecular Diode Driven by Charge-Induced Conformational Changes,” *J.Am.Chem.Soc.*, vol. 125, no. 47, pp. 14240–14241, 2003.

[162] Y. Xue and M. A. Ratner, “End Group Effect on Electrical Transport through Individual Molecules: A Microscopic Study,” *Phys.Rev.B*, vol. 69, p. 085403, 2004.

[163] A. W. Ghosh, T. Rakshit, and S. Datta, “Gating of a Molecular Transistor: Electrostatic and Conformational,” *Nano Lett.*, vol. 4, no. 4, pp. 565–568, 2004.

[164] F. Evers, F. Weigend, and M. Koentopp, “Conductance of Molecular Wires and Transport Calculations based on Density-Functional Theory,” *Phys.Rev.B*, vol. 69, p. 235411, 2004.

[165] U. Gunsenheimer and A. D. Zaikin, “Ballistic Charge Transport in Superconducting Weak Links,” *Phys.Rev.B*, vol. 50, no. 9, pp. 6317–6331, 1994.

[166] W. I. Babiaczyk and B. R. Bulka, “Electronic Transport in Molecular Systems with Para- and Ferromagnetic Leads,” *J.Phys.:Condensed Matter*, vol. 16, no. 23, pp. 4001–4012, 2004.

[167] S. Krompiewski, “Modelling a Spin-Selective Interface between Ferromagnetic Electrodes and a Carbon Nanotube–Towards the Enhanced Giant Magnetoresistance Effect,” *J.Phys.:Condensed Matter*, vol. 16, pp. 2981–2990, 2004.

[168] M. A. Davidovich, E. V. Anda, C. Tejedor, and G. Platero, “Interband Resonant Tunneling and Transport in InAs/AlSb/GaSb Heterostructures,” *Phys.Rev.B*, vol. 47, no. 8, pp. 4475–4484, 1993.

[169] G. Klimeck, R. Lake, and D. K. Blanks, “Role of Interface Roughness Scattering in Self-Consistent Resonant-Tunneling-Diode Simulations,” *Phys.Rev.B*, vol. 58, no. 11, pp. 7279–7285, 1998.

[170] A. Groshev, T. Ivanov, and V. Valtchinov, “Charging Effects of a Single Quantum Level in a Box,” *Phys.Rev.Lett.*, vol. 66, no. 8, pp. 1082–1085, 1991.

[171] L. Y. Chen and C. S. Ting, “Coulomb Staircase in the I-V Characteristic of an Ultrasmall Double-Barrier Resonant-Tunneling Structure,” *Phys.Rev.B*, vol. 44, no. 11, pp. 5916–5918, 1991.

[172] S. Hershfield, J. Davies, and J. Wilkins, “Probing the Kondo Resonance by Resonant Tunneling through an Anderson Impurity,” *Phys.Rev.Lett.*, vol. 67, no. 26, pp. 3720–3723, 1991.

[173] S. Hershfield, J. Davies, and J. Wilkins, “Resonant Tunneling through an Anderson Impurity. I. Current in the Symmetric Model,” *Phys.Rev.B*, vol. 46, no. 11, pp. 7046–7060, 1992.

[174] Y. Meir, N. S. Wingreen, and P. A. Lee, “Low-Temperature Transport through a Quantum Dot: The Anderson Model out of Equilibrium,” *Phys.Rev.Lett.*, vol. 70, no. 17, pp. 2601–2604, 1993.

[175] N. S. Wingreen and Y. Meir, “Anderson Model out of Equilibrium: Noncrossing-Approximation Approach to Transport through a Quantum Dot,” *Phys.Rev.B*, vol. 49, no. 16, pp. 11040–11052, 1994.

[176] Y. Xue and M. A. Ratner, “Microscopic Theory of Single-Electron Tunneling through Molecular-Assembled Metallic Nanoparticles,” *Phys.Rev.B*, vol. 68, p. 235410, 2003.

[177] S. Hershfield, “Resonant Tunneling through an Anderson Impurity. II. Noise in the Hartree Approximation,” *Phys.Rev.B*, vol. 46, no. 11, pp. 7061–7076, 1992.

[178] S. Datta and M. P. Anantram, “Steady-State Transport in Mesoscopic Systems Illuminated by Alternating Fields,” *Phys.Rev.B*, vol. 45, no. 23, pp. 13761–13764, 1991.

[179] M. P. Anantram and S. Datta, “Effect of Phase Breaking on the AC Response of Mesoscopic Systems,” *Phys.Rev.B*, vol. 51, no. 12, pp. 7632–7639, 1995.

[180] N. S. Wingreen, A. Jauho, and Y. Meir, “Time-Dependent Transport through a Mesoscopic Structure,” *Phys.Rev.B*, vol. 48, no. 11, pp. 8487–8490, 1993.

[181] A. Jauho, N. S. Wingreen, and Y. Meir, “Time-dependent transport in interacting and noninteracting resonant-tunneling systems,” *Phys.Rev.B*, vol. 50, no. 8, pp. 5528–5544, 1994.

[182] C. A. Stafford and N. S. Wingreen, “Resonant Photon-Assisted Tunneling through a Double Quantum Dot: An Electron Pump from Spatial Rabi Oscillations,” *Phys.Rev.Lett.*, vol. 76, no. 11, pp. 1916–1919, 1996.

[183] P. Kral, “Linearized Quantum Transport Equations: AC Conductance of a Quantum Wire with an Electron-Phonon Interaction,” *Phys.Rev.B*, vol. 53, no. 16, pp. 11034–11050, 1996.

[184] P. Kral and A.-P. Jauho, “Resonant Tunneling in a Pulsed Phonon Field,” *Phys.Rev.B*, vol. 59, no. 11, pp. 7656–7662, 1999.

[185] H. Haug and A.-P. Jauho, *Quantum Kinetics in Transport and Optics of Semiconductors*, vol. 123 of *Springer Series in Solid-State Sciences*. Berlin, New York: Springer, 1996.

[186] S. Datta, “Nanoscale Device Modeling: the Green’s Function Method,” *Superlattices & Microstructures*, vol. 28, no. 4, pp. 253–278, 200.

[187] R. K. Lake and R. R. Pandey, *Handbook of Semiconductor Nanostructures and Devices*, vol. 3, ch. Non-Equilibrium Green Functions in Electronic Device Modeling, pp. 409–443. Los Angles: American Scientific Publishers, 2006.

[188] W. Fichtner, “Quantum Transport for Nanostructures,” tech. rep., Integrated Systems Laboratorym, ETH Zürich, 2006.

[189] A. L. Fetter and J. D. Walecka, *Quantum Theory of Many-Particle Systems.* San Francisco: McGraw-Hill, 1971.

[190] G. D. Mahan, *Many-Particle Physics.* Physics of Solids and Liquids, New York: Plenum Press, 2nd ed., 1990.

[191] R. P. Feynman, “Space-Time Approach to Quantum Electrodynamics,” *Phys.Rev.*, vol. 76, no. 6, pp. 769–789, 1949.

[192] M. Gell-Mann and F. Low, “Bound States in Quantum Field Theory,” *Phys.Rev.*, vol. 84, no. 2, pp. 350–354, 1951.

[193] T. Matsubara, “A New Approach to Quantum-Statistical Mechanics,” *Prog.Theor.Phys.*, vol. 14, no. 4, pp. 351–378, 1955.

[194] V. Korenman, “Nonequilibrium Quantum Statistics: Application to the Laser,” *Ann. Phys.*, vol. 39, no. 1, pp. 72–126, 1966.

[195] A. Schmid, “On a Quasiclassical Langevin Equation,” *J.Low.Temp.Phys.*, vol. 49, no. 5-6, pp. 609–626, 1982.

[196] J. Rammer and H. Smith, “Quantum Field-Theoretical Methods in Transport Theory of Metals,” *Rev.Mod.Phys.*, vol. 58, no. 2, pp. 323–359, 1986.

[197] R. Mills, *Propagators for Many-Particle Systems: An Elementary Treatment.* New York: Gordon and Breach, 1969.

[198] S. Fujita, “Thermodynamic Evolution Equation for a Quantum Statistical Gas,” *J.Math.Phys.*, vol. 6, no. 12, pp. 1877–1885, 1965.

[199] S. Fujita, “Resolution of the Hierarchy of Green’s Functions for Fermions,” *Phys.Rev.A*, vol. 4, no. 3, pp. 1114–1122, 1971.

[200] A. G. Hall, “Non-Equilibrium Green’s Functions: Generalized Wick’s Theorem and Diagrammatic Perturbation Theory with Initial Correlations,” *J.Phys.A:Math.Gen.*, vol. 8, no. 2, pp. 214–224, 1975.

[201] Y. A. Kukharenkov and S. G. Tikhodeev, “A Diagram Technique in the Theory of Relaxation Processes,” *Soviet Phys.JETP*, vol. 56, no. 4, pp. 831–838, 1982.

[202] L. V. Keldysh, “Diagram Technique for Nonequilibrium Processes,” *Soviet Phys.JETP*, vol. 20, no. 4, pp. 1018–1026, 1965.

[203] P. Danielewicz, “Quantum Theory of Nonequilibrium Processes, I,” *Ann. Phys.*, vol. 152, no. 2, pp. 239–304, 1984.

[204] J. Goldstone, “Derivation of the Brueckner Many-Body Theory,” *Proc.Phys.Soc.A*, vol. 239, no. 12173, pp. 267–279, 1957.

[205] W. Schäfer and M. Wegener, *Semiconductor Optics and Transport Phenomena.* Berlin, New York: Springer, 2002.

[206] D. C. Langreth, *Linear and Non-linear Electron Transport in Solids*, vol. 17 of *NATO Advanced Study Institute Series: Series B*, pp. 3–18. New York: Plenum Press, 1976.

[207] A. Gehring and S. Selberherr, "Evolution of Current Transport Models for Engineering Applications," *J.Comp.Electronics*, vol. 3, no. 3-4, pp. 149–155, 2004.

[208] S. Datta, "A Simple Kinetic Equation for Steady-State Quantum Transport," *J.Phys.:Condensed Matter*, vol. 2, no. 40, pp. 8023–8052, 1990.

[209] M. Büttiker, Y. Imry, R. Landauer, and S. Pinhas, "Generalized Many-Channel Conductance Formula with Application to Small Rings," *Phys.Rev.B*, vol. 31, no. 10, pp. 6207–6215, 1985.

[210] M. Büttiker, "Four-Terminal Phase-Coherent Conductance," *Phys.Rev.Lett.*, vol. 57, no. 14, pp. 1761–1764, 1986.

[211] G. Lindblad, "On the Generators of Quantum Dynamical Semigroups," *Communications in Mathematical Physics*, vol. 48, no. 2, pp. 119–130, 1976.

[212] H. J. Kreuzer, *Nonequilibrium Thermodynamics and Its Statistical Foundations*. New York: Oxford University Press, 1981.

[213] M. V. Fischetti, "Theory of Electron Transport in Small Semiconductor Devices Using the Pauli Master Equation," *J.Appl.Phys.*, vol. 83, no. 1, pp. 270–291, 1998.

[214] M. V. Fischetti, "Master-Equation Approach to the Study of Electronic Transport in Small Semiconductor Devices," *Phys.Rev.B*, vol. 59, no. 7, pp. 4901–4917, 1998.

[215] W. R. Frensley, "Boundary Conditions for Open Quantum Systems Driven Far From Equilibrium," *Rev.Mod.Phys.*, vol. 62, no. 3, pp. 745–791, 1990.

[216] R. Gebauer and R. Car, "Kinetic Theory of Quantum Transport at the Nanoscale," *Phys.Rev.B*, vol. 70, p. 125324, 2004.

[217] R. Gebauer and R. Car, "Current in Open Quantum Systems," *Phys.Rev.Lett.*, vol. 93, p. 160404, 2004.

[218] E. Wigner, "On the Quantum Correction For Thermodynamic Equilibrium ," *Phys.Rev.*, vol. 40, no. 5, pp. 749–759, 1932.

[219] H. Kosina and M. Nedjalkov, *Handbook of Theoretical and Computational Nanotechnology*, vol. 10, ch. Wigner Function Based Device Modeling, pp. 731–763. Los Angeles: American Scientific Publishers, 2006.

[220] R. K. Mains and G. I. Haddad, "Wigner Function Modeling of Resonant Tunneling Diodes With High Peak-to-Valley Ratios," *J.Appl.Phys.*, vol. 64, no. 10, pp. 5041–5044, 1988.

[221] K. L. Jensen and F. A. Buot, "The Effects of Scattering on Current-Voltage Characteristics, Transient Response, and Particle Trajectories in the Numerical Simulation of Resonant Tunneling Diodes," *J.Appl.Phys.*, vol. 67, no. 12, pp. 7602–7607, 1990.

[222] K. Hess, ed., *Monte Carlo Device Simulation: Full Band and Beyond*. Kluwer International Series in Engineering and Computer Science, Boston: Kluwer Academic, 1991.

[223] R. Stratton, “Diffusion of Hot and Cold Electrons in Semiconductor Barriers,” *Phys.Rev.*, vol. 126, no. 6, pp. 2002–2014, 1962.

[224] K. Blotekjaer, “Transport Equations for Electrons in Two-Valley Semiconductors,” *IEEE Trans. Electron Devices*, vol. 17, no. 1, pp. 38–47, 1970.

[225] M. Lundstrom, *Fundamentals of Carrier Transport.* Cambridge, New York: Cambridge University Press, 2nd ed., 2000.

[226] S. Selberherr, *Analysis and Simulation of Semiconductor Devices.* Vienna, New York: Springer-Verlag, 1984.

[227] T. Grasser, T.-W. Tang, H. Kosina, and S. Selberherr, “A Review of Hydrodynamic and Energy-Transport Models for Semiconductor Device Simulation,” *Proc.IEEE*, vol. 91, no. 2, pp. 251–274, 2003.

[228] T. Grasser, H. Kosina, M. Gritsch, and S. Selberherr, “Using Six Moments of Boltzmann’s Transport Equation for Device Simulation,” *J.Appl.Phys.*, vol. 90, no. 5, pp. 2389–2396, 2001.

[229] W. Liang, N. Goldsman, I. Mayergoyz, and P. J. Oldiges, “2-D MOSFET Modeling Including Surface Effects and Impact Ionization by Self-Consistent Solution of the Boltzmann, Poisson, and Hole-Continuity Equations,” *IEEE Trans. Electron Devices*, vol. 44, no. 2, pp. 257–267, 1997.

[230] N. Goldsman, C.-K. Lin, Z. Han, and C.-K. Huang, “Advances in the Spherical Harmonic-Boltzmann-Wigner Approach to Device Simulation,” *Superlattices & Microstructures*, vol. 27, no. 2/3, pp. 159–175, 2000.

[231] M. Karner, A. Gehring, S. Holzer, M. Pourfath, M. Wagner, W. Goes, M. Vasicek, O. Baumgartner, C. Kernstock, K. Schnass, G. Zeiler, T. Grasser, H. Kosina, and S. Selberherr, “VSP-A Multi-Purpose Schrödinger-Poisson Solver for TCAD Applications,” *J.Comp.Electronics*, vol. 6, no. 1-3, pp. 179–182, 2007.

[232] M. Krüger, M. R. Buitelaar, T. Nussbaumer, , C. Schönenbergera, and L. Forró, “Electrochemical Carbon Nanotube Field-Effect Transistor,” *Appl.Phys.Lett.*, vol. 78, no. 9, pp. 1291–1293, 2001.

[233] S. Rosenblatt, Y. Yaish, J. Park, J. Gore, V. Sazonova, and P. L. McEuen, “High Performance Electrolyte Gated Carbon Nanotube Transistors,” *Nano Lett.*, vol. 2, no. 8, pp. 869–872, 2002.

[234] W. B. Choi, J. U. Chu, K. S. Jeong, E. J. Bae, J. W. Lee, J. J. Kim, and J. O. Lee, “Ultrahigh-Density Nanotransistors by Using Selective-Grown Vertical Carbon Nanotubes,” *Appl.Phys.Lett.*, vol. 79, no. 22, pp. 3696–3698, 2001.

[235] A. V. Melechko, V. I. Merkulov, T. E. McKnight, M. A. Guillorn, K. L. Klein, D. H. Lowndes, and M. L. Simpson, “Vertically Aligned Carbon Nanofibers and Related Structures: Controlled Synthesis and Directed Assembly,” *J.Appl.Phys.*, vol. 97, p. 041301, 2005.

[236] F. Zahid, A. Ghosh, M. Paulsson, E. Polizzi, and S. Datta, “Charging-Induced Asymmetry in Molecular Conductors,” *Phys.Rev.B*, vol. 70, p. 245317, 2004.

[237] D. John, L. Castro, P. Pereira, and D. Pulfrey, "A Schrödinger-Poisson Solver for Modeling Carbon Nanotube FETs," in *Proc. NSTI Nanotech*, vol. 3, pp. 65–68, 2004.

[238] A. Okabe, B. Boots, and K. Sugihara, *Spatial Tessellations: Concepts and Applications of Voronoi Diagrams.* Chichester, New York: Wiley, 1992.

[239] J. Cervenka, *Three-Dimensional Mesh Generation for Device and Process Simulation.* Dissertation, Technische Universität Wien, 2004.

[240] S. Wagner, *Small-Signal Device and Circuit Simulation.* Dissertation, Technische Universität Wien, 2005.

[241] F. Leonard and J. Tersoff, "Dielectric Response of Semiconducting Carbon Nanotubes," *Appl.Phys.Lett.*, vol. 81, no. 25, pp. 4835–4837, 2002.

[242] D. Z. Y. Ting and Y.-C. Change, "Γ-X Mixing in GaAs/Al_xGa_{1-x}As and Al_xGa_{1-x}As/AlAs Superlattices," *Phys.Rev.B*, vol. 36, no. 8, pp. 4359–4374, 1987.

[243] J. Guo, S. Datta, M. Lundstrom, and M. Anantram, "Multi-Scale Modeling of Carbon Nanotube Transistors," *The International Journal of Multiscale Computational Engineering*, vol. 2, no. 2, pp. 257–278, 2004.

[244] N. Nemec, D. Tománek, and G. Cuniberti, "Contact Dependence of Carrier Injection in Carbon Nanotubes: An *Ab Initio* Study," *Phys.Rev.Lett.*, vol. 96, p. 076802, 2006.

[245] D. Kienle and A. W. Ghosh, "Atomistic Modeling of Metal-Nanotube Contacts," *J.Comp.Electronics*, vol. 4, no. 1-2, pp. 97–100, 2005.

[246] A. B. Migdal, "Interaction Between Electrons and Lattice Vibrations in a Normal Metal," *Soviet Phys.JETP*, vol. 7, no. 6, pp. 996–1001, 1958.

[247] P. Davis and P. Rabinowitz, *Methods of Numerical Integration.* Orlando: Academic Press, 2nd ed., 1984.

[248] J. Lyness, "Notes on the Adaptive Simpson Quadrature Routine," *J.ACM*, vol. 16, no. 3, pp. 483–495, 1969.

[249] T. Espelid, "Adaptive Doubly Quadrature Routines based on Newton-Cotes Rules," *BIT*, vol. 43, no. 2, pp. 319–337, 2003.

[250] T. Espelid, "DQAINT: An Algorithm for Adaptive Quadrature over a Collection of Finite Intervals," *Numerical Integration, Recent Developments, Software and Applications, NATO Advanced Study Institute Series C: Mathematical and Physical Sciences*, vol. 357, p. 367, 1992.

[251] M. Malcolm and R. Simpson, "Local Versus Global Strategies for Adaptive Quadratures," *ACM Trans.Math. Software*, vol. 1, no. 2, pp. 129–146, 1975.

[252] C. Fernando and W. Frensley, "An Efficient Method for the Numerical Evaluation of Resonant States," *J.Appl.Phys.*, vol. 76, no. 5, pp. 2881–2886, 1994.

[253] O. Pinaud, "Transient Simulations of a Resonant Tunneling Diode," *J.Appl.Phys.*, vol. 92, no. 4, pp. 1987–1994, 2002.

[254] S. Laux, A. Kumar, and M. Fischetti, "Analysis of Quantum Ballistic Electron Transport in Ultrasmall Silicon Devices Including Space-Charge and Geometric Effects," *J.Appl.Phys.*, vol. 95, no. 10, pp. 5545–5582, 2004.

[255] F. Stern, "Iteration Methods for Calculating Self-Consistent Fields in Semiconductor Inversion Layers," *J.Comput.Phys.*, vol. 6, no. 1, pp. 56–67, 1970.

[256] T. Kerkhoven, A. Galick, U. Ravaioli, J. Arends, and Y. Saad, "Efficient Numerical Simulation of Electron States in Quantum Wires," *J.Appl.Phys.*, vol. 68, no. 7, pp. 3461–3469, 1990.

[257] A. Trellakis, A. T. Galick, A. Pacelli, and U. Ravaioli, "Iteration Scheme for the Solution of the Two-Dimensional Schrödinger-Poisson Equations in Quantum Structures," *J.Appl.Phys.*, vol. 81, no. 12, pp. 7880–7884, 1997.

[258] F. Venturi, R. Smith, E. Sangiorgi, M. Pinto, and B. Ricco, "A General Purpose Device Simulator Coupling Poisson and Monte Carlo Transport with Applications to Deep Submicron MOSFETs," *IEEE Trans.Computer-Aided Design*, vol. 8, no. 4, pp. 360–369, 1989.

[259] A. Pacelli, "Self-Consistent Solution of the Schrödinger Equation in Semiconductor Devices by Implicit Iteration," *IEEE Trans. Electron Devices*, vol. 44, no. 7, pp. 1169–1171, 1997.

[260] S. Heinze, M. Radosavljevic, J. Tersoff, and P. Avouris, "Unexpected Scaling of the Performance of Carbon Nanotube Schottky-Barrier Transistors," *Phys.Rev.B*, vol. 68, p. 235418, 2003.

[261] S. Heinze, J. Tersoff, and P. Avouris, "Electrostatic Engineering of Nanotube Transistors for Improved Performance," *Appl.Phys.Lett.*, vol. 83, no. 24, pp. 5038–5040, 2003.

[262] M. Radosavljevic, S. Heinze, J. Tersoff, and P. Avouris, "Drain Voltage Scaling in Carbon Nanotube Transistors," *Appl.Phys.Lett.*, vol. 83, no. 12, pp. 2435–2437, 2003.

[263] J. Guo, A. Javey, H. Dai, and M. Lundstrom, "Performance Analysis and Design Optimization of Near Ballistic Carbon Nanotube Field-Effect Transistors," in *IEDM Tech.Dig.*, (San Francisco), pp. 703–706, IEEE, 2004.

[264] D. John, L. Castro, and D. Pulfrey, "Quantum Capacitance in Nanoscale Device Modeling," *J.Appl.Phys.*, vol. 96, no. 9, pp. 5180–5184, 2004.

[265] P. J. Burke, "An RF Circuit Model for Carbon Nanotubes," *IEEE Trans.Nanotechnology*, vol. 2, no. 1, pp. 55–58, 2003.

[266] P. Burke, "AC Performance of Nanoelectronics: Towards a Ballistic THz Nanotube Transistors," *Solid-State Electronics*, vol. 48, no. 10-11, pp. 1981–1986, 2004.

[267] J. Guo, S. Datta, and M. Lundstrom, "Assesment of Silicon MOS and Carbon Nanotube FET Performance Limits using a General Theory of Ballistic Transistors," in *IEDM Tech.Dig.*, (San Francisco), pp. 711–714, IEEE, 2002.

[268] A. Keshavarzi, A. Raychowdhury, J. Kurtin, K. Roy, and V. De, "Carbon Nanotube Field-Effect Transistors for High-Performance Digital Circuits-Transient Analysis, Parasitics, and Scalability," *IEEE Trans. Electron Devices*, vol. 53, no. 11, pp. 2718–2726, 2006.

[269] A. Raychowdhury, A. Keshavarzi, J. Kurtin, V. De, and K. Roy, “Carbon Nanotube Field-Effect Transistors for High-Performance Digital Circuits-DC Analysis and Modeling Toward Optimum Transistor Structure,” *IEEE Trans. Electron Devices*, vol. 53, no. 11, pp. 2711–2717, 2006.

[270] Y.-M. Lin, J. Appenzeller, J. Knoch, and P. Avouris, “High-Performance Carbon Nanotube Field-Effect Transistor with Tunable Polarities,” *IEEE Trans.Nanotechnology*, vol. 4, no. 5, pp. 481–489, 2005.

[271] J. Chen, C. Klinke, A. Afzali, K. Chan, , and P. Avouris, “Self-Aligned Carbon Nanotube Transistors with Novel Chemical Doping,” in *IEDM Tech.Dig.*, (San Francisco), pp. 695–698, IEEE, 2004.

[272] A. Javey, R. Tu, D. Farmer, J. Guo, R. Gordon, and H. Dai, “High Performance n-Type Carbon Nanotube Field-Effect Transistors with Chemically Doped Contacts,” *Nano Lett.*, vol. 5, no. 2, pp. 345–348, 2005.

[273] J. Appenzeller, Y.-M. Lin, J. Knoch, Z. Chen, and P. Avouris, “Comparing Carbon Nanotube Transistors - The Ideal Choice: A Novel Tunneling Device Design,” *IEEE Trans. Electron Devices*, vol. 52, no. 12, pp. 2568–2576, 2005.

[274] J. Knoch, S. Mantl, and J. Appenzeller, “Comparison of Transport Properties in Carbon Nanotube Field-Effect Transistors with Schottky Contacts and Doped Source/Drain Contacts,” *Solid-State Electronics*, vol. 49, no. 1, pp. 73–76, 2005.

[275] J. Appenzeller, Y.-M. Lin, J. Knoch, and P. Avouris, “Band-to-Band Tunneling in Carbon Nanotube Field-Effect Transistors,” *Phys.Rev.Lett.*, vol. 93, p. 196805, 2004.

[276] S. O. Koswatta, S. Hasan, M. Lundstrom, M. P. Anantram, and D. E. Nikonov, “Ballisticity of Nanotube FETs: Role of Phonon Energy and Gate Bias,” *Appl.Phys.Lett.*, vol. 89, p. 023125, 2006.

[277] M. Lundstrom, “Elementary Scattering Theory of the Si MOSFET,” *IEEE Electron Device Lett.*, vol. 18, no. 7, pp. 361–363, 1997.

[278] A. Javey, J. Guo, D. Farmer, Q. Wang, E. Yenilmez, R. Gordon, M. Lundstrom, and H. Dai, “Self-Aligned Ballistic Molecular Transistors and Electrically Parallel Nanotube Arrays,” *Nano Lett.*, vol. 4, no. 7, pp. 1319–1322, 2004.

[279] J. Park, S. Rosenblatt, Y. Yaish, V. Sazonova, H. Ustunel, S. Braig, T. Arias, P. Brouwer, and P. McEuen, “Electron-Phonon Scattering in Metallic Single-Walled Carbon Nanotubes,” *Nano Lett.*, vol. 4, no. 3, pp. 517–520, 2004.

[280] D. Singh, K. Jenkins, J. Appenzeller, D. Neumayer, A. Grill, and H.-S. P. Wong, “Frequency Response of Top-Gated Carbon Nanotube Field-Effect Transistors,” *IEEE Trans.Nanotechnology*, vol. 3, no. 3, pp. 383–387, 2004.

[281] Y. Yoon, Y. Ouyang, and J. Guo, “Effect of Phonon Scattering on Intrinsic Delay and Cutoff Frequency of Carbon Nanotube FETs,” *IEEE Trans. Electron Devices*, vol. 53, no. 10, pp. 2467–2470, 2006.

[282] R. Binder and S. W. Koch, “Nonequilibrium Semiconductor Dynamics,” *Prog.Quant.Electr.*, vol. 19, no. 4/5, pp. 307–462, 1995.

[283] N. Ashcroft and N. Mermin, *Solid State Physics*. New York: Holt, Rinehart and Winston, 1976.

[284] A. Wacker, “Semiconductor Superlattices: A Model System for Nonlinear Transport,” *Physics Reports*, vol. 357, no. 1, pp. 1–111, 2002.

[285] M. P. Anantram, M. S. Lundstrom, and D. E. Nikonov, “Modeling of Nanoscale Devices,” *cond-mat/0610247*, 2006.

Own Publications

Publications in Journals

[J01] M. Pourfath, A. Gehring, E. Ungersboeck, H. Kosina, S. Selberherr, B.-H. Cheong, and W. Park, "Separated carrier injection control in carbon nanotube field-effect transistors," *Journal of Applied Physics*, vol. 97, no. 10, pp. 1061031–1061033, 2005.

[J02] M. Pourfath, E. Ungersboeck, A. Gehring, B.-H. Cheong, W. Park, H. Kosina, and S. Selberherr, "Optimization of Schottky Barrier Carbon Nanotube Field Effect Transistors," *Journal of Microelectronic Engineering*, vol. 81, no. 2-4, pp. 428–433, 2005.

[J03] M. Pourfath, E. Ungersboeck, A. Gehring, W. Park, B.-H. Cheong, H. Kosina, and S. Selberherr, "Numerical Analysis of Coaxial Double Gate Schottky Barrier Carbon Nanotube Field Effect Transistors," *Journal of Computational Electronics*, vol. 4, no. 1-2, pp. 75–78, 2005. in press.

[J04] E. Ungersboeck, M. Pourfath, A. Gehring, H. Kosina, B.-H. Cheong, W. Park, and S. Selberherr, "Optimization of Single Gate Carbon Nanotube Field Effect Transistors," *IEEE Transaction on Nanotechnology*, vol. 4, no. 5, pp. 533–538, 2005.

[J05] L. Castro, D. John, D. Pulfrey, M. Pourfath, A. Gehring, and H. Kosina, "Method for Predicting f_T for Carbon Nanotube FETs," *IEEE Transaction on Nanotechnology*, vol. 4, no. 6, pp. 699–704, 2005.

[J06] M. Pourfath, H. Kosina, and S. Selberherr, "Rigorous Modeling of Carbon Nanotube Transistors," *IOP Journal of Physics: Conference Series*, vol. 38, pp. 29–32, 2006.

[J07] M. Pourfath and H. Kosina, "Fast Convergent Schrödinger-Poisson Solver for the Static and Dynamic Analysis of Carbon Nanotube Field Effect Transistors," *Journal of Computational Electronics*, vol. 5, no. 2-3, pp. 155–159, 2006.

[J08] M. Karner, A. Gehring, S. Holzer, M. Pourfath, M. Wagner, H. Kosina, T. Grasser, and S. Selberherr, "VSP-A Multi-Purpose Schrödinger-Poisson Solver for TCAD Applications," *Journal of Computational Electronics*, vol. 6, no. 1-3, pp. 179–182, 2007.

[J09] M. Pourfath, H. Kosina, and S. Selberherr, "Tunneling CNTFETs," *Journal of Computational Electronics*, vol. 6, no. 1-3, pp. 243–246, 2006.

[J10] M. Pourfath, H. Kosina, and S. Selberherr, "Dissipative Transport in CNTFETs," *Journal of Computational Electronics*, vol. 6, no. 1-3, pp. 321–324, 2007.

[J11] M. Pourfath, H. Kosiba, and S. Selberherr, "Numerical Study of Quantum Transport in Carbon Nanotube Transistors," *Mathematics and Computers in Simulation*, in press.

Publications in Conference Proceedings

[C01] E. Ungersboeck, M. Pourfath, A. Gehring, H. Kosina, B.-H. Cheong, and S. Selberherr, "Optimization of Carbon Nanotube Field Effect Transistors," in *Proceedings of the Symposium on Nano Device Technology*, (Hsinchu), pp. 117–120, 2004. Talk: Symposium on Nano Device Technology (SNDT).

[C02] M. Pourfath, E. Ungersboeck, A. Gehring, B.-H. Cheong, H. Kosina, and S. Selberherr, "Three-Dimensional Analysis of Schottky Barrier Carbon Nanotube Field Effect Transistors," in *Simulation of Semiconductor Processes and Devices 2004*, (Munich), pp. 149–152, Springer, 2004. Talk: International Conference on the Simulation of Semiconductor Processes and Devices (SISPAD).

[C03] M. Pourfath, E. Ungersboeck, A. Gehring, B.-H. Cheong, W. Park, H. Kosina, and S. Selberherr, "Optimization of Schottky Barrier Carbon Nanotube Field Effect Transistors," in *Nano and Giga Challenges in Microelectronics Book of Abstracts*, (Krakau), p. 201, 2004. Talk: Nano and Giga Challenges in Microelectronics (NGCM).

[C04] M. Pourfath, E. Ungersboeck, A. Gehring, B.-H. Cheong, W. Park, H. Kosina, and S. Selberherr, "Improving the Ambipolar Behavior of Schottky Barrier Carbon Nanotube Field Effect Transistors," in *Proceeding of the 34th European Solid-State Device Research Conference*, (Leuven), pp. 429–432, IEEE, 2004. Talk: European Solid-State Device Research Conference (ESSDERC).

[C05] M. Pourfath, E. Ungersboeck, A. Gehring, W. Park, B.-H. Cheong, H. Kosina, and S. Selberherr, "Numerical Analysis of Coaxial Double Gate Schottky Barrier Carbon Nanotube Field Effect Transistors," in 10^{th} *International Workshop on Computational Electronics Book Abstracts*, (West Lafayette), pp. 237–238, 2004. Poster: International Workshop on Computational Electronics (IWCE).

[C06] M. Pourfath, B.-H. Cheong, W. Park, H. Kosina, and S. Selberherr, "High Performance Carbon Nanotube Field Effect Transistor with the Potential for Tera Level Integration," in *ULIS 2005 6th International Conference on Ultimate Integration of Silicon Proceedings of the Conference*, (Bologna), pp. 95–98, 2005. Talk: International Conference on Ultimate Integration of Silicon (ULIS).

[C07] M. Pourfath, A. Gehring, B. Cheong, W. Park, H. Kosina, and S. Selberherr, "Vertically Grown Coaxial Double Gate Carbon Nanotube Field Effect Transistors for Tera Level Integration," in *NSTI Nanotech Technical Proceedings*, vol. 3, (Anaheim), pp. 128–131, 2005. Talk: The Nanotechnology Conference and Trade Show.

[C08] M. Pourfath, B. Cheong, H. Kosina, and S. Selberherr, "Fast Convergent Schrödinger-Poisson Solver for the Static and Dynamic Analysis of Carbon Nanotube Field Effect Transistors," in *5th International Conference on Large-Scale Scientific Computations*, no. 50-51, (Sozopol), 2005. Talk: International Conference on Large-Scale Scientific Computations (LSSC).

[C09] M. Pourfath, H. Kosina, B.-H. Cheong, W. Park, and S. Selberherr, "The Effect of Device Geometry on the Static and Dynamic Response of Carbon Nanotube Field Effect Transistors," in *Proceedings of the 2005 5th IEEE Conference on Nanotechnology*, (Nagoya), 2005. Talk: 5th IEEE Conference on Nanotechnology (IEEE-Nano).

[C10] M. Pourfath, B.-H. Cheong, W. Park, and H. Kosina, "Geometry-dependence of the DC and AC Response of Ohmic Contact Carbon Nanotube Field Effect Transistors," in *Simulation of Semiconductor Processes and Devices 2005*, (Tokyo), pp. 91–94, 2005. Talk: International Conference on the Simulation of Semiconductor Processes and Devices (SISPAD).

[C11] M. Pourfath, H. Kosina, B. Cheong, W. Park, and S. Selberherr, "Improving DC and AC Characteristics of Ohmic Contact Carbon Nanotube Field Effect Transistors," in *Proceeding of the 35th European Solid-State Device Research Conference*, (Grenoble), pp. 541–544, 2005. Talk: European Solid-State Device Research Conference (ESSDERC).

[C12] M. Pourfath, H. Kosina, and S. Selberherr, "On the Effect of Scattering on the Performance of Carbon Nanotube Field-Effect Transistors," in *Proceedings of the 14th Iranian Conference on Electrical Engineering ICEE 2006*, 2006. Oral: Iranian Conference on Electrical Engineering (ICEE).

[C13] M. Pourfath, H. Kosina, and S. Selberherr, "Tunneling CNTFETs," in *11th International Workshop on Computational Electronics Book of Abstracts*, (Vienna), pp. 291–292, 2006. Poster: International Workshop on Computational Electronics (IWCE).

[C14] M. Pourfath, H. Kosina, and S. Selberherr, "Dissipative Transport in CNTFETs," in *11th International Workshop on Computational Electronics Abstracts*, (Vienna), pp. 345–346, 2006. Oral: International Workshop on Computational Electronics (IWCE).

[C15] M. Karner, A. Gehring, S. Holzer, M. Pourfath, M. Wagner, H. Kosina, T. Grasser, and S. Selberherr, "VSP-A Multi-Purpose Schrödinger-Poisson Solver for TCAD Applications," in *11th International Workshop on Computational Electronics Abstracts*, (Vienna), pp. 255–256, 2006. Poster: International Workshop on Computational Electronics (IWCE).

[C16] M. Pourfath, H. Kosina, , and S. Selberherr, "Optimizing the Performance of Carbon Nanotube Transistors," in *Sixth IEEE Conference on Nanotechnology*, vol. 2, (Cincinnati), pp. 520–523, 2006. Poster: IEEE Conference on Nanotechnology (IEEE-NANO).

[C17] M. Pourfath and H. Kosina, "On the Effect of Electron-Phonon Interaction Parameters on the Performance of Carbon Nanotube Based Transistors," in *Proceedings Trends in Nanotechnology*, (Grenoble), p. 2 pages, 2006. Poster: Trends in Nanotechnology Conference (TNT).

[C18] M. Pourfath, H. Kosina, B.-H. Cheong, and J. Park, "The Effect of Electron-Phonon Interaction on the Static and Dynamic Response of CNTFETs," in *International Conference on Simulation of Semiconductor Processes and Devices 2006*, (Monterey), pp. 208–211, 2006. Poster: International Conference on the Simulation of Semiconductor Processes and Devices (SISPAD).

[C19] M. Pourfath, H. Kosina, and S. Selberherr, "Optimal Design for Carbon Nanotube Transistors," in *Proceedings of the 36th European Solid-State Device Research Conference*, (Montreux), pp. 210–213, 2006. Talk: European Solid-State Device Research Conference (ESSDERC).

[C20] M. Pourfath, H. Kosina, and S. Selberherr, "A Comprehensive Study of Carbon Nanotube Based Transistors: The Effects of Geometrical, Interface Barrier, and Scattering Parameters," in *International Electron Devices Meeting 2006 Technical Digest*, (San Francisco), pp. 31.5.1–31.5.4, 2006. Talk: International Electron Devices Meeting (IEDM).

[C21] M. Pourfath, H. Kosina, and S. Selberherr, "Carbon Nanotube Based Transistors: A Computational Study," in *Physics of Semiconductors: 28th International Conference on the Physics of Semiconductors - ICPS 2006*, vol. 893 of *American Institute of Physics Conference Series*, pp. 1041–1042, 2007.

[C22] O. Baumgartner, M. Karner, S. Holzer, M. Pourfath, T. Grasser, and H. Kosina, "Adaptive Energy Integration of Non-Equilibrium Green's Function," in *NSTI Nanotech Technical Proceedings*, vol. 3, (Santa Clara), pp. 145–148, 2007. Poster: The Nanotechnology Conference and Trade Show.

[C23] M. Pourfath and H. Kosina, "The Effect of Optical Phonon Scattering on the On-Current and Gate Delay Time of CNTFETs," 2007 *accepted.* Poster: International Conference on the Simulation of Semiconductor Processes and Devices (SISPAD).

[C24] M. Pourfath, H. Kosina, and S. Selberherr, "The Role of Inelastic Electron-Phonon Interaction on the On-Current and Gate Delay Time of CNT-FET," 2007 *accepted.* Talk: European Solid-State Device Research Conference (ESSDERC).

Chapter in Books

[B01] M. Pourfath and H. Kosina, "Fast Convergent Schrödinger-Poisson Solver for the Static and Dynamic Analysis of Carbon Nanotube Field Effect Transistors," in *Large Scale Scientific Computing* (I. Lirkov, S. Margenov, and J. Wasniewski, eds.), vol. 3743 of *Lecture Notes in Computer Science*, pp. 578–585, Springer, 2006.

Patents

[P01] M. Pourfath, H. Kosina, W. Park, B.-H. Cheong, and E.-J. Bae, "Transistor with Carbon Nanotube Channel and Method of Manufacturing the Same." Patent: No. EP1655791, submitted: 09-09-2005, granted: 05-10-2006.

	Author	Co-Author	Total
Journals	8	3	11
Conferences	21	3	24
Chapter in Books	1	0	1
Patents	1	0	1
Total	31	6	37

Table 1: Publication Statistics.

Curriculum Vitae

July 18th, 1978
Born in Tehran, Iran.

June 1996
High school graduation in *Mathematics & Physics*.

September 1996
Enrolled in *Electrical Engineering* at the Sharif University of Technology, Tehran, Iran.

September 2000
Received the degree of B.Sc. in *Electronics* from the Sharif University of Technology.

September 2002
Received the degree of M.Sc. in *Electronics* from the Sharif University of Technology.

October 2003
Entered doctoral program at the Institute for Microelectronics, TU Wien.